



DI Christiane Essl, BSc

# **Analysis and early detection of failing automotive lithium-ion batteries**

**DOCTORAL THESIS**

to achieve the university degree of  
Dr. techn.

submitted to

**Graz University of Technology**

Supervisor: Adj.-Prof. Dr. Anton Fuchs  
**Institute of Electrical Measurement and Sensor Systems**

Graz, February 2021

## **EIDESSTATTLICHE ERKLÄRUNG**

Ich erkläre an Eides statt, dass ich die vorliegende Arbeit selbstständig verfasst, andere als die angegebenen Quellen/Hilfsmittel nicht benutzt, und die den benutzten Quellen wörtlich und inhaltlich entnommenen Stellen als solche kenntlich gemacht habe. Das in TUGRAZonline hochgeladene Textdokument ist mit der vorliegenden Dissertation identisch.

---

Datum

---

Unterschrift

Ein Diamant ist ein Stück Kohle, das Ausdauer hatte. – Louis Tiffany

Die vorliegende Arbeit wurde im Zeitraum von November 2016 bis Februar 2021 als industriennahe Dissertation am VIRTUAL VEHICLE Research GmbH im Rahmen der Doktoratsstudien an der Technischen Universität in Graz unter Anleitung von Adj.-Prof. Dr. Anton Fuchs durchgeführt.

## - Danke -

Mein besonderer Dank gilt meinen lieben Eltern Franz und Elisabeth. Danke für die stets freundschaftliche und herzliche Unterstützung! Ebenso möchte ich meiner lieben Großmutter Theresia danken, die mir wortwörtlich die Arbeit versüßt hat. Natürlich auch meiner besseren Hälfte, Michael, herzlichen Dank für Deine Motivation ❤️ Werte Geschwister, liebe Nichten und Neffen, liebe Freunde, besonders liebe Julia, ein großes DANKE für euer Verständnis und die Motivation.

Ein großer Dank gilt dem VIRTUAL VEHICLE, insbesondere Alex Thaler und Andrej Golubkov, für die Möglichkeit der kooperativen Zusammenarbeit im Batterie Team und der Möglichkeit eigene Themen zu entwickeln und voranzutreiben. Danke dem gesamten Labor Team für die gute Zusammenarbeit und die gewissenhafte Durchführung der Experimente im Reaktor. Gemeinsam haben wir das Labor zu hochqualitativen und stets ausgebuchten Prüfständen entwickelt ;). Ebenfalls danke der gesamten Batterie Gruppe – es ist mir eine Freude mit euch zu arbeiten. Danke für die gute Stimmung im Team.

Für die wissenschaftliche Unterstützung bedanke ich mich herzlichst bei Anton Fuchs, der sich trotz seines vollen Terminkalenders immer wieder Zeit für meine Fragen genommen hat und tatkräftig bei Publikationen unterstützt hat. Vielen Dank für die Betreuung meiner Doktorarbeit, Dein konstruktives Feedback und die Möglichkeit selbstständig an diesem aktuellen und spannenden Thema zu arbeiten!

Ein herzlicher Dank gilt auch Marcelina Pyschik, die mir die einzigartige Möglichkeit gegeben hat, bei AUDI AG mitzuarbeiten und wertvolle Einblicke in die Serien- und Vorentwicklung ermöglicht hat! Vielen Dank für Deinen wissenschaftlichen Rat und Dein Interesse an der Untersuchung von aktuellen automotiven Batterien! Danke auch an die gesamte Abteilung I/EA-31 in der AUDI AG für die freundliche Aufnahme bei meinen Ingolstadt-Aufenthalten und für das Interesse an meiner Dissertationsarbeit – es hat mich immer sehr gefreut mit euch in der Abteilung zu arbeiten und euch von den neusten Ergebnissen zu berichten! Ein besonderes Danke auch an Paul Schneider, Peter Juris und Peter Pilgram für die gute weiterführende Zusammenarbeit.

Es freut mich wirklich sehr, dass Interesse an meinem Dissertationsthema bestand und besteht, und dass die Ergebnisse auch Einsatz in hochwertigen Serienprodukten finden.

Dankbar bin ich für die finanzielle Unterstützung meiner Arbeit durch die Österreichische Forschungsförderungsgesellschaft mbH (FFG) im Rahmen des COMET K2 Digital Mobility Programms, der „Industrienahen Dissertationen“ sowie der beiden FFG Projekte GALION und SafeBattery. Mein Dank gilt auch der finanziellen Unterstützung durch das AUDI Doktorandenprojekt.



## Abstract

Lithium-ion batteries (LIBs) are a state-of-the-art energy storage system for the growing electric vehicle (EV) market. Although less vehicle fires per kilometers driven are reported in EVs compared to combustion engine vehicles, exothermic chemical reactions like the thermal runaway (TR), fire or explosions are possible. New regulations (GB 38031-2020) prescribe a warning of the passengers at least five minutes prior to serious incidents. However, current battery monitoring systems are not designed to detect battery failures before the TR. Additionally, comprehensive battery failure analyses before the TR and TR influencing factors are rarely addressed in literature. Thus, detailed insights in the battery failing behavior, improvements of battery safety and contributions to early battery failure detections are necessary.

This thesis focuses on two main research topics, which have not been sufficiently investigated in open literature: first, a detailed investigation of battery failure cases before the TR and the TR itself, with a special focus on vent gas composition; second, an intensive study of early detection of battery failures. Four battery failure cases were investigated in detail: unwanted electrolysis of voltage carrying parts, electrolyte vapor of damaged cell housings, first opening of failing cells (first venting) and the TR. Factors influencing the TR such as TR trigger, the cell type or cell design, different aging paths and the state-of-charge were analyzed using large high-energy automotive pouch and hard case cells, which are currently used in modern EVs. Single cells were triggered by overtemperature, overcharge or nail-penetration into failing state and the results were compared in three main hazard categories: the thermal behavior, the vent gas emission, and the vent gas composition. The gained knowledge helped to find commercially available sensors used as early battery failures detectors.

The experiments show that there are serious risks (safety and health) from failing LIBs resulting from vaporizing electrolyte, generated heat, gas emission (amount and concentration) and particle emission during the TR. For each hazard category, safety relevant parameters were quantified and used for comparison. Novel insights in the failing behavior of large LIBs were generated: Failure cases before the TR can be detected due to gas emission, consisting mainly of H<sub>2</sub> and volatile organic compounds (electrolyte vapor). The temperature measurement of the cell surface most likely does not detect the failure stages before the TR. Cells charged up to 30% SOC could not be triggered into TR, but each fully charged cell could. If a TR can be triggered, a large amount of vent gas is produced, consisting of toxic (CO) and burnable (H<sub>2</sub>) components, accompanied by an extreme rise in cell temperature. The TR trigger turned out to be decisive for the failing behavior. The overcharge trigger in particular has the highest impact resulting in higher amounts of produced vent gas, increased toxicity (CO amount) of the vent gas components and higher mass loss. The cell type and the burst design also influences the failing behavior, especially on the opening of the cell housing, when the TR starts, and the duration of the TR event. Aged cells showed a reduced failing reaction, reduced maximal temperatures, lower amount of produced gas, significantly lower amount of CO in the vent gas and lower mass loss than fresh cells. In conclusion, early battery failure detection using gas sensors was tested. The most promising gas sensors can detect H<sub>2</sub> produced in unwanted electrolysis, electrolyte vapor and gases produced by degassing of LIBs and contribute significantly to battery failure detection.

The results and findings are valuable for the scientific and industrial community dealing with LIBs, such as battery pack producers, car manufacturers, testing institutions for the development of future battery testing facilities and regulations as well as sensor manufacturers and may significantly contribute to battery failure detection and improvement of battery safety.

## Kurzfassung

Lithium-Ionen-Batterien (LIBs) sind als Energiespeicher für den wachsenden Elektrofahrzeug (EVs) Markt sehr attraktiv. Obwohl deutlich weniger Fahrzeugbrände von EVs gemeldet werden als bei Fahrzeugen mit Verbrennungsmotoren, können Fehler in der Batterie zu exothermen chemischen Reaktionen wie den Thermal Runaway (TR), Feuer oder Explosion führen. Neue Vorschriften (z.B. GB 38031-2020) fordern für EVs eine Warnung der Fahrgäste mindestens fünf Minuten vor möglicher Gefährdung. Die aktuellen Systeme sind jedoch nicht darauf ausgelegt, Batteriefehler vor dem TR zu erkennen. Des Weiteren gibt es kaum Literatur über Batteriefehler vor dem TR oder von den TR-Einflussfaktoren. Detaillierte Untersuchungen von möglichen Batteriefehlern sind somit notwendig, um Fehler von Batterien frühestmöglich zu erkennen und darauf reagieren zu können.

Diese Doktorarbeit fokussiert sich auf zwei Hauptforschungsbereiche: Erstens, eine detaillierte Untersuchung von Batteriefehlerfällen vor dem TR und dem TR selbst und zweitens, eine intensive Studie zur frühzeitigen Erkennung von Batteriefehlern.

Dazu wurden vier Batteriefehlerfälle untersucht: ungewollte Elektrolyse zwischen spannungsführenden Teilen, austretender Elektrolytdampf aus einer beschädigten Zelle, erste Öffnung des Zellgehäuses bei einer fehlerhaften Zelle und der TR selbst. TR-Einflussfaktoren wie TR-Trigger, der Zelltyp oder das Zelldesign, verschiedene Alterungspfade und der Ladezustand wurden anhand moderner Pouch-Zellen und prismatischen Zellen analysiert, die derzeit in EVs eingesetzt werden. Einzelne Zellen wurden durch Übertemperatur, Überladung oder Nageltrigger in den Versagenszustand geführt und die Ergebnisse in drei Hauptkategorien verglichen: thermisches Verhalten, Gasemission und Gaszusammensetzung. Die gewonnenen Erkenntnisse wurden für die Suche nach geeigneten Sensoren zur Früherkennung von Batteriefehlern verwendet.

Ernsthafte Risiken für die Sicherheit und Gesundheit bestehen durch austretenden Elektrolytdampf (z.T. brennbar, toxisch), große Mengen an Gas, welches giftige (CO) und brennbare (H<sub>2</sub>) Bestandteile enthält, extremen Anstieg der Zelltemperatur bis über 800°C und der Emission von heißen Partikeln während eines TR. Für jede Gefahrenkategorie wurden sicherheitsrelevante Parameter definiert und für die untersuchten Zellen quantifiziert. Es wurden neue Erkenntnisse über das Fehlverhalten großer LIBs gewonnen: Der TR-Auslöser erwies sich als entscheidend für das Fehlverhalten, besonders Überladung führt zu höheren Mengen an Gas, erhöhter Toxizität der Gasbestandteile und höherem Massenverlust. Der Batteriezelltyp und das Design der Berstscheibe beeinflussen das Fehlverhalten ebenfalls, insbesondere die Öffnung des Zellgehäuses, den Zeitpunkt des TR-Starts und die Dauer des TR. Gealterte Zellen zeigten eine reduzierte Reaktion: geringere Maximaltemperaturen, eine geringere Menge an produziertem Gas, eine signifikant geringere Menge an CO und einen geringeren Massenverlust als frische Zellen. Durch die Messung von Gasemission (H<sub>2</sub> und volatile organische Komponenten (Elektrolytdampf)) ist die Erkennung von Batteriefehlern vor dem TR möglich. Für die frühzeitige Erkennung wurden deshalb Gassensoren getestet. Die vielversprechendsten Gassensoren können H<sub>2</sub>, das bei unerwünschter Elektrolyse entsteht, Elektrolytdampf und Gase, die bei der Ausgasung von fehlerhaften LIBs entstehen, detektieren und tragen somit wesentlich zur frühzeitigen Erkennung von Batteriefehlern bei.

Eine umfassende Analyse des Fehlverhaltens moderner hochenergetischer Batterien ist relevant, um ein akzeptables Sicherheitsniveau in EVs zu erreichen. Die Ergebnisse und Erkenntnisse sind wertvoll für Wissenschaft und Industrie, die sich mit LIBs beschäftigt, wie z.B. Batteriepack-Designer, Automobilhersteller und Prüfinstitute für die Entwicklung zukünftiger Batterietesteinrichtungen und Vorschriften. Die Ergebnisse können einen wichtigen Beitrag zur Fehlererkennung und Verbesserung der Batteriesicherheit leisten.

# Contents

- Danke -.....	iv
<b>Abstract.....</b>	<b>v</b>
<b>Kurzfassung.....</b>	<b>vi</b>
<b>Contents .....</b>	<b>vii</b>
<b>1 Motivation.....</b>	<b>1</b>
<b>2 Introduction .....</b>	<b>2</b>
2.1 Lithium-ion batteries in electric vehicle applications.....	2
2.2 Battery cell chemistry and aging .....	3
2.3 Battery decomposition reactions .....	5
2.4 Safety relevant parameters of failing lithium-ion batteries.....	5
2.4.1 Electrolyte vaporization .....	6
2.4.2 Heat generation/thermal behavior .....	6
2.4.3 Gas emission.....	6
2.4.4 Gas composition.....	6
2.4.5 Particle emission.....	7
2.5 Battery thermal runaway analysis.....	7
2.5.1 Influence of the energy content.....	8
2.5.2 Influence of the chemistry .....	8
2.5.3 Influence of the state-of-charge.....	8
2.5.4 Influence of the thermal runaway trigger .....	8
2.5.5 Influence of the cell type.....	9
2.5.6 Influence of the aging path .....	9
2.5.7 Thermal runaway analysis at VIRTUAL VEHICLE.....	10
2.6 Early battery failure detection with gas sensors.....	11
2.7 What is missing in current literature and what is needed? .....	12
2.8 Research focus.....	15
2.9 Thesis outline .....	16
<b>3 Methods and measurement technologies .....</b>	<b>17</b>
3.1 Investigated cells .....	17
3.2 Thermal runaway reactor setup.....	19
3.2.1 Experimental method.....	19
3.2.2 Thermal runaway trigger.....	21
3.3 Safety-relevant thermal runaway parameters.....	21

3.3.1	Thermal behavior .....	22
3.3.2	Vent gas emission.....	23
3.3.3	Vent gas composition .....	23
3.3.4	Particle collection and particle analysis .....	25
3.3.5	Additional safety-relevant parameters .....	26
3.4	Early failure detection method development .....	26
3.4.1	Investigated battery failure cases .....	27
3.4.2	Analysis of produced gases .....	28
3.4.3	Sensor selection .....	29
3.4.4	Sensor test setup.....	30
3.4.5	Event detection .....	30
3.5	Designs of experiments .....	31
3.5.1	DoE – Comprehensive hazard analysis and SOC influence.....	32
3.5.2	DoE – TR trigger and cell type influence .....	33
3.5.3	DoE – Aging paths influence.....	33
3.5.4	DoE – Early battery failure detection with gas sensors.....	35
<b>4</b>	<b>Experimental results and discussion .....</b>	<b>36</b>
4.1	Comprehensive hazard analysis and SOC influence.....	36
4.1.1	Thermal behavior .....	37
4.1.2	Vent gas emission.....	39
4.1.3	Vent gas composition .....	41
4.1.4	Particle emission.....	45
4.1.5	Mass reduction.....	48
4.1.6	Optical observation of the cell after TR.....	48
4.2	Influence of thermal runaway trigger and cell type.....	49
4.2.1	Thermal behavior .....	50
4.2.2	Vent gas emission.....	54
4.2.3	Vent gas composition .....	57
4.2.4	Mass reduction.....	59
4.2.5	Comparing the trigger .....	60
4.3	Influence of aging .....	62
4.3.1	Thermal behavior .....	63
4.3.2	Vent gas emission.....	65
4.3.3	Vent gas composition .....	66
4.4	Reproducibility of the thermal runaway experiments .....	72

<b>5</b>	<b>Early failure detection</b> .....	<b>73</b>
5.1	Gases produced in the investigated four battery failures.....	73
5.2	Sensor selection .....	74
5.3	Sensor tests .....	76
5.3.1	Electrolysis.....	76
5.3.2	Electrolyte vapor .....	77
5.3.3	First venting and thermal runaway .....	78
5.3.4	Additional failure cases .....	83
5.3.5	Event detector .....	84
5.4	Comparison of different sensor types.....	86
5.4.1	Detectability of tracer gases.....	86
5.4.2	Lifetime of the sensors .....	87
5.4.3	Cross sensitivity .....	87
5.4.4	Most promising sensors for battery failure applications .....	88
<b>6</b>	<b>Summary and conclusion</b> .....	<b>89</b>
a.	Comprehensive hazard analysis and influence of SOC.....	89
b.	Influence of thermal runaway trigger and cell type.....	90
c.	Influence of aging .....	91
d.	Early failure detection of battery failures using gas sensors .....	92
<b>7</b>	<b>Outlook</b> .....	<b>94</b>
<b>8</b>	<b>Publications</b> .....	<b>95</b>
8.1	Journal publications .....	95
8.2	Scientific presentations .....	95
<b>9</b>	<b>Appendix</b> .....	<b>97</b>
9.1	Supplementary material vent gas analysis.....	97
9.1.1	FTIR spectrometer settings .....	97
9.1.2	Gas chromatography accuracy .....	98
9.1.3	Specification of used test gases .....	99
9.2	Supplementary material particle analysis.....	100
<b>10</b>	<b>References</b> .....	<b>103</b>

## Abbreviations

LIB	lithium-ion battery
EV	electric vehicle
BEV	battery electric vehicle
HEV	hybrid electric vehicle
PHEV	plug-in hybrid vehicle
FCEV	fuel cell electric vehicle
TR	thermal runaway
BMS	battery management system
BMU	battery management unit
FTIR	Fourier-transform infrared (spectroscopy)
ppm	parts per million
GC	gas chromatography
TCD	thermal conductivity detector
SOC	state-of-charge
SOH	state-of-health
SEI	solid electrolyte interface
CEI	cathode electrolyte interface
OSD	overcharge safety device
OCV	open circuit voltage
ARC	accelerated rate calorimetry
EC	ethylene carbonate
DMC	dimethyl carbonate
DEC	diethylene carbonate
EMC	ethyl methyl carbonate
PC	propylene carbonate
O <sub>2</sub>	oxygen
H <sub>2</sub>	hydrogen
CO	carbon monoxide
CO <sub>2</sub>	carbon dioxide
C <sub>2</sub> H <sub>2</sub>	acetylene
C <sub>2</sub> H <sub>4</sub>	ethylene
C <sub>2</sub> H <sub>6</sub>	ethane
C <sub>3</sub> H <sub>6</sub>	propene
CH <sub>4</sub>	methane
H <sub>2</sub> O	water (gaseous)
C <sub>4</sub> H <sub>10</sub>	butane
C <sub>6</sub> H <sub>14</sub>	hexane
HF	hydrogen fluoride
NMC	LiNiMnCoO <sub>2</sub>
NCA	LiNiCoAlO <sub>2</sub>
LMO	LiMn <sub>2</sub> O <sub>4</sub>
LFP	LiFePO <sub>4</sub>
LCO	LiCoO <sub>2</sub>
LLI	loss of mobile Li inventory
LAM	loss of active material
SEM	scanning electron microscope

EDX	energy dispersive X-ray spectroscopy
BSE	backscattered electrons
SE	secondary electrons
PSD	particle size distribution
IC	ion chromatography
LOQ	limit of quantification
UNECE	United Nations Economic Commission for Europe
EVS-GTR	Electrical Vehicle Safety - Global Technical Regulation"
TR5	TR-propagation regulation (being developed by EVS-GTR)
MOx	metal oxide semiconductor, also MOS (sensor)
NDIR	nondispersive infrared (sensor)
VOC	volatile organic compound
BL	baseline
MNG	maximal negative gradient
MPG	maximal positive gradient
DoE	design of experiment
PCB	printed circuit board
ADC	analog-to-digital converter
I <sup>2</sup> C	inter-integrated circuit
CID	current interrupt device
SNR	signal-to-noise ratio
BL	baseline
ED1	event detector 1
ED2	event detector 2
ICTM	Institute of Chemistry and Technology of Materials, Graz University of Technology
FELMI	Institute of Electron Microscopy and Nanoanalysis, Graz University of Technology

# 1 Motivation

Lithium-ion batteries (LIBs) are currently a dominant state-of-the-art energy storage system [1,2] and gain importance in the automotive sector because of the potential of electric vehicles (EVs) to reduce greenhouse gas emissions and air pollution. The market of battery electric vehicles (BEVs), hybrid electric vehicles (HEVs) and plug-in hybrid vehicles (PHEVs) increases, especially in China, the U.S. and the EU [3,4]. Forecasts show a significant importance of EVs in the future transport sector. Still there are challenging requirements for LIBs in the automotive sector such as costs, fast charging, aging effects, increasing energy density and safety [5]. The global competition forces the battery producer to increase the energy density, to reduce the costs of their products and to keep an acceptable safety level at the same time. With increasing energy density this is very challenging.

There are serious hazards resulting from failing battery cells which lead to exothermic chemical reactions inside the cell. The worst case is the uncontrollable exothermic chemical reaction—the thermal runaway (TR) [5]. The TR caused most of EV fires [6] and is a self-accelerating exothermic chemical reaction inside the cell which can be started by a hot spot produced inside the cell (e.g., particle short circuit) or by a heat source outside the cell (e.g., electrical failure) [7–10]. These possible defects inside or outside the cell causing exothermic reactions challenge the safety for LIB applications. During TR, extensive amounts of heat, toxic and flammable gas and hot particles are generated with critical consequences like fire, explosion and toxic atmosphere [5,9,11].

Although current statistics indicate that fewer vehicle fires per one billion kilometers driven occur for EVs than for vehicles with internal combustion engines [12–14], safety concerns about this high energy storage system are present and fire incidents of EVs have attracted media attention [6,15]. Thus, a detailed analysis of possible failures and the TR behavior need to be investigated in detail in order to minimize the risks from failing LIB and to increase safety.

To understand the LIB failing behavior and to prevent failures and their consequences, different LIB safety tests, also called abuse tests, have been developed. Experts aim to find standardized TR test procedures, but currently no agreement could be found. No detailed comparison of the thermal behavior, the vent gas emission and the vent gas composition are currently available in open literature. These abuse tests help to understand the failing behavior, to develop a safer battery pack design, build up safety measures and develop methods for early battery failure detection.

New regulations such as the Chinese regulation GB 38031-2020 and the global discussions by Electrical Vehicle Safety - Global Technical Regulation (EVS-GTR) prescribe a warning of passengers at least five minutes before serious incidents [16,17]. Developing methods for early failure detection and reducing safety risks from failing high energy LIB has become a major challenge for industry, research and development [18]. State-of-the-art battery monitoring equipment applied in a modern EV battery pack, like cell voltage measurement and temperature sensors, is inadequate to reach the upcoming level of safety requirements and to reliably enable early failure detection.

In order to enhance battery safety and to fulfill EVS-GTR20 and GB 38031-2020, a detailed investigation of hazards from failing LIBs, the influence of different abuse triggers on the failing behavior and early battery failure detection methods would be valuable for the scientific community in this field and the industry. For instance, gas sensor measurement additional to the existing battery monitoring system is promising to detect a battery failure in an early stage but needs to be investigated in more detail.

## 2 Introduction

*Parts of this chapter were already published in:*

Essl C, Golubkov AW, Gasser E, Nachtnebel M, Zankel A, Ewert E, Fuchs A. Comprehensive hazard analysis of failing automotive Lithium-ion batteries in overtemperature experiments. *Batteries* 2020; **6**(30): 1–28. DOI: 10.3390/batteries6020030.

Essl C, Golubkov AW, Fuchs A. Comparing Different Thermal Runaway Triggers for Two Automotive Lithium-Ion Battery Cell Types. *Journal of The Electrochemical Society* 2020; **167**(130542): 1–13. DOI: 10.1149/1945-7111/abbe5a.

Essl C, Seifert L, Rabe M, Fuchs A. Early detection of failing automotive batteries using gas sensors. *Batteries* 2021 (accepted March 2021).

Essl C, Golubkov AW, Fuchs A. Influence of aging on the failing behavior of automotive lithium-ion batteries. *Batteries* 2021 (accepted March 2021).

### 2.1 Lithium-ion batteries in electric vehicle applications

LIBs, initially commercialized by Sony 1991, are now a dominant state-of-the-art energy storage system [1,2], and are still the most promising candidates for storing electrical energy [19,20]. LIB technology provides the best mix of key battery performance metric such as high specific energy, high energy density, high power density, long lifetime, costs and safety [1], that currently cannot be achieved with any other available technology. Therefore, this technology is attractive for portable electronic devices, consumer electronics and the automotive industry. Especially for EVs like full BEVs, HEVs, PHEVs and also in fuel cell electric vehicles (FCEV), the LIB technology is currently very promising. Current orders of magnitude for battery capacities (in kWh) for EVs are typically in the range of 17.4 – 100 kWh for BEVs [21], 4.4 – 27.2 kWh for PHEVs [22] and about 1.6 kWh for HEVs and FCEVs [23].

Reliable battery packs are a key component of EVs. For EV applications three main battery cell types are used at the moment, which are presented in **Figure 1**: pouch bag cells (sealed laminated foils), and two cell types using metallic hard case housing: the prismatic hard case cell and the cylindrical hard case cell. The metallic housing is typically made out of aluminum or stainless steel. Each cell type is available in different dimensions with different cell chemistry, energy content and energy density.

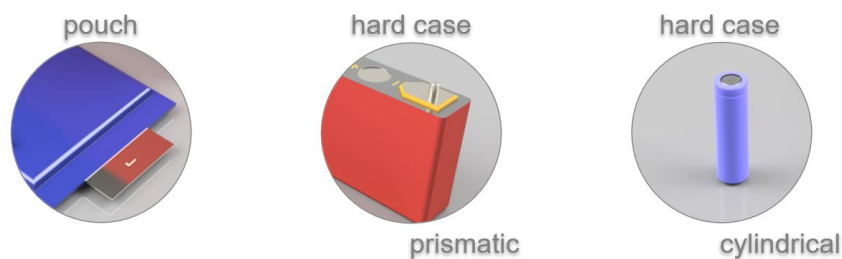


**Figure 1: Three main cells types are used in modern electric vehicles from left to right: pouch bag cell, and two cell types using a hard case housing: the prismatic hard case cell and the cylindrical hard case cell.**

For the EV application the single cells are mechanically assembled to a battery module. Several battery modules are electrically and mechanically connected to form a battery pack. The battery management system (BMS), also named battery management unit (BMU) forms the control unit of the batteries to the vehicle. The BMS is the heart of battery operation, performance, monitoring and failures detection inside EVs. The BMS is designed to ensure safe and reliable operation of the batteries [24] and should meet the functional safety standards ISO 26262. This control unit manages cell balancing, thermal management, charge and discharge control, state estimation such as state-of-charge (SOC) and state-of-health (SOH) and cell monitoring [25]. A good BMS is designed particularly for the specific cells and modules according to their safety limits.

LIBs operate best in a cell specific temperature range [12]. Consequently, a thermal management system is recommended to prevent cell damaging operation such as overheating of the cells or fast charging at very low temperatures, which may lead to unwanted lithium (Li) plating [26]. The cooling or heating of the battery cells can be achieved for instance with liquid direct or indirect cooling and can also help to prevent TR propagation [27]. Additional to thermal TR propagation measures the use of extra resistant layers between neighboring cells is recommended [28]. The extra resistive layer prevents or at least slows down TR propagation from one failing cell to the neighboring cells due to abrasive gas and particle stream.

## 2.2 Battery cell chemistry and aging

The chemistry of the cell plays an important role to reach a high energy density and also for the safety behavior. In general to reach the goal of a high energy density (gravimetric in W/kg or volumetric in W/L) two criteria need to be fulfilled: “a high number of available charge carriers per mass or per volume unit of the material”, and a high cell voltage, which depends on “a high (positive electrode) and low (negative electrode) standard redox potential of the respective electrode redox reaction” [29]. Li as electrode material has the highest electrode potential [1], and consequently is highly attractive as electrode material. But Li or also carbon intercalated Li is highly reactive with all polar aprotic solvents, salts, anions and many conducting polymers [30].

So, state-of-the-art battery chemistries used in EVs are based on Li-ion technology. Currently used LIB materials are: LiNiMnCoO<sub>2</sub> (NMC), LiNiCoAlO<sub>2</sub> (NCA), LiMn<sub>2</sub>O<sub>4</sub> (LMO), LiFePO<sub>4</sub> (LFP) and LiCoO<sub>2</sub> (LCO) as cathode; graphite, carbonaceous materials and Si-alloys as anode [31]. Organic carbonates are used as state-of-the-art solvents in commercial LIB electrolytes [31]. The main composition of modern electrolytes used in LIB consist of lithium hexafluorophosphate (LiPF<sub>6</sub>) dissolved in a mixture of cyclic carbonate ethylene carbonate (EC) and propylene carbonate (PC), and the linear carbonates such as dimethyl carbonate (DMC), ethyl methyl carbonate (EMC), or diethyl carbonate (DEC) [1]. A separator between the electrodes is used [32]. These separators are characterized by their “thinness and thermal shutdown properties” [33]. For safety improvements ceramic coatings on one or both sides of the separator are used. The cells are encased with sealed laminated foils (pouch cells) or metallic hard housings. During the first charge of the LIB a passivation layer—the so-called solid electrolyte interface (SEI)—develops on the anode.

Since the commercialization of LIBs, the technology, the production, the material and chemistry were continuously improved [1]. Due to the good energy density of NMC chemistries (see **Figure 2**) compared to other battery chemistries, NMC is the most widely used cathode material in current EV applications. The combination of nickel, cobalt and manganese is described with the following

expression of  $\text{LiNi}_x\text{Mn}_y\text{Co}_z\text{O}_2$  (NMC). Recently the combination of  $x:y:z = 1:1:1$ , also written as NMC (111), or with higher nickel content such as NMC (442), (523), (622) or (811) are used. Because the failing behavior itself, the aging and the chemical reactions during the battery failing behavior is influenced by the cell chemistry, the focus in the following chapters is laid on literature of LIBs with NMC – graphite-based cell chemistry.

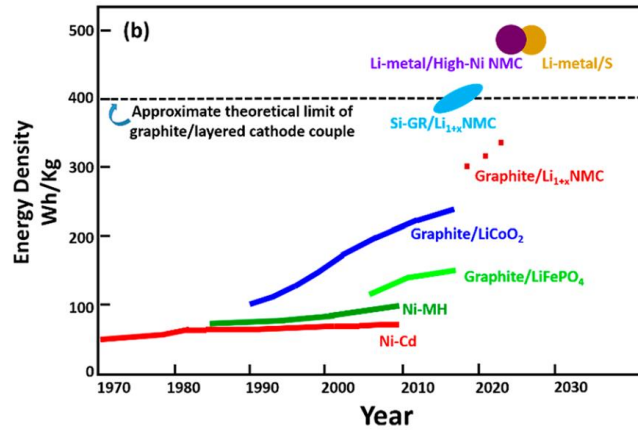


**Figure 2: Evolution of the gravimetric energy densities for various battery chemistries [1].**

Beside the advantages of LIBs, they still suffer from degradation of the cell components, which is called aging. Several researchers have studied the capacity fading and consequently the aging of different Li-ion cell chemistries. The cell capacity in general is strongly influenced by the amount of mobile lithium (Li) (transferable Li between anode and cathode) and the capacity of the cathode and anode to take up this mobile Li. If parts of this mobile Li are demobilized or the active material is limited to take up Li, the capacity fades irreversibly.

Main degradation mechanism for capacity fading/aging of LIBs with graphite anodes are [34–36]:

- Formation, decomposition, reformation and continuous growth of the SEI on the anode surface: active Li is irreversibly demobilized [35,37].
- Formation and growth of the CEI on the cathode: active Li is irreversibly demobilized [36].
- Consumption and decomposition of the electrolyte (also part of SEI growing), gas formation due to electrolyte decomposition [38].
- Structural and compositional changes at the cathode/electrolyte interface, the cathode and the anode : particle cracking at the cathode and at the anode and loss of electrical contact [34]. The active mass is no longer available for insertion of Li [34].
- Transition metal dissolution of the cathode [39].
- Decomposition of the binder and/or conductive agent [35].
- Limited Li absorption capacity of an electrode. Li gets lost on the other electrode (for instance in anode unavailable Li) [35].
- Metallic Li plating on the graphite anode [35,40].
- Gas formation due to impurities in the cathode material [40].
- Increasing ionic pore resistance in the anode, cathode, and separator due to mechanical compression [41,42].

This degradation mechanism leads to two main degradation modes: loss of mobile Li inventory (LLI) and loss of active material (LAM) at the anode and at the cathode [43]. Consequences of LLI and LAM

are capacity fade and power fade. According to Broussely et al. the most critical part of the cell is the interface between the negative electrode (anode) and the electrolyte [40]. They state that a good choice of materials stabilizes the negative electrode and then the reactivity of the positive electrode defines the battery aging mechanisms. Aging of current state-of-the-art LIBs during operation is inevitable, the capacity decreases and the resistance of the cell grows [44].

### 2.3 Battery decomposition reactions

Batteries are safe in normal operation condition without any internal defects. But if there is a defect inside or outside the cell causing exothermic reactions challenge the safety for LIB applications. Failure cases of LIB may cause high temperatures and undesirable chemical reactions, which can result in exothermic reactions with the worst case, the TR. TR is a self-accelerating exothermic chemical reaction inside the cell which can be started by a hot spot produced inside the cell (hot spot, particle short circuit) or by a heat source outside the cell (electrical failure) [7–10].

The TR mechanism are described in recent literature in [45–47]. Several decomposition stages of those cell materials in overheated LIBs have been published [48–51]. Main reactions according to literature include for the listed cell chemistries in general:

- >70 °C: The conducting salt starts to decompose and reacts with solvents and the SEI [52–55].
- >120 °C: Reaction between intercalated Li in the anode and electrolyte occur initiated by the SEI breakdown (90–130 °C [56]). Heat is generated [10,56]. Li and electrolyte reaction can occur between 90–230 °C [56] and produces gases like ethylene (C<sub>2</sub>H<sub>4</sub>), ethane (C<sub>2</sub>H<sub>6</sub>) and propene (C<sub>3</sub>H<sub>6</sub>) [8].
- >130 °C: Further gas develops, and electrolyte vaporizes. The cell internal pressure increases until the cell housing opens at the weakest point. Accumulated gas vents from inside the cell into the battery pack (so called first venting). It can occur at about 120–220 °C cell surface temperature [36,57]. Separator melts between 130 °C–190 °C [9,58].
- ~160 °C: Starting at about 160 °C the exothermic process inside the cell accelerates the self-heating and results in a TR. The TR is accompanied by violent gas and particle release (second venting). Electrolyte decomposes exothermally [8,59] between 200–300 °C [56]. At the TR, the cell temperature increases enormously due to chemical reactions inside the cell. Metal oxide cathodes decompose and produce oxygen (O<sub>2</sub>) [60–62]. O<sub>2</sub> further reacts with electrolyte and produces carbon dioxide (CO<sub>2</sub>) and water (H<sub>2</sub>O) vapor [59,61].

During battery failures, like the TR, violent reactions inside the cell produce significant amounts of hot, toxic and flammable gas and the cell ejects hot particles [5]. The released gas and particles may cause serious safety and health risks, like fire, explosion, and toxic atmosphere.

### 2.4 Safety relevant parameters of failing lithium-ion batteries

It is essential to identify comparable hazards and safety parameters to evaluate the failing behavior of different cell types reliably and to set necessary safety measures. Especially for large automotive batteries designed for EV applications safety considerations are especially important [63]. But which hazards need to be addressed, which safety-relevant parameters need to be quantified and which methods are suitable for a comprehensive hazard analysis of a cell?

In literature several important hazards from failing state-of-the-art batteries are reported resulting in main five hazards, which may lead to safety and health risks (**Figure 3**). These hazards can be categorized into two failing states: The first venting, which leads to the hazard electrolyte vaporization and the TR itself with the hazards of heat generation, gas emission, gas concentration and particle emission. Hazards based on high voltage and current are not considered in this thesis. The first venting and the TR of the cell can cause the following hazards:

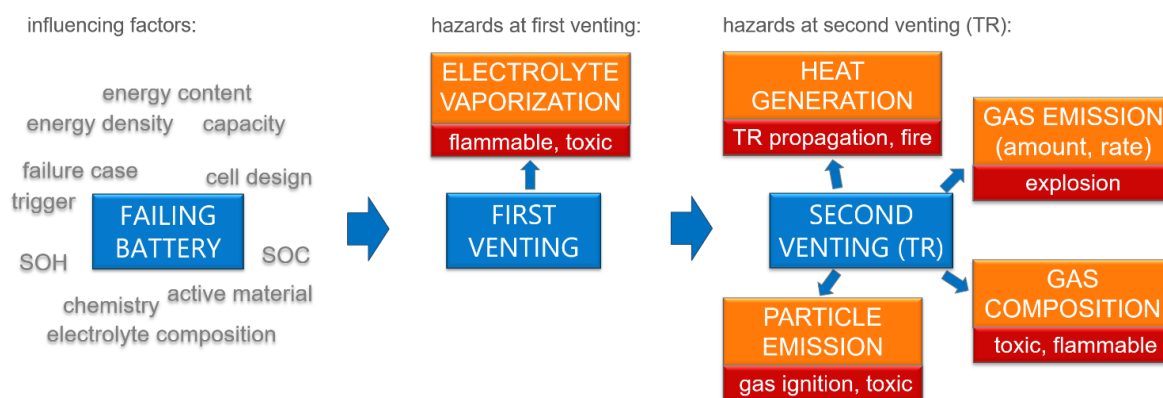


**Figure 3: A failing battery can lead to hazards produced at the opening of the cell housing (first venting) and at the TR. Five categorized hazards (orange) and their consequences on safety and health (red) are presented. The battery failures are influenced by several factors. This figure is based on [5].**

#### 2.4.1 Electrolyte vaporization

Electrolyte vaporizes starting at the opening of the cell housing. Contemporary electrolytes for LIBs are known to be flammable, irritant, toxic, and/or corrosive depending on the exact composition of the electrolyte mixture [7,64,65] and need to be considered as a safety and health risk. Electrolytes are assumed to be a major source of poor safety with high volume gas decomposition, large combustion enthalpy and flammability of solvent vapor [66].

#### 2.4.2 Heat generation/thermal behavior

Heat generation [7,57,67–69] and significant temperature increase is one safety hazard of the TR, which may lead to TR propagation to neighboring cells or battery fire [70]. Safety-relevant parameters are the cell temperature at the first venting of the cell, the TR onset temperature, the maximum reached cell surface temperature and the vent gas temperature. The temperature of the produced vent gas and the ejected particles out of the cell can reach critical high temperatures up to 1000°C [57] and may damage the cell surrounding materials irreversibly.

#### 2.4.3 Gas emission

Gas emission [7,61,71,72] is another hazard with the possible consequence of explosion and rapid destruction of the pack. At the TR significant amount of gas [73,74] is produced within seconds. Safety-relevant parameters are the amount of produced gas (in mol or liter) and the venting rate (in mol/s or L/s). The gas emission at TR for current state-of-the-art batteries with regular electrolytes is expected in the range of 1.3 L/Ah up to 2.5 L/Ah (at STP: 298.15 K, 100 kPa) [11,73]. At heat ramp TR experiments of 50 Ah prismatic LMO cells characteristic venting rates were  $(0.8 \pm 0.3)$  mol/s [57].

#### 2.4.4 Gas composition

Main gas compounds at TR are CO<sub>2</sub>, carbon monoxide (CO), hydrogen (H<sub>2</sub>) and hydrocarbons [70,71]. The produced gas is toxic and flammable [64,75]. Except for CO<sub>2</sub> and H<sub>2</sub>O all produced gases are

flammable, explosive and deflagration of the produced vent gas in contact with O<sub>2</sub> is possible. In addition, small amounts of toxic gases like hydrogen fluoride (HF) can be produced by decomposition of fluorine compounds as LiPF<sub>6</sub> [70,76].

### 2.4.5 Particle emission

At TR solid hot particles of active materials and aerosols can be released by the failing cell, which are critical to ignite the combustible vent gas [7,77] or can lead to a short circuit between two neighboring cells or on the electronics. Particles should be considered as additional toxic hazard [7] and health risk. The ejected material is a mixture of solid particles, aerosols of active material, parts of current collector foil and electrolyte from the cell.

## 2.5 Battery thermal runaway analysis

To understand the LIB failing behavior and to prevent failures and their consequences, different LIB safety tests, also called abuse tests, have been developed. Thermal, electrical and mechanical abuse scenarios attempt to mimic the behavior of the failing battery in real applications [78,79]. Different kinds of battery abuse tests were developed and investigated [80]. The most investigated battery failure case is the TR itself. In general, requirements for TR test methods are to be meaningful (i.e., field-relevant), realistic, reproducible, easy to perform by different test labs and they should not be easy to manipulate. The tests are carried out and documented in literature on single cell, module or even battery pack level. Popular examples are: TR triggered by overtemperature, hot spots, overcharge, external and internal short circuit, crush or the penetration of the cell with foreign objects, like nail-penetration [81].

Experts from United Nations Economic Commission for Europe (UNECE) discuss suitable TR tests for the EVS-GTR. Due to missing standardized TR test procedures and varying cell formats, there is currently no agreement which test procedure should be favored to accurately define the TR [17,82]. TR-propagation regulation (TF5) being developed in EVS-GTR contains three testing methods: heating, overcharge and nail-penetration [83].

Many researchers have studied single hazard categories from failing LIBs for different cell types and different chemistries [57,67,71,72], but mainly for small capacity cells with <5 Ah [71,72,84,85]. NMC/graphite composites are currently one of the preferred LIB chemistries in EVs and higher cell capacities and higher energy densities lead to more severe TR reaction [46,73].

Single hazard categories from NMC and NMC/LMO cells with >20 Ah are published in [46,52,64,73,77,83,86]: Fang and Gao et al. concentrate on the heat generation during heat triggered TR for 25 Ah NMC [52], 1–50 Ah NMC and NMC/LMO [46] and TR propagation of 42 Ah prismatic BEV [83] cells. Ren et al. evaluate heat generation at different SOH [36]. Koch et al. focus on gas emission (amount), gas composition and mass loss at overtemperature experiments in an atmosphere of air (present O<sub>2</sub>) [73]. Nedjalkov et al. analyze the gas composition in air (present O<sub>2</sub>) with a nail trigger to force TR [64]. Zhang et al. focus on particle emission [77] and gas composition [86] after heating the cell.

The battery failing behavior on cell level and the resulting hazards are influenced by several factors [5]: the energy content of the cell (capacity and energy density) [73,74,82], the chemistry/active material and separator [7,87], the electrolyte composition and additives [66,88], the state-of-charge (SOC)

[56,61,85,89], the failure case/trigger [7,84], the cell type (pouch versus prismatic hard case) [67], and the SOH/aging history [36,90]. Additionally, the presence of surrounding gases like O<sub>2</sub> changes the resulting hazards [84] due to additional chemical reactions.

### 2.5.1 Influence of the energy content

Increasing energy content inside the cell translate to higher probability of fire in case of cell deformation in crash incidents [63] and higher energy densities lead to more severe TR reaction [46,73]. That means that increasing energy density and capacity lead to a lower TR onset temperature (earlier TR) as well as a higher mass loss and a higher amount of gas produced during TR [73]. Feng et al. state that cells with higher energy density are more prone to TR [82]. Garche et al. mentioned the “correlation between increasing energy density and decreasing thermal stability” [91].

The trend in automotive industry goes in the direction of further increase energy density of the cells. This increases the requirements for safety measures as well.

### 2.5.2 Influence of the chemistry

Abuse tests show the influence of cell chemistry on the failing behavior and the thermal stability of the cell [4]. The stability of the battery and consequently the failing behavior depends on the chemistry, the use of active material, separator and electrolyte [7,62,66,74,87,88]. The stability of the delithiated cathode material plays an important role for exothermic phase degradation [91]. According to Fleischhammer et al. one of the safety risks contribute to TR is the loss of cathode stability leading to an exothermic degradation accompanied with oxygen release [62]. Additionally, the electrolyte composition and additives also influence the failing behavior [66,88]. Additives were developed to improve properties such as safety, flame retardance, SEI building, overcharge protection and reducing degassing [92,93].

Fleischhammer et al. stated that to reach a high capacity Li extraction from the cathode material is essential, but it is linked to a loss of stability [62]. With increasing Ni content in modern NMC cathode materials (high Ni content to low: NMC 811; 622; 532 and 111) the phase degradation is shifted towards lower temperature because of decreased stability effects of Ni [62]. Consequently the thermal stability of LIBs with higher Ni content is decreased [94].

### 2.5.3 Influence of the state-of-charge

If the cell is fully charged during thermal abuse the electrolyte reacts with the lithiated anode after the SEI breakdown [10,56]. Additionally, the stability of the delithiated cathode material is decreased with increasing SOC [89,91]. Consequently, decreased safety with increasing SOC is observed in [51,56,85,89] for different cell chemistries: NCA and LFP [85]; NCA [89]; NMC/LTO [51]. Increasing SOC leads to higher maximum temperature of the cell surface and to a higher amount of produced gas during TR [74]. Zhao et al. investigated the influence of increasing SOC up to 100% SOC and the 100% SOC charged fresh NMC cells released the higher thermal energy of all tests. Liu et al. observed decreasing onset temperature and increasing maximum battery surface temperature with increasing SOC [95]. The thermal interactions between several binder materials and anode carbon at 50% and 100% SOC is reported in [56].

### 2.5.4 Influence of the thermal runaway trigger

Current methods to characterize possible battery failures are battery abuse tests like overcharge, overtemperature, over-discharge, nail penetration and fire tests.

According to Feng et al., there is a lack of reproducibility in nail-penetration and overcharge tests [69]. Feng et al. reviewed abuse conditions of LIBs during accidents and stated that overcharge induced TR

can be more intense than other abuse conditions, because of excessive energy filled into the LIB [69]. Diaz et al. compared the gas generation of 2.5 Ah LCO pouch cells and 3 Ah LCO, 2.6 Ah NMC and 1.1 Ah LFP cylindrical cells at thermal abuse and nail-penetration and detected significant lower vent gas amount and mass loss for nail-penetrated cells than for thermal abused cells [84]. For nail-penetrated cells without TR, less than 20% of the vent gas and less toxic gas were produced than during thermal abuse at the same SOC (100%) [84]. Fernandez et al. explained differences in gas composition results from their overcharge abuse tests on 2.5 Ah LFP cells and overtemperature results in literature with the influence of different temperature inside and outside the cell on the vent composition [71]. Koch et al. tested sensors at TR on modules with heating and nail-penetration [96], but did not present the results of the different triggers concerning temperature of the failing cell, the amount of vent gas or the gas composition because the focus was set elsewhere. Larsson et al. published abuse tests by external heating, overcharge and short circuit of LFP and stated that overcharge or heating can theoretically end up in more severe reaction than in other abuse tests, due to the input of electric power or heat [97].

### 2.5.5 Influence of the cell type

Koch et al. stated that the “basic” effects occurring at the TR (loss of cell voltage, self-heating of the cell, production of gas, cell rupture, particle ejection) are similar for all cell types (cylindrical hard case, prismatic hard case and pouch cell) [96]. Beside the similar basic TR effects, the cell and venting design affects the cell reaction and might result in different thermal response of the cell, vent gas amounts and vent gas velocities [67,73,84]. Hard case cells have usually a defined cell vent, the so-called burst plate or safety vent. This burst plate is the weakest point of the cell housing and opens if a defined pressure inside the cell is reached. Pouch cells on the other hand have no defined cell vent and rupture along the pouch welded sides. Typically, the hard case cells can resist higher internal pressures than the soft pouch package [7], due to their vent design. Koch et al. identified more solid mass ejection during TR for hard case cells than for pouch cells and explains the observation with the higher stream velocities through the burst plate [73]. Huang et al. showed the failing behavior of 40 Ah NMC pouch and prismatic cells at 1 C overcharge experiments [98]. The pouch cell reached higher maximum temperatures on the cell surface than the prismatic cell, although the pouch cell had a better overcharge tolerance [98]. Additionally, the cell design, format and use of the package material (pouch, hard case) may influence the TR propagation as stated in [7].

### 2.5.6 Influence of the aging path

The influencing factor SOH includes capacity and power fading, but also the aging history and aging mechanisms play an important role. Researchers reported that the exact aging mechanisms and degradation modes depend highly on the used materials [40,99].

The changes in TR behavior of aged cells depend strongly on aging paths and aging mechanism: Ren et al. stated at the investigation of aging effects on the TR behavior, that the thermal stability of the anode and electrolyte exhibit obvious changes, whereas for the cathode the thermal stability remained unchanged during cyclic and storage aging [36]. Zhang et al. observed in calendar aged  $\text{LiMn}_2\text{O}_4$  (LMO) cells improved thermal safety after calendar aging at 55°C, 100% SOC: self-heating and the TR started at higher temperatures, exothermal rate during the TR decreased [100].

They compared characteristic temperatures at which the self-heating started and the open circuit voltage (OCV) dropped. Röder et al. investigated the correlation between calendric aging at 60°C and the thermal safety of LIBs [101]. They found out that the SEI and the cathode material influence the safety of the cells after aging. Röder et al. observed reduced onset temperature and reduced energy

release of aged cells and explained the results in the following way: less intercalated Li is in the anode and therefore less Li can react with the electrolyte. Fleischhammer et al. conducted high rate cyclic aging at low temperature and investigated the influence of aged and unaged LMO/NMC blend cells using accelerated rate calorimetry (ARC) [102]. They observed a strong correlation between the aging mechanisms and the battery safety. Cycling with low temperature leads to an increase in heat generation and reduced safety whereas the cells cycled with high rates showed only a slight change in the safety behavior compared to fresh cells. The main effect was observed in the self-heating rate of high rate cycled cells.

Also Feng et al. found a worse thermal stability of cells cycled at low temperature than for fresh cells and cells treated by high temperature [44]. They observed that cells aged at high temperatures show an improved thermal stability. In contrast, but if Li deposit on the surface of the anode (e.g., during low temperature cycling), the thermal stability becomes worse. The improvement of thermal stability after high temperature exposure can be explained by growth of the SEI and demobilized Li. For low temperature, cycling Li deposit outside the original SEI and enables reaction between the Li and the electrolyte. The reactivity of the anode is increased and consequently the onset temperature of self-heating decreases [44]. Li plating was investigated by Li et al. and they state that the reaction between the plated Li and the electrolyte is the triggering factor of TR [99]. They compared characteristic temperatures from aged cells with partial cells and observed an exothermic reaction peak at low temperatures at fast charging when the plated Li consumed electrolyte.

According to literature the worst case for TR of aged cells is observable if Li plating at the anode happens during aging [44,102]. Consequently, the surface at the anode plays a significant role concerning safety of LIBs.

### **2.5.7 Thermal runaway analysis at VIRTUAL VEHICLE**

Golubkov et al. started in 2011 investigating the failing behavior of small 18650 cells (< 5 Ah) inside a self-constructed heavy-duty reactor. The aim of this test stand was to gain first results of failing LIBs up to 5 Ah using triggers such as overtemperature and overcharge. Golubkov et al. developed and realized the TR test stand and published the results of failing 18650 cells in [87] and [85]. Temperature was measured on the cell surface and inside the TR reactor, the pressure inside the test has been recorded. The total amount of produced gas was calculated and the vent gas composition after TR was measured with a gas chromatograph (GC) [85,87]. In cooperation with Graz University of Technology, Institute of Chemical Engineering and Environmental Technology (CEET), the test stand was used for fuel cell testing and further investigation of the failing behavior of small 18680 cells. In 2014, a larger TR test bed was developed at VIRTUAL VEHICLE to test larger automotive LIBs. Golubkov et al. published the first results of failing large automotive LIB (LMO cathode chemistry) in [57,103].

The larger test bed designed in 2014 was used in this present thesis for TR tests. Since the beginning of this PhD thesis in 2016, the TR test stand was continuously augmented and improved. In the course of this thesis especially the gas analysis was improved (with a high-end FTIR spectrometer), HF was investigated in detail, the particle analysis method was developed and investigated, and several new detection methods were introduced: gas sensors, humidity sensors and video cameras were added inside the TR test bed. New sample holders were constructed to enable testing with new triggers and additional laboratory space with large fume hood was opened for special gas sensor and decomposition tests.

## 2.6 Early battery failure detection with gas sensors

Developing methods for early failure detection and reducing safety risks from failing high energy LIBs has become a major challenge for industry, research and development [18]. The BMS is designed to ensure safe and reliable operation of the batteries as good as possible. Current functional-safety cell monitoring means monitoring the electric and thermal behavior of the cell in real-time: the cell voltage and current can be measured directly by on-board current and voltage sensors and the surface temperature of battery pack components directly with temperature sensors [24]. Different strategies about temperature measurement are currently on the market: While some manufacturers use temperature sensors on each cell surface, some reduced the number of temperature sensors inside the battery pack to an absolute minimum [104]. Additional monitoring systems are insulation detection and the high-current fuse. To the author's current knowledge, no additional early failure detection methods are used in series products. As soon as an abnormal behavior of the cell voltage, the current or the cell temperature of one or more batteries is detected, predefined actions are executed by the BMS (e.g., control unit activates cooling or interrupts the power circuit). In case of a detected failure different shutdown procedures are followed aiming to give the passengers sufficient time to leave the vehicle safely [16,96].

The standard state-of-the-art battery monitoring equipment in current EV battery packs is inadequate to reach the upcoming level of safety requirements (GB 38031-2020) and to reliably enable early failure detection, because battery failure cases such as electrolysis, an open cell housing and electrolyte vaporization or the first venting are very unlikely to be detected by the classical monitoring system. For cells without current interrupt device (CID) or overcharge safety device (OSD), the first venting precedes the cell voltage break down and is detectable through a small temperature increase directly at the venting position of the failing cell [11]. It is not possible to measure this venting with thermocouples applied on the cell surface, with cell voltage monitoring and with current monitoring. It is very likely that these thermocouples, the voltage or current measurement only detect the failing behavior if at least one of the cells is already in the state of a TR.

In order to enhance battery safety and to fulfill EVS-GTR20 and GB 38031-2020, the use of additional gas sensors combined with state-of-the-art battery failure monitoring such as voltage, temperature, pressure measurement is promising and needs to be investigated in more detail.

The basic idea of using gas sensors for detecting battery vent gases produced during battery failures additional to the existing BMS monitoring sensors is not new. Researchers have published suggestions of using gas sensors for detecting battery failures [18,96,105–108] and they reported field experiments of gas sensors in battery TRs [96,104,109]. Also patent applications have been published proposing the implementation of gas sensors for TR detection [18,110]. The following literature review is divided into two groups: Literature focusing on gases produced during the TR and literature focusing on gases produced before the TR reaction.

For detecting the TR itself and gases developed during the TR reaction, gases such as CO, CO<sub>2</sub>, H<sub>2</sub>, CH<sub>4</sub>, C<sub>2</sub>H<sub>4</sub>, C<sub>2</sub>H<sub>6</sub>, C<sub>3</sub>H<sub>8</sub> are addressed [5], and sensors to detect at least one of these gases are chosen:

Cai et al. used early failure detection by means of detection of CO<sub>2</sub> gas produced at the TR of the first cell [105]. They stated that the measurement of CO<sub>2</sub> allows a significantly faster TR detection than the conventional surface temperature sensing. Koch et al. tested a sensor set consisting of voltage sensor, temperature sensor, pressure sensor, gas sensor, smoke sensor, creep distance sensor in TR experiments [96]. They found that the gas sensor can detect the TR event earlier than the other sensors

during nail-penetration tests. Koch et al. used a SnO<sub>2</sub> gas sensor (metal oxide semiconductor (MOx or also named MOS)) sensitive to CH<sub>4</sub>, C<sub>3</sub>H<sub>8</sub>, CO. Each tested sensor detected the TR independently of battery size and energy density. The authors stated that the combination of several sensors might lead to an improvement of the system. Mateev et al. proposed gas detection with a MQ-7 (TR gases CO and H<sub>2</sub> are the target gases) MOx gas sensor [106]. One sensitive MOx layer was applied on the relatively large analogue sensor. Liao et al. published a survey of methods for monitoring and detection of TR of LIBs [18]. They stated that the combination of voltage, cell surface temperature, inner cell temperature and gas monitoring in battery applications is the most efficient method to promote safety of LIBs. Concerning the vent gas detection, they described target gases produced during the TR like CO, CO<sub>2</sub>, C<sub>2</sub>H<sub>4</sub>, C<sub>2</sub>H<sub>6</sub>, H<sub>2</sub>O, C<sub>3</sub>H<sub>6</sub> and O<sub>2</sub>, but they stated that gas sensors can detect battery failure related signals 7 to 8 minutes before the TR, which would mean earlier detection of the gas signal compared to the voltage drop or a temperature signal.

Other researchers focused on volatile organic compounds (VOCs) such as electrolyte components, which can be measured at battery failure stages before the TR:

Cummings et al. proposed in the US patent application monitoring of electrolyte vapor such as DEC and DMC [110]. Hill et al. introduced the principle of off gas sensing prior to TR in overcharge experiments [109]. They tested the chemi-resistive sensor offered by NexTech sensitive to CO, CH<sub>4</sub>, C<sub>2</sub>H<sub>6</sub>, VOCs, C<sub>2</sub>H<sub>4</sub>, C<sub>3</sub>H<sub>8</sub>, HF, but did not disclose details on the sensing material or operating conditions. The lifetime of the tested sensor is lower than five years. They observed in overcharge tests that the sensor reacted to battery off-gassing 10 minutes before the TR itself. Swartz et. al. promoted the same NexTech chemi-resistive sensor element for H<sub>2</sub> measurements and announced to refine formulations for detecting CO, CH<sub>x</sub> and VOCs [111]. Wenger et al. presented insight into the gas sensor response of MOx sensors during electrolyte leakage and battery overcharge experiments [104]. They stated that a first venting eventually happens and that the time between the first venting and the TR depends on the applied current in the overcharge test. The manufacturer of the sensor is not disclosed in their paper. Herold et al. promoted sensors fabricated by AMS for detecting critical battery states (overcharge, nail penetration) [108]. They tested their MOx gas sensor in abuse tests such as nail-penetration, overcharging, short circuit and leakage as well as during charging and temperature cycles and demonstrated the reaction of the MOx sensor to electrolyte vapor. They suggested to focus on the resistance change relative to the background rather than to the absolute resistance value.

## 2.7 What is missing in current literature and what is needed?

Four main topics require additional investigations to achieve significant enhancements in research and industrial development and match with the four main publications within this doctoral thesis:

- a. Comprehensive hazard analysis and investigation of the SOC influence on the failing behavior
- b. Investigation of the influence of different TR triggers and cell types on the failing behavior
- c. Investigation of the influence of aging on the failing behavior
- d. Early detection of battery failures using gas sensors

### **a. Comprehensive hazard analysis and influence of SOC**

Beside valuable information on single hazard categories of failing batteries, to the best of the author's knowledge, only little information is available in literature on the following hazards and safety-relevant parameters of high capacity NMC or NMC/LMO cells. Nevertheless, this information is of relevance for

various R&D activities towards significant safety improvements of batteries. Relevant information comprises:

- A detailed analysis of the gas amount produced at failing high capacity NMC/LMO cells in N<sub>2</sub>.
- An analysis of the venting rate (mol/s or L/s) of failing NMC and NMC/LMO pouch cells.
- A comprehensive gas analysis at heat triggered TR in N<sub>2</sub> including electrolyte quantification and HF analysis. As well as a comprehensive gas composition analysis after the first venting or at abuse experiments of cells with low SOC, where no self-heating into TR can be triggered.
- There is a need to further investigate the size and content of particles produced at TR with a nondestructive analysis method.
- A study of all five mentioned hazards presented in chapter 2.4 including quantification of the safety-relevant parameters for the same specific automotive cell at different SOCs.

For a comprehensive hazard analysis a study on relevant parameters and measurement principles needs to be addressed for all five mentioned hazards from a failing large automotive cell:

- Vent gas composition at first venting (gas concentrations including electrolyte vapor).
- Thermal behavior at TR (cell surface temperatures including maximum reached temperature).
- Vent gas emission at TR (amount of produced gas and venting rate).
- Vent gas composition at TR (gas concentrations).
- Particle emission at TR (particle size distribution and composition).

In the first part of this thesis, these five hazards are characterized, safety-relevant parameters are quantified, and measurement principles are provided from a large capacity NMC/LMO cell currently used in modern EVs. Overtemperature experiments are conducted for three cells with different SOCs (100%, 30% and 0%, see chapter 3.5.1). Hazards from these automotive NMC/LMO pouch cells have, to the author's knowledge, not been the subject of scientific publications, but, as will be shown, are important to investigate. Findings for this topic have been published [5].

### **b. Influence of thermal runaway trigger and cell type**

TR-propagation regulation (TF5) being developed in EVS-GTR contains three testing methods: heating, overcharge and nail-penetration [83]. But do the suggested testing methods/triggers (heating, overcharge and nail-penetration) influence the TR behavior and the TR results? The type of abuse affects the cell reaction and the TR results [71,84,97], but a detailed comparison of the thermal behavior, the vent gas emission and the vent gas composition is currently not available in open literature. A detailed comparison of results of different TR triggers tested on high capacity NMC cells, which is currently one of the preferred cell chemistries for EVs, is missing in literature.

Additionally, it would be relevant to investigate how the different EV cell designs, such as pouch cells or hard case cells, influence the results of different TR trigger. Information on the failing behavior of two commonly used EV cell types (pouch and hard case) would be relevant for the scientific community in this field. This information is of relevance for various R&D activities towards significant safety improvements of batteries.

Therefore, the aim in the second part of this thesis is to compare the results of three different TR triggers (overtemperature, overcharge and nail-penetration) on two different automotive NMC cell types (pouch and hard case). Both cell types have a high capacity (60 Ah) and a high energy density and are used in modern EVs. Each experiment is repeated in order to comment on the reproducibility

of the experiments. Hazards from these automotive NMC cells have, to the author's knowledge, not been the subject of any scientific publication, but, as will be shown, are important to investigate. These results have been published [11].

### **c. Influence of aging**

Several researchers have investigated the influence of aging paths on the thermal stability of the cells, but the influence of different degradation paths on the degassing behavior in failing state is currently not sufficiently addressed. Is there an influence of different aging paths on the amount of produced gas or the gas composition after the first venting and after the TR? These safety-relevant parameters have not yet been sufficiently investigated in open literature but are relevant since statistically most EV accidents happen when the cells are aged.

The third part of this thesis analyzes the influence of three different aging paths on the failing behavior in detail and compares the results with failing fresh cells. The results are discussed in three main categories: thermal behavior, vent gas emission and vent gas composition at TR. For the investigation the same automotive pouch cell with a capacity of 60 Ah was used as for the research topic b "Influence of thermal runaway trigger and cell type". These results have been accepted for publication in March 2021.

### **d. Early detection of battery failures using gas sensors**

A detailed analysis of produced gases during battery failure cases before TR is poorly reported in current literature. Most literature exist on gases produced at the TR itself [5,65,71,73,85,87]. For this research field it is relevant to gain insight into the gas production even before the TR in order to identify suitable gas sensors. The possible battery failure case of unwanted electrolysis between two voltage carrying parts and resulting H<sub>2</sub> production is rarely addressed in the literature but it is a possible and serious battery failure case because of the high flammability of H<sub>2</sub>. While detecting the TR allows to set actions to prevent TR propagation to the neighboring cells, focusing on the failure stages before the TR is indispensable to prevent even the TR itself. Thus, a detailed analysis of evolving gases at battery failure stages before the TR is valuable.

Even though TR monitoring with gas sensors has been claimed to be more efficient than voltage and temperature monitoring for failure detection [18], validation and comparison of several possible gas sensors for early detection of battery failures is currently insufficiently addressed in the open literature but would be valuable for research and industry concerned with battery safety.

Since the first venting occurs not in all failure cases [11] and the exact time, when the cell housing opens and releases gases depends on more parameters than the overcharge current, it is relevant to investigate which failure cases can be detected and if it is possible to detect battery failures with gas sensors at an early stage.

Furthermore, an algorithm for event detection is needed and the measurement with the gas sensor approach needs to be stable against false positives. Considerations to enable distinguishing between battery failure cases and prevent false positives is necessary.

In the final part of this thesis battery failure cases BEFORE the TR are investigated in detail, including electrolysis, identification and quantification of gas components and assessment of several commercially available sensors to detect compounds emitted during the gas producing events before the TR. Different sensor principles and sensors from different manufacturers were benchmarked in special test setups. The most promising gas sensors were tested inside a TR test bed using more than

30 different state-of-the-art automotive LIBs in three different TR triggers: overtemperature, overcharge and nail-penetration. Thus, the influence of the failure case on the battery failing behavior is explored and algorithms for event detection are suggested. Additionally, sensors were targeted, which enable distinguishing between different failure cases, and which allow to find algorithms to prevent false positives produced by surrounding gases. These results have been accepted for publication in March 2021.

## 2.8 Research focus

After the evaluation of what is missing in current literature and what is needed, this PhD thesis focuses on two main research fields to generate new scientific value:

1) <b>Analysis of failing batteries</b>	2) <b>Early battery failure detection</b>
a detailed analysis of failing high energy automotive battery cells with a special focus on vent gas analysis	the investigation of using gas sensors as additional early failure detectors to the existing battery monitoring system

The first of these research fields deals with the detailed investigation of the battery failing behavior and battery failure influencing factors (see structure in section 2.7):

### a. Comprehensive hazard analysis and influence of SOC

Which hazards need to be investigated for a comprehensive hazard analysis of a failing cell? What are the results of a failing modern EV battery cell in different SOCs (100%, 30%, 0%)?

How do the cells behave in failing state in the categories vent gas composition at first venting, thermal behavior at TR, vent gas composition after TR, vent gas and particle emission at TR?

How to develop a new gas analysis method for a detailed analysis of the vent gas composition (including electrolyte vapor and HF)?

### b. Influence of thermal runaway trigger and cell type

Do the suggested testing methods/triggers (heating, overcharge and nail-penetration) developed in EVS-GTR influence the TR behavior and the TR results? How do the different EV cell designs, such as currently used pouch cells or hard case cells, influence the results of different TR trigger? And how do these influencing factors trigger and cell design affect the thermal behavior, the degassing behavior, and the resulting vent gas composition?

### c. Influence of aging

How do different degradation paths influence the failing behavior of modern large LIBs? A special focus is set on the degassing behavior in failing state. Is there an influence of the aging paths on the amount of produced gas or the gas composition after the first venting and after the TR?

The second of these main research fields is based on an intensive investigation of battery failures before the TR and deals with the detection of battery failures at an early stage:

### **d. Early failure detection of battery failures using gas sensors**

What happens at battery failures before and during the TR (gas emission and gas composition)? Which gases can be detected at battery failures before the TR? Which currently available sensor(s) is/are most suitable for early battery failure detection? Is it possible to detect battery failures with gas sensors at an early stage? Which failure cases can be detected?

The research questions focus on currently used automotive cell chemistry. Especially the NMC – graphite chemistry with a combination of linear and cyclic electrolyte solvents and LiPF<sub>6</sub> conducting salt is used in modern EVs. Consequently, this cell chemistry is chosen to be investigated in the thesis herein in detail.

## **2.9 Thesis outline**

After the literature review in chapter 2, starting in chapter 3 the methods and measurement technologies for the investigation of the research questions are explained. Chapter 3 starts with the presentation of the four investigated automotive cell types. Afterwards, the TR test bed, the especially designed sample holders, the applied TR trigger methods and the analysis methods are introduced. Chapter 4 presents the experimental results of the identified gases at battery failures as well as the results of the comprehensive hazard investigation and the influence of the SOC, TR trigger, the cell type and the aging paths. The results are discussed and compared with existing literature in the same chapter. At the end of the chapter 4 the reproducibility of the TR experiments is commented. An extra chapter, chapter 5, deals with early battery failure detection. Different sensor principles and sensors from different manufacturers are benchmarked in special test setups. Out of these the most promising gas sensor was tested inside a TR testbed using a state-of-the-art automotive LIB in three different TR triggers: overtemperature, overcharge and nail-penetration. Thus, the influence of the failure case on the battery failing behavior is explored.

### 3 Methods and measurement technologies

*Parts of this chapter were already published in:*

Essl C, Golubkov AW, Gasser E, Nachtnebel M, Zankel A, Ewert E, Fuchs A. Comprehensive hazard analysis of failing automotive Lithium-ion batteries in overtemperature experiments. *Batteries* 2020; **6**(30): 1–28. DOI: 10.3390/batteries6020030.

Essl C, Golubkov AW, Fuchs A. Comparing Different Thermal Runaway Triggers for Two Automotive Lithium-Ion Battery Cell Types. *Journal of The Electrochemical Society* 2020; **167**(130542): 1–13. DOI: 10.1149/1945-7111/abbe5a.

Essl C, Seifert L, Rabe M, Fuchs A. Early detection of failing automotive batteries using gas sensors. *Batteries* 2021 (accepted March 2021).

Essl C, Golubkov AW, Fuchs A. Influence of aging on the failing behavior of automotive lithium-ion batteries. *Batteries* 2021 (accepted March 2021).

In this chapter the investigated cell types, the TR reactor setup, safety relevant parameters and the early failure detection method development are presented. For each research focus a special design of experiment (DoE) was used, which are presented in chapter 3.5.

#### 3.1 Investigated cells

Four large automotive modern cell types, labeled with #1, #2, #3 and #4, with different cell capacity and different cell design are investigated in this study (see **Figure 4**): Three different types of pouch cells (#1, #3 and #4) and one type of prismatic hard case cell (#2).

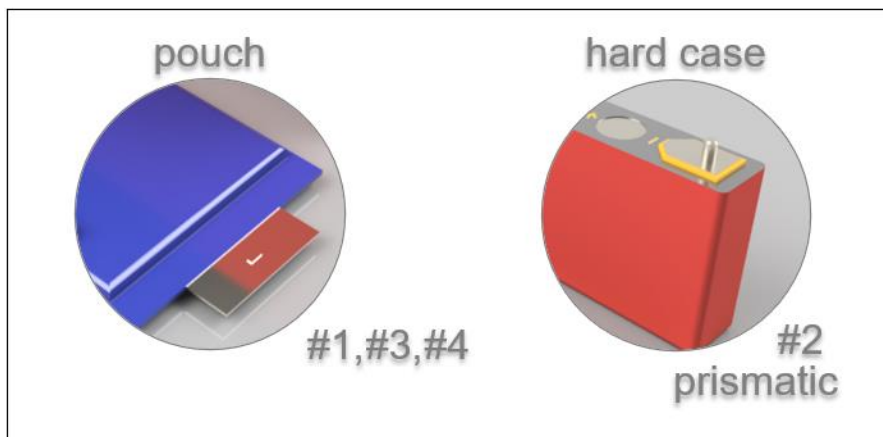


**Figure 4:** Four different cell types #1, #2, #3 and #4 were chosen for the analysis in failing state: three different types of pouch cells (#1, #3, #4) and one type of prismatic hard case cell (#2).

All investigated cell types are currently used in modern EVs and are based on a NMC cathode and graphite anode (see **Table 1**). Cell type #1 and #2 have the same proportion of Ni, Mn and Co (622). Cell type #3 and #4 are also based on NMC cathodes, but #3 has an NMC- LMO (spinel) cathode. The exact proportion of the cathode of cell type #4 is unknown.

### 3.1 Investigated cells

All investigated cells have different electrolyte solvent mixtures, but all are based on EC and a combination of linear carbonates such as DEC, DMC and EMC. Cell type #2 is the only tested cell type with a jelly roll electrode design. The other cell types, #1, #3 and #4 consists of an electrode stack, which is sealed in laminated pouch foil.

**Table 1: Specification of the investigated automotive Li-ion cells.**

parameter	cell type #1	cell type #2	cell type #3	cell type #4
design	pouch	prismatic hard case	pouch	pouch
cathode material	NMC	NMC	NMC/LMO	NMC
anode material	graphite	graphite	graphite	graphite /LTO
electrolyte	EC:EMC (1:1)	EC:DMC:EMC (2:3:3)	EC:DEC:DMC (12:12:1)	EMC:PC:EC (4:2:1)
capacity	60 Ah	60 Ah	41 Ah	37 Ah
nominal voltage	3.6 V	3.6 V	3.8 V	3.6 V
gravimetric energy density	250 Wh/kg	225 Wh/kg	180 Wh/kg	190 Wh/kg
aging state	fresh & aged	fresh	fresh	fresh
start SOC	100%	100%	0%, 30%,100%	100%
cell thickness	11.2 mm	28.0 mm	7.66 mm	10.17 mm
electrode design	stacked	2 jelly rolls	stacked	stacked

The description which cell type was used in the special designs of experiment is described in chapter 3.5.

For the example of cell type #3 a mass split was estimated. The mass split of the discharged cell type #3 is presented in **Figure 5** and estimated based on the investigations of the cell material and considers the cell design and data from literature for NMC cells [71,85]. The mass of SEI, binder and carbon black are omitted. It is assumed that 14% of the initial mass of the cell is electrolyte and conducting salt. This corresponds to 121.5 g of electrolyte, consisting of 44 g of EC, 59 g of DEC, 3.7 g of DMC and 14.8 g of LiPF<sub>6</sub>.

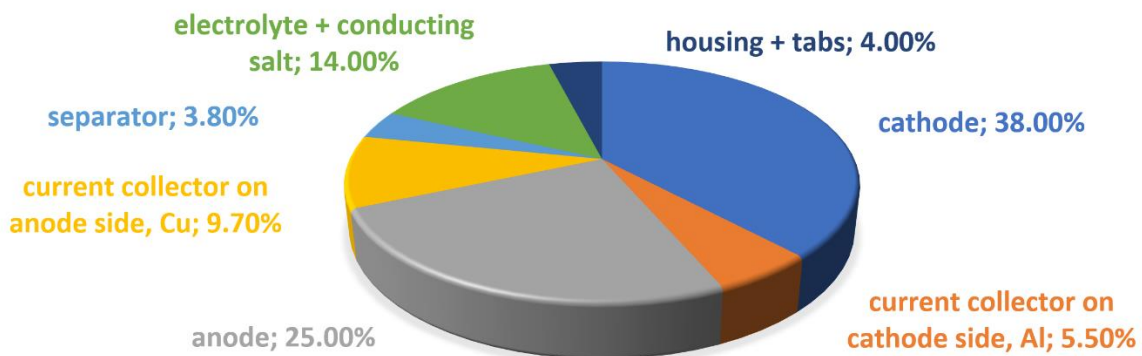


**Figure 5: Estimated mass split of the investigated fresh automotive pouch cell in discharged condition [5].**

The disassembling of cell type #3 out of the battery pack and the electrode structure was investigated by Kovachev et al. and published in [112]. To the author's knowledge information on the other three investigated cell types (#1, #2 and #4) are not published in open literature.

## 3.2 Thermal runaway reactor setup

In the experiments the response of each test sample (cell mounted inside a sample holder) to the applied TR trigger is measured and safety-relevant parameters are quantified. Inside the sample holder several single cells can be tested within one experiment. In this study, only results of experiments on one single cell inside the sample holder are presented and discussed. The advantages of this testing methods are that the tests can be carried out in a controlled manner and safety-relevant parameters such as thermal behavior, vent gas emission and gas composition can be determined and compared from one cell to the other.

### 3.2.1 Experimental method

The TR experiments are carried out inside a gastight 40 bar pressure resistant stainless-steel reactor. This custom-made reactor is shown in **Figure 6** and published in [5,11,57,76,103]. The experiments can be done in nitrogen ( $N_2$ ) atmosphere or in air. For safety reasons most experiments are done in  $N_2$  atmosphere, as are the presented ones.

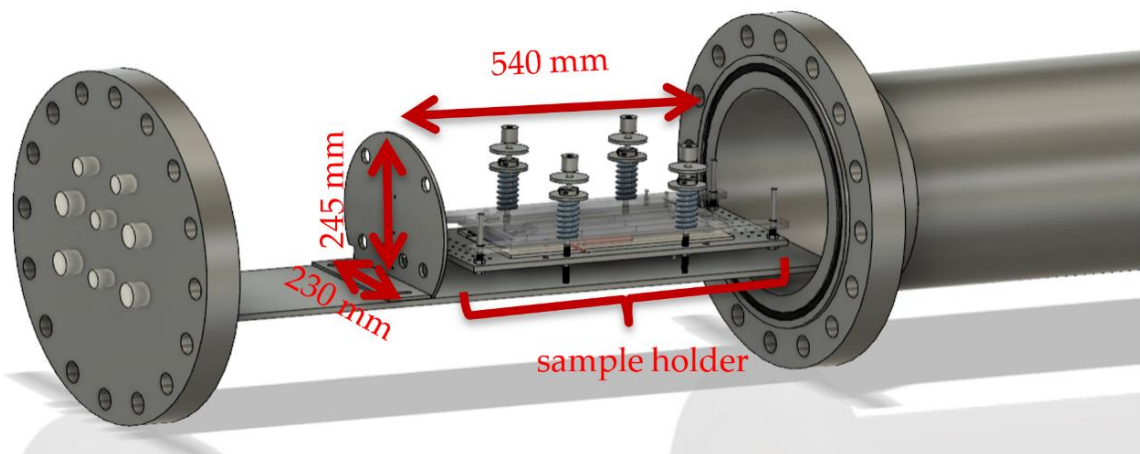


**Figure 6: Stainless-steel reactor setup. Inside the reactor the cell sample is fixed inside the sample holder. The presented sample holder is used for overtemperature and overcharge experiments. For nail-penetration a different upper sample holder plate is used (see Figure 7 (c)) [11].**

In **Figure 6** and **Figure 7** (a) and (b) the standard sample holder for overtemperature and overcharge experiments is shown. It consists of a lower and an upper stainless-steel plate. The cell is positioned horizontally between the two plates. The setup can apply a defined force to the cell (3000 N, recommended by our industry partners) using four springs. Between the cell and the two stainless-steel plates, mica sheets are applied to minimize the thermal coupling between the stainless-steel plates and the cell. This insulating mica sheets (thermal conductivity of 0.23 W/mK) are 2 mm thick and provide channels for the thermocouple wires. The thermocouples are positioned in well-defined distances to each other depending on the cell geometry. The tips of the thermocouples protrude through the mica sheets and are squeezed between the mica sheet and the cell surface. Because the mica sheets are thermal insulators, the thermocouple tips measure the cell surface temperature. Instead of the described standard sample holder also different other sample holders can be positioned inside this reactor. **Figure 7** (c) presents the nail-penetration add on to the upper sample holder plate. Inside each sample holder, the cell is electrically connected to a cycler. The reactor, including the implemented standard sample holder, has a free volume of 121.5 l.

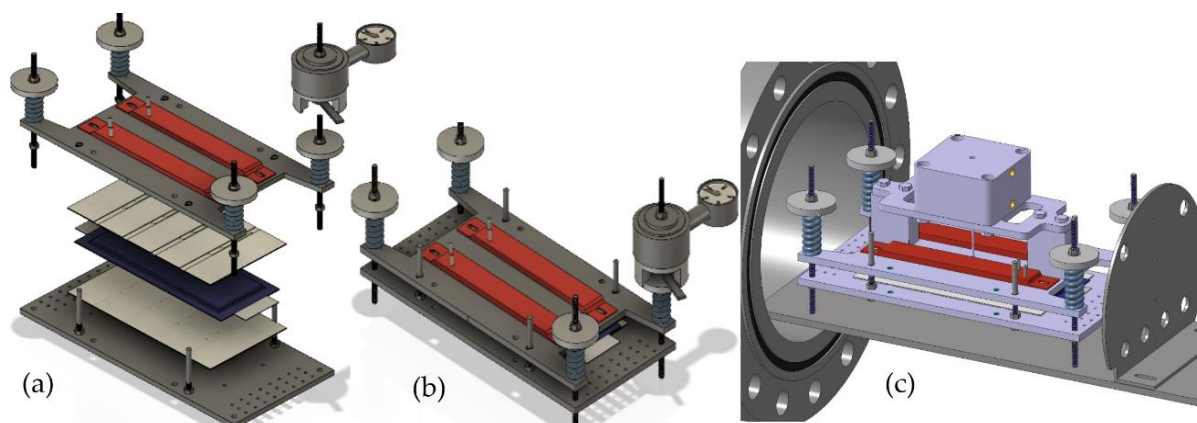


**Figure 7: Sample holder setup: (a) the components of the standard sample holder and (b) the assembled standard sample holder. The standard sample holder consists of two stainless-steel plates (dark grey) with two heater stripes (red) on the top and two on the bottom side of the stainless-steel plates, mica sheets (beige) with thermocouples between the cell (symbolic design of a pouch cell (blue)) and the stainless-steel plate. With four springs a defined force can be applied to the cells. (c) shows the additional nail-penetration setup positioned on the top of the upper stainless-steel plate [11].**

After the cell is positioned in the sample holder inside the reactor and the measurement equipment is fixed, the reactor is closed and flushed with  $N_2$ . When the setup is prepared, different triggers are tested on single cells.

In detail, the experimental method consists of several subsequent steps:

#### **Sample and experiment preparation:**

1. Insulating mica sheets with thermocouples for temperature measurement are placed on the top and the bottom side of the cell (beige plates in **Figure 7** (a), the thermocouple positions are shown in chapter 3.3.1).
2. The sample is fixed in the sample holder with a defined force of 3000 N (54 kPa).
3. Reactor is closed and evacuated.
4.  $N_2$  is added until ambient pressure. Step 3 and 4 are repeated at least 2 times.
5. All gas valves are closed (the reactor is hermetically sealed).
6. Sample is charged to the desired SOC.

#### **Experimental steps:**

7. The data acquisition system is started: measurement of cell surface temperature, cell voltage, temperature and pressure inside the reactor. In overtemperature and nail-penetration trigger the cell is pulsed with a battery cycler ( $\pm 1$  A pulses) to get information on the cell resistance.
8. The desired TR trigger (overtemperature, overcharge, nail-penetration, described in chapter 3.2.2) is chosen.
9. In overtemperature and overcharge experiments the sample exhibits a first venting and, after reaching the critical state, the TR. If the vent gases produced at the first venting are of interest, the valves to the gas analysis section are opened after the first venting and the vent gas composition analysis is started.
10. After reaching the maximum temperature during the exothermic reaction, the TR, the heating in overtemperature trigger or the power supply in overcharge trigger is switched off. The cell starts to cool down. Wait 5 min to start the experiment after-treatment.

#### Experiment after-treatment:

11. The valves to the gas analysis section are opened. The vent gas composition analysis is started.
12. After finishing the gas measurement series, the data acquisition is stopped.
13. The reactor is heated up to 200°C, evacuated to about 1 kPa absolute pressure and flushed with N<sub>2</sub> several times before the reactor is opened again.
14. If needed, ejected particles are sampled.
15. The test cell is removed and the setup is cleaned.

#### 3.2.2 Thermal runaway trigger

The TR events were triggered in this study according to the research questions by three different methods, which are published in [11]. The basic TR trigger was the overtemperature trigger.

- **Overtemperature:** homogeneously external heating of the two largest surfaces of the cell. On top and bottom of the two sample holder plates, heater stripes with a heating power of max. 500 W are applied (see red heater stripes in **Figure 7** (a) and (b)). The overtemperature experiment is designed to increase the cell surface temperature with  $\sim 2^\circ\text{C}/\text{min}$ . Two ventings are expected: a first venting and opening of the cell housing due to overheated cell materials such as electrolyte, and a second venting accompanied by violent gas and particle emission during TR [57].
- **Overcharge:** charging the cell with 1 C rate (1 C is the cell capacity divided by 1 h) until the TR happens. The final SOC is calculated with coulomb counting (integrate current (A) over time). At the prismatic hard case cells an overcharge safety device (OSD) is implemented. In order to trigger the cell into false state by overcharge, this OSD needed to be blocked, otherwise it would disconnect the cell tabs and the active material, and the cell cannot be charged anymore. This blocking is done by isolating the corresponding cell tab from the OSD. The isolation is done outside of the cell housing. Therefore, the cell housing remains closed and the inside of the cell is not influenced.
- **Nail-penetration:** a nail (material: 42CrMo4) with 3 mm diameter and 60° angle of the nail tip is pushed with compressed air into the center of the large surface of the cell. The nail is inserted 8 mm into the cell. Only one venting is expected immediately after the penetration of the nail into the cell. The nail remains stuck in the cell until the experiment after-treatment, when the cell is removed from the reactor.

### 3.3 Safety-relevant thermal runaway parameters

All results of differently triggered TR are compared in at least three main hazard categories: thermal behavior, vent gas emission and vent gas composition (see **Figure 8**). The category gas composition also includes the hazard category from the first venting, the electrolyte vaporization. For cell type #3 an additional category was investigated, the particle emission.

Investigated hazard categories:

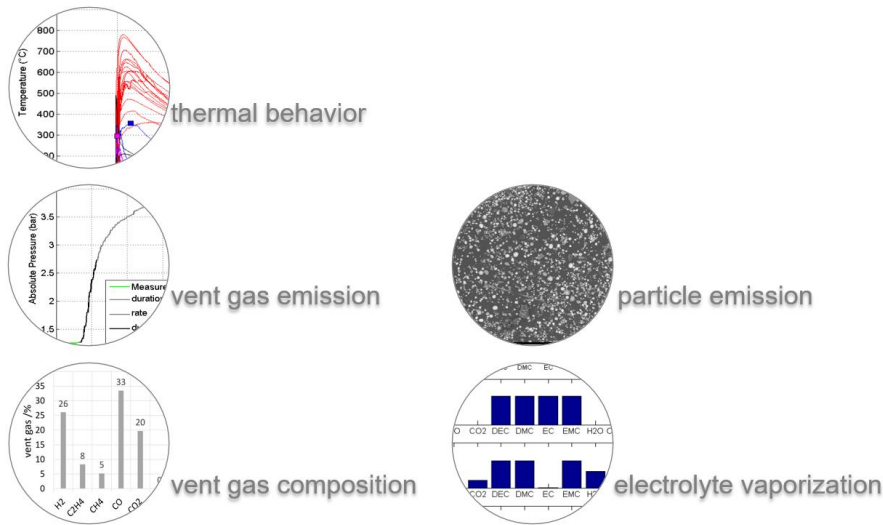


**Figure 8: Investigated hazard categories from failing batteries: thermal behavior, vent gas emission, vent gas composition (including electrolyte vaporization) and particle emission. For each hazard category safety-relevant parameters are analysed for each TR experiment.**

### 3.3.1 Thermal behavior

Inside the reactor, the thermal behavior of the cell is recorded with type-K thermocouples on both sides of the cell surface (type #1, #2, #3, and #4), the cell tabs (type #1, #4) and close to the burst plate of the cell (type #2). The thermocouple positions for the investigated cell type #1, #2, #3, and #4 are presented in **Figure 9**. Different thermocouple patterns on the cell surfaces were used because of the different geometries of the cell types. Additionally, the temperature inside the TR reactor (type #1, #2, #3, and #4) is measured on four different positions. Since the pouch cell (type #1, #3 and #4) design has no defined burst plate like the prismatic hard case cell (type #2), three thermocouples were positioned on the welded pouch foil on the long side of the cell (type #1, #4).

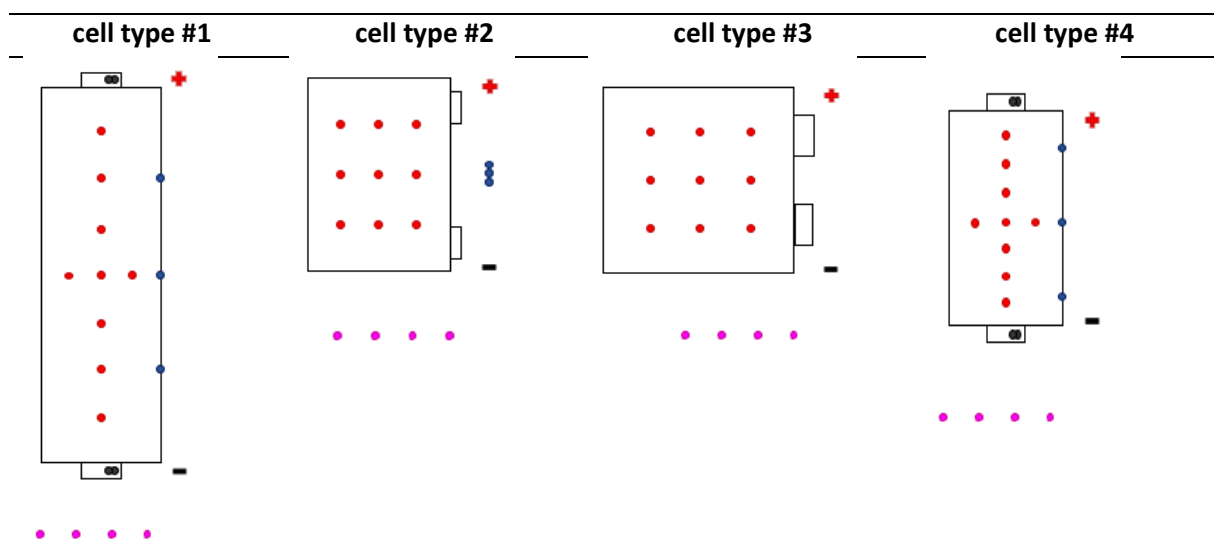


**Figure 9: Scheme of the investigated cell types (#1, #2, #3 and #4) presenting the thermocouples positions on the cell surface (red), at different positions inside the TR reactor (pink), on the cell tabs (black) and at the venting positions (blue).**

Safety-relevant thermal parameters are:

- $\bar{T}_{cell}^{v1}$  (°C) the average measured temperature of all thermocouples on the cell surface when the first venting starts.
- $T_{cell}^{crit}$  (°C) the temperature of the one cell-surface thermocouple, which is the first to exceed the temperature rate of 10°C/min (detailed description in [57]).
- $\bar{T}_{cell}^{v2}$  (°C) the average measured temperature of all thermocouples on the cell surface when the second venting starts.
- $T_{cell}^{max}$  (°C) the maximum recorded temperature of one of the thermocouples on the cell surface.
- $T_{vent}^{max}$  (°C) the maximum recorded temperature of one of the thermocouples at the venting positions.
- $\bar{T}_{reactor}$  (°C) the average gas temperature inside the reactor.

#### 3.3.2 Vent gas emission

With GEMS 3300B06B0A05E000 pressure sensors inside the reactor, the pressure increase due to gas generation is recorded during the whole TR experiment. With the ideal gas law, the amount of produced, not condensed vent gas can be calculated. The same calculation is used as presented in [57].

Safety-relevant parameters are:

- $n_v$  (mol or liter) the total amount of released gas (in STP: 298.15 K, 100 kPa).
- $n_{v1}$  (mol) the amount of gas produced starting at  $T_{cell}^{v1}$  and ending at the  $T_{cell}^{v2}$ .
- $n_{v2}$  (mol) the gas produced after  $T_{cell}^{v2}$  and during the TR.
- $\dot{n}_{ch}$  (mol/s or l/s) the characteristic venting rate based on the minimal duration  $\Delta t_{50\%}$  (s) when 50% of the venting gas  $n_{ch50\%}$  (mol) is produced.

#### 3.3.3 Vent gas composition

A special focus is set on the vent gas analysis and a new analysis method has been developed. The vent gas composition is measured with a FTIR spectrometer and GC in parallel. The pipes from the reactor towards the gas analysis are closed during the TR experiment and opened after the first venting or the TR happened. They are heated to 130°C. Safety-relevant parameters are the quantified gas concentrations of gases like: H<sub>2</sub>, CO, CO<sub>2</sub>, CH<sub>4</sub>, C<sub>2</sub>H<sub>6</sub>, C<sub>2</sub>H<sub>4</sub>, C<sub>2</sub>H<sub>2</sub>, DEC, DMC, EC, EMC, H<sub>2</sub>O, C<sub>6</sub>H<sub>14</sub>, HF, C<sub>4</sub>H<sub>10</sub>, C<sub>3</sub>H<sub>8</sub> and O<sub>2</sub>. Since N<sub>2</sub> is not produced by battery failures, N<sub>2</sub> is used as inert gas.

The reactor gas consists of the inert gas N<sub>2</sub> and the vent gas, which is added by the failing cell. Since the produced vent gas does not contain N<sub>2</sub>, the amount of N<sub>2</sub> in the reactor gas can be subtracted to calculate the concentration of each component of the vent gas only. The concentration of any gas component ( $c_v$  /%) in the vent gas is calculated with the measured concentration of this gas component in the reactor gas ( $c_m$ ) and the measured N<sub>2</sub> concentration ( $c_{N2}$ ) in the reactor gas:

$$c_v = ((c_m * 100) / (100 - c_{N2})) \tag{1}$$

$c_{N2}$  was verified before each measurement with an external standard measurement (ExtSt100% and ExtSt80%).

The concentrations / gas quantities of toxic, flammable, or explosive vent gas components are safety relevant. Examples are especially gases in high quantities, such as CO, H<sub>2</sub> [64], but also toxic gas components in small quantities such as fluor (F) containing decomposition products like HF [75].

#### 3.3.3.1 FTIR spectrometer (FTIR)

A Bruker MATRIX-MG01 FTIR is used with 0.5 cm<sup>-1</sup> wavenumber resolution. The MCT detector is N<sub>2</sub> (l) cooled. The FTIR measurement chamber itself is heated to 190°C. The interior space of the FTIR spectrometer is purged with N<sub>2</sub> (g) for at least 2 h to reduce the influence of surrounding gases to the measurement. For the background measurement 100 scans are averaged. A number of 40 scans are used for each data point. To avoid contamination a cold trap and a particle filter are added in front of the FTIR gas measurement chamber. The quantification of the gas compounds is done with the software OPUS GA by Bruker. For each gas analyzed with FTIR a certain absorbance wavenumber region is chosen and compared with a reference spectrum (see supplementary material in chapter 9.1.1). The setting of the software OPUS GA is optimized for the expected gases and concentrations and validated with the test gas. The FTIR spectrometer is currently optimized for: CO, CO<sub>2</sub>, CH<sub>4</sub>, C<sub>2</sub>H<sub>6</sub>, C<sub>2</sub>H<sub>4</sub>, C<sub>2</sub>H<sub>2</sub>, DEC, DMC, EC, EMC, H<sub>2</sub>O, C<sub>6</sub>H<sub>14</sub>, HF, C<sub>4</sub>H<sub>10</sub> and C<sub>3</sub>H<sub>8</sub>.

#### 3.3.3.2 Gas chromatograph (GC)

For gas analysis with GC the 3000 Micro GC (G2802A) is used with three columns and thermal conductivity detectors (TCD). The three-channel system includes Molsieve (10 m × 320 μm × 12 μm), Plot U (8 m × 320 μm × 30 μm) and OV1 (8 m × 150 μm × 2.0 μm). The injector temperature and the sample inlet temperature are set to 100 °C for all three channels. The column temperature of the Molsieve channel is 80 °C (at 30 psi) and 60 °C for the Plot U and OV1 channel (40 psi each). Injection time for Molsieve and Plot U is 15 ms and 10 ms for the OV1 channel.

Since the GC uses corrosion sensitive columns, the gas is washed in water washing bottles at room temperature before entering the GC. These washing bottles are directly applied after passing the FTIR gas measurement chamber. Gases that do not dissolve or condensate in the water can be measured. Each GC gas measurement was repeated at least three times. The GC is calibrated for: H<sub>2</sub>, O<sub>2</sub>, N<sub>2</sub>, CH<sub>4</sub>, CO, CO<sub>2</sub>, C<sub>2</sub>H<sub>6</sub>, C<sub>2</sub>H<sub>4</sub>, C<sub>2</sub>H<sub>2</sub> using different test gases. For the quantification of each vent gas component the GC was calibrated using special fillings from Linde Gas GmbH (see specifications in chapter 9.1.3). For the calibration itself, the test gases and additional N<sub>2</sub> (5.0) gas was used in least at three different concentration ranges in the calibrated ranges listed in **Table 2**.

#### 3.3.3.3 Accuracy of the gas quantification

The accuracy of the gas analysis for the presented experiments is validated with test gas of different concentrations and the systematic and statistic uncertainties for FTIR and GC analyzed gas components are added up (**Table 2** and supplementary material in chapter 9.1). The FTIR measures spectra continuously over time with a low standard deviation of the measured value (dependent on gas compound <0.2% of the measured value).

The gas quantification method of the FTIR measured spectra is optimized for the expected gas concentrations produced at first venting and during TR. FTIR measurements have advantages at low gas concentrations like for gaseous and toxic HF, but disadvantages in symmetric molecules without change of dipole moment like H<sub>2</sub> and if the absorption peaks of gases are at similar wavelengths. The GC has its benefits at high concentrations of permanent gases, especially H<sub>2</sub>, N<sub>2</sub> and O<sub>2</sub> which cannot be measured with FTIR spectrometer.

**Table 2: Accuracy of the measured concentration  $c_m$  for each gas component in the reactor gas using FTIR and GC optimized for expected gas concentrations.**

gas	$c_m$ FTIR			$c_m$ GC		
	optimized concentration /%	accuracy /% rel.	LOQ /ppm	calibrated concentration /%	accuracy /% rel.	LOQ /ppm
O <sub>2</sub>	-	-	-	0–20	±5	14
N <sub>2</sub>	-	-	-	22–100	±3	220000
H <sub>2</sub>	-	-	-	0.1–35	±6	22
C <sub>2</sub> H <sub>2</sub>	0–10	±4	81	0.1–5	±4	200
C <sub>2</sub> H <sub>4</sub>	2–10	±5	14	0.1–5	±4	195
C <sub>2</sub> H <sub>6</sub>	0–10	±6	33	0.1–2	±5	184
CH <sub>4</sub>	0–10	±4	114	0.1–5	±5	272
CO	0–30	±4	65	0.1–55	±6	534
CO <sub>2</sub>	0–35	±4	121	0.1–28	±4	189
DEC	-	±4	20	-	-	-
DMC	-	±4	28	-	-	-
EC	-	±4	2	-	-	-
EMC	-	±4	25	-	-	-
H <sub>2</sub> O	0–3	±4	120	-	-	-
C <sub>6</sub> H <sub>14</sub>	-	±4	16	-	-	-
HF	0–30	±4	4	-	-	-
C <sub>4</sub> H <sub>10</sub>	-	±4	15	-	-	-
C <sub>3</sub> H <sub>8</sub>	-	±4	30	-	-	-

LOQ: limit of quantification at the specific setting in parts per million (ppm).

-: not calibrated for quantitative analysis or not possible to measure.

From the gas compounds quantified with both methods the result of one method, either FTIR or GC, is chosen depending on expected gas components and their concentration range. For small concentrations of CO, CO<sub>2</sub>, CH<sub>4</sub>, C<sub>2</sub>H<sub>6</sub>, C<sub>2</sub>H<sub>4</sub>, C<sub>2</sub>H<sub>2</sub> the measured FTIR concentration values are chosen because of the lower LOQ. If the measured concentration of C<sub>2</sub>H<sub>4</sub> is significantly higher than the LOQ, the GC measured value is chosen because of the higher accuracy compared to the FTIR.

### 3.3.4 Particle collection and particle analysis

The ejected particles were sampled after the TR and investigated using scanning electron microscopy (SEM) at the Institute of Electron Microscopy and Nanoanalysis (FELMI) at Graz University of Technology. The analysis was focused on particle size distribution (PSD) and particle composition. A ZEISS Sigma 300 VP (Variable Pressure) and a FEI Quanta 200 ESEM (Environmental SEM) were used for the investigation of the released particles after TR. The following SEM detection modes were used:

- For material contrast: imaging with backscattered electron (BSE).
- For topographic contrast: imaging with secondary electrons (SE).
- For elemental analysis: energy dispersive X-ray spectroscopy (EDX).

For the SEM investigations the particles needed to be fixed on a sample holder. The fixation must enable a homogeneous distribution without agglomeration of the particles. Gasser showed that the most reliable sampling method was to collect particles from inside the reactor with a spatula and spraying them by a jet of air on a double-sided adhesive carbon tape [113]. This method was used for

the sample preparation and subsequently the particles were analyzed with SEM/EDX to measure particle size and particle elemental composition.

Prior to the investigation, EDX simulations were performed with the public access program NIST DTSA-II [114]. Therewith the electron beam interaction was simulated, to be able to assess the best beam energy for SEM-EDX measurements of particles with the measured particle sizes [113].

#### **3.3.5 Additional safety-relevant parameters**

Beside the main investigated hazard categories and their resulting safety-relevant parameters, the total duration of the venting during TR and the mass reduction of the cell in TR are evaluated and compared.

##### **Duration of the venting during TR**

The duration of the venting during TR is defined as the time between the start of the TR (at the second venting when the pressure increase inside the reactor exceeds 200 mbar/s) until the maximum pressure in the reactor is reached.

##### **Mass reduction**

The weight of the test sample is measured before and after the experiment using a scale (KERN K8) with a measurement uncertainty of  $\pm 0.01$  g. The weight of the remaining cell including large parts (>30 mm length) of the cell outside the cell housing are measured after the experiment after-treatment including the heating of the reactor, the vacuum and the N<sub>2</sub> flushing.

##### **Repetition of the experiments**

Each TR experiment with unused fresh type #1 and #2 cells was repeated in order to comment on the reproducibility of the experiments and the quantification of the safety-relevant parameters. For the repeated experiments, the safety-relevant parameters, such as the maximum reached cell surface temperature, are presented as the average value of the repeated experiments and the deviation from one experiment to the other.

Due to the high costs of each TR experiment and the limited number of test cells available the tests had to be carefully planned.

### **3.4 Early failure detection method development**

The following chapter describes the methods used to find suitable gas sensors for early detection of battery failures and to benchmark them.

The idea of this study is to enhance battery safety and improve the concept of early detection of battery failures using gas sensors and pressure monitoring inside the battery pack additional to state-of-the-art battery failure monitoring. To do so, the use of gas sensors was tested in possible battery failure cases. The diagram in **Figure 10** shows the improved concept for early detection of battery failures. The new concept adds the detection of battery failures associated with gas emissions by means of gas sensor technologies, as well as the monitoring of the pressure inside the battery pack (cell pressure to neighboring cells and ambient pressure). In this study, the focus is put on the additional benefit of using gas sensors for early failure detection.

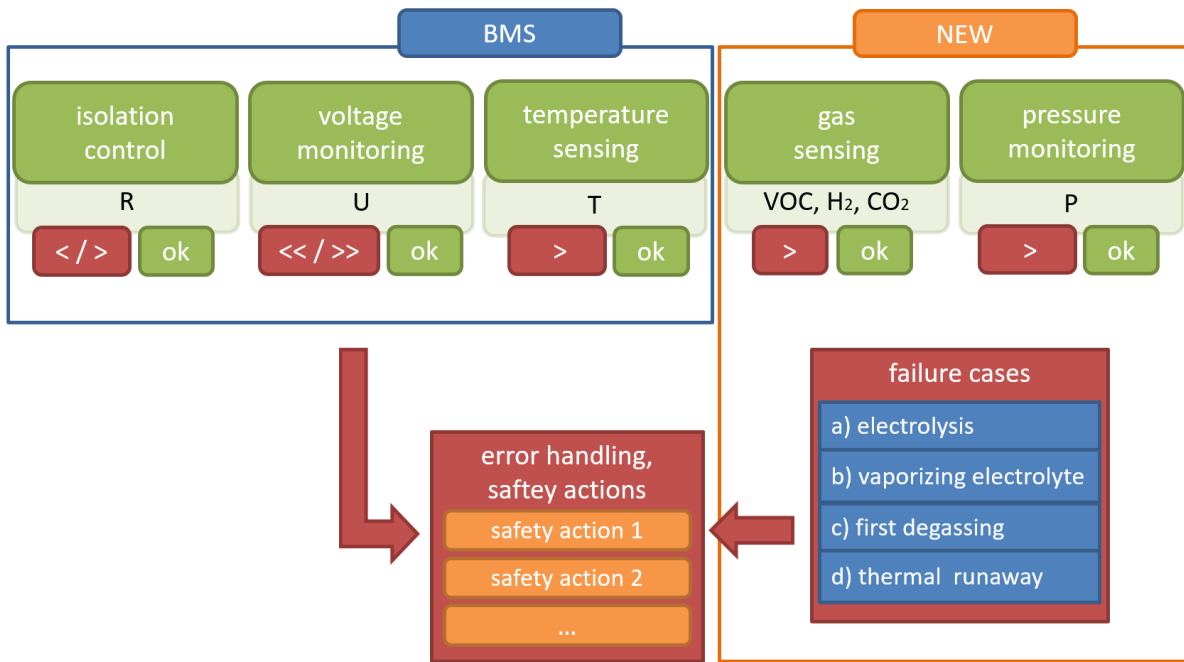


**Figure 10: The basic idea of this study is to improve the concept of early detection of battery failures with gas sensors and pressure monitoring inside the battery pack additional to the existing state-of-the-art battery failure monitoring by the battery management system (BMS). The proposed extended concept of early detection of battery failures is framed in orange and labelled with “NEW”.**

Upon exceeding defined operation thresholds, a warning is sent out and a reduction of power supply is requested, or the BMS disconnects the system from the mains. The other components (cells, cooling system, cabling) and functions (tightness of the battery housing, tightness of the cooling system) are secured by quality management in production. Monitoring of these components and functions with gas sensors (VOCs, H<sub>2</sub>, CO<sub>2</sub>, CO) and environmental sensors (pressure, air humidity) is planned as a supplement in the enhanced concept for early detection of battery failures. The concrete action of the BMS, the quality management in production and the implementation of the gas sensors into the application are not part of this study. Suggestions for the implementation of the sensors inside the battery pack are listed in [104].

### 3.4.1 Investigated battery failure cases

Under normal operation condition of the battery no gas emission is expected. In order to find suitable early failure detection methods, four concrete battery failure cases known to involve gas emissions were investigated experimentally in this study: a) unwanted electrolysis of liquid coolant or condensed water between battery parts under voltage, b) vaporizing electrolyte (VOCs) of leaky damaged cells, c) the first venting of a failing cell when the cell can opens above ~ 120-140°C in thermal abuse and d) the TR (see **Figure 11**). Failure case a) is critical because of the possible H<sub>2</sub> production during the electrolysis process of water molecules [115]. H<sub>2</sub> has a broad flammability range between 4 vol.% and 77 vol.% (20°C, 1.01 bar) in air atmosphere [116] and consequently after reaching the lower explosion limit H<sub>2</sub> production is a serious risk. Failure case b) vaporizing electrolyte components is critical due to the flammable, toxic, and irritant characteristics of commonly used liquid electrolyte additives [5,64,65] as described in chapter 2.4.1. Failure case c) and d) might lead to safety critical hazards from state-of-the-art batteries such as electrolyte vaporization, enormous heat generation, hazardous vent gas emission, toxic vent gas composition and particle emission [5], as described in chapter 2.4. If

oxygen is available during the TR reaction, the vent gases ignite. Battery fire e) was not investigated in this study.

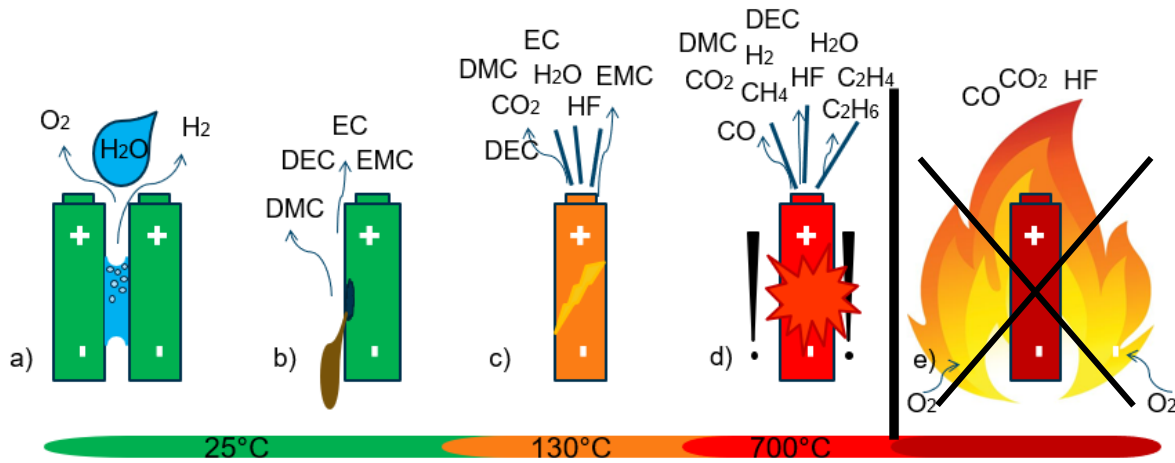


**Figure 11: Investigated battery failure cases, which involve gas emissions. a) unwanted electrolysis, b) vaporizing electrolyte of damaged cells, c) the first venting of a failing cell and d) the TR. e) battery fire is not investigated herein.**

Additional to the mentioned battery failure cases, the sensor response to overheated electronic components and cables as well as possible interfering gases potentially triggering false positives are investigated.

### 3.4.2 Analysis of produced gases

For the failure case a), unwanted electrolysis, a simplified test setup was constructed simulating the electrolysis of two voltage carrying hard case cells with water assembled between them. The aim of this study is not to investigate the electrolysis itself, but to get a rough estimation of possible  $H_2$  production in case of unwanted electrolysis.

For this reason, the amount of produced  $H_2$  in the electrolysis was calculated under certain assumptions (constant current  $I$  (A), a 100% Faraday's yield for  $H_2$  production and neglecting of heat production) using the Faraday's law.  $H_2$  production on the cathode in water electrolysis is described as [117].

The resulting electric current and consequently the amount of produced  $H_2$  depends on several factors: the electrode material, the conductivity of the electrolyte, the distance between the voltage carrying parts, the applied voltage and the area of the voltage carrying parts [118]. For simplicity reasons the tests were carried out using the housing of prismatic hard case cans (aluminum) and water (tap water and deionized water were tested) as electrolyte. The electrodes were cut out of the cell housing into several pieces of the same size. Voltage between 4.15 V (voltage of one single cell) and 48 V (typical electric vehicle system voltage) was applied between the two electrodes. Electrode distances between 4 mm and 15 mm were tested. The resulting electric current was measured with an Agilent multimeter 34410A. For the qualitative detection of the produced  $H_2$ , a  $H_2$  sensitive sensor (Sensirion SPG30) was used. This setup was chosen to simulate a real failure case of battery electrolysis, where water penetrated unintentionally the battery pack of 48 V. For the calculation of the  $H_2$  amount produced in the electrolysis, the highest experimentally measured current (710 mA) was taken (48 V, 8 mm distance, 1500 mm<sup>2</sup> surface area per electrode, tap water electrolyte).

The produced gases at the failure cases b) to d) were quantified with FTIR and GC in parallel according to chapter 3.3.3. The gas analysis method and calculations are published and described in detail in [5]. Failure cases c) and d) were analysed in the TR reactor presented in chapter 3.2. For failure case b) a simplified setup was constructed consisting of a sample chamber, sensor chamber and gas analysis afterwards (detailed description in section 3.4.4 and **Figure 12**).

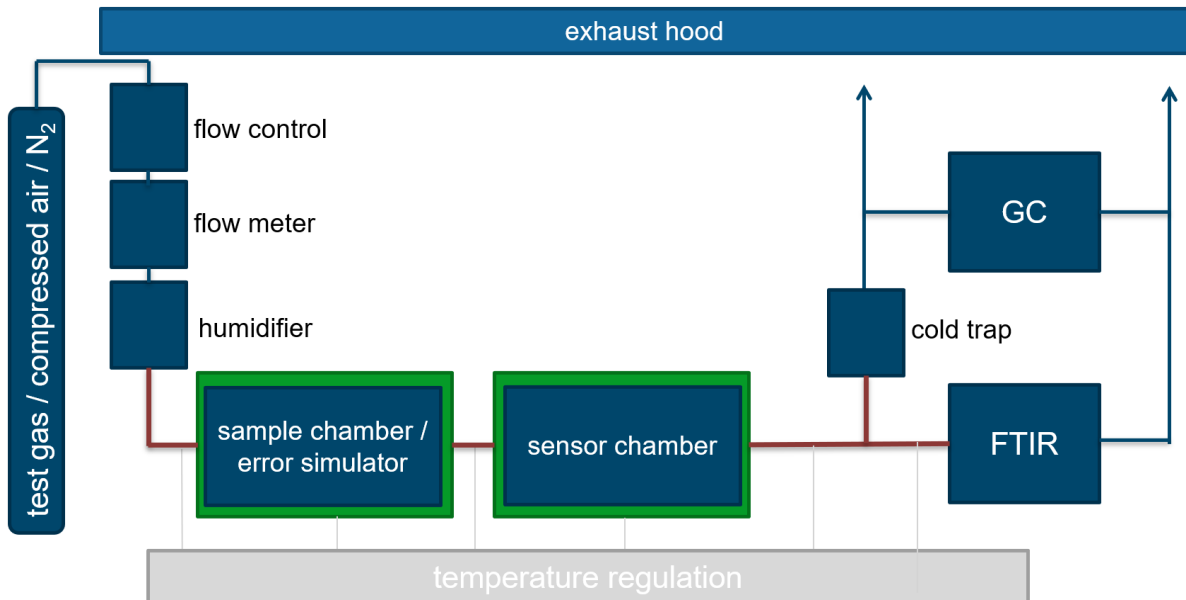


**Figure 12: Sensor test setup: inside an exhaust hood the sensor reactions to different target gases, at different temperature, humidity, and flow rate were investigated. The test sample was positioned inside the sample chamber; the sensors are placed inside the sensor chamber.**

### 3.4.3 Sensor selection

Based on the gases measured at the four failure cases, suitable low-cost and commercially available gas sensors were chosen and tested in laboratory settings and in TR experiments. The selection of the sensors was carried out under the following criteria:

- Target gas: The sensor must detect emitted gases from battery failures such as electrolyte vapor (VOCs), H<sub>2</sub>, CO, CO<sub>2</sub> in a suitable concentration range.
- Price: The sensor must be inexpensive for the end application (<<10 €). Furthermore, no additional costs for maintenance/calibration should be incurred.
- Lifespan/ certification: The sensor should meet automotive lifetime expectations (typically >10 years or > 8000- 10000 hours of continuous operation) and ideally shall be qualified according to automotive requirements.
- Size: The sensor must be dimensioned according to its place of use, maximum size as 40 mm x 30 mm x 10 mm.

If all criteria are met, the sensor measurement technology and the manufacturer are of minor importance. In this study, different measurement principles were investigated in order to be able to provide comparisons (therefore, also sensors with higher prices were chosen) and the sensors were purchased from various established manufacturers in order to meet the state-of-the-art.

### 3.4.4 Sensor test setup

The chosen sensors were purchased as ready-to-use evaluation boards (on printed circuit boards (PCBs)) and assembled on a sensor platform (see **Figure 13** (a)). A Raspberry Pi 3B+ was used for data acquisition, storage, and transfer making use of its integrated inter-integrated circuit (I<sup>2</sup>C) interfaces. While the I<sup>2</sup>C interfaces were used for the digital sensors, the analog sensors were connected to external analog-to-digital converter (ADC) chips and read out with the I<sup>2</sup>C interface. Almost 20 sensors were operated simultaneously on such a compact sensor platform.

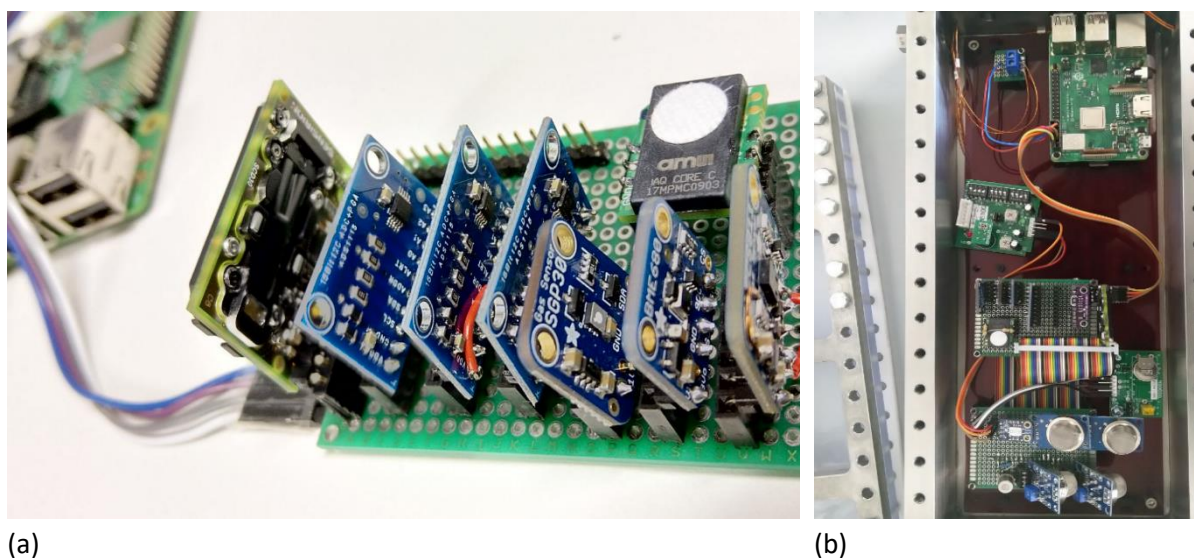


**Figure 13: (a) gas sensor platform with several sensors on PCB boards (b) sensor platform inside the sensor chamber.**

For validation tests this sensor platform was placed inside the sensor chamber (see **Figure 13** (b)). The complete setup for sensor validation consisted of flow control, flow meter, humidifier, sample chamber, sensor chamber, cold trap, and optional gas analysis with FTIR and GC in parallel (see **Figure 12**). Different test gases were applied, and the total setup could be heated. Also, the reaction of the sensors to overheated liquid or solid samples was investigated using this setup.

The sensors were validated for several electrolyte mixtures, relevant test gases H<sub>2</sub>, CO, CH<sub>4</sub>, CO<sub>2</sub>, interfering gases, which might trigger false positives and overheated electronic components and cables.

### 3.4.5 Event detection

Based on the gas sensor response to the investigated battery failures, a method for event detection was investigated. To detect a failure event fast, the deviation of the low pass filtered sensor signal is used in this study. For the low pass filter the following common algorithm was used:

$$data_{low\ pass}(i) = (1 - \alpha) * data_{low\ pass}(i - 1) + \alpha * data(i) \quad (2)$$

In this study, results with a value of  $\alpha = 0.1$  are presented. The difference of two neighboring low pass filtered values highlights the battery failure event (event detector 1 (ED1)). The detected events exceed a predefined minimum signal-to-noise ratio (SNR). The SNR is defined as the ratio between the mean

value  $\overline{data}$  (here the low passed value) and the standard deviation  $\sigma$  according to the National Institute of Standards and Technology [119,120]:

$$SNR = \frac{\overline{data}}{\sigma} \quad (3)$$

Based on the low pass filtered values the baseline (BL) was calculated:

$$\Delta data\_BL(i) = data_{low\ pass}(i) - BL(i - 1) \quad (4)$$

For the BL the following criteria were used:

- If the value  $\Delta data\_BL$  is higher than the maximal positive gradient (MPG), the MPG is added to the previous BL value.
- If the  $\Delta data\_BL$  is lower than the maximal negative gradient (MNG), the MNG is added.
- If both criteria are not valid, the current  $\Delta data\_BL$  value is added to the previous BL value.

Consequently, the baseline follows the low pass filtered signal as long as the difference between two neighboring values is between the defined MPG and MNG. But if the difference is higher, the BL differs from the low pass filtered values. Depending on the setting of MPG and MNG, the BL follows the low pass filtered values faster or slower.

As second indicator to detect the failure event, the value  $\Delta data\_BL$  was used (event detector 2 (ED2)). Therefore, the combination of two event detectors was used in this study: the difference of two neighboring of low pass filtered sensor signals (ED1) and the difference between the low pass filtered values and the calculated BL (ED2). In order to distinguish between the failure cases, the reaction change of the different sensor pixels to the different failure cases need to be analysed.

### 3.5 Designs of experiments

In this chapter the DoEs using different cell types are described. The overtemperature TR trigger was chosen as the basic TR trigger. The basic TR trigger was used to investigate the factors influencing the failing behavior (SOC, aging). A brief summary of the different DoEs is as follows:

- Cell type #3 was used for the comprehensive investigation of the five hazard categories and the SOC. The cells were tested in (unused) fresh state in three different SOCs (100%, 30% and 0%).
- Cell type #1 and #2 were investigated in (unused) fresh state in three different TR trigger (overtemperature, overcharge and nail-penetration) in order to quantify the influence of different cell designs and different TR triggers.
- Cell type #1 was also chosen for the quantification of the effect of different aging paths on the failing behavior. Failing cells with three different aging paths (cyclic aging at very low (-10°C) and high temperature (+45°C) and high temperature calendric aging(60°C)) were tested.
- Cell type #4 and #2 were chosen for the benchmark of the gas sensors as early battery failure detector in more than 30 overtemperature, overcharge and nail-penetration TR experiments.

In the following subsections, the focus of each study is framed in color gray.

For unused, fresh cell type #1 and cell type #2 each experiment is repeated in all three TR triggers in order to comment on the reproducibility of the experiments and the quantification of the safety-relevant parameters.

### 3.5.1 DoE – Comprehensive hazard analysis and SOC influence

Cell type #3 was chosen for the investigation of all five hazards from failing LIB (gas composition at first venting (electrolyte vapor), thermal behavior at TR, vent gas emission at TR, vent gas composition at TR, particle emission at TR, see **Figure 14**). The TR experiments of the type #3 cell were conducted using three different SOC (100%, 30% and 0%), in overtemperature TR trigger. The results are compared to evaluate the influence of SOC to the failing behavior (see [5]).

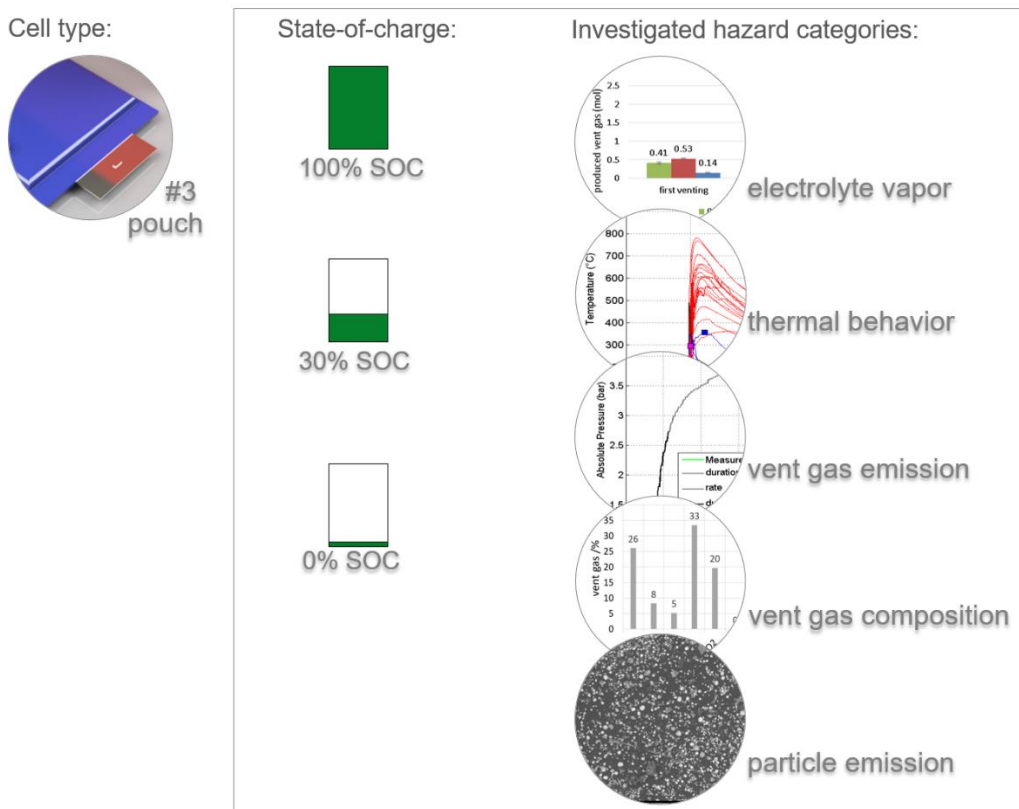


**Figure 14: Design of experiment – Comprehensive hazard analysis and influence of SOC of cell type #3: gas composition at first venting (electrolyte vapor), thermal behavior at TR, vent gas emission at TR, vent gas composition at TR, particle emission at TR. Three different SOC stages (100%, 30% and 0%) were tested in overtemperature experiments.**

For this investigation, three overtemperature experiments with fresh automotive pouch cells type #3 were conducted. In the first experiment the cell was charged to 100%. In the second experiment the cell was charged to 30% and in the third to 0%. Each single cell was triggered into the failing behavior separately by heat. The cell was heated by the sample holder with a constant rate of temperature increase from both sides and a specified heat ramp (0.39 °C/min for 100% SOC; 0.36 °C/min for 30% SOC until 38,000 s, then increased rate; 0.33 °C/min for 0% SOC). Only in this experimental setup the chosen heat ramp deferred from the description of the overtemperature trigger in chapter 3.2 (standard heat ramp of ~ 2°C/min).

### 3.5.2 DoE – TR trigger and cell type influence

Cell type #1 and #2 have the same capacity, have both a NMC (622) cathode, graphite anode and are covered in two different cell housing types – pouch versus prismatic hard case. Consequently, these two different cell types are chosen to be compared in order to quantify the influence of the cell design (pouch versus hard case cells) on the failing behavior of LIB. The DoE is presented in **Figure 15**. Additionally, both cell types are tested with three different TR triggers (overtemperature, overcharge and nail-penetration) starting at 100% SOC before each TR experiment. The trigger settings are described in chapter 3.2.2.

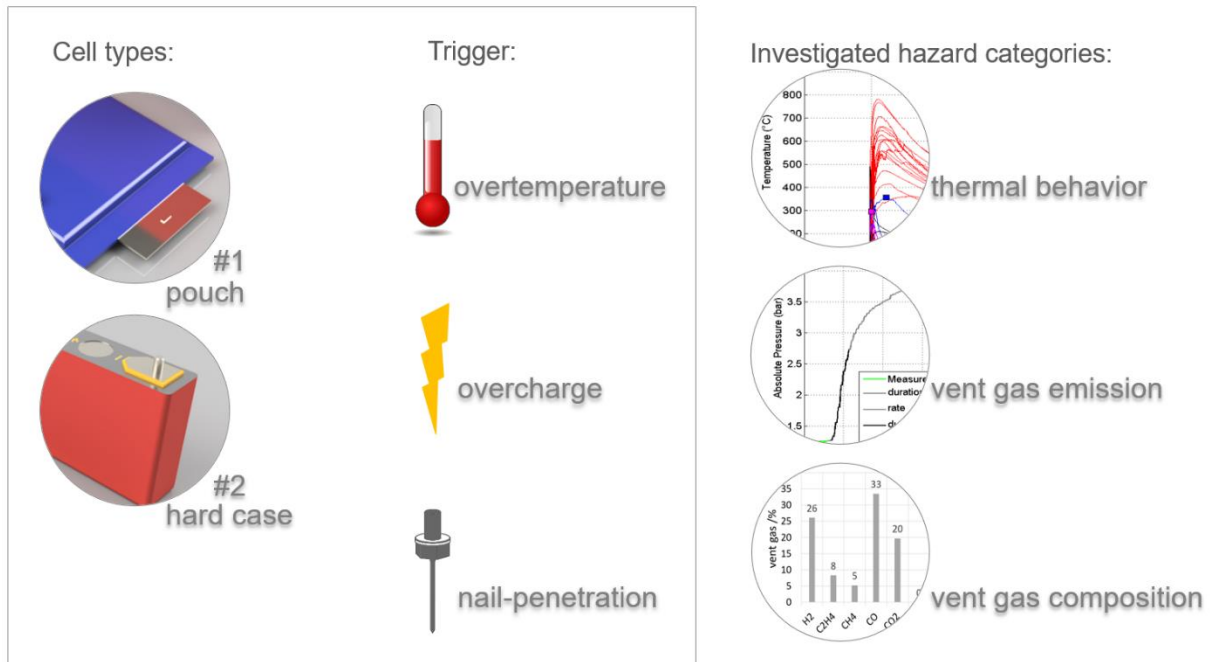


**Figure 15: Design of experiment - influence of TR trigger and cell type: two cell types (#1 pouch and #2 hard case) were tested in three different TR triggers (overtemperature, overcharge and nail-penetration) one cell after the other. Fresh unused cells at 100% SOC are chosen for this test setup. The results were discussed in three main hazard categories: thermal behavior, vent gas emission and vent gas composition [11].**

The capacity of the two commercially available cell types is the same, but the cells are series products of two different cell manufacturer and the active material and electrolyte composition is not the exact same and different additives might be added [11].

### 3.5.3 DoE – Aging paths influence

Cell type #1 was tested in unused fresh state and after three different aging paths (cyclic aging at -10°C (cy-10) and at 45°C (cy+45) and high temperature calendric aging at 60°C (ca60)). The design of the aging experiment and the experiments itself have been provided by a partner institution. The key aging parameters are described in **Table 3**. After the end of the aging experiment, the cells were shipped to our institution and stored at room temperature for another five months before the experiment inside the TR reactor.

**Table 3: Key parameters of the aging experiments using cell type #1.**

aging description	abbr.	T / °C	SOC / %	charge current / A	discharge current / A	$\Delta$ SOC / %	duration / days	nr. of cycles	SOH / %
calendric 60°C	ca60	60	100	-	-	-	150 days	-	94
cycling -10°C	cy-10	-10	-	12	20	0-100	-	800	85
cycling 45°C	cy+45	45	-	20	20	0-100	-	1000	76

During the aging experiments the cells were under compression inside sample holders comparable to the mechanical tension inside the battery pack. The parameter SOH in **Table 3** represents the SOH immediately before the TR experiment. The SOH was determined by dividing the measured capacity (calculated with coulomb counting according to the voltage limits given in the data sheets) by the nominal capacity and is expressed as a percentage.

The single fresh and aged cells were experimentally tested with an overtemperature trigger. The design of the TR experiment is shown in **Figure 16**. Each cell was charged to 100% SOC before the experiment. For this investigation exactly the same experimental methods for overtemperature trigger and the same analysis of safety-relevant parameters were used as described in chapter 3.5.2 [11]. For each experiment three hazard categories are discussed: thermal behavior, vent gas production and vent gas composition.

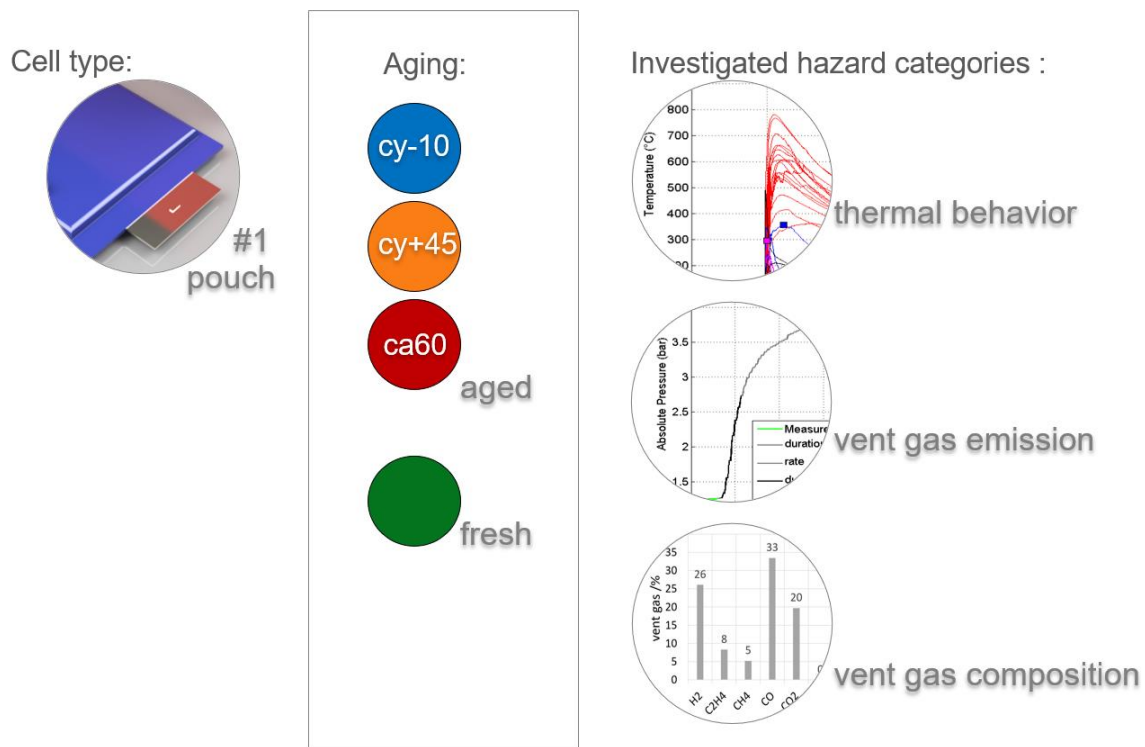


**Figure 16: Design of experiment – Influence of different aging paths on the failing behavior of cell type #1. Three different aging paths were investigated: high temperature calendric aging, cyclic aging at -10°C and 45°C and compared with the results of fresh type #1 cells. The results were discussed in three main hazard categories: thermal behavior at TR, vent gas emission at TR and vent gas composition at TR. Each cell was charged to 100% SOC and was tested in overtemperature experiments.**

### 3.5.4 DoE – Early battery failure detection with gas sensors

Four concrete battery failure cases known to involve gas emissions were investigated experimentally in this study (see **Figure 11**) in order to find suitable gas sensors for early detection of battery failures. Additional to the described methods in chapter 3.4.1 the failure cases c) the first venting and d) the TR were analysed inside the TR reactor. Cell type #4 and #2 were used in field-experiments for the most promising gas sensor as early battery failure detector. The gas sensor was tested in more than 30 different TR experiments of unused fresh LIBs starting at 100% SOC. The sensor response was investigated in overtemperature, overcharge and nail-penetration triggered TR experiments (see **Figure 17**). In this study, the results of failing type #4 and #2 cells are presented. The focus was set on the reaction of the chosen gas sensor to the failing behavior of the automotive LIBs.

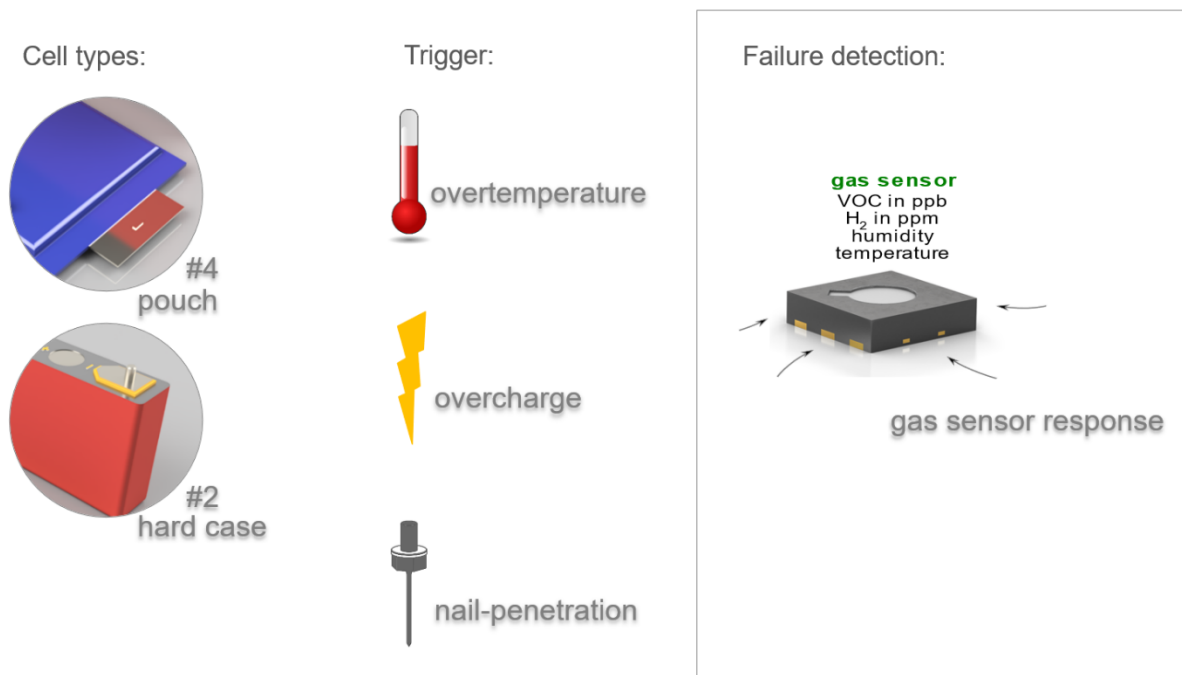


**Figure 17: Design of experiment – Early failure detection with gas sensors. Different automotive cell types were tested in three different TR triggers (overtemperature, overcharge and nail-penetration) one cell after the other. In this study, results of cell type #2 and #4 are presented. Fresh unused cells at 100% SOC were chosen for this test setup. The main focus was set on the reaction of the chosen gas sensor to the failing behavior of the cell.**

## 4 Experimental results and discussion

The structure of this chapter is based on the research questions listed in chapter 2.8.

### 4.1 Comprehensive hazard analysis and SOC influence

*This chapter is already published in:*

Essl C, Golubkov AW, Gasser E, Nachtnebel M, Zankel A, Ewert E, Fuchs A. Comprehensive hazard analysis of failing automotive Lithium-ion batteries in overtemperature experiments. *Batteries* 2020; **6**(30): 1–28. DOI: 10.3390/batteries6020030.

Three experiments with fresh automotive pouch cells (cell type #3) were conducted (one with 100% SOC, one with 30% and one with 0%). The first venting of the cell could be observed at all three test samples. The TR could only be triggered at the fully charged cell.

The heat triggered TR experiments of a currently used high capacity cell - extracted from a modern mass-produced EV - enables studying hazards and quantify safety relevant parameters from this automotive cell type #3. Since there are few papers available for failing high capacity NMC/LMO cells, the study of those hazards is even more important. This research concentrates on all five categorized hazards and the safety relevant parameters at different SOC (100%, 30%, 0%). **Table 4** sums up all safety relevant findings of the heat triggered battery failures of the fresh automotive pouch cell.

**Table 4: Summary of safety relevant parameters of overtemperature experiment of the fresh automotive pouch cell at 100%, 30% and 0% SOC [5].**

safety relevant parameter	100% SOC	30% SOC	0% SOC
first venting (electrolyte vapor)	yes	yes	yes
thermal runaway	yes	no	no
start voltage (V)	4.18	3.67	3.11
heat ramp (°C/min)	0.39	0.36	0.33
$T_{cell}^{V1}$ (°C)	130	127	120
$T_{voltage=0}$ (°C)	203	190	190
$T_{cell}^{crit}$ (°C)	231	-	-
$T_{cell}^{max}$ (°C)	715 (self-heating)	309 (external heating)	242 (external heating)
duration of TR (s)	4	-	-
amount of vent gas $n_v$ (mol)	2.31 (57 l)	0.53 (13 l)	0.41 (10 l)
characteristic venting rate $\dot{n}_{ch}$ (mol/s)	0.8 (18.7 L/s)	-	-
main gas compounds	CO <sub>2</sub> , CO, H <sub>2</sub>	DEC, CO <sub>2</sub> , H <sub>2</sub> O	DEC, CO <sub>2</sub> , H <sub>2</sub> O
C <sub>H2</sub> (vol.%)	23	4	1
C <sub>CO</sub> (vol.%)	17	5	1
particle release (g)	~300	-	-

At 30% SOC and lower, it was not possible to trigger the cell into TR with the same heat setup (**Table 4**). If the cell is fully charged during thermal abuse the electrolyte reacts with the lithiated anode after the SEI breakdown [10,56]. Additionally, the stability of the delithiated cathode material is decreased [89]. If the cell is at 0% or 30% SOC the reaction of the lithiated anode with the electrolyte is reduced

due to the lack of Li in the anode. No exothermal decomposition of those cells is observed. Increased safety with decreasing SOC is consistent with [51,56,85,89], although referenced literature describes different chemistries and cell components: NCA and LFP [85]; NCA [89]; NMC/LTO [51]. The thermal interactions between several binder materials and anode carbon at 50% and 100% SOC is reported in [56].

Still one question is remaining: Which SOC is the minimum to trigger TR thermally?  $SOC_{crit}$  is defined as the lowest SOC to trigger TR. For this investigated cell it seems to be  $>30\%$ , but there is no general answer for other cells, especially not for higher energy density cells. The SOC influences hazards, consequently safety and health risks from failing LIBs. At failing cells with  $SOC < SOC_{crit}$  the vaporizing electrolyte and the electrolyte decomposition has the risk of developing flammable, toxic and corrosive gases. At cells with  $SOC > SOC_{crit}$  additional serious risks from heat generation, hot gas and particle emission due to the uncontrollable exothermal reaction need to be considered.

#### 4.1.1 Thermal behavior

One critical hazard of a failing cell is heat generation, which can be detected by measuring the temperature response of the cell to the trigger (**Figure 18**). The experiment of the fresh automotive pouch cell at 100% SOC is compared to the 30% SOC cell in **Figure 18** (a),(c) during the whole heat ramp experiment and **Figure 18** (b),(d) at the main exothermic event.

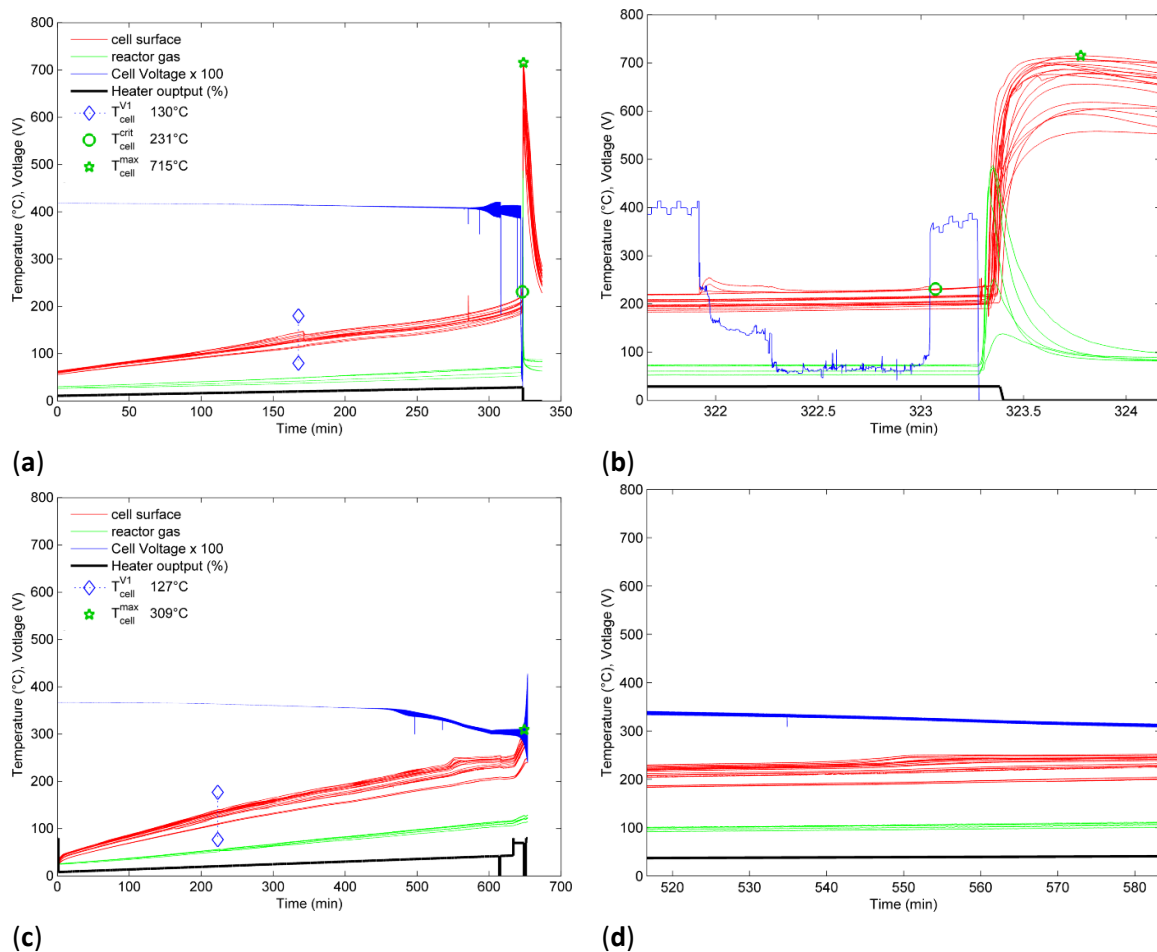


**Figure 18: Overtemperature experiments of a fresh automotive pouch cell type #3 at (a)(b) 100% SOC and (c)(d) 30% SOC: (a) and (c) show the temperatures at up to 30 different positions during the heat ramp experiment measured on the cell surface (red) and inside the reactor (green). The heater output of the sample holder in % is plotted (black line). The cell voltage times 100 is plotted in blue. (b)(d) show the temperature measured at the main exothermic event. In (b)  $\pm 1$  A pulses are visible (blue) [5].**

#### 4.1.1.1 Experiment with the 100% SOC cell

As the fully charged cell was heated it showed a minor temperature excursion in the range of  $T_{cell}^{V1} = 130^{\circ}\text{C}$ —the first venting of the cell—10.300 s after activating the heat ramp (**Figure 18** (a)). The pouch cell opened. The cell reached the onset temperature after further heating. The onset of the main exothermic reaction was detected at  $T_{cell}^{onset} = 170^{\circ}\text{C}$ . The voltage of the cell started decreasing during the heating phase at  $70^{\circ}\text{C}$  and dropped completely to 0 V at  $203^{\circ}\text{C}$  cell surface temperature. The second venting started at  $T_{cell}^{V2} = 212^{\circ}\text{C}$ . The main exothermic reaction developed to a rapid TR at  $T_{cell}^{crit} = 231^{\circ}\text{C}$  (self-heating beyond  $10^{\circ}\text{C}/\text{min}$ ). At 100% SOC the cell exhibited an exothermic reaction after 19.397 s and reached a maximum temperature of  $T_{cell}^{max} = 715^{\circ}\text{C}$  on the cell surface. The main exothermic reaction begun at a location between the center of the cell and the positive tab of the cell. Within 4.28 s the exothermic reaction propagated through the cell (time between the rapid increase of the first thermocouple and the increase of the last thermocouple in **Figure 18** (b)).

#### 4.1.1.2 Experiment with the 30% and 0% SOC cell

Compared to the fully charged fresh cell, the cell with 30% SOC behaved differently using the same overtemperature setup (**Figure 18** (c),(d)). After reaching the first venting at about  $T_{cell}^{V1} = 127^{\circ}\text{C}$ , no exothermic reaction was detected even by heating beyond  $231^{\circ}\text{C}$ . The 30% SOC cell was heated with a constant rate of  $0.36^{\circ}\text{C}/\text{min}$  until 38.000 s and afterwards with an increased rate up to  $309^{\circ}\text{C}$  (**Figure 18** (c)). After reaching the  $309^{\circ}\text{C}$  maximum cell surface temperature, the heat ramp was stopped. The 0% SOC cell also could not be triggered into TR by heat. At  $T_{cell}^{V1} = 120^{\circ}\text{C}$  cell surface temperature, the first venting was detected. The experiment was stopped heating up to  $240^{\circ}\text{C}$ .

#### 4.1.1.3 Discussion thermal behavior

Temperature sensors on the cell surface showed the TR propagation through the cell in 4.28 s. This rapid exothermal reaction and maximal cell temperatures above  $700^{\circ}\text{C}$  can challenge prevention of TR propagation to neighboring cells and increase resulting risks and damage.

The comparison of the experiments at 100%, 30% and 0% SOC illustrates that the first venting of the investigated cell begun between  $T_{cell}^{V1} = 120^{\circ}\text{C}$ – $130^{\circ}\text{C}$  cell surface temperature. The deviations between the measured  $T_{cell}^{V1}$  values may not be connected to the SOC and is explained as a measurement uncertainty for this type #3 cell.  $T_{cell}^{V1}$  is comparable with the measured temperature rate change (first venting) of overheated NMC pouch cells at about  $120^{\circ}\text{C}$  plotted by Ren et al. [36]. Ren et al. showed in [36] (**Figure 11**) that the first venting appeared almost at the same temperature  $\sim 120^{\circ}\text{C}$  independent of the four different degradation paths and SOH. This would mean that aging effects, like SEI growth and electrolyte consumption, does not influence the first venting. For 50 Ah LMO prismatic hard case cells at our test stand the first venting was observed between  $T_{cell}^{V1} = 194^{\circ}\text{C}$ – $220^{\circ}\text{C}$  [57]—far apart from our measured values for the pouch cell. This may indicate the influence of different cell design (hard case), vent design and chemistry (LMO) to  $T_{cell}^{V1}$ .

The next important temperature is the critical temperature  $T_{cell}^{crit}$ , where the temperature rate of the hottest sensor exceeds  $10^{\circ}\text{C}/\text{min}$ , immediately before the full TR. At the fully charged cell  $T_{cell}^{crit} = 231^{\circ}\text{C}$  is comparable with the defined temperature  $T_2$  by Feng et al. [46]. Feng et al. correlated the influence of gravimetric energy density to the maximum reached temperature in [46] (**Figure 6**). Our result of  $T_{cell}^{max} = 715^{\circ}\text{C}$  fits the presented maximum temperature of NMC/LMO and NMC cells with similar energy density measured in [36] and [46]. At the TR, the cell temperature increases enormously due to chemical reactions inside the cell mainly produced by NMC degradation and reaction of the cathode and the solvent according to [46,56]. The maximum reached temperature can be significantly higher than  $715^{\circ}\text{C}$  on the surface of the cell and even more inside the cell itself as demonstrated by [52]. The

exothermic decomposition of the delithiated cathode material and the reaction between the released  $O_2$  with the solvent is speculated to be the reason for reaching the maximum cell surface temperature [56,60] at the fully charged cell.

Energy density, cathode material and cell design seem to be a main influencing factor for safety relevant and critical temperatures like the first venting as well as the maximum reached cell surface temperature.

## 4.1.2 Vent gas emission

### 4.1.2.1 Experiment with the 100% SOC cell

The pressure inside the reactor increased slowly at the first venting of the pouch cell and abruptly at the TR (**Figure 19 (a)**). **Figure 19 (b)** shows that the gas emission of the cell at the TR took in total about 4 s. About 50% of the gas was produced in  $\Delta t_{50\%} = 1.44$  s and 90% in  $\Delta t_{90\%} = 3.22$  s.

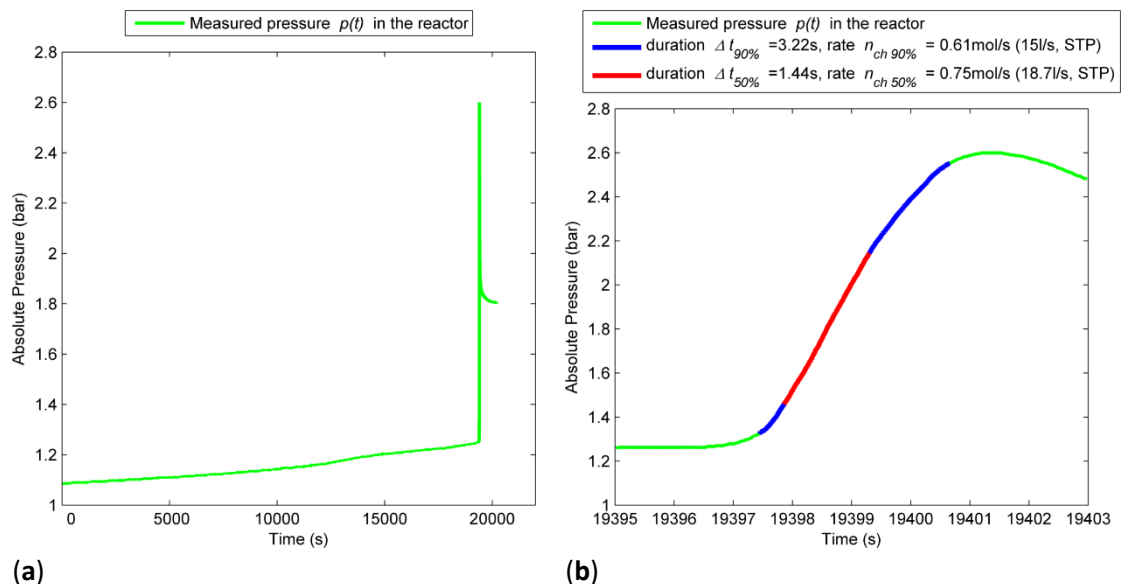


**Figure 19: Absolute pressure (green) versus time of the fully charged cell (a) during the whole experiment and (b) at the TR only. The maximum pressure was reached 4 s after the TR started. 50% of the gas was produced in 1.44 s (red line). 90% of the gas was produced in 3.22 s (blue) [5].**

The fully charged cell released during the first venting  $n_{v1} = 0.14$  mol of gas (**Figure 20 (a)**). During the main TR reaction, the cell released additional  $n_{v2} = 2.17$  mol of gas with a characteristic venting rate of  $\dot{n}_{ch} = 0.8$  mol/s (18.7 L/s). The calculated produced vent gas amount is shown in **Figure 20 (a)**. At 100% SOC in total  $n_v = 2.31$  mol gas, which is equivalent to 52 norm liters (at  $0^\circ\text{C}$ , 1013.25 hPa) and 57 L at STP, are produced. The fully charged cell produced 0.06 mol/Ah (equivalent to 15 mol/kWh, 1.3 L/Ah) during the overtemperature TR experiment.

### 4.1.2.2 Experiment with the 30% and 0% SOC cell

The 30% SOC cell released  $n_v = 0.53$  mol (13 L) gas during the first venting and constant evaporation of electrolyte until the heating is stopped at  $309^\circ\text{C}$  (**Figure 20 (b)**). Compared with  $n_{v1}$  of the fully charged cell, the 30% cell released  $n_v = 0.11$  mol until  $T_{cell} = 212^\circ\text{C}$ . The discharged cell showed a similar behavior and produced  $n_v = 0.41$  mol (10 L) gas until the heating is stopped at  $240^\circ\text{C}$ . In these cases, after the first venting, additional gas was produced during the heating phase.

## 4.1 Comprehensive hazard analysis and SOC influence

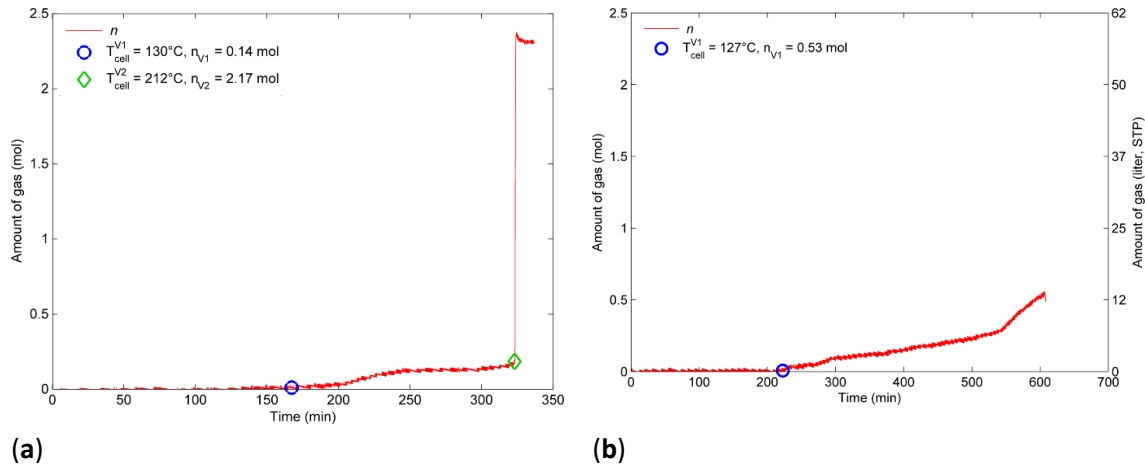


**Figure 20: Produced vent gas amount  $n_v$  in mol and liter at STP during the experiments of the (a) 100% and (b) 30% SOC cell. At the 100% SOC cell two venting stages are measured: A first venting starting at  $T_{cell}^{V1}$  and a second venting starting at  $T_{cell}^{V2}$ . The 30% SOC cell released gas starting at the first venting at  $T_{cell}^{V1}$  until the heating was stopped [5].**

Figure 21 shows the produced gas amount in mol of the 0%, 30% and 100% charged cell for the first venting, the second venting and the total gas emission. In case of the 0% and 30% cell no second venting could be triggered, therefore, the gases produced until the heating was stopped were added up to the first venting. Hence, the amount of produced gas at the first venting was higher at the 0% and the 30% SOC cells than at the 100% SOC cell.

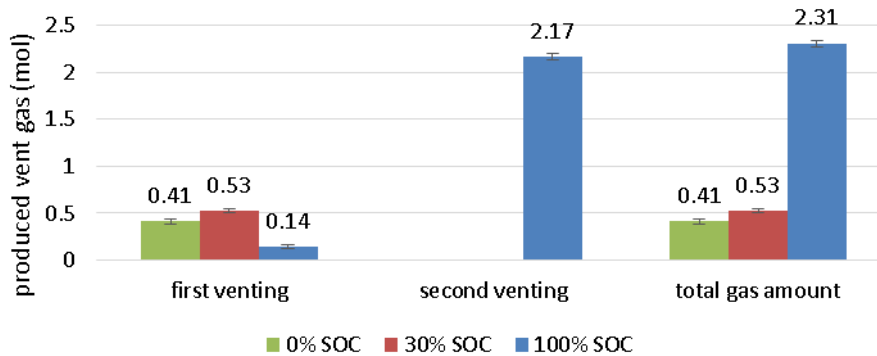


**Figure 21: Produced vent gas amount in mol for 0% (green), 30% (red) and 100% SOC (blue) pouch cell at overtemperature experiments after the first venting and the second venting in comparison [5].**

### 4.1.2.3 Discussion vent gas emission

The pressure increase itself at the first venting does not present any hazards. But the abrupt gas production at the TR and the venting rate of 18.7 L/s can lead to explosion of a battery pack.

The soft pouch packaging ruptured at  $T_{cell}^{V1}$  and the cell started to release gas continuously until the TR happened or the heating was stopped. The 100% SOC cell released 0.14 mol gas before the TR. During the TR, the cell released abrupt additional 2.17 mol of gas within 4 s. The 4 s reaction time was observed in the measured temperature and pressure data at the TR. The characteristic venting rate was 0.8 mol/s (18.7 L/s) and is comparable with the published results of Golubkov et al. for heated 50 Ah prismatic LMO cells ( $0.8 \pm 0.3$ ) mol/s [57]. This parameter is a relevant parameter for battery pack design and vent design. For higher energy densities and higher capacities increased maximum gas rates are expected. In addition, the reaction time of 4 s observed by the pouch cell may be different for prismatic hard case cells.

The measured 1.3 L/Ah vent gas for this cell is barely within the literature review of Koch et al. of 1.3 L/Ah–2.5 L/Ah for current state-of-the-art batteries [73] and shows that the presented cell produced less gas compared with cells of similar capacity, energy density and chemistry, but the vent gas emission still needs to be considered as a serious safety risk. Compared to other state-of-the-art automotive pouch and hard case cells analyzed in our test setup, this investigated cell produced less gas per Ah at 100% SOC heat trigger, although no gas reducing electrolyte additives could be found. Roth et al. investigated the vent gas amount for different cathode materials (LCO, NCA, NMC, LFP, LMO) and found that all cells produce about 1.2 L/Ah and that a main factor of predicting gas generation is the volume of the used electrolyte [66]. It needs to be mentioned that more vent gas is expected at the presence of O<sub>2</sub> (as measured by Koch et al. as 1.96 L/Ah [73]) and at increasing SOC, like published at overcharge experiments of NCA and LFP cells in [85]. Additional published gas emission values are for NMC 1.2 L/Ah (0.9 Ah NMC) [66], 1.4 L/Ah (2 Ah NMC) [74] and 0.9 L/Ah (2.6 Ah NMC in air) [84]. Deviations from [84] may be explained due to different vent gas amount calculation. The literature source reporting of 2.5 L/Ah is not experimentally determined. Therefore, we assume that NMC/LMO cells produce between 1.2 L/Ah–2 L/Ah gas at thermal abuse. If the cell goes into TR (SOC ≥ SOC<sub>crit</sub>) main influencing factors seem to be the capacity of the cell, the electrolyte amount, the SOC, different trigger and present O<sub>2</sub>. According to Roth et al. cathode material has a minor influence on the gas amount.

#### 4.1.3 Vent gas composition

The main gas components at the heat triggered cell at 0% and 30% SOC were CO<sub>2</sub>, DEC, H<sub>2</sub>O with minor components like CO, H<sub>2</sub>, C<sub>2</sub>H<sub>4</sub>, CH<sub>4</sub>, C<sub>3</sub>H<sub>8</sub>, C<sub>2</sub>H<sub>6</sub>, C<sub>2</sub>H<sub>2</sub> (Figure 22). The main gas components of the fully charged cell were in descending order at the first venting DEC, H<sub>2</sub>O, CO<sub>2</sub>, CO, C<sub>2</sub>H<sub>6</sub>, H<sub>2</sub>, C<sub>2</sub>H<sub>4</sub> and at the TR CO<sub>2</sub>, H<sub>2</sub>, CO, H<sub>2</sub>O, C<sub>2</sub>H<sub>4</sub>, CH<sub>4</sub>, DEC, C<sub>4</sub>H<sub>10</sub>, C<sub>2</sub>H<sub>6</sub>, C<sub>2</sub>H<sub>2</sub>. In **Table 5** the measured gas concentration values of the experiment at 100% and 30% SOC are listed as well as the vent gas composition in vol.% and mol according to equation (1).

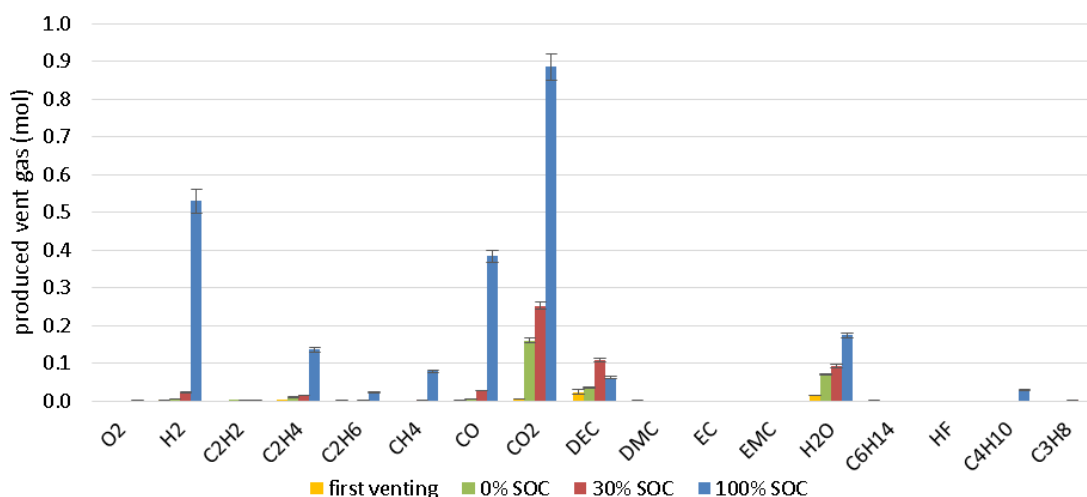


**Figure 22: Measured gas composition in mol: immediately after the first venting at  $T_{cell}^{V1}$  of the 100% SOC cell (yellow); after the heat ramp was stopped at the 0% (green) and 30% SOC cell (red); and after the TR of the 100% SOC cell (blue); experimental setup in N<sub>2</sub> [5].**

The measured gas components at the 30% SOC and 0% SOC cell match with the gas compounds measured at the beginning of the first venting of the 100% SOC cell at about 120–130°C cell surface temperature. Additionally, it is assumed that the quantified gases at the 30% and 0% SOC cell are

dominated by SEI decomposition, electrolyte vapor and decomposition reaction of the electrolyte above 200°C [8]. At the experiments of the 100%, 30% and 0% SOC cell no HF was detected.

**Table 5: Measured gas concentration values at heat triggered fresh automotive pouch cell at 100% SOC versus 30% SOC in N<sub>2</sub> [5].**

gas	100% SOC			30% SOC		
	measured gas	vent gas (without N <sub>2</sub> )	vent gas (without N <sub>2</sub> )	measured gas	vent gas (without N <sub>2</sub> )	vent gas (without N <sub>2</sub> )
	c <sub>m</sub> / vol.%	c <sub>v</sub> / vol.%	c <sub>v</sub> /mol	c <sub>m</sub> / vol.%	c <sub>v</sub> / vol.%	c <sub>v</sub> /mol
O <sub>2</sub>	0.01	0.04	0.00	0.00	0.00	0.00
N <sub>2</sub>	69.21			89.01		
H <sub>2</sub>	7.06	22.93	0.53	0.41	4.47	0.02
C <sub>2</sub> H <sub>2</sub>	0.02	0.05	0.00	0.01	0.12	0.00
C <sub>2</sub> H <sub>4</sub>	1.81	5.88	0.14	0.27	2.93	0.02
C <sub>2</sub> H <sub>6</sub>	0.30	0.99	0.02	0.03	0.36	0.00
CH <sub>4</sub>	1.06	3.46	0.08	0.05	0.52	0.00
CO	5.11	16.59	0.38	0.47	5.15	0.03
CO <sub>2</sub>	11.80	38.33	0.89	4.39	47.73	0.25
DEC	0.83	2.69	0.06	1.91	20.72	0.11
DMC	0.00	0.00	0.00	0.00	0.00	0.00
EC	0.00	0.00	0.00	0.00	0.00	0.00
EMC	0.00	0.00	0.00	0.00	0.00	0.00
H <sub>2</sub> O	2.32	7.55	0.17	1.61	17.50	0.09
C <sub>6</sub> H <sub>14</sub>	0.00	0.00	0.00	0.00	0.00	0.00
HF	0.00	0.00	0.00	0.00	0.00	0.00
C <sub>4</sub> H <sub>10</sub>	0.39	1.26	0.03	0.00	0.00	0.00
C <sub>3</sub> H <sub>8</sub>	0.00	0.00	0.00	0.05	0.50	0.00
gas amount			2.31 mol			0.53 mol

c<sub>m</sub>: measured gas concentration including N<sub>2</sub> atmosphere; c<sub>v</sub>: vent gas concentration in vol.% according to equation (1), or in mol.

The FTIR spectra of vent gases produced at the 100% (blue) and the 30% (red) charged cell are compared directly in **Figure 23**. The absorbance spectrum shows for the 30% SOC cell significant higher absorption peaks of the used electrolyte DEC between 1000–1850 cm<sup>-1</sup> than at the venting of the fully charged cell. In the spectrum of the gas produced at the 100% SOC cell the electrolyte absorption peaks decreased (decomposition of the electrolyte, TR reaction and less long heating time at the 100% SOC cell) and CO, CO<sub>2</sub>, CH<sub>4</sub> and C<sub>2</sub>H<sub>4</sub> increased.

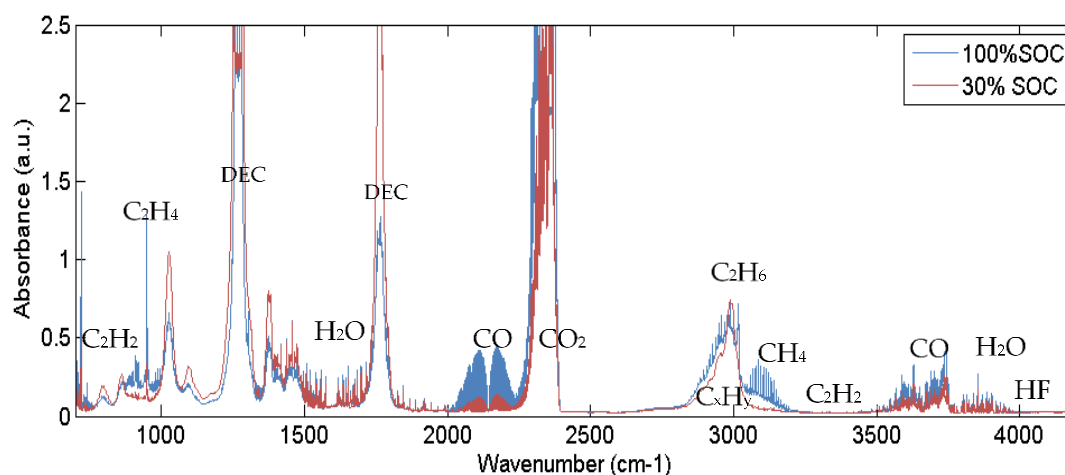


**Figure 23: FTIR spectrum of the gas composition measured after the TR of the 100% SOC cell (blue) in comparison to the spectrum measured after stopping the heat ramp at the 30% SOC cell (red) [5].**

#### 4.1.3.1 Discussion gas composition below $SOC_{crit}$ —30% and 0% SOC

Vent gases measured at the 30% and 0% SOC cell and the first venting were dominated by electrolyte vapor,  $CO_2$  and  $H_2O$ . At this cell EC (irritant, PAC-1:  $30\text{ mg/m}^3$ ) and DEC (flammable, PAC-1:  $2\text{ mg/m}^3$ ) were the main electrolyte components. Lebedeva et al. stated clear that most of the currently used LIB electrolytes are toxic, irritant or harmful in addition to being flammable and may even be carcinogenic [65]. Therefore, the opening of the cell and first venting below  $SOC_{crit}$  need to be handled as a serious risk due to irritant, toxic and flammable composites, especially at the early opening soft pouch packing and the vaporization of electrolyte inside a closed system (pack, garage, tunnel).

Beside significant electrolyte vapors the following gas components were measured at the heated 30% and 0% SOC cell in descending order:  $CO_2$ ,  $H_2O$ , DEC, CO,  $H_2$ ,  $C_2H_4$ ,  $CH_4$ ,  $C_3H_8$ ,  $C_2H_6$ ,  $C_2H_2$ . There are many studies reporting gas generation from electrolyte at cycling, formation and heating. The main gas components are similar to the measured gas components in this experiment ( $CO_2$ , CO,  $C_2H_4$ ,  $CH_4$ ,  $C_3H_8$ ,  $H_2$ ,  $C_2H_6$  [121–123]), although the exact gas concentration depends highly on the used electrolyte composition and the additives.

Gas generated at overheating of cells below  $SOC_{crit}$  are rarely published. Literature on high capacity NMC or NMC/LMO cells concerning the first venting or gassing at cells with  $SOC < SOC_{crit}$  is missing. Literature from small capacity cells: For a 3.35 Ah NCA cell Golubkov et al. presented on 25% SOC 18650 cells at heating similar main gas compounds:  $CO_2$ ,  $H_2$ ,  $CH_4$ ,  $C_2H_4$ , CO [85] (electrolyte and higher hydrocarbons were not quantified). For a 1 Ah LCO cell with 50% PC, 20% EMC, 15% DEC and 10% DMC Kumai et al. measured before and after cycling tests significant different gas compositions, but also the same main gas components:  $CH_4$ ,  $CO_2$ , CO,  $C_2H_6$ ,  $C_3H_8$  and  $C_3H_6$  [61] ( $H_2$  and electrolyte compounds were not quantified). The produced gases can also be compared with gases produced at the formation process and cycling of NMC cells: At a NMC(422)/graphite cell with 3:7 EC:EMC and  $LiPF_6$  at 100% SOC  $CO_2$ ,  $C_2H_4$ ,  $C_2H_6$ ,  $C_2H_5F$ ,  $C_3H_8$  and  $CH_4$  were measured in decreasing order [121]. Wu et al. investigated at LTO/NMC cells the gas generation at different electrolyte compositions with and without cell formation (SEI) and found significant reduction in  $CO_2$  compared to cells with SEI [123].

Possible sources of the identified gases are therefore: for  $CO_2$ : electrolyte decomposition [48,122] and SEI decomposition [8,123] (especially the organic components of the SEI), reaction of electrolyte and positive electrode [40]; for CO: EC [122] DEC and EMC [8]; for  $C_2H_4$ : EC [122], SEI decomposition [8]; for  $C_2H_6$ : DEC [122] and DMC [8]; for  $H_2$ : reaction between linear carbonates and anode [123], Li with water containing electrolyte [124], binder [125][10]; for  $C_3H_8$  and  $CH_4$ : DMC [123].

It seems that the cathode material plays a minor role for the gas composition at the first venting and at thermal abuse of cells below  $SOC_{crit}$ . The major influence appears to be the electrolyte composition and the reaction of the electrolyte with the Li in the anode after the SEI breakdown.

#### 4.1.3.2 Discussion gas composition —100% SOC

Main components after TR were: 38%  $CO_2$ , 23%  $H_2$ , 17%  $CO$ , 8%  $H_2O$ , 6%  $C_2H_4$ , 4%  $CH_4$  and electrolyte vapor 3% DEC. TR vent gas consisted—apart from  $CO_2$  and  $H_2O$ —of mainly toxic ( $CO$ ) and flammable ( $H_2$ ,  $CH_4$ , DEC) gases. Beside the risk of toxic and flammable atmosphere, fire and explosion are serious consequences.

$CO_2$  was the most abundant gas component in the vent gas at the heat triggered TR at 100%, 30% and 0% SOC. At the 100% charged cell a 3.9 times higher  $CO_2$  amount was measured than at the 30% SOC cell. The ratio of  $CO_2:CO = 9.3:1$  for the 0% SOC and 30% SOC cell and  $CO_2:CO = 2.3:1$  for the 100% SOC cell. This observation can change at TR of LIBs with higher energy density, where  $CO_2:CO$  ratios less than one were possible at TR [73] and more  $CO$  than  $CO_2$  was produced due to incomplete combustion reaction. Similar  $CO_2:CO$  ratios of measured gases at heat triggered TR of NMC cells were observed in [87], although the investigated cell was a 1.5 Ah 18650 cells with DMC:EMC:EC:PC (7:1:1:1) and an energy density of 133 Wh/kg (only  $CO_2$ ,  $H_2$ ,  $CO$ ,  $CH_4$  and  $C_2H_4$  were analyzed). In addition, perfect comparable main gas concentrations were measured for NMC cells with different electrolyte compositions by Koch et al. The mean substance concentration values over 51 NMC LIBs fit perfectly for the presented results in this study: 37%  $CO_2$ , 22%  $H_2$ , 6%  $C_2H_4$  and 5%  $CH_4$  [73] with the difference in  $CO$  amount (28%  $CO$  by Koch et al.). The different  $CO$  amount can be explained by the lower energy density at our NMC/LMO cell. Koch et al. did not quantify gaseous  $H_2O$  and electrolyte [73]. For different cathode materials similar gases, but different gas concentrations, were observed [87]. If the same cell chemistry is analyzed, but different triggers are used (like overcharge or nail penetration instead of overtemperature), different preferred chemical reactions take place ending up in different gas compositions [71] (see chapter 4.2).

As stated by Zhang et al. in literature no more than 10 gas species in the vent gas were quantified except for their own study [86]. Thus, in this study, 18 possible gas compounds during battery failures are presented. Additional gases identified by other authors, but not listed in this study, for instance  $C_3H_6$  [73] and other higher hydrocarbons (less than 1.7% of the total gas emission according to [86]), were not identified. The deviations may be explained by different cell chemistry, different reaction probability, the test setup and the gas analysis methods. Commonly used electrolytes as EC, DEC, DMC and EMC absorb at similar wavenumber regions and can only be identified clearly at certain wavenumber regions with the FTIR.

Although for the presented experiments no HF could be detected, HF is expected to be released by the cell in small amounts [71,75] and to undergo further reactions with the materials inside the reactor, the analysis region and the released particles. Beside the HF production, F may also remain in the cell itself and  $LiF$  can be formed. For another aged 18 Ah cell with NMC/LTO chemistry in our test setup, 66 ppm (0.396 mmol) HF were measured [76].

Adding up all quantified gas components at the presented results does not sum up to 100% in total. Possible reasons of the deviation are the sum of uncertainties of each gas component and gases which could not be identified/measured in this experiment.

In addition to the listed gases produced at the venting of cells with  $SOC < SOC_{crit}$ , at TR an increase of especially  $H_2$ ,  $CO_2$  and  $CO$  were observed. Though the total amount of measured electrolyte at the fully charged cell was reduced in comparison to the cell at 30% SOC (**Figure 23**), parts of the vent gas resulted from decomposing parts of 44 g EC, 59 g DEC, 3.7 g DMC according to [10,126,127] and

resulted in mainly CO<sub>2</sub> and H<sub>2</sub>O. Further sources for the gases are for H<sub>2</sub>: the reaction of binder material and Li in the anode [84]; for CO<sub>2</sub>: oxidation of the electrolyte on the negative electrode surface and LiPF<sub>6</sub> and further reaction with the released O<sub>2</sub> of the decomposing cathode [8,59,66,122].

Concluding, the vent gas composition of a failing LIB may be highly sensitive to the SOC, the failure mode/trigger, the used electrolyte composition (especially for cells with SOC < SOC<sub>crit</sub>) and the chemistry. This NMC/LMO cell produces similar gases and concentrations as published NMC cells.

#### 4.1.4 Particle emission

Imaging of particles collected after the TR was performed using SEM. SE images deliver topographic contrast (**Figure 24 (a)**). Although BSE imaging enables material contrast (**Figure 24 (b)**), where particles with higher mean atomic number appear comparatively brighter and particles of different composition could be discerned by different gray levels, SE imaging was used to enhance the visibility of carbonated particles on the carbon substrate. To determine the PSD, SE images were binarized by gray value thresholding. Results of the measured average particle areas are presented in **Table 6**. Due to different reasons, like image noise or image resolution, particles segmented with the threshold method which were beneath 2 μm<sup>2</sup> in area had a big relative uncertainty. The investigation of the particle size showed that most of the particles had an area smaller than 10 μm<sup>2</sup> and about half of the particles were smaller than 5 μm<sup>2</sup>.

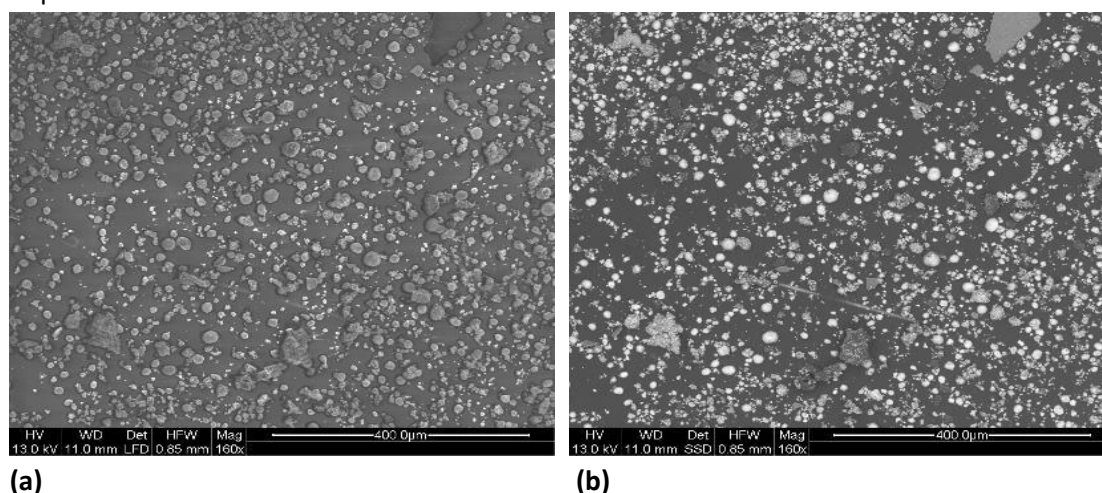


**Figure 24: SEM images of particles assembled after the TR. (a) SE image shows the topographic contrast; (b) BSE measurement shows the material contrast of the same area of the sample. Particles were positioned on a carbon adhesive tape [5].**

**Table 6: Average measured area (a) of particles and average number of particles produced from an automotive pouch cell (at 100% SOC) in overtemperature experiments [5].**

area of particles/μm <sup>2</sup>	average number of particles/%
1 < a ≤ 2	21.8 ± 7.6
2 < a ≤ 3	11.6 ± 2.2
3 < a ≤ 5	12.2 ± 2.7
5 < a ≤ 10	15.8 ± 0.6
10 < a ≤ 50	26.2 ± 5.5
50 < a ≤ 100	6.6 ± 3.4
100 < a	5.9 ± 5.5

To obtain a precise particle composition EDX analysis was used. Therefore, the combination of the SEM with an Oxford XMax 80 EDX detector was applied using the software AZtec for EDX control an evaluation. Therewith it was possible to simultaneously obtain the PSD and the elemental composition of every individual particle. With this setup five different categories of particles were identified and assigned the following classes:

1. Particles mainly consisting of Al and O. Their assumed chemical formula is  $\text{Al}_2\text{O}_3$  (**Figure 25**).
2. Particles with huge amounts of nickel (Ni), manganese (Mn), O and smaller amounts of cobalt (Co). The assumed chemical formula is  $(\text{Li} + \text{NMC})_3\text{O}_4$ .
3. Particles mainly consisting of Mn and O. The average elemental composition has the estimated chemical formula  $\text{Mn}_2\text{O}_3$  or its decomposition products.
4. Particles with a high content of C. Very small EDX peaks of O, F and phosphorus (P) were measured.
5. The fifth particle class describes agglomerates with several different material composites which do not fit into one of the listed classes.

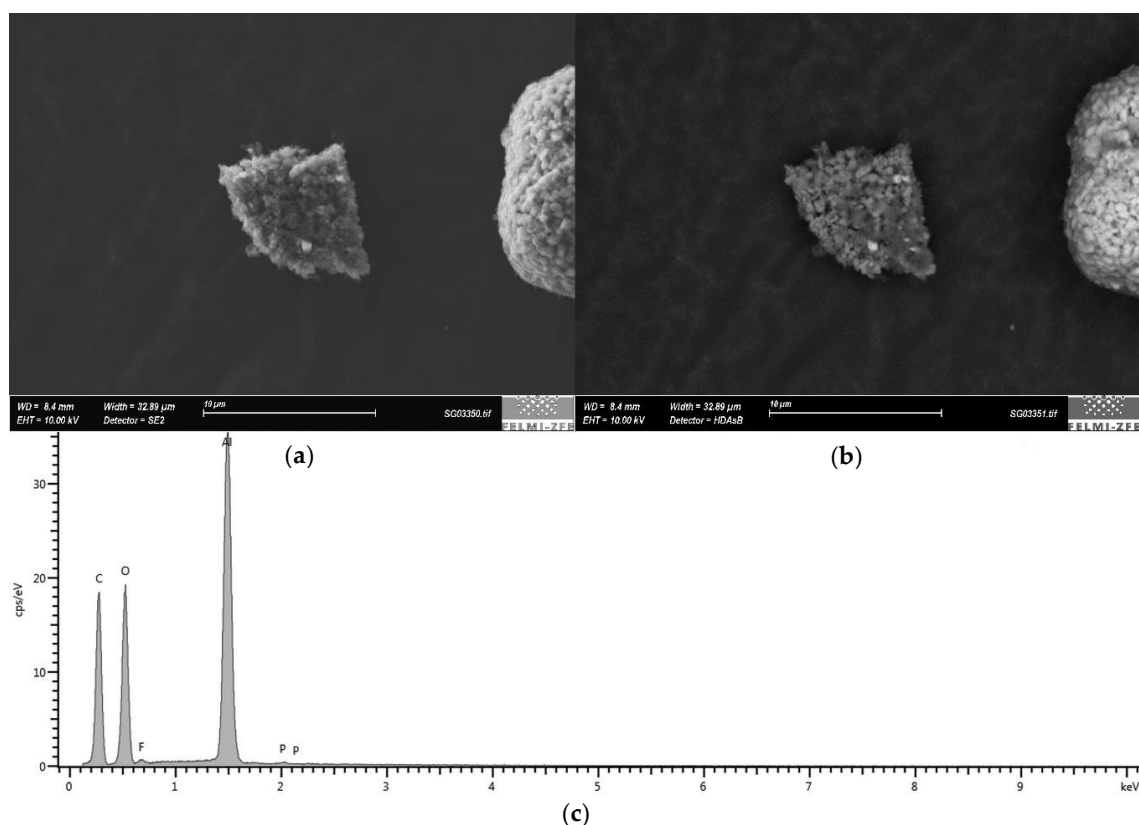


**Figure 25: Analysis of a class 1 particle: (a) SE image, (b) BSE image, (c) EDX spectrum. The presented scale in (a) and (b) is 10  $\mu\text{m}$  [5].**

The identified particles were parts of the cell active material and were ejected by the cell due to the exothermic reaction. The Mn rich particles (class 2 and 3) resulted from the cathode. The C rich particles originated from the anode. F and P may result from the salt  $\text{LiPF}_6$ . A small amount of C measured at almost every particle might result from the used carbon tape, the conducting carbon in the cathode or the carbon coating which was performed prior to the investigation in order to get an electrically conductive surface of the specimen.

In the appendix chapter 9, supplementary materials, SEM images of particles of the listed classes and the correlated spectra are explained. Exemplarily **Figure 25** shows (a) the SE image, (b) the BSE image

and (c) the EDX spectrum of a particle of class 1. The main elements in this particle were O and Al, as shown in the EDX spectrum. For the most particles of this class the chemical formula  $\text{Al}_2\text{O}_3$  was assumed.

### 4.1.4.1 Discussion particle emission

The ejected particles contain elements that are potentially toxic and could act as an ignition source of the emitted burnable gases, due to their high temperature [7,77]. Furthermore, most of the particles are smaller than  $10\ \mu\text{m}^2$  and can therefore be inhaled deeply into the lungs [128].

Challenges to the particle analysis were the sampling method and the evaluation of the exact particle size and composition. Sampling is the bottleneck of any analytic method and may compromise the results, even when using a measurement method with high precision. During sampling, the material of interest should not be altered, and the sample should be representative. Several methods were tested and are described in [113]. However, the jet of air sampling method used in the end provided a uniform distribution of the particles on the carbon tape used in the SEM measurements, allowing the individual analysis of the particles regarding their size and composition. It has to be mentioned that the air sampling method was selective concerning the dimensions of the particles, but we assume that it is representative for these particles, which are relevant concerning hazards during inhalation.

The particles contain elements that are potentially toxic for humans including Al, Ni, F. Those elements were also reported in [77]. Thus, safety equipment for people handling cells after TR is important such as particle masks and protective clothing. However, the measured major particle size ( $< 10\ \mu\text{m}^2$ ) and the reported mass loss does not match with the observations of [77,86]. Zhang et al. show in [77] for a fully charged prismatic hard case cell particle matter account for 11.20% of the cell mass. Measured particle sizes were less than 0.85 mm at nearly 45% of particles. In [86] Zhang et al. report a mass loss of 28.53% at a 50 Ah cell due to gas and particle emission with a near 90% of the particles with a size of 0.5 mm in diameter. Zhang et al. measured lower maximum cell surface temperature ( $438^\circ\text{C}$ ) [86]. The deviation in particle size may be explained due to differences in the cell design (prismatic hard case versus pouch), the chemical composition, the sample preparation techniques and the analysis methods.

In [77] and [86] four different methods were used for the characterization of settleable particulate matter in the chamber, where the thermal runaway was investigated. In fact, very precise methods were applied, which have the drawback, that not one and the same sample can be used for each method. This is a great advantage of SEM combined with EDX, because after getting a specimen holder with disjunct fixated (carbon tape) particles the number, morphology, size and elemental composition (from the element boron (B) to uranium (U)) can be measured using only one methodical approach on the same sample. Hence a good statistic can be achieved, and even individual information of each particle was enabled. Additionally, it has to be highlighted that the only alteration of the sample is the application of a thin carbon layer on the particles, which is fundamental for imaging without charging, but is not compromising the elemental assessment. Thus, using SEM/EDX no heating of the material or dilution in a supporting liquid is needed as is prerequisite at several chemical or elemental analytical methods.

Beside elemental analysis using EDX even chemical analysis via Raman spectroscopy would help to identify particles. Especially organic materials (e.g., carbon rich particles) could be assessed. A new system called RISE (Raman Imaging and SEM) combines high resolution imaging using an SEM with chemical analysis by an integrated Raman microscope [129]. Thus, correlative microscopy combining morphologic, elemental and chemical investigation could be realized. In this special case the application of a carbon layer would be obstructive since it would mask the signal for Raman

measurements. However, the used SEM enables a special vacuum mode (variable pressure), where imaging without charging and subsequent EDX and Raman analysis can be realized.

### 4.1.5 Mass reduction

Since no TR could be triggered at the 0% and 30% SOC cell, the initial cell mass of 865 g was reduced by 15% during the whole experimental test including the after-treatment. Considering the amount of vent gas and the molar mass of the measured main gas components produced until the heat ramp was stopped, the 30% SOC cell released in total 27 g uncondensed gas during the heat ramp experiment. We assume that the mass reduction of 15% was due to the measured gas, condensed gas and additional gases produced at the experiment after-treatment.

At the 100% SOC overtemperature experiment the initial cell mass of 868 g reduced to 491 g after the TR. This means a cell mass reduction by 43%. This mass reduction can be explained as the sum of released gas, liquids and ejected particles at the TR. Considering the amount of vent gas and the molar mass of the measured main gas components  $H_2$ , CO and  $CO_2$  and the side products  $CH_4$ ,  $C_2H_4$ , DEC,  $H_2O$ ,  $C_2H_6$ ,  $C_4H_{10}$  in total 74 g not condensed gas was released during the TR experiment. The measured gas components were about 20% of the lost cell mass during TR and about 9% of the initial cell mass. The result of the total mass of produced gas was used to assume the mass of the produced particles at the TR. The total mass loss (377 g) minus the gas amount (74 g) resulted in  $\sim 300$  g particles. We assumed that EC, one of the main electrolyte components, condensed after the TR. Gas with high boiling temperature condensed on the colder reactor walls, but the amount of condensed gas is not the focus of this study.

At the TR, the investigated cell reduced the initial mass by 43% due to gas and particle emission. This result is comparable with pouch and hard case cells at 100% SOC overtemperature experiments by [73] reporting mass loss of 15–60% for NMC cells with 20–81 Ah. Zhang et al. measured significant lower mass loss (29%) for overheated prismatic NMC cell [86]. The mass loss of the 0% and 30% charged cells after the experiment after-treatment (15%) is comparable with the assumed amount of electrolyte (14%). Therefore, it is assumed that the mass loss of the 0% and 30% charged cell was mainly due electrolyte vaporization and decomposition of SEI, electrolyte and synthetic material. The quantified mass reduction seems to depend on the SOC, the energy content of the cell, the cell design (hard case prismatic or cylindrical versus pouch cell) and the TR trigger.

### 4.1.6 Optical observation of the cell after TR

The pouch foil of the fully charged cell was heavily damaged on the top and bottom side after the TR and the Cu foil was visible on the top. The foil opened on all three welded sides except for the side with the terminals. In **Figure 26** the cell stack including metallic glossy droplets are visible. We assume that these are Al droplets from the Al current collector. At the 30% and the 0% SOC cell no visible openings of the pouch foil surface were observed. The pouch was still closed on the sides of the terminals. An opening was observed opposite the terminals.



**Figure 26: The pouch cell after TR was opened on the welded sides. Droplets were visible between the stacked cell layers [5].**

## 4.2 Influence of thermal runaway trigger and cell type

*This chapter is already published in:*

Essl C, Golubkov AW, Fuchs A. Comparing Different Thermal Runaway Triggers for Two Automotive Lithium-Ion Battery Cell Types. *Journal of The Electrochemical Society* 2020; **167**(130542): 1–13. DOI: 10.1149/1945-7111/abbe5a.

In total twelve TR experiments on single EV cells were conducted (see **Figure 27**).

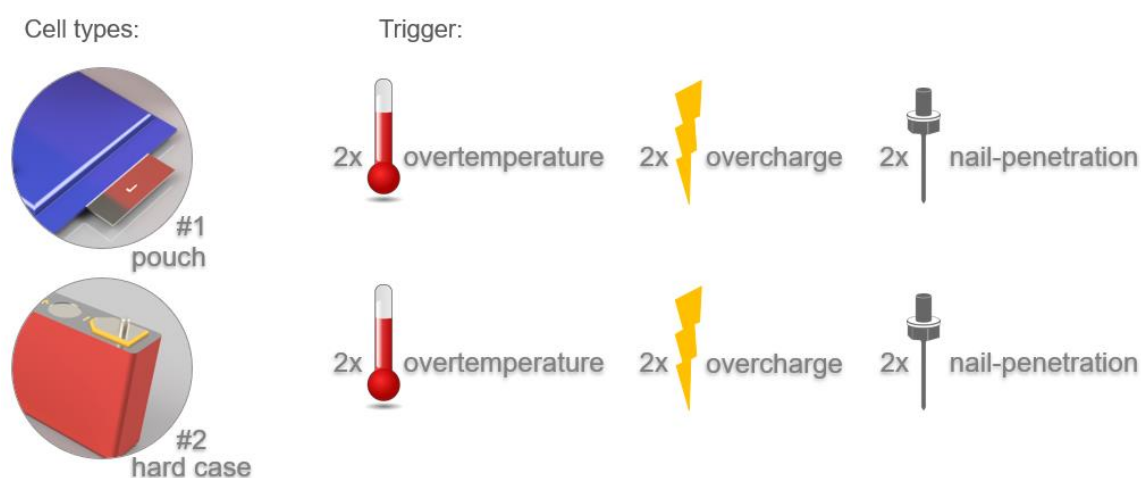


**Figure 27: Experiment matrix: for each cell type (#1 and #2) two overtemperature, two overcharge and two nail-penetration experiments were conducted [11].**

Each cell was triggered into TR. The experiments were reproducible in the categories thermal, electrical, mechanical and venting behavior. As Koch et al. referred in [96] the basic effects occurring during the TR (loss of cell voltage, self-heating of the cell, production of gas, cell rupture, particle ejection) were very similar for both cell types, but there are small but safety relevant differences in the failing behavior of both cell types and for the three different triggers:

- **Overtemperature:** The homogenous heating from both large sides of the cell forced cell type #1 to the first venting at  $(121 \pm 1)^\circ\text{C}$  and cell type #2 at  $(138 \pm 1)^\circ\text{C}$ . The first venting can be explained by pressure increase inside the cells due to gases produced at the solid electrolyte interface (SEI)

decomposition [7,66], electrolyte decomposition [74] and continuous evaporation of the electrolyte [5]. The cell housing opens at the weakest point. After the first venting and the continuous heating, the critical temperature for TR of cell type #1 was reached at  $(206 \pm 1)^\circ\text{C}$  and for cell type #2 at  $(192 \pm 1)^\circ\text{C}$ . Reaching the critical temperature indicates the start of the exothermic process inside the cell, which accelerates the self-heating of the cell and results in a TR. Gas producing reactions are the reaction of the conducting salt with solvent and the SEI [52–54], the reaction of intercalated lithium in the anode and electrolyte initiated by the SEI breakdown [56] and the decomposition of the cathode producing oxygen [8,59], which further reacts with the electrolyte [60,61].

- **Overcharge:** The cell type #1 was triggered into TR by charging with 1 C up to  $(146 \pm 1)\%$  SOC ending up in  $(4.93 \pm 0.03)$  V before the voltage dropped completely. Cell type #2 was triggered into TR after reaching  $(147 \pm 1)\%$  SOC, which is similar to the SOC of cell type #1. Cell type #2 ended in  $(4.85 \pm 0.09)$  V before the voltage dropped completely. In the overcharge failure case after the anode is fully lithiated, lithium metal deposits on the anode surface during overcharge [51,130]. Additional to the above-mentioned reactions in overtemperature failure, this lithium deposit reacts with the electrolyte under generation of heat and gas [51]. Two ventings were detected for both cell types in the overcharge trigger: the pouch cell vented 240 seconds and the hard case cell 50 seconds before the second venting started. Huang et al. observed a better overcharge tolerance (using 1C) for tested pouch cells (154.6% SOC) than for the tested hard case cells (148% SOC) with the same capacity, active material and electrolyte composition (40 Ah, NMC111, EC:DEC:DMC = 1:1:1) [98]. In this study, the capacity of the two commercial cell types is the same, but the cells are series products of two different cell manufacturer and the exact active material and electrolyte composition is not the same and different additives might be added.
- **Nail-penetration:** Immediately after inserting the nail 8 mm deep into the cells, type #1 and type #2 cells were triggered into the TR and the voltage dropped to zero. Sparks were visible at the intrusion of the nail. In nail penetration, a high discharge current passes through the cell, which leads to heat generation due to joule heat. This heat generation leads to decomposition and release of oxygen of the delithiated cathode [131]. Neither cell type was completely penetrated by the nail (see cell thicknesses in **Table 1**).

The following results and discussion are structured in the three main categories: thermal behavior, vent gas production and vent gas composition, and minor categories: mass loss and reproducibility. In each category, the results of the three different triggers are presented. First the results of cell type #1 are presented, then the results of cell type #2. In the end of each category, the results of the two different cell designs are compared and discussed.

#### 4.2.1 Thermal behavior

**Figure 28** shows the temperature measured on the cell surface, vent positions and inside the reactor for all three TR trigger of one representative experiment for each cell type. The first venting of the cells can be identified as a small increase in the temperature and reactor pressure signal for both cell types. In **Figure 28** (a), (b), (d) and (e) the first venting of the cells is marked with a red dot.

## 4.2 Influence of thermal runaway trigger and cell type

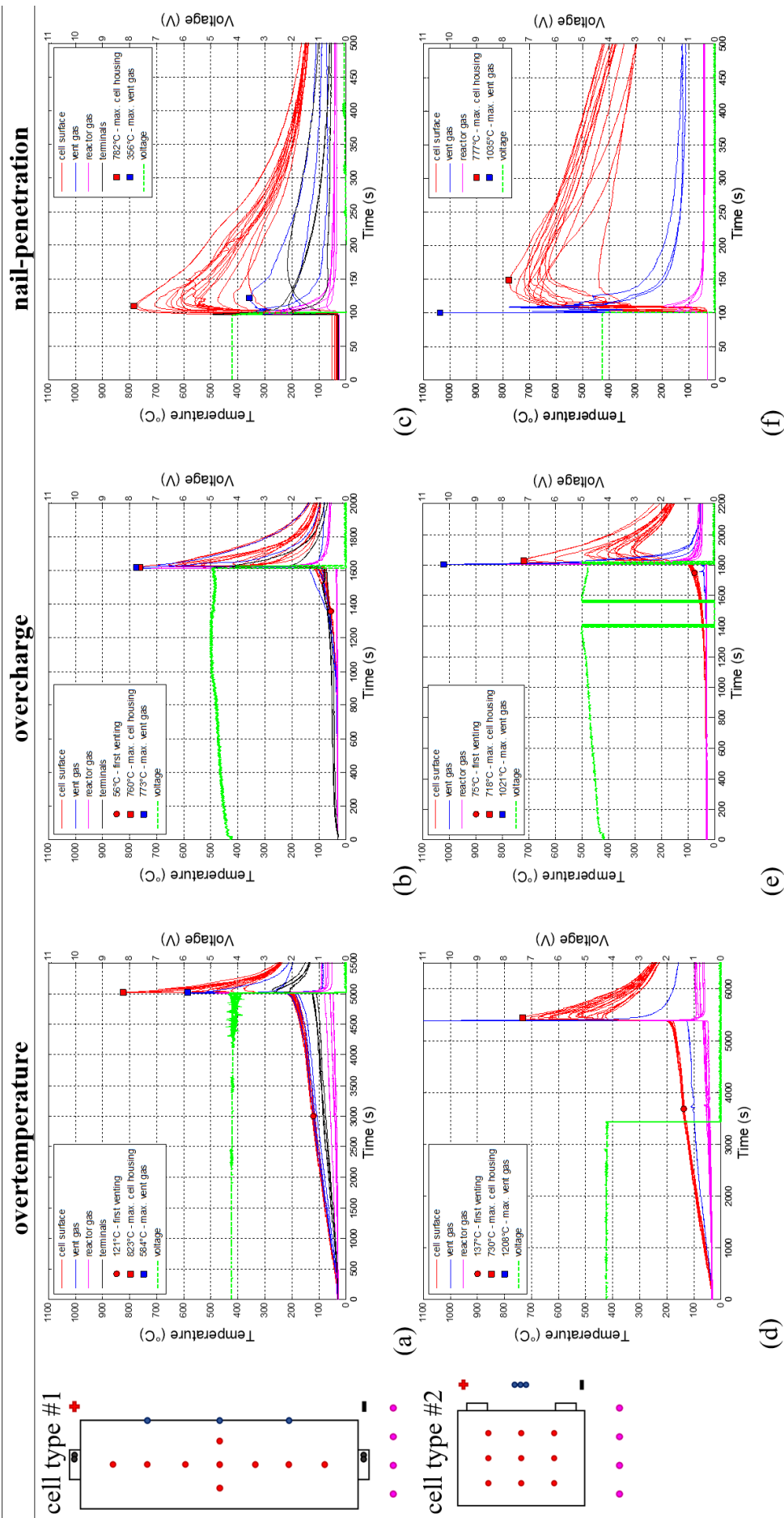


Figure 28: Temperature response of one representative (a)(d) overtemperature, (b)(e) overcharge and (c)(f) nail-penetration experiment of cell type #1 and #2 in comparison. For cell type #1 nine thermocouples were positioned on both large cell surfaces in a cross pattern (red) to document the cell surface temperature, four thermocouples were positioned inside the TR reactor (pink) to measure the gas temperature in the reactor at different positions, three thermocouples were positioned in the pouch foil welded sides (blue) to measure the vent gas temperature and two thermocouples were positioned on each terminal of the cell (black). For cell type #2 nine thermocouples were positioned on both large cell surfaces in a 3x3 pattern (red) to document the cell surface temperature, four thermocouples were positioned inside the TR reactor (pink) to measure the reactor temperature at different positions, three thermocouples were positioned in front of the burst plate (blue) to measure the vent gas temperature. The cell voltage is plotted on the second y-axis with a dashed line (green) [11].

In the overtemperature triggered TR, (Figure 28 (a) and (d)) the temperature of the cell surface increased constantly due to the homogenous heating from both sides of the sample holder. In Table 7 the thermal parameters are compared for both cell types and all three TR trigger. The first venting  $\bar{T}_{cell}^{v1}$  of the cell type #1 happened at a lower average cell surface temperature (difference of 18°C) than of cell type #2. The second venting  $\bar{T}_{cell}^{v2}$  for type #1 was at  $(204 \pm 1)^\circ\text{C}$ , which was higher than for cell type #2 at  $(190 \pm 2)^\circ\text{C}$ . The maximum recorded temperature  $T_{cell}^{max}$  was similar for both cell designs.  $T_{vent}^{max}$  for cell type #1 reached  $584^\circ\text{C}$ , which is a lower temperature than measured at the cell surface. This is due to the undefined pouch foil opening. In comparison,  $T_{vent}^{max}$  for cell type #2 with the defined cell opening reached more than  $1200^\circ\text{C}$ .

In the overcharge triggered TR, in Figure 28 (b) for the pouch cell and (e) for the hard case cell, a first venting happened for cell type #1 at  $(56 \pm 1)^\circ\text{C}$  and for cell type #2 at  $(66 \pm 9)^\circ\text{C}$ . The first venting was detected as a small increase of the temperature signal and cross checked with video recordings inside the test chamber.  $\bar{T}_{cell}^{v1}$  in overcharge experiments is not as meaningful as in overtemperature experiments, but also shows that cell type #2 can withstand higher internal pressure than the soft pouch foil, although the aluminum hard case is a better heat conductor than the pouch foil. The second venting in the overcharge trigger was measured at  $(82 \pm 17)^\circ\text{C}$  for cell type #1 and at  $(96 \pm 4)^\circ\text{C}$  for cell type #2. In comparison to overtemperature trigger, in overcharge the temperature of second venting decreases due to the destabilization of the cathode and the Li plating at the anode side. The maximum recorded temperature  $T_{cell}^{max}$  was for type #1  $(906 \pm 146)^\circ\text{C}$  and for type #2  $(579 \pm 139)^\circ\text{C}$ . In the case of cell type #2 the jelly roll was found outside of the aluminum housing after the experiment. Therefore, the thermocouples on the aluminum hard case measured a lower maximum cell-housing surface temperature because the reacting active material was not inside the case anymore.  $T_{vent}^{max}$  for cell type #1 reached in one experiment also temperatures above  $1000^\circ\text{C}$ .  $T_{vent}^{max}$  for cell type #2 reached  $1021^\circ\text{C}$  in one experiment and in the second experiment all thermocouples at the vent position were destroyed during the TR and the vent gas temperature could not be measured.

In the nail triggered TR, (Figure 28 (c)) for the pouch cell and (f) for the hard case cell the first venting happened at the nail-penetration itself and both cell designs heated up exothermally immediately after the nail-penetration of the cells. The maximum recorded temperature  $T_{cell}^{max}$  was similar for both cell designs. For cell type #1  $T_{vent}^{max}$  was lower than the maximum recorded cell surface temperature.  $T_{vent}^{max}$  for cell type #2 reached again temperatures above  $1000^\circ\text{C}$ .

**Table 7: Thermal parameters of two automotive cell types in overtemperature, overcharge and nail-penetration abuse tests in comparison [11].**

	overtemperature		overcharge		nail-penetration	
	cell type #1 pouch	cell type #2 hard case	cell type #1 pouch	cell type #2 hard case	cell type #1 pouch	cell type #2 hard case
$\bar{T}_{cell}^{v1}$ ( $^\circ\text{C}$ )	$121 \pm 1$	$138 \pm 1$	$56 \pm 1$	$66 \pm 9$	-	-
$T_{cell}^{crit}$ ( $^\circ\text{C}$ )	$206 \pm 1$	$192 \pm 1$	-	-	-	-
$\bar{T}_{cell}^{v2}$ ( $^\circ\text{C}$ )	$204 \pm 1$	$190 \pm 2$	$82 \pm 17$	$96 \pm 4$	-	-
$T_{cell}^{max}$ ( $^\circ\text{C}$ )	$819 \pm 5$	$782 \pm 50$	$906 \pm 146$	$579 \pm 139$	$783 \pm 1$	$743 \pm 33$
$T_{vent}^{max}$ ( $^\circ\text{C}$ )	$584 \pm 1$	$1169 \pm 39$	$1044 \pm 271$	1021	$482 \pm 127$	$850 \pm 185$

Independent of the trigger and the cell design, in each experiment the maximum measured cell-case temperature was above  $718^\circ\text{C}$ , which is higher than the melting temperature of aluminum. The highest

$T_{cell}^{max} = (906 \pm 146)^{\circ}\text{C}$  was measured for cell type #1 in the overcharge triggered experiment (see **Table 7** and **Figure 29** (a)).

Comparing the results of cell type #1 and #2. As reported by Pfrang et al. [7] we observed that prismatic hard case cells can withstand a higher internal pressure until they open compared to pouch cells. This can be observed in overtemperature and overcharge experiments. The maximum expansion of the cell during the experiment was measured against the spring force of the sample holder with a micrometer screw. The force with which the cell presses against the upper pressure plate was calculated. This force divided by the area of the cell gives the pressure. This pressure was evaluated for the pouch cells and the hard case cells. For the pouch cell values between 223 kPa – 411 kPa and for the hard case cell 386 kPa – 855 kPa before the first venting were observed. Video recordings proved the maximum expansion of the cell before the first venting. These observed pressure values also prove, that the pouch cells opened at a lower internal pressure than the hard case cells. The temperature at the first venting of the pouch cell is consistent with the temperature of  $120^{\circ}\text{C}$  reported by Ren et al. on overheated 24 Ah pouch cells in [36]. When the burst plate of the hard case cells opens, at the first venting gas is ejected. At the second venting and TR at both cell types, gas and particles with high temperatures are ejected [5]. The second venting  $\bar{T}_{cell}^{v2}$  and the critical temperature  $T_{cell}^{crit}$  for cell type #1 was observed in overtemperature trigger at a higher temperature than for cell type #2. This indicates that cell type #1 could withstand overtemperatures longer than type #2. Reason for the higher  $T_{cell}^{crit}$  and  $\bar{T}_{cell}^{v2}$  for cell type #1 might be the different delithiation percent of the cathode and consequently the cathode stability, the stacking of the active layers or the earlier opening of the pouch foil. The percent of delithiation of the cathode and lithiation of the anode at 100% SOC were not known and were not analysed in this study. What was known is, that both cell types have NMC cathode and graphite anode and were series products from two different cell manufacturers. The two cell types have different electrolyte composition, different packaging material, the active material is stacked inside the pouch foil and rolled inside the hard case.

$T_{vent}^{max}$  for cell type #2, the hard case cell, reached in all three trigger types higher maximum values than the pouch cell design type #1. This can be explained due to the defined venting of the hard case cell. The vent gas temperature can be measured more easily for hard case cells with a defined burst plate, than for pouch cells, because the pouch foil can open at all pouch welded sides simultaneously. Nevertheless, the nail-penetration experiment showed that the vent gas of the pouch cell (type #1) can also reach temperatures above  $1000^{\circ}\text{C}$ . It needs to be mentioned that the maximum measured vent gas temperature might also be affected by the ejection of hot particles, nevertheless, can damage surrounding material irreversibly.

The maximum recorded temperature  $T_{cell}^{max}$  does not vary significantly for both cell types. But comparing the average  $T_{cell}^{max}$  for all three triggers in **Figure 29** (a) and (e) the cell type #1 reached higher values than cell type #2, especially in the overcharge experiment. Huang et al. also observed in overcharge experiments that the pouch cell reached higher maximum temperature on the cell surface than the prismatic cell [98]. Additionally, the slightly higher  $T_{cell}^{max}$  for cell type #1 might also indicate the influence of the higher energy density of cell type #1 compared to type #2. The influence of the energy density on the  $T_{cell}^{max}$  is published in [46].

Although several thermocouples on the cell surface were used in the experiment, the thermocouple positions in our test setup were limited in amount and in position. At some experiments the thermocouple was close to the hottest position of the cell, and sometimes not. The hottest position

## 4.2 Influence of thermal runaway trigger and cell type

on the cell surface was not known before the experiment. Therefore, sometimes a higher deviation of the recorded  $T_{cell}^{max}$  and also  $T_{vent}^{max}$  from one experiment to the other experiment was observed. Other temperature values such as  $\bar{T}_{cell}^{v1}$ ,  $\bar{T}_{cell}^{v2}$  and  $T_{cell}^{crit}$ , have a good reproducibility (see **Table 7**).

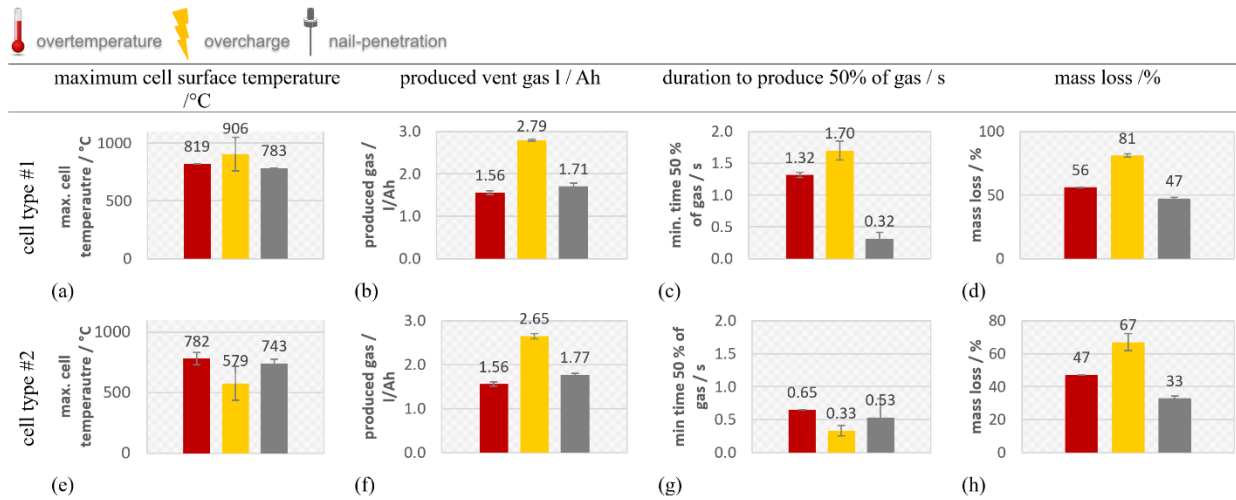


**Figure 29: Safety relevant parameters compared in overtemperature (left bar, red), overcharge (middle bar, yellow) and nail-penetration (right bar, grey) TR experiments of automotive cell type #1 and #2 in comparison: (a) maximum reached cell surface temperature during the TR experiment; (b) the amount of produced vent gas per Ah; (c) the minimal venting duration to produce 50% of the gas and (d) the total loss of the cell mass during the whole experiment [11].**

### 4.2.2 Vent gas emission

As reported in the overtemperature and overcharge experiments, a first venting and opening of the cell case was observed for both cell types before the TR.

In the overtemperature triggered TR, the pressure inside the reactor increased slowly after the first venting and opening of the cells ending up in  $n_{v1} = 0.15$  mol of gas before the TR. The continuous pressure increase is due to the ongoing evaporation of electrolyte out of the opened cell. During the main TR reaction, both cell types released significant additional amount of gas and the pressure inside the sealed reactor increased within seconds up to a maximum value shown in **Figure 30** (a) for cell type #1 and (d) for cell type #2. The duration of the venting during TR of cell type #1 was  $(3.5 \pm 0.1)$  s. In this time the main amount of gas was produced with a characteristic venting rate of  $\dot{n}_{ch} = (34 \pm 2)$  L/s. The cell type #2 released gas in less time  $(2.0 \pm 0.1)$  s than type #1. The characteristic venting rate of cell type #2 was therefore higher  $\dot{n}_{ch} = (67 \pm 4)$  L/s. Cell type #1 produced in total  $(1.56 \pm 0.04)$  L/Ah in the overtemperature experiment. For cell type #2 also  $(1.56 \pm 0.05)$  L/Ah were measured. The produced gas amount fits to reported values in literature between 1.2 – 2 L/Ah [66,73,74] for overtemperature triggered NMC cells.

In the overcharge triggered TR, the first venting ended up in  $n_{v1} = 0.13$  mol of gas for both cell types. During the main TR reaction, both cell types released significant amounts of gas and the pressure inside the sealed reactor increased up to a maximum value shown in **Figure 30** for (b) cell type #1 and (e) cell type #2. The duration of the venting during TR for cell type #1 was  $(5.2 \pm 0.8)$  s with a characteristic venting rate of  $\dot{n}_{ch} = (47 \pm 4)$  L/s. The cell type #2 released during the TR in  $(1.1 \pm 0.1)$  s gas with consequently much higher characteristic venting rate of  $\dot{n}_{ch} = (250 \pm 56)$  L/s. Cell type #1 and #2 produced in total significantly more gas during overcharge than during overtemperature. Cell type #1 released  $(2.79 \pm 0.02)$  L/Ah and cell type #2  $(2.65 \pm 0.06)$  L/Ah.

nail-penetration

overcharge

overtemperature

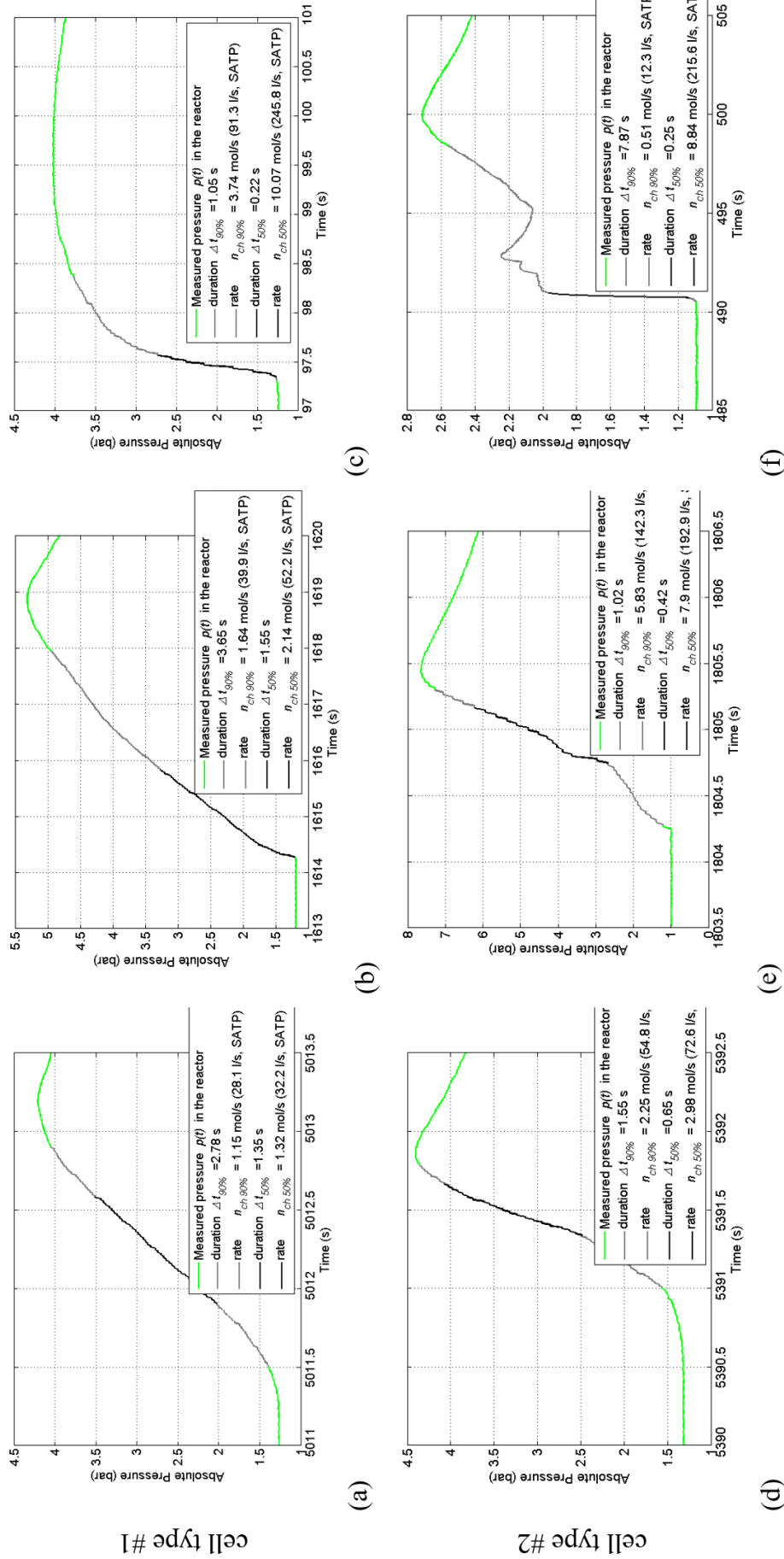


Figure 30: Measured pressure response inside the reactor (green) during the TR of one representative (a)(d) overtemperature, (b)(e) overcharge and (c)(f) nail-penetration experiment of automotive cell type #1 and #2 in comparison. In the graph the minimal time when 50% of the gas was produced is marked with a black line. The time when 90% of the gas was produced is marked in grey. The experiment time in seconds (s) is plotted on the x-axis [11].

In the nail triggered TR, both cell types released significant amounts of gas immediately after the nail penetrated the cell. The pressure inside the sealed reactor increased up to a maximum value shown in **Figure 30** for (c) cell type #1 and (f) cell type #2. The duration of the venting during TR of the stacked cell type #1 in nail-penetration was  $(3.1 \pm 0.9)$  s, which was faster than in overtemperature or overcharge. The characteristic venting rate of cell type #1 in nail-penetration was therefore  $\dot{n}_{ch} = (182 \pm 65)$  L/s. The cell type #2 behaved differently than the pouch cell, because the gas release took  $(11.5 \pm 2.5)$  s during the TR. In **Figure 30** (f) a stepwise increase of the pressure inside the reactor could be observed. The characteristic venting rate of cell type #2 in nail-penetration was  $\dot{n}_{ch} = (140 \pm 76)$  L/s. Cell type #1 produced in total  $(1.71 \pm 0.07)$  L/Ah in nail-penetration experiments and cell type #2 also  $(1.77 \pm 0.03)$  L/Ah. In nail-penetrated TR, less gas was produced than in the overcharge triggered TR, but more gas than in the overtemperature triggered TR (see **Figure 29** (b) and (f)). Therefore, we do not confirm the statement of Diaz et al., that for nail-penetrated cells lower vent gas amounts are produced than in thermal abused cells. The divergence of the observations might be because Diaz et al. did not observe a TR.

Note, that since the characteristic venting rate is defined as the minimum duration when 50% of the gas is produced during the TR, the numeric value of the characteristic venting rate can exceed the numeric value of the maximum amount of released gas. The minimum duration to produce 50% of the vent gas during the TR is plotted in **Figure 29** (c) for cell type #1 for all three TR trigger in comparison and in **Figure 29** (g) for cell type #2.

Comparing the results of cell type #1 and #2. The TR duration (pressure increase during the TR) was in overtemperature and overcharged experiments for cell type #1 longer than for cell type #2. In **Figure 30** (e) the pressure increases inside the reactor during overcharge of type #2 (hard case) cell. For the hard case cell, the pressure increase was not as smoothly as it was for the pouch cell, and two peaks were visible before reaching the maximum pressure. This observation of two peaks can be seen even more clearly for the nail-penetrated hard case cell in **Figure 30** (f). The nail-penetrated 8 mm into each cell. The cell thickness of the cell type #2 is 28 mm; more than twice the nail-penetrated length. At the disassembling of the test setup after the TR, for cell type #2 two jelly rolls were visible inside the hard case. Therefore, the stepwise increasing pressure for the nail-penetrated hard case cell indicates that the penetrated jelly roll was triggered into the TR first, and the TR propagated to the second jelly roll after some seconds. A closer look to the thermocouples positioned on the bottom side of the cell confirms that the temperature at the bottom side (opposite to the nail-penetration position) increased some seconds after the temperature on the top of the cell, where the nail penetrated the cell.

The measured vent gas amounts per Ah of cell type #1 and cell type #2 were very similar for both cell types, if the TR trigger was the same! In this case, both cell types had the same capacity (Ah) and also similar cathode and anode chemistry, but different electrolyte composition (see **Table 1**). Therefore, we assume that the exact electrolyte composition does not influence the produced vent gas amount. The minimum duration to produce 50% of the vent gas during the TR was different for both cell types (**Figure 29** (c) and (g)). For cell type #1 the venting time for 50% of the vent gas was higher than for cell type #2, especially in the overtemperature and the overcharge trigger. Also, the duration of the venting during TR for cell type #1 in overtemperature and in overcharge was longer than for the hard case cell. This also results for cell type #1 in lower characteristic venting rates and less intense pressure peaks during the TR. In the nail-penetration experiment the duration of the venting during TR for cells with more than one jelly roll was longer, but a high characteristic venting rate was still possible.

Therefore, the cell and venting design as well as the packaging of active material layers seems to influence the reaction time of the TR, and consequently the safety relevant parameters such as the characteristic venting rate and maximum pressures reached inside a sealed volume.

### 4.2.3 Vent gas composition

The gas composition was measured about 10 min after each TR happened. In **Figure 31** the vent gas composition for (a) cell type #1 and (b) cell type #2 is compared using all three TR trigger. The main gas compounds produced during the TR of both EV cell types are CO, CO<sub>2</sub>, H<sub>2</sub> and higher hydrocarbons. These main compounds are similar to published gas compositions at other NMC LIBs with commercial electrolyte solvents (such as EC, DEC, DMC, EMC) like published in [73,87]. Although the investigated cells in [87] were small cylindrical hard case 18650 cells with LCO/NMC and NMC cathode, DMC:EMC:EC:PC electrolyte.

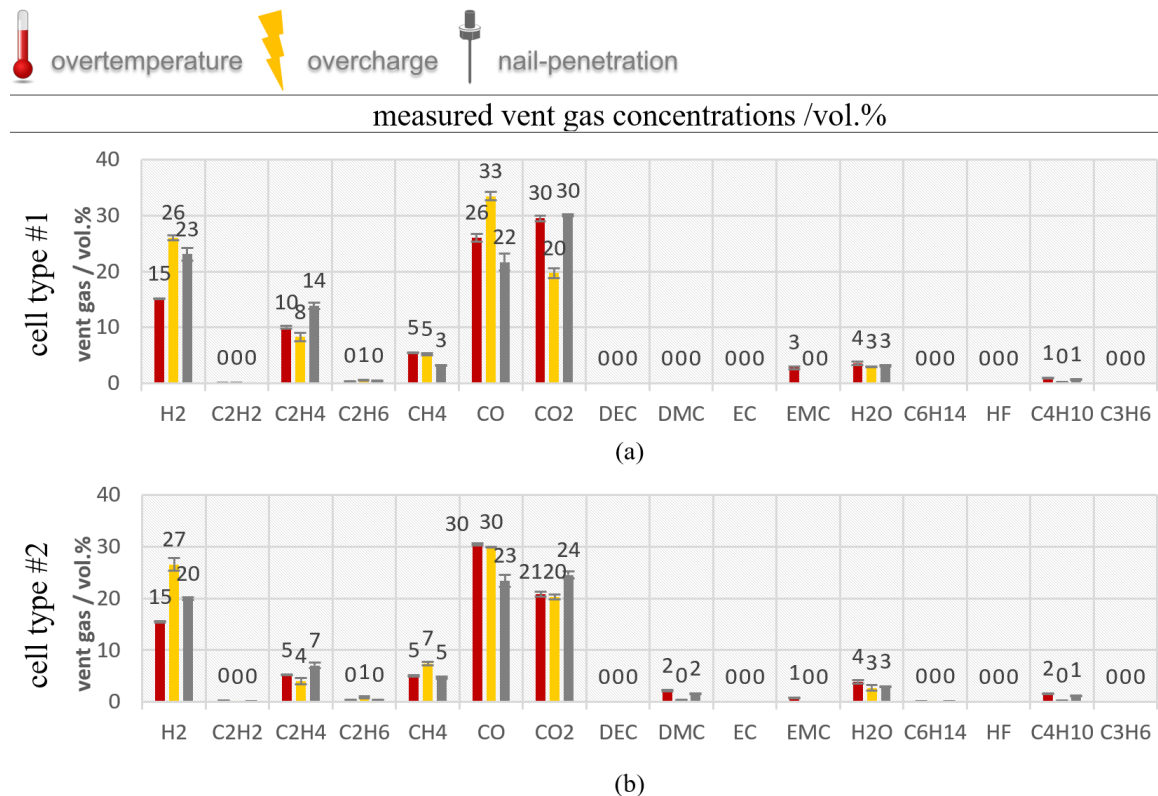


**Figure 31: Vent gas composition in vol.% after the overtemperature (left bars, red), overcharge (middle bars, yellow) and nail-penetration (right bars, grey) experiments in comparison of automotive cell type #1 and #2 [11].**

Beside the similar main gas components there were differences in gas compositions measured at the three TR trigger and the investigated cells:

In the overtemperature experiment the main gas components were in descending order for cell type #1: 30% CO<sub>2</sub>, 26% CO, 15% H<sub>2</sub>, 10% C<sub>2</sub>H<sub>4</sub>, 5% CH<sub>4</sub>, 4% H<sub>2</sub>O, 3% EMC and below 1 % C<sub>4</sub>H<sub>10</sub>, C<sub>2</sub>H<sub>6</sub>, C<sub>2</sub>H<sub>2</sub>. Cell type #2 produced in descending order: 30% CO, 21% CO<sub>2</sub>, 15% H<sub>2</sub>, 5% C<sub>2</sub>H<sub>4</sub>, 5% CH<sub>4</sub>, 4% H<sub>2</sub>O, 2% DMC, 2% C<sub>4</sub>H<sub>10</sub>, and lower 1 % EMC, C<sub>2</sub>H<sub>6</sub>, C<sub>2</sub>H<sub>2</sub>, C<sub>6</sub>H<sub>14</sub> (see **Figure 31** red bars). Differences in gas concentrations from both cell types were observed in C<sub>2</sub>H<sub>4</sub>, CO, CO<sub>2</sub> and DMC. These differences will be discussed in the comparison of the results of both cell types. The average substance concentration values published by Koch et al. in [73] over 51 overtemperature triggered NMC LIBs fit to the presented

results in this paper: 28% CO, 37% CO<sub>2</sub>, 22% H<sub>2</sub>, 6% C<sub>2</sub>H<sub>4</sub> and 5% CH<sub>4</sub> [73]. Our results are within the error bars of each gas component presented in [17, Fig.4.]. The gases produced during the TR can be explained by SEI decomposition [7,123], electrolyte decomposition [122,126], NMC (cathode) degradation and reaction of the solvent with the cathode [51,56].

In the overcharge experiment beside higher amounts of gas than in overtemperature trigger both cell types produced significant higher amounts of CO and H<sub>2</sub>, and a little higher amount of CO<sub>2</sub> and CH<sub>4</sub>. To emphasize the higher amounts of CO, H<sub>2</sub> in overcharge experiments compared to overtemperature, **Figure 32** presents the main gas composition in mol for all three TR trigger. Cell type #1 produced in overcharge two times as much CO ((2.27 ± 0.05) mol) and three times as much H<sub>2</sub> ((1.77 ± 0.03) mol) than in overtemperature and nail trigger. Cell type #2 also produced 1.6 times higher amounts of CO ((1.93 ± 0.06) mol) and 2.8 times higher H<sub>2</sub> ((1.71 ± 0.04) mol) in overcharge experiments compared to overtemperature. In **Figure 31** yellow bars the relative vent gas composition is presented. Additional to the above-mentioned reactions producing gases, the lithium metal deposit on the anode surface reacts with the electrolyte under generation of heat and gas [130]. According to Ohsaki et al. CO and CO<sub>2</sub> were mainly produced at the cathode side during overcharge and on the anode side the main component is H<sub>2</sub> and small amounts of CH<sub>4</sub>, C<sub>2</sub>H<sub>4</sub>, C<sub>2</sub>H<sub>6</sub>, CO and CO<sub>2</sub> were measured [132].

In the nail triggered TR both cell types produced the lowest CO volume percent values and the highest C<sub>2</sub>H<sub>4</sub> value of all three triggers. The H<sub>2</sub> values were lower than in the overcharge experiment, but higher than in overtemperature (see grey bars in **Figure 31** and **Figure 32**). CO<sub>2</sub> values were increased for the cell type #2 compared to the overtemperature trigger. Diaz et al. observed for nail-penetrated cells without TR less toxic gas than in thermal abuse using cells with the same state-of-charge (SOC) (100%) [84]. Although Diaz et al. refers to gas results without TR, we also observed lower CO values in the nail-penetration experiments than in overtemperature experiments.

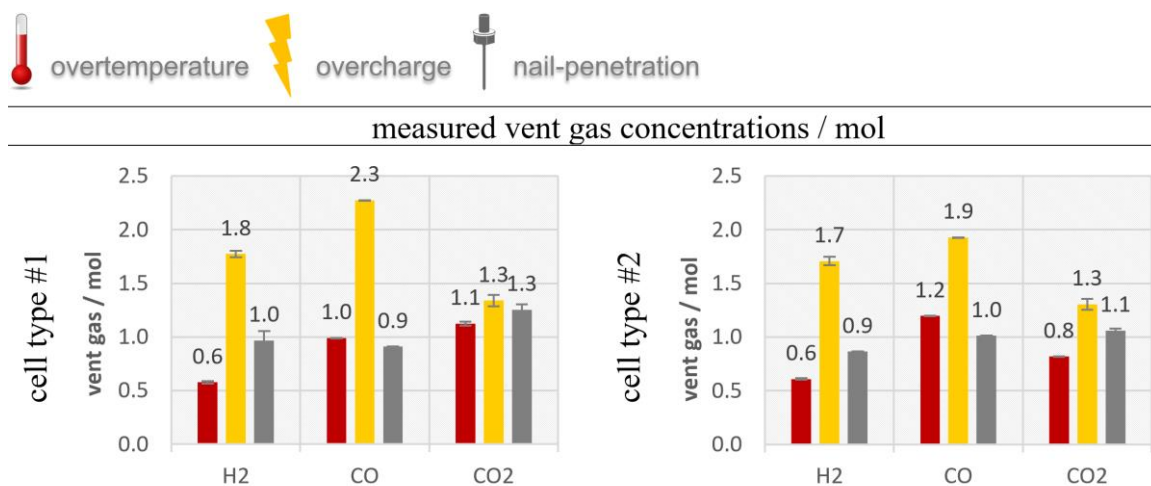


**Figure 32: Main vent gas components converted into mol after the overtemperature (left bars, red), overcharge (middle bars, yellow) and nail-penetration (right bars, grey) experiments in comparison of automotive cell type #1 and #2. The concentration of the gas component H<sub>2</sub>, CO and CO<sub>2</sub> in the vent gas in vol.% multiplied with the measured amount of released vent gas  $n_v$  in mol gives the concentration of the gas component in mol [11].**

The gas compositions measured in the repeated experiments showed high agreement and for most gas components deviations between the two measured values were below 3%. Exceptions were in some experiments the values of H<sub>2</sub>O, higher hydrocarbons with low concentrations such as C<sub>2</sub>H<sub>2</sub>, C<sub>2</sub>H<sub>4</sub> and C<sub>2</sub>H<sub>6</sub> and in nail-penetration tests the CO concentration.

We assume that the trigger and consequently the reaction mechanism and the reached temperatures influences the decomposition reactions and the resulting the vent gas composition. The influence of temperature inside the cell during the reactions on the resulting gas composition was also stated by Fernandez et al. in [71].

Comparing the results of cell type #1 and #2. For both cell types significant amounts of CO were produced, especially in overtemperature and overcharge experiments. In overcharge experiments the CO amount was higher than the CO<sub>2</sub> amount. The observation of CO<sub>2</sub>:CO ratio was less than one can be explained by the high gravimetric energy density of both cell types. As observed by Koch et al. the CO<sub>2</sub>:CO ratio decreased with increasing gravimetric energy density of the cells [73]. This was also observed in the overheated LCO/NMC cell by Golubkov et al., which produced significant higher CO values than the NMC cells with lower energy density [87].

The exact gas composition varies with different electrolyte composition. In this case, the active material of both cell types is very similar, but different electrolyte compositions are used. Internal investigations of car manufacturers reveal that in cell type #1 the main electrolyte components are EC:EMC (1:1) and in cell type #2 EC:DMC:EMC (2:3:3). In **Figure 31** (a) and (b) different electrolyte vapor was identified for both cell types. For cell type #1 EMC was identified, but no EC could be identified. EC is very unlikely to be measured with the presented gas analysis setup. We assume that parts of EC decompose and parts condensate inside the TR reactor or before the gas analysis section, because the boiling point of EC is higher than the gas temperature inside the reactor. For cell type #2 DMC and EMC were measured. Typical decomposition reactions of electrolyte components such as EC are CO<sub>2</sub>, CO, C<sub>2</sub>H<sub>4</sub>, EMC, DEC [59,122], for EMC: CO<sub>2</sub>, CO, DMC, DEC, for DEC CO<sub>2</sub>, C<sub>2</sub>H<sub>6</sub>, [122] and for DMC: CO, CO<sub>2</sub>, CH<sub>4</sub>, C<sub>2</sub>H<sub>6</sub>, H<sub>2</sub>O [59,61,123]. Major varying gas concentrations between both cell types were observed in C<sub>2</sub>H<sub>4</sub>, CO, CO<sub>2</sub> and DMC values. Onuki et al. observed that C<sub>2</sub>H<sub>4</sub> was only formed from EC [122]. Cell type #1 produced significant higher C<sub>2</sub>H<sub>4</sub> concentrations at all three triggers (twice as much than cell type #2) and also CO<sub>2</sub> values were higher than for cell type #2. This observation correlates with the significant higher amount of EC in cell type #1 (twice as much) compared to cell type #2. Therefore, we assume that the higher C<sub>2</sub>H<sub>4</sub> amount in the vent gas composition of cell type #1 was because of the higher amount of decomposed EC. Only minor varying gas concentrations were measured in H<sub>2</sub> and CH<sub>4</sub> values.

In the presented results no hydrogen fluoride (HF) was identified with the FTIR spectrometer inside the FTIR gas measurement chamber. Although it is assumed that small amounts of HF were released by the cells according to [48,75], but the highly reactive HF reacted with materials inside the test reactor, the analysis pipes and the ejected particles. Additionally, we assume that modern mass produced EV cells produce less HF than older cells. We measured inside our test setup for an older aged 18 Ah cell with NMC/LTO chemistry 66 ppm (0.396 mmol) HF after the TR [76] and for another modern automotive pouch cell 0 ppm HF [5].

#### 4.2.4 Mass reduction

In all experiments the TR could be triggered, and the cells ejected gas and particles during the TR. In **Figure 29** (d) and (h) the mass losses of the investigated cells during the TR including the experiment after-treatment are compared for all three TR trigger. In the overtemperature triggered TR cell type #1 lost (56 ± 1)% of the initial weight and cell type #2 (47 ± 1)% during the whole TR experiment and the experiment after-treatment. These results are comparable with reported mass loss of 15 –60% for

NMC cells with 20- 81 Ah in overtemperature trigger in [73]. The overcharged cells lost significant higher mass than in overtemperature trigger. In both repeated overcharged hard case cells, the whole jelly roll was found outside of the hard case after the experiment. In the nail triggered TR both cell types had the lowest mass loss of all three trigger. The reduced mass loss for nail-penetrated cells compared to overtemperature trigger was also observed by Diaz et al. in [84]. Diaz et al. explained the reduced mass loss in nail-penetration “as the main reaction happening was the boiling of electrolyte solvents after opening the batteries”. In the presented results the nail got stuck in the cell and was removed during disassembly after the experiment. The nail inside the cell may have prevented further particle emission.

Comparing the results of cell type #1 and #2. At each tested TR trigger cell type #1 lost higher amounts of mass than cell type #2. This observation is not consistent with the identified higher mass loss of hard case cells compared to pouch cells of Koch et al. in [73]. Koch et al. explains the observation of higher mass loss at hard case cells with the higher stream velocities through the burst plate [73]. We assume, that the different housing and the different gravimetric energy density influenced the mass loss. For cell type #2, the metal housing had a higher mass than the pouch foil and this metal housing contributed to the measurement of the weight. Beside the housing, the pouch cell type #1 might lost additionally higher amounts of mass than the hard case cell type #2, because cell type #1 had a higher gravimetric energy density.

#### 4.2.5 Comparing the trigger

In overtemperature and overcharge experiments a first venting before the TR could be measured at both cell types. For nail-penetration only one venting starting immediately after the nail-penetration was observed.

The presented results show that overcharge triggered TR can be harsher than other abuse triggers such as overtemperature and nail-penetration. This is in good agreement with [69]. For both cell types in the overcharge experiments, significantly more gas was produced, a higher mass loss was observed and the gas components had higher volume percent in flammable, explosive and toxic gas compounds such as H<sub>2</sub> and CO than in overtemperature or nail-penetration. A reason for the harsher TR behavior might be the additional energy filled into the cells, the extreme delithiation and destabilization of the cathode and the lithium metal deposits on the anode surface. Although, overcharge experiments of the presented cell types were proofed to end up in a more severe abuse than thermal or nail-penetrated cells, our results partly agree with the statement of Larsson et al. in [97] that the abuse by overcharge and heating can end up in more severe abuse, due to the input of electric power or heat. We can confirm the statement for overcharge, but we cannot confirm the statement for overtemperature.

**Table 8** presents a summary of safety relevant parameters of the two tested cell types during and after TR for all three different triggers.

Thermal behavior. In each experiment independent of the trigger and the cell design the maximum measured temperature was above 718°C. Under consideration of the standard deviation of measured temperature values and different cell design all three TR trigger resulted for both cell geometries in similar  $T_{cell}^{max}$  and  $T_{vent}^{max}$ . In overtemperature and in nail-penetration the SOC was 100% and therefore, we assume that the delithiation of the cathode and the lithiation of the anode were the same. Here the  $T_{cell}^{max}$  values were comparable. Cell type #1 reached in nail-penetration the lowest  $T_{cell}^{max}$  values and in overcharge the highest (see **Figure 29** (a) and (e)). Cell type #2 reached the lowest  $T_{cell}^{max}$  values

in overcharge experiments due to the ejection of the jelly roll during the overcharge and the highest value in overheated TR.

**Table 8: Summary of safety relevant parameters of two automotive cell types in overtemperature, overcharge and nail-penetration abuse tests in comparison [11].**

	overtemperature		overcharge		nail-penetration	
	cell type #1 pouch	cell type #2 hard case	cell type #1 pouch	cell type #2 hard case	cell type #1 pouch	cell type #2 hard case
first vent	yes	yes	yes	yes	no	no
$\bar{T}_{cell}^{v1}$ (°C)	121 ± 1	138 ± 1	-	-	-	-
SOC <sub>max</sub>	100	100	146 ± 1	147 ± 1	100	100
TR	yes	yes	yes	yes	yes	yes
$T_{cell}^{crit}$ (°C)	206 ± 1	192 ± 1	-	-	-	-
$\bar{T}_{cell}^{v2}$ (°C)	204 ± 1	190 ± 2	82 ± 17	96 ± 4	-	-
$T_{cell}^{max}$ (°C)	819 ± 5	782 ± 50	906 ± 146	579 ± 139	783 ± 1	743 ± 33
duration TR venting (s)	3.50 ± 0.01	2.00 ± 0.01	5.2 ± 0.8	1.1 ± 0.1	3.1 ± 0.9	11.5 ± 2.5
amount of gas (mol)	3.8 ± 0.1	3.8 ± 0.1	6.9 ± 0.1	6.5 ± 0.2	4.2 ± 0.2	4.3 ± 0.1
venting rate $\dot{n}_{ch}$ (L/s)	34 ± 2	67 ± 4	47 ± 4	250 ± 56	182 ± 65	140 ± 76
main gas compounds	CO, H <sub>2</sub> , CO <sub>2</sub>	CO, H <sub>2</sub> , CO <sub>2</sub>	CO, H <sub>2</sub> , CO <sub>2</sub>			
C <sub>H2</sub> (vol.%)	15 ± 1	15 ± 1	26 ± 1	25 ± 1	23 ± 1	20 ± 1
C <sub>CO</sub> (vol.%)	26 ± 1	30 ± 1	33 ± 1	30 ± 1	22 ± 1	23 ± 1
mass loss (%)	56 ± 1	47 ± 1	81 ± 1	67 ± 5	47 ± 1	33 ± 1

Vent gas emission. Cell type #1 and #2 produced in total significantly more gas in overcharge than in overtemperature and nail-penetration experiments. Overtemperature triggered cells produced the lowest gas amounts of the three tested triggers. For the amount of produced gas for overtemperature triggered NMC cells in literature values between 1.2 – 2 L/Ah were reported [66,73,74]. The measured values of both cell types in this publication fit into the reported gas amount per liter for heat trigger. No literature was found presenting the gas amount per Ah at NMC cells triggered by overcharge or nail-penetration. But the presented experiments show that overcharge trigger forces the batteries to produce significantly more gas per Ah than using other trigger methods. The venting rates  $\dot{n}_{ch}$  were for overtemperature TR lower than for overcharge or nail-penetration trigger. Concerning the venting rate  $\dot{n}_{ch}$  nail-penetration trigger as well as overcharge for hard case cells might challenge closed battery packs most.

Vent gas composition. The trigger influences the vent gas composition, especially the CO, CO<sub>2</sub>, H<sub>2</sub>, C<sub>2</sub>H<sub>4</sub>, CH<sub>4</sub>, and electrolyte concentrations. Beside higher amounts of gas were produced in overcharge tests, for both cell types the highest H<sub>2</sub> values were measured in the overcharge failure case and the least H<sub>2</sub> values in the overtemperature trigger. Nail-penetration trigger forced both cell types to produce higher C<sub>2</sub>H<sub>4</sub> and CO<sub>2</sub> vol.% values and lower CH<sub>4</sub> vol.% values that in the other two triggers.

Mass loss. The highest mass loss was observed for overcharged cell and the lowest mass loss for nail-penetrated cells.

### 4.3 Influence of aging

*This chapter has been accepted for publication in MDPI Batteries Journal in March 2021 under the title “Influence of aging on the failing behavior of automotive lithium-ion batteries”.*

Five overtemperature experiments were conducted on single aged type #1 cells (see **Figure 33**). Cells with three different aging paths (cyclic aging at  $-10^{\circ}\text{C}$  (cy-10) and at  $+45^{\circ}\text{C}$  (cy+45) and calendric aging at  $60^{\circ}\text{C}$  (ca60)) were tested and compared with the results of fresh cells. Each experiment was repeated, except the experiment with the calendric aged cell (ca60), because there was only one cell available. All experiments were conducted using fully charged cells inside the same overtemperature test setup.

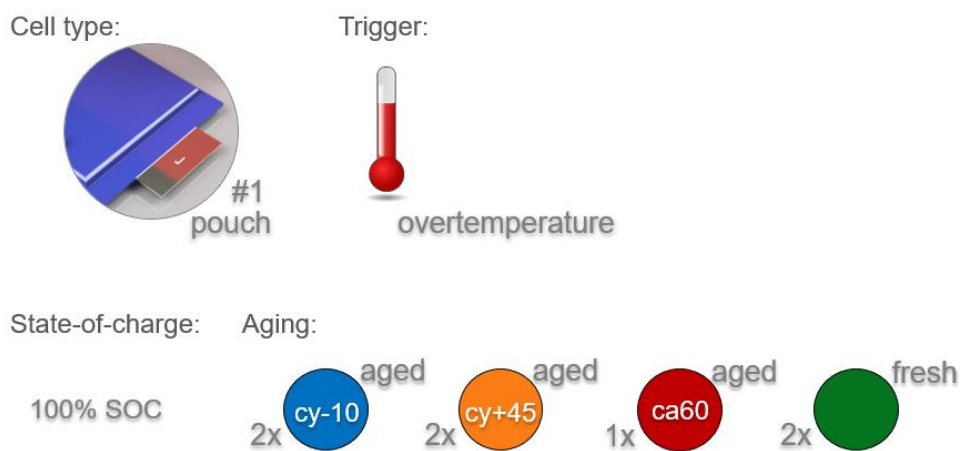


**Figure 33: Design of experiment to investigate the influence of aging on the failing behavior: In total five aged and two fresh type #1 pouch cells were triggered into TR using overtemperature TR trigger.**

The cyclic aged cells at  $45^{\circ}\text{C}$  showed the highest capacity fade compared to the other two aging paths and the calendric aged cells at  $60^{\circ}\text{C}$  the lowest capacity fade (see **Figure 34** (a)).

This can be explained in the following way: the storage temperature, the cell chemistry, the SOC and the storage duration affect the calendric aging. The calendric aging is dominated by side reactions between the used chemical substances [133] and is accelerated with increasing temperature [134]. A major side reaction affecting the cell capacity during storage at high temperature ( $60^{\circ}\text{C}$ ) is the Li oxidation on the negative electrode [135]. Röder et al. showed that calendric aging is mainly affected by loss of cyclable Li due to SEI growth [101].

The aging mechanism of the cycled cells at  $45^{\circ}\text{C}$  and  $-10^{\circ}\text{C}$  can be explained due to the additional aging mechanisms: additional to the aging mechanisms described for calendric aged cells, for the cyclic aged cells high and low temperature, external electrical, electromechanical, and mechanical stress influence the aging process. Waldmann et al. investigated aging mechanisms of NMC/LMO cells during cyclic aging between  $-20^{\circ}\text{C}$  and  $+70^{\circ}\text{C}$  [136] and they found out that the predominant aging mechanism below  $25^{\circ}\text{C}$  is Li plating and above  $25^{\circ}\text{C}$  it is the cathode degradation (Mn loss on the cathode side and Mn deposition on the anode side) and the SEI growth on the anode. Mn dissolution is also reported in [137,138]. During charging at low temperature, metallic Li deposits on the anode outside the SEI because of the negative anode potential versus  $\text{Li}/\text{Li}^{+}$  [90,136]. The probability of this Li plating is affected by the temperature, the charging rates and the SOC [139]. A rest time after the Li plating, can

reduce Li plating. Waldmann et al. reported a reduction of Li plating during a rest time due to “chemical intercalation of the metallic Li into the graphite particles” [90]. In general, TR experiments on cells with Li plating lead to a reduced thermal stability [44,140] and a stronger TR reaction [90,102].

At temperatures above 25°C Li plating does not occur and instead degradation of the cathode and SEI growth dominate the degradation reactions [136]. Damage of the cathode structure [141] and particle cracking [34] were reported. The SEI growth correlates with loss of mobile Li. Consequently, the internal resistance of the cell increases and the capacity decreases. A reduced exothermic reaction is expected for these cells [100,101].

The investigated aged cells had different remaining capacity before TR testing (see **Figure 34** (a)). The first venting of the cell was observed in all aged test samples and each cell was triggered into TR afterwards. The basic effects occurring during the TR of these investigated #1 cells (such as loss of cell voltage, self-heating of the cell, production of gas, cell rupture, particle ejection) were very similar to the results of other different cell types tested in the same TR reactor (see [5,11]).

The tested aged cells did not show a more harmful failing reaction compared to fresh cells. This correlates with the literature of aged cells at higher temperature without metallic Li plating. Consequently, during cyclic aging at -10°C, either no Li-plating was produced, or the produced Li plating reacted in the meantime between the aging experiment and the TR experiment, because the cells were not tested immediately after the aging experiment. The cy-10 cells were stored at 25°C for another five months before the TR tests. In this time, if there was produced metallic Li plating, this Li plating might have reacted. A possible Li plating reaction is chemical intercalation into the graphite particles, which has been reported by Waldmann et al. during rest periods [90]. Additionally, Liu et al. published that in EC containing electrolytes, EC passivates metallic Li plating [26]. Consequently, if the cell can rest after metallic Li plating was produced, the failing reaction is not more harmful than for other cells. In this study, the aged cells showed in the TR experiments reduced maximal temperatures, lower amount of produced gas and significantly lower CO amounts in the vent gas than fresh cells. In the next chapters the thermal behavior, the vent gas emission, vent gas composition and the mass loss of aged cell type #1 cells are presented and discussed in comparison to the fresh cells.

### 4.3.1 Thermal behavior

In **Table 9** the most important thermal parameters during failing aged type #1 LIBs are compared with the results of the fresh type #1 cells. The average value over repeated experiments is presented with the deviation between the repeated experiments, except for the ca60 aging path, there was only one cell available.

**Table 9: Thermal parameters of failing aged cell type #1 cells in overtemperature abuse tests in comparison to fresh cells.**

	aged cy-10 cell type #1	aged cy+45 cell type #1	aged ca60 cell type #1	fresh cell type #1
$\bar{T}_{cell}^{v1}$ (°C)	119 ± 5	123 ± 1	124	122 ± 1
$T_{cell}^{crit}$ (°C)	199 ± 4	217 ± 2	203	206 ± 1
$\bar{T}_{cell}^{v2}$ (°C)	190 ± 1	219 ± 2	205	204 ± 1
$T_{cell}^{max}$ (°C)	763 ± 5	762 ± 9	794	819 ± 5
$T_{vent}^{max}$ (°C)	982 ± 238	934 ± 202	1306	584 ± 1

The main results are presented graphically in the following figures always in the same order: First the results of the cy-10 cells are plotted, then cy+45, ca60 and finally the results of the fresh cells.

Our test results show that there were no significant changes in  $\bar{T}_{cell}^{v1}$  from fresh cells to aged cells (see **Figure 34** (b)), but there was a trend towards higher  $\bar{T}_{cell}^{v1}$  for aged cells. Only one cyclic aged cell at -10°C showed an earlier opening of the pouch bag. This observation is consistent with the investigations of Ren et al., who measured the first venting almost at the same temperature ~120 °C independent of the four different degradation paths and SOH [36]. Slightly increased  $\bar{T}_{cell}^{v1}$  might be explained with the degradation of electrolyte and subsequent lower amount of electrolyte inside the cells, which forces the cell housing to open due to vaporization of the electrolyte.

For the parameter  $\bar{T}_{cell}^{v2}$ , the second venting, a correlation between the aging path and the failing behavior was observed (see **Figure 34** (c)). Both cells with the highest capacity fade (cy+45) showed a significant higher average temperature for  $\bar{T}_{cell}^{v2}$  than for fresh cells and an increase in thermal stability. These results are comparable with the observations of Feng et al. for cyclic aging at higher temperature [44] and Zhang et al. for calendric aging [100]. Because the loss of mobile Li, lower amount of Li can react with the electrolyte and consequently the exothermic reaction starts at a higher average temperature. In contrast to the cy+45 cells, both cy-10 aged cells showed a lower  $\bar{T}_{cell}^{v2}$ . The decreased thermal stability of cells aged at low temperature was also observed by Fleischhammer et al. in [102], and Feng et al. in [44]. This might be explained due to the Li deposits outside the SEI in course of cycling at low temperature and the enabled reaction between the Li and the electrolyte after the decomposition of the passivation of the metallic Li. The second venting, the TR, was observed at a lower average temperature than for fresh cells. The calendric aged cell  $\bar{T}_{cell}^{v2}$  was comparable with the results of the fresh cells, which can be explained due to the lower capacity fade of the calendric aged cell.

The parameter  $T_{cell}^{crit}$  is comparable with the defined TR onset temperature in other literature [44,101] and correlates with the observations of  $\bar{T}_{cell}^{v2}$ .  $T_{cell}^{crit}$  increased for the cy+45 aged cells, what is consistent with the literature [100,101], but decreased for the cy-10 aged cells.

A clear reduction of the maximum temperatures on the cell surface  $T_{cell}^{max}$  was observed for all aged cells (see **Figure 34** (d)), although the thermocouple positions in our test setup were limited in amount and in position and this parameter showed higher deviations from one experiment to the other. The hottest position on the cell surface was not known before the experiment and consequently in some experiments the hottest cell surface spot was not covered. Independent of the aging path, in each experiment the maximum measured cell-case temperature was above 740°C, which is higher than the melting temperature of aluminum.

The vent gas temperature  $T_{vent}^{max}$  can be measured more easily for hard case cells with a defined burst plate, than for pouch cells, because the pouch foil can open at all pouch foil welded sides simultaneously. Since there was no defined burst plate for the pouch cells, the thermocouples positioned on the pouch foil welded sides did not guarantee to measure the vent gas temperature and certainly did not measure the highest vent gas temperature. Although remarkably high  $T_{vent}^{max}$  could be measured (up to 1300°C) during the experiments with the five aged type #1 cells.

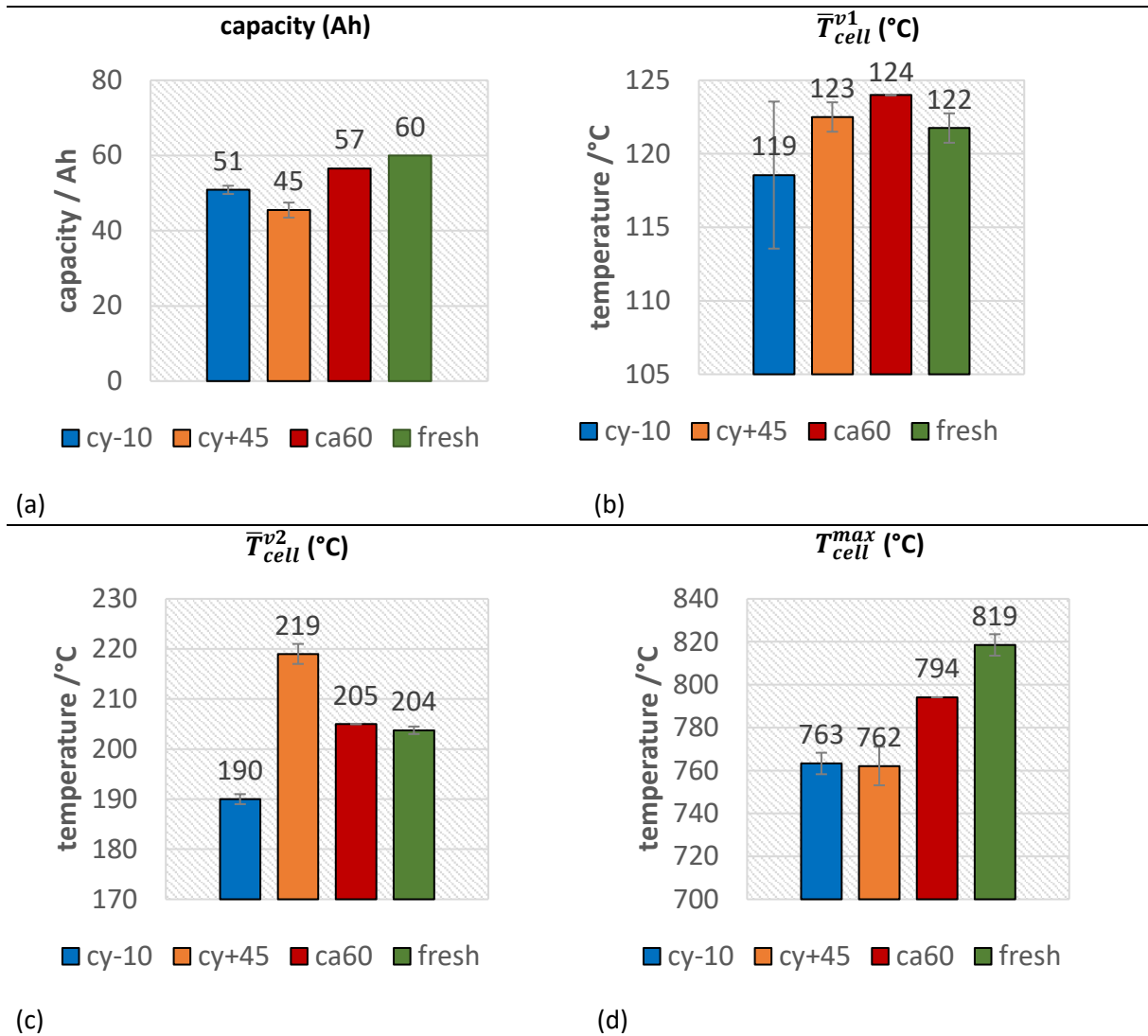


**Figure 34: Comparison of safety relevant thermal parameters in overtemperature triggered TR of fresh (green) and aged (cy-10: blue, cy+45: orange, ca60: red) #1 cells. a) the measured capacity of the cells immediately before the TR experiment; the average cell surface temperature at b) the first venting and at c) the second venting; d) the maximal measured temperature on the cell surface.**

#### 4.3.2 Vent gas emission

As in the experiments with the fresh cells, the pressure inside the reactor increased slowly during the first venting of the pouch cell and abruptly at the TR of the fully charged cells. The main amount of gas was produced during the TR itself.

**Figure 35** (a) shows the amount of gas produced starting at  $T_{cell}^{v1}$  and ending at the  $T_{cell}^{v2}$  ( $n_{v1}$ ). The aged and the fresh type #1 cells produced comparable amounts of vent gas after the opening of the cell housing until  $T_{cell}^{v2}$ . Only the cyclic aged cell at -10°C (cy-10) produced lower amounts of gas during the first venting. **Figure 35** (b) presents the amount of gas produced after the start of the second venting for aged cells and fresh cells in overtemperature TR trigger in comparison. The aged cells produced significantly lower total amount of gas than the fresh cells. This might be explained due to the reduced amount of reactive Li and reduced amount of electrolyte. A linear correlation between the amount of produced vent gas and the current capacity of each cell can be seen in **Figure 35** (c) and (d). Cell type #1 produced independently of the investigated aging path about 0.06 mol vent gas per Ah in overtemperature triggered TR experiments. No literature could be found on the effect of the aging

path on the vent gas amount in failing state for comparison. As shown in our previous study on the trigger influence [11], another series product cell (type #2) from a different cell manufacturer with NMC 622 chemistry and graphite anode also produced about 0.06 mol/Ah in overtemperature trigger. Consequently, a vent gas production of 0.06 mol/Ah could be a general relation describing the degassing amount of NMC (622)-graphite chemistry cells with liquid electrolyte mixture (EC, EMC, DMC, DEC) for overtemperature TR experiments. We have shown that the use of different TR trigger has an influence on the amount of produced vent gas and that in overcharge experiments higher amounts of gas are produced [11].

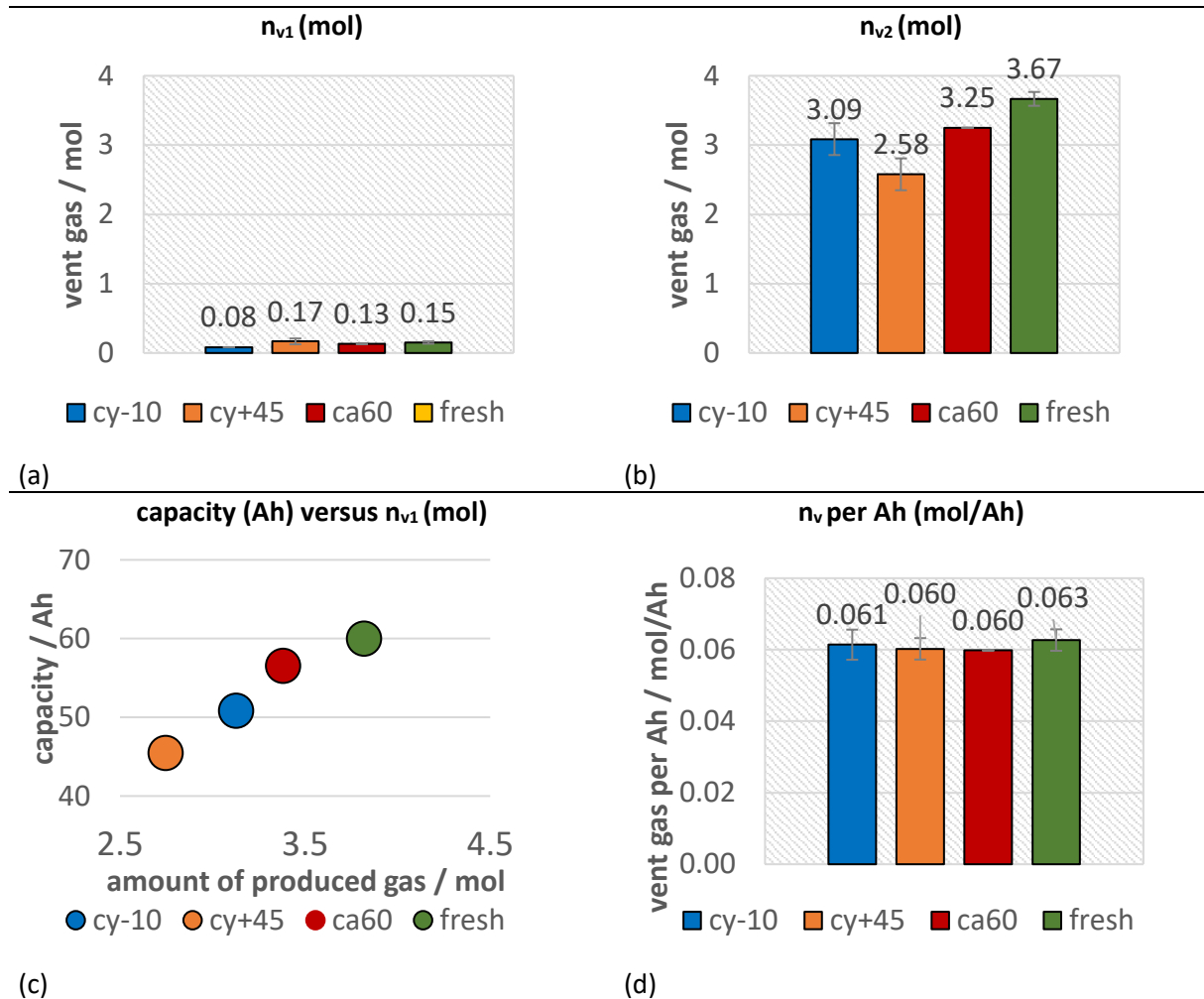


**Figure 35: Vent gas emission during overtemperature TR experiments of aged cells (cy-10: blue, cy+45: orange, ca60: red) compared to fresh cells (green): a) vent gas emission  $n_{v1}$  starting at  $T_{cell}^{v1}$  and ending at  $T_{cell}^{v2}$ , b) vent gas emission  $n_{v2}$ , c) current capacity of aged and fresh cells versus the total vent gas emission; d) the total vent gas emission per Ah.**

### 4.3.3 Vent gas composition

The vent gas composition was measured roughly about ten minutes after the first venting and after the TR. The vent gas composition after the first venting of the aged type #1 cells were compared with the vent gases measured after the first venting of fresh cells. For the calendric aged cell at 60°C and for the fresh cells only one gas measurement after the first venting was taken, consequently only one measurement can be presented.

In overtemperature experiments the measured gases after the first venting describe the sum of accumulated gases evolved from inside the cell at the opening of the cell housing (here EMC, H<sub>2</sub>O, CO<sub>2</sub>,

CO, C<sub>4</sub>H<sub>10</sub>, CH<sub>4</sub>, H<sub>2</sub>) and gases produced continuously due to constant heating. Constant heating leads to additional evaporation of electrolyte (here EMC) and further decomposition gases (here CO<sub>2</sub>, CO, C<sub>4</sub>H<sub>10</sub>, H<sub>2</sub>O). Consequently, the total amount of gas and the gas composition highly depends on the exact time when this measurement is taken. In **Figure 36** (a) the vent gas measurements (in volume percent (vol.%)) are ranked according to the time between the first venting and the gas measurement: the gas measurement of one cy-10 cell was taken eight minutes after the venting and is shown in the first row and the measurement of one cy+45 cell was taken 19 minutes after the venting and is presented furthest back. After the first venting the main gas components are electrolyte components (for this cell type #1 EMC), and decomposition products of the electrolyte and the SEI (H<sub>2</sub>O, CO<sub>2</sub>). In **Figure 36** (a) it can be seen that the concentration of the electrolyte vapor EMC increases with increasing time between the venting and the gas measurement. During one experiment using a cy-10 cell, the vent gas after the first venting was unintentionally diluted with additional N<sub>2</sub> (additional 4.3 mol N<sub>2</sub> was added to about 5.4 mol N<sub>2</sub> from the beginning of the experiment). So, the measured gas concentrations of this experiment using a cy-10 cell (dark blue measured gas concentration in **Figure 36** (a)) were lower than the other gas concentrations measured about the same time after opening of the cell housing.

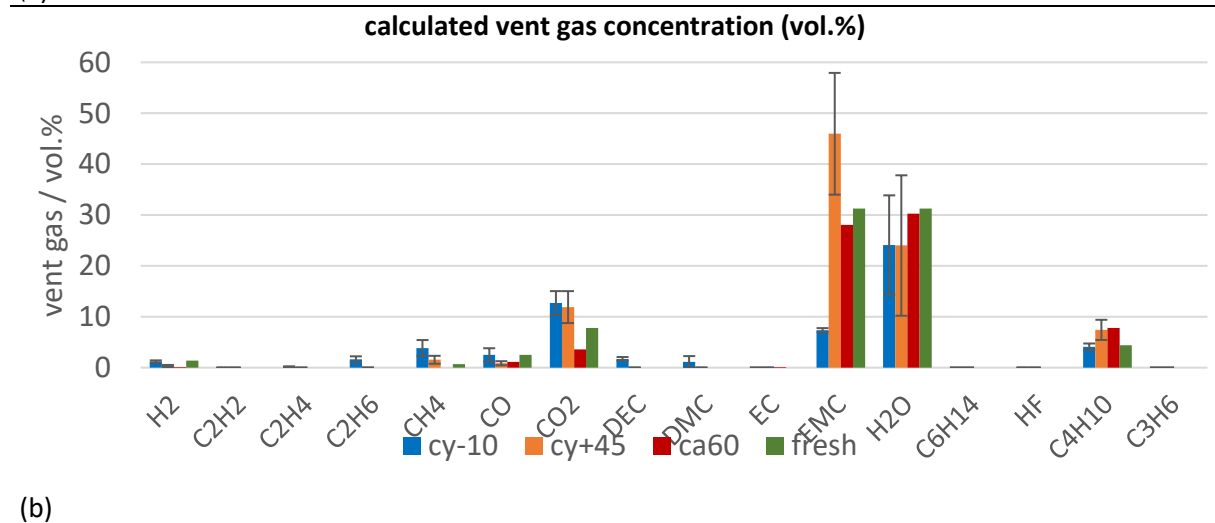
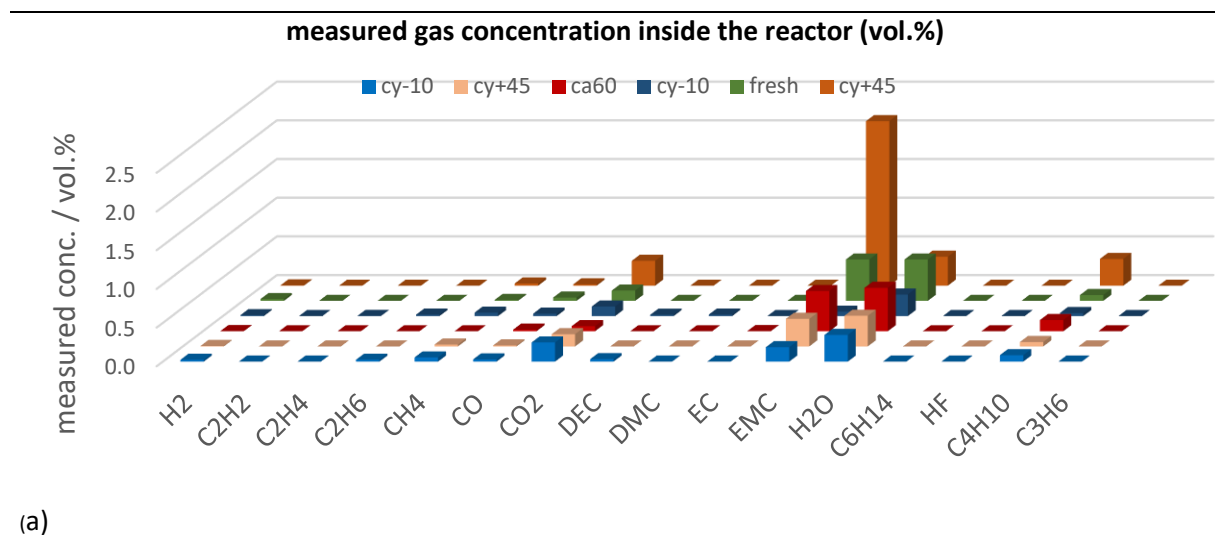


**Figure 36: Vent gas composition after the first venting of aged type #1 cells (cy-10: blue, cy+45: orange, ca60: red) in overtemperature experiments in comparison to the results of fresh cells (green). a) measured gas concentration (in vol.%) inside the reactor ranked according to the time between the venting and the gas measurement; b) calculated vent gas composition in vol.% (presenting the battery vent gases only).**

The main gas compounds measured after the first venting of fresh cells and the different aging paths of cell type #1 lead to the same main gases, but the exact vent gas composition differs between the different aging paths, as can be seen in **Figure 36** (b). Here the average calculated vent gas composition (according to equation (1) in [11]) of the repeated experiments is presented in vol.%, which is independent of the total amount of produced gases.

The calendric high temperature aged cells showed the lowest capacity fade compared to the other two aging paths and consequently the gas composition after the first venting of the calendric aged cells was most comparable to the vent gases produced for fresh cells.

The cyclic aging at  $-10^{\circ}\text{C}$  led to decomposition products of the electrolyte component EMC into DEC, DMC,  $\text{C}_2\text{H}_6$  and  $\text{CH}_4$ , which were measured after the opening of the cell housing. The transesterification reaction of EMC into DEC and DMC was described by Blomgren et al. in [142].  $\text{CH}_4$  and  $\text{C}_2\text{H}_6$  as decomposition products might be produced from the methyl radicals ( $\text{CH}_3$ ) [143], which are formed from decomposing EMC [64]. As a consequence of the SEI decomposition small amounts of  $\text{H}_2$  were measured, because  $\text{H}_2$  most probably developed due to the reaction of the linear electrolyte component EMC and the anode [123]. Very low  $\text{C}_2\text{H}_4$  concentrations were measured after the first venting. Because  $\text{C}_2\text{H}_4$  is mainly produced during the decomposition of EC, we can assume that only minor parts of EC were decomposed after the first venting.

The presented vent gases after the first venting highly depend on the used electrolyte. This can be observed by comparing the vent gases produced at the first venting in overtemperature of cell type #1 and cell type #3 published in [5]. For cell type #3, DEC,  $\text{H}_2\text{O}$ ,  $\text{CO}_2$ , CO,  $\text{C}_2\text{H}_6$ ,  $\text{H}_2$ ,  $\text{C}_2\text{H}_4$  were the main gas compounds. The degradation paths of the electrolyte components are described in [59].

During the TR, the main amount of vent gas is produced. The main gas compounds produced during the TR of cell type #1 are  $\text{CO}_2$ , CO,  $\text{H}_2$  and higher hydrocarbons (see **Figure 37**). These main vent gas compounds are similar to published vent gas compositions from other NMC LIBs with commercial electrolyte solvents (such as EC, DEC, DMC, EMC) like published in [73,87]. The presented results are within the error bars of each gas component presented in [73][Fig.4.]. The gases produced during the TR can be explained by SEI decomposition [7,123], electrolyte decomposition [122,126], NMC (cathode) degradation and reaction of the solvent with the cathode [51,56]. As shown in the investigation of the TR trigger in chapter 4.2 also the failing mechanism driven by the Li deposit inside the cathode/anode (see overtemperature versus overcharge) influences the vent gas composition.

The vent gas composition is also influenced by the used electrolyte components and additives [144]. Although parts of the electrolyte were consumed in the SEI, or decomposed, EMC is still measurable in the vent gas in a significant amount. EC is unlikely to be measured in this setup, because of the high boiling point and EC is not volatile enough to be detected in this setup.

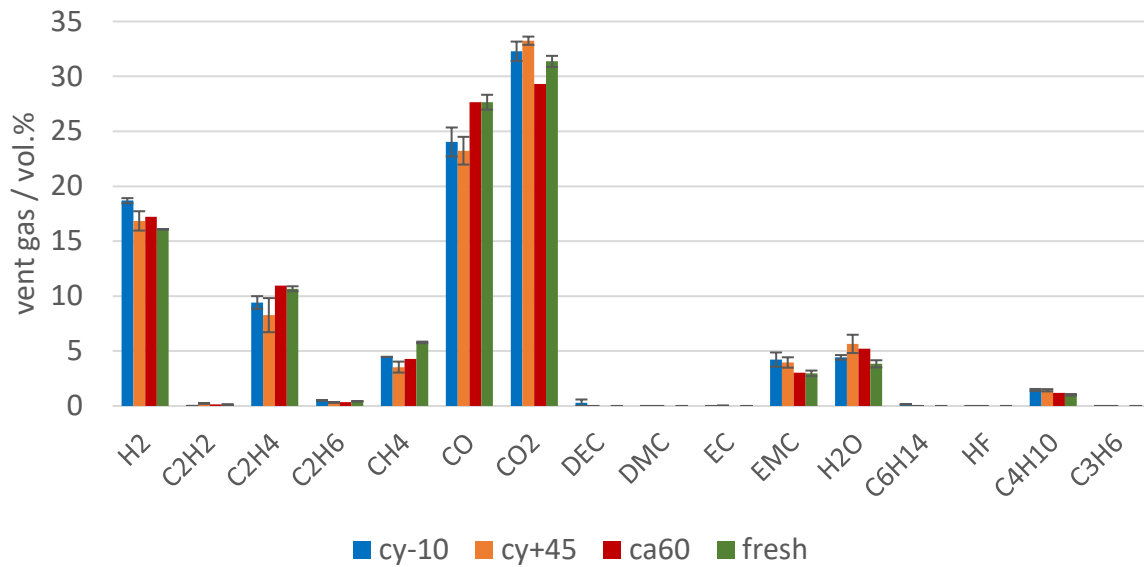


**Figure 37: Vent gas composition in vol.% after the TR of aged type #1 cells (cy-10: blue, cy+45: orange, ca60: red) in overtemperature experiments in comparison to the results of fresh cells (green).**

**Figure 38** shows the amount of produced vent gas in mol in order to emphasize on the reduced gas production of failing aged cells. Beside the reduced amount of vent gas emission of aged LIBs the aging influence can also be observed in the vent gas composition. Capacity and power fade, irreversibly loss of reactive Li and electrolyte led to a significant decrease of the amount of toxic gas CO, but also the total amount (in mol) of CO<sub>2</sub>, H<sub>2</sub>, C<sub>2</sub>H<sub>4</sub>, CH<sub>4</sub> were reduced. C<sub>2</sub>H<sub>4</sub> was produced during EC reduction [59]. For the cells with the highest capacity fade (cy+45 and cy-10) the amount of C<sub>2</sub>H<sub>4</sub> was reduced compared to fresh cells, because parts of EC were already consumed irreversibly due to aging effects. At the same time a decrease of the CO<sub>2</sub> amount was measured for the aged cells (cy+45 and cy-10). CO<sub>2</sub> was produced mainly during electrolyte decomposition [48,122] and SEI decompositions [8,123]. Broussely et al. also mentioned CO<sub>2</sub> gas evolution resulting from the electrolyte oxidation on the positive electrode interface [40]. Although for the aged cells with the highest capacity fade (cy+45 and cy-10), the SEI grew due to aging effects and the SEI decomposition also generates CO<sub>2</sub>, not the same amount on CO<sub>2</sub> was produced during the overtemperature experiment than using fresh cells. Consequently, if electrolyte is consumed in the SEI growth, less CO<sub>2</sub> is produced (and less CO and higher hydrocarbons).

Although the calendric aged cell lost less capacity than the cells with other aging paths, differences in the vent gas composition after the TR can be observed. Lammer et al. observed higher amounts of H<sub>2</sub> for failing aged cells compared to the fresh cells. In this study, the vol.% of H<sub>2</sub> in the vent gas increased for aged cells but did not increase in total amount (compare **Figure 37** and **Figure 38**). The highest H<sub>2</sub> reduction was observed for the cells with the highest capacity fade. This can be explained due to the reduced amount of electrolyte available for the reaction. H<sub>2</sub> was most probably produced by the reaction between the linear electrolyte components and the anode [123]. Aurbach et al. also stated the H<sub>2</sub> production by the reaction of Li with water contaminated electrolyte solutions [124]. In this study, the amount of produced H<sub>2</sub> does not decrease as much as the CO or CO<sub>2</sub> amount for failing aged cells. The high amount of H<sub>2</sub> produced from the cy-10 cells might be explained due to the reaction of plated Li at the anode side with the electrolyte. Du Pasquier et al. assume that hydrogen is generated during the reaction between the PVDF binder and Li<sub>x</sub>C<sub>6</sub> at T > 300°C [125]. Wang et al. also stated that

the collapsed graphite particles  $\text{Li}_x\text{C}_6$  can react with PVDF and lead to further electrolyte decomposition, heat generation and  $\text{H}_2$  production [10]. The amount of produced CO decreased significantly with the loss of capacity. A linear correlation between the current capacity (Ah) and the amount of measured CO (mol) can be seen in **Figure 39** (a).

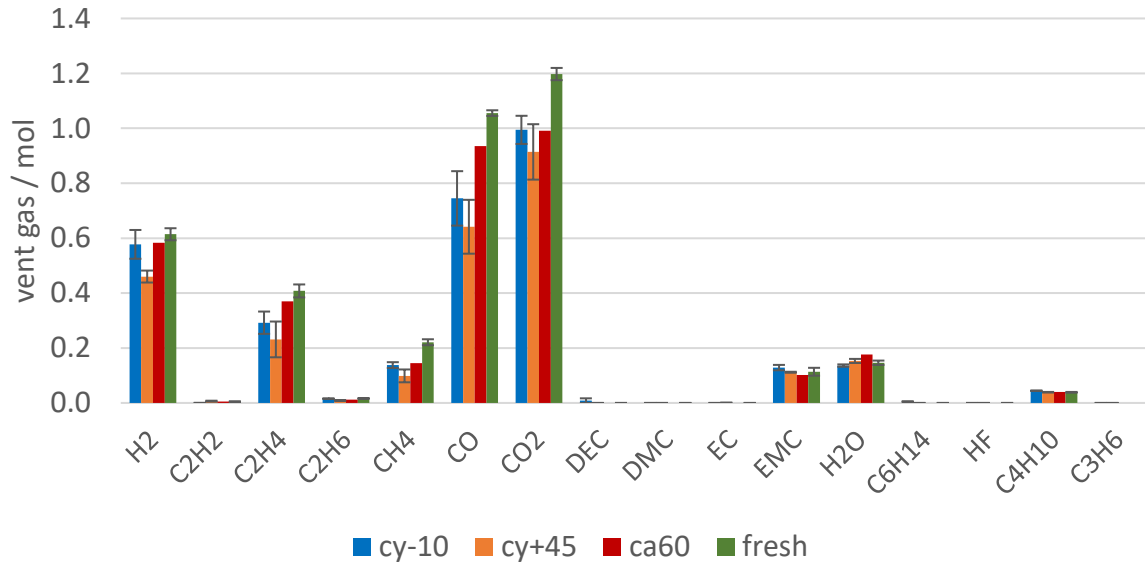


**Figure 38: Vent gas composition in mol after the TR of aged type #1 cells (cy-10: blue, cy+45: orange, ca60: red) in overtemperature experiments in comparison to the results of fresh cells (green).**

Since the TR was triggered for all 100% SOC charged cells, all cells lost a significant amount of weight during the experiment due to particle and gas emission (see **Figure 39** (b)). The mass loss during the TR of aged cells was reduced compared to fresh cells. This is consistent with a reduced heat release during the TR reaction for aged cells and can be explained with less available reactive Li and less available electrolyte. The cells with the highest capacity fade (cy+45) showed the lowest mass loss during the overtemperature TR experiment. The mass loss of the LIBs during overtemperature experiments also correlates with the capacity of the cells before the failure event.

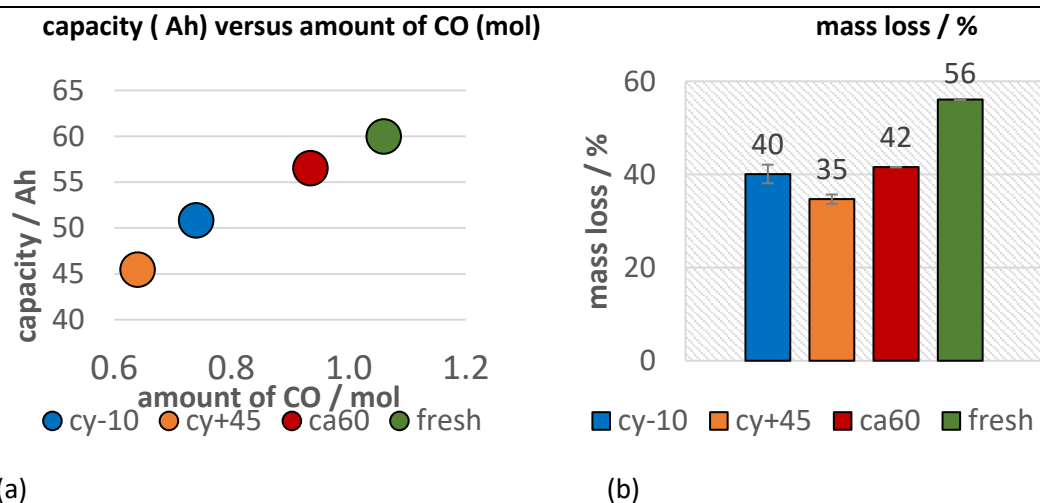


**Figure 39: a) current capacity (Ah) of aged cells versus the amount of produced CO (mol) b) mass reduction after TR of the aged (cy-10: blue, cy+45: orange, ca60: red) type #1 cells in comparison to the fresh type #1 cells (green).**

In **Table 10** the safety relevant parameters are summarized for the failing aged, investigated cells and compared to the results of fresh cells during overtemperature TR trigger. Only one ca60 cell was available, consequently no variation between repeated experiments is shown.

First and second degassing were observed in all experiments, independent of the aging path. The calendric aged cells showed the lowest capacity fade compared to the other two aging paths.

Additional to the mentioned safety relevant parameters, the duration of the TR venting and the venting rates were analyzed. The duration of the TR venting was the shortest for the ca60 cell and the longest for one cy+45 cell. This cyclic aged cell at 45°C vented significantly longer than the other investigated type #1 cells, because according to the thermocouple measurement, the TR started close to the second nearest thermocouple to the cathode tab and needed more time to spread through the cell. Therefore, the duration of the TR venting depends also on the origin of the TR. The reproducibility of this parameter was surprisingly high for the experiments with the fresh type #1 cells and the cyclic aged cells at -10°C.

**Table 10: Summary of safety relevant parameters of differently aged automotive type #1 cells using overtemperature trigger in comparison to the results of fresh cells.**

	aged cy-10 cell type #1	aged cy+45 cell type #1	aged ca60 cell type #1	fresh cell type #1
capacity (Ah)	51 ± 1	45 ± 2	57	60
first vent	yes	yes	yes	Yes
$\bar{T}_{cell}^{v1}$ (°C)	119 ± 5	123 ± 1	124	122 ± 1
TR	yes	yes	yes	Yes
$T_{cell}^{crit}$ (°C)	199 ± 4	217 ± 2	203	206 ± 1
$\bar{T}_{cell}^{v2}$ (°C)	190 ± 1	219 ± 2	205	204 ± 1
$T_{cell}^{max}$ (°C)	763 ± 5	762 ± 9	794	819 ± 5
$T_{vent}^{max}$ (°C)	982 ± 238	934 ± 202	1306	584 ± 1
duration TR venting (s)	3.0 ± 0.2	4.0 ± 1.0	2.5	3.5 ± 0.1
amount of gas (mol)	3.1 ± 0.3	2.7 ± 0.3	3.4	3.8 ± 0.1
vent gas/ capacity (mol/Ah)	0.061	0.060	0.060	0.063
venting rate $\dot{n}_{ch}$ (L/s)	39 ± 5	25 ± 5	42	34 ± 2
main gas compounds	CO <sub>2</sub> , CO, H <sub>2</sub>			
c <sub>H2</sub> (vol.%)	19 ± 1	17 ± 1	17	16 ± 1
c <sub>CO</sub> (vol.%)	24 ± 1	23 ± 1	28	28 ± 1
mass loss (%)	40 ± 2	35 ± 1	42	56 ± 1

The reproducibility of the overtemperature TR experiments for the investigated cell type is shown in [11] and confirmed with low standard deviations of the quantification of safety relevant parameters. Though the ca60 experiment could not be repeated, based on the repeatability shown in the other experiments and the reproducible gas quantity (0.06 mol/Ah) the ca60 results are representative. For further information on aging effects and aging models see [133,145–148]. Aging models are not content of this study.

This observed influence of aging is valid for the investigated pouch cell type #1 for the investigated aging paths. Although the results are representative for currently used mass-produced EV cells, the

results might be slightly different for other cell types from different cell manufacturers. Though a proper choice of materials and additives may lead to certain changes in the aging behavior, the cycle stability and the failing behavior, these observed results may not be true for different cell chemistries. For a different cell type, such as prismatic hard case cells, differences in the opening of the cell housing (the first venting), the duration of the TR event and consequently the characteristic venting rates are expected [11]. Additionally, external compression of the cell during aging might lead to changes in the TR results. The mechanical pressure increases the electrical contact [41] and the wettability of the electrodes [38], but too high applied external compression leads to reduced ionic transport, separator creep, power fade and capacity fade [38][149][42]. Again, it needs to be mentioned that the TR tests were not conducted immediately after the aging tests, the cells were stored at room temperature for another five months before testing inside the TR reactor.

Compared to literature, a general rule might be, that a less violent TR behavior is observed for aged cells with power and capacity fade, if no metallic Li plating is produced. But if fresh metallic Li plating is produced a more intense TR reaction is expected. To be able to predict the exact failing behavior, a detailed analysis for each cell chemistry/cell type is highly recommended.

#### 4.4 Reproducibility of the thermal runaway experiments

*This chapter is already published in:*

Essl C, Golubkov AW, Fuchs A. Comparing Different Thermal Runaway Triggers for Two Automotive Lithium-Ion Battery Cell Types. *Journal of The Electrochemical Society* 2020; **167**(130542): 1–13. DOI: 10.1149/1945-7111/abbe5a.

The experiments were reproducible in the categories thermal, electrical and mechanical behavior. The presented standard deviation of safety relevant parameters in **Table 8** shows, that deviations of the values  $\bar{T}_{cell}^{v1}$ ,  $T_{cell}^{crit}$  are lower than 1% of the measured value. Also, the deviations in the gas composition values of the main safety relevant gases such as CO and H<sub>2</sub> were in overtemperature and overcharge experiments below 1% of the measured values. These values were rounded up to 1 % in **Table 8**. Only the gas composition measured for the nail-penetrated cells varied about 5% of the measured value. A conservative accuracy analysis of the gas composition analysis with FTIR and GC in parallel also resulted in a 3%-6% relative accuracy of the measured gas value depending on the gas compound (see [5]). Therefore, the measured gas composition values for three different TR trigger were surprisingly in a good agreement. Although  $T_{cell}^{max}$  and  $T_{vent}^{max}$  might depend on the thermocouple positions, which is limited, in most TR experiments the results fit together very well. For overtemperature and overcharge the deviation of the parameters duration of the venting during TR, the amount of vent gas, the venting rate and mass loss were also rounded up to the significant measurement values.

To sum up, the reproducibility of the experiments with the presented three TR trigger, overtemperature, overcharge and nail-penetration is given, and the results disagrees with the assertion of Feng et al. that there is a lack of reproducibility in nail-penetration and overcharge tests [69].

## 5 Early failure detection

*This chapter has been accepted for publication in MDPI Batteries Journal in March 2021 under the title “Early detection of failing automotive batteries using gas sensors”.*

First, the target gases for each battery failure case were identified and based on the results, suitable sensors were chosen. These sensors were benchmarked and tested in real battery failure cases. At the end of this study, the most promising gas sensors for early battery failure detection are presented.

### 5.1 Gases produced in the investigated four battery failures

Target gases for each battery failure case could be identified (see **Table 11**). The produced gases before the TR can be classified in two main groups: H<sub>2</sub> produced at the electrolysis, and electrolyte vapor (VOCs), evaporated from a leaky damaged cell or a first venting. In **Table 11** produced gases identified at the investigated four failure cases are listed. The gas amounts are presented for a state-of-the-art 60 Ah automotive NMC (622) cell as published in [11] tested inside a 120 l free gas volume.

**Table 11: Representative gas components measured in the investigated failure cases including assumed maximum gas amount bases on a failing automotive 60 Ah cell.**

battery failure case	(vent) gases	gas amount / mol
a) electrolysis	H <sub>2</sub> , O <sub>2</sub>	up to 0.013 mol H <sub>2</sub> /h
b) electrolyte vapor	electrolyte	up to 1.4 mol
c) first degassing	electrolyte, H <sub>2</sub> O, CO <sub>2</sub> , CO, C <sub>2</sub> H <sub>6</sub> , H <sub>2</sub> , C <sub>2</sub> H <sub>4</sub>	up to 1.8 mol
d) thermal runaway	CO, H <sub>2</sub> , CO <sub>2</sub> , H <sub>2</sub> O, C <sub>2</sub> H <sub>4</sub> , CH <sub>4</sub> , C <sub>4</sub> H <sub>10</sub> , C <sub>2</sub> H <sub>6</sub> , C <sub>2</sub> H <sub>2</sub> , electrolyte	up to 0.11 mol/Ah, for 60 Ah, 7 mol

The exact electrolyte composition varies strongly between cell manufacturers and cell type. The most frequently used electrolyte components are listed in **Table 11** including concentration ranges, assuming that the total amount of electrolyte vaporized (1.4 mol for the representative 60 Ah cell). The electrolyte of currently used LIBs for automotive applications consists of a varying mixture of linear carbonates such as DMC, DEC, ethyl methyl carbonate (EMC) and the cyclic carbonate ethylene carbonate (EC) [1]. In **Table 11**, the calculated H<sub>2</sub> amount according to the assumptions from chapter 2.1.2 are listed. Higher amounts of produced hydrogen are possible if the distance between the electrodes is further reduced, the immersed electrode area increased, an electrolyte with higher conductance is used, or the applied voltage is increased. Here we assume a 100% Faraday’s yield for H<sub>2</sub> production. For detailed analysis during water electrolysis using aluminum as electrode material see [150]. For the first venting, failure case c), the amount of produced gas depends on the total amount of electrolyte used inside the cell, the used electrolyte components, the TR trigger, and the time between the first venting and the TR. For the first venting up to 0.4 mol gas consisting of the gas components presented in **Table 11** were measured in overtemperature or overcharge experiments. For the TR, failure case d), the amount of produced gas depends on the used TR trigger [11], the cell chemistry, the electrolyte, and the energy of the cell. Up to 0.11 mol/Ah vent gas can be produced during overcharge triggered TR using the representative 60 Ah NMC cell [11]. The gases produced

during failure case a) – c) are independent of the used cathode material, because in particular failure case b) and c) are dominated by the used electrolyte mixture. For the TR behavior itself, the cathode material is decisive for the thermal stability of the cell, the start of the decomposition and the release of oxygen [60] and the oxygen further reacts with electrolyte and produces  $\text{CO}_2$  and  $\text{H}_2\text{O}$  [59][61].

**Figure 40** shows the gases and their volumetric proportion produced at a) the electrolysis and b) failure case vaporizing electrolyte solvents. To make a general statement about electrolytes in failure case b), the measured electrolyte concentration was uniformly distributed to the electrolyte components DEC, DMC, EMC and EC. A detailed analysis of gases produced at the first venting c) and the TR d) is published in [5,11] and one representative example is graphically shown in **Figure 40** c) and d). **Figure 40** c) and d) present the results of real gas measurements using modification of the measured electrolyte component. The main gas components during the first venting are typically DMC, DEC and EMC. EC has a significantly higher boiling point ( $248^\circ\text{C}$ ) than the linear carbonates (DMC  $91^\circ\text{C}$ , DEC  $126^\circ\text{C}$  and EMC  $110^\circ\text{C}$ ) and consequently the amount of EC in the vent gas of the first venting is observed to be lower than the amount of the linear carbonates inside our test bed. After the first venting in a few experiments even no  $\text{CO}_2$  or  $\text{CO}$  gas was measured. In the experiment presented in **Figure 40**, 2 mmol  $\text{CO}$  (2000 ppm) and 5 mmol  $\text{CO}_2$  (5000 ppm) were measured about 10 min after the opening of the cell. The gases measured after the first venting are a sum of the gases from the first opening of the cell and gases produced due to the further evaporating and decomposition reactions.

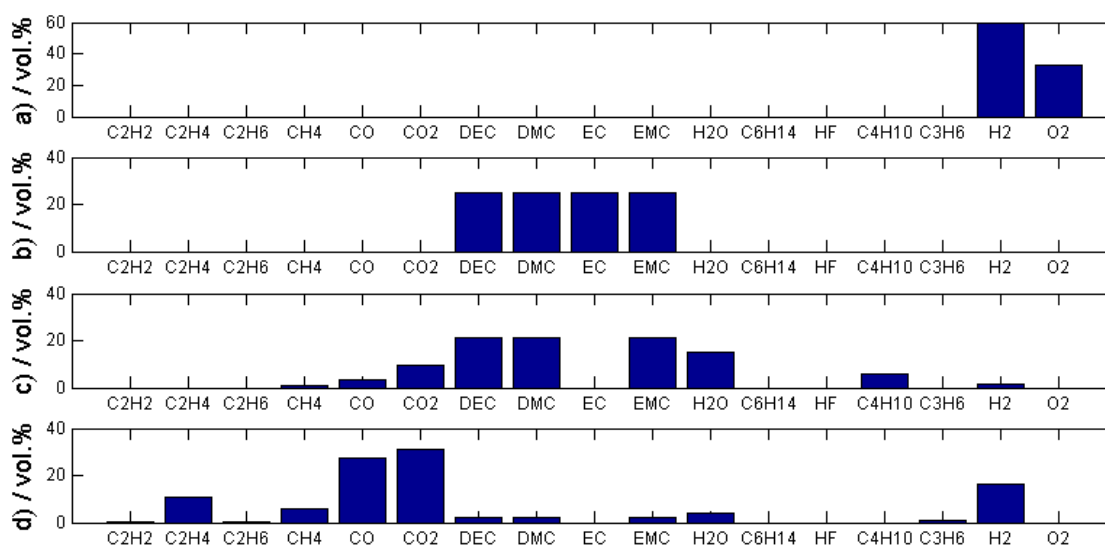


**Figure 40: Representative examples of measured gases in volume percent for the investigated four battery failure cases a) electrolysis b) electrolyte vapor c) first venting and d) thermal runaway. The electrolyte composition varies from cell to cell – here it is assumed that the linear electrolyte components DMC, DEC and EMC are present in the same amount.**

## 5.2 Sensor selection

The detailed analysis of produced gases for the four battery failure cases shows, that focusing on  $\text{CO}_2$  and  $\text{CO}$  sensors allows to measure the TR, and maybe the first venting, as long as  $\text{CO}$  and  $\text{CO}_2$  gas is produced and the gas sensor is close to the failing cell and sensitive enough to the small amounts of  $\text{CO}$  or  $\text{CO}_2$  produced at the opening of the cell housing. Concentrating on electrolyte (VOCs) detection and  $\text{H}_2$  detection has the major benefit of being able to detect the failure earlier. The tracer gas

electrolyte is independent of the used cell chemistry, since state-of-the-art electrolyte solvents consist of a mixture of EC, DEC, DMC and EMC in varying ratios [1].

Based on the measured gas components for the four battery failures and the sensor requirements, several sensors were chosen to be benchmarked (see **Table 12**). Sensors with different measuring principles were chosen: MOx sensors, electrochemical sensors, nondispersive infrared sensor (NDIR) and environmental sensors such as hygrometer and thermometer. Since the MOx technology seems to be quite promising according to different publications [104,108–110], MOx sensors from different manufacturers have been chosen, tested and compared. Still, the challenge is to find suitable low-cost sensors with long lifetime and automotive qualification.

**Table 12: Selected and tested sensors for the usage as early battery failure detector.**

sensor	manufacturer	sensor principle	target gas
MiCS-5524	SGX Sensortech	MOx	CO, H <sub>2</sub> , CH <sub>4</sub> ,
MiCS-6814	SGX Sensortech	MOx	CO, NH <sub>3</sub> , NO <sub>x</sub>
iAQ-core	AMS	MOx	VOCs
CCS811	AMS	MOx	VOCs
TGS 8100	Figaro	MOx	ethanol, H <sub>2</sub>
TGS 5141	Figaro	electrochemical (solid electrolyte)	CO, H <sub>2</sub>
TGS 2620	Figaro	MOx	ethanol, H <sub>2</sub>
MQ-2	Winsen	MOx	smoke, LPG, ethanol
MQ-8	Winsen	MOx	H <sub>2</sub>
SCD30	Sensirion	NDIR, hygrometer, thermometer	CO <sub>2</sub>
SGP30	Sensirion	MOx	VOCs, H <sub>2</sub>
SGP4x_eng	Sensirion	MOx	VOCs, NO <sub>x</sub> , VOCs, S
SGAS701	IDT	MOX	H <sub>2</sub>
SHT31	Sensirion	hygrometer, thermometer	water vapor, temperature
BME 680	Bosch	MOx, hygrometer, thermometer, barometer	VOCs, temperature, pressure, water vapor
BME 280	Bosch	hygrometer, thermometer, barometer	temperature, pressure, water vapor

More expensive, larger and more selective electrochemical sensors have been chosen as reference sensors: Alphasense – NO<sub>2</sub> A43F, Alphasense NO – A4 and Alphasense-PID (photoionization detector) sensor. These sensors were used as reference to the low-cost commercially available sensors listed in **Table 12**.

The chosen MOx sensors can be divided into two groups: gas sensors with one single pixel and consequently one resulting raw signal (MiCS-5524, iAQ-core C, CCS811, TGS 8100, TGS 2620, MQ-2, MQ-8) versus gas sensors with multi-pixel and resulting two to four readable raw signals (MiCS-6814 (3: reducing (CO), oxidizing (NO<sub>x</sub>) and one for ammonia (NH<sub>3</sub>)), SGP30 (2: one for VOCs and one for H<sub>2</sub>), engineering prototype SGP4x\_eng (4: VOCs, NO<sub>2</sub>, VOCs and one tuned for sulfur containing compounds)). The tested SGP4x\_eng is an engineering product that has four readable MOx pixels. The consumer product of SGP4x\_eng, SGP40, could not be tested, but has four pixels of which only one pixel is readable for the user [151]. In this document we refer only to the user-readable number of pixels.

### 5.3 Sensor tests

The gas sensors were tested in the four battery failure cases and compared. The target gases  $H_2$  and VOCs can be reliably, fast and cost efficiently detected. Different sensor types and manufacturers were tested and most promising sensors for battery failure detection were found.

#### 5.3.1 Electrolysis

The electrolysis tracer gas  $H_2$  was tested in different dilution series inside the sensor test setup with all chosen sensors. One exemplary measurement of a TGS-8100 MOx sensor (blue) compared to an electrochemical sensor TGS-5141 (green) is shown in **Figure 41**. All MOx sensors showed a clear response to the reducing gas  $H_2$ , even if  $H_2$  was not listed as target gas in the sensor specification. Also, the electrochemical sensor TGS-5141 reacted to  $H_2$ , but the sensor could not measure concentrations below 300 ppm  $H_2$ . As expected, the SCD30 sensor did not react to the  $H_2$  gases. The humidity measurement on the SCD30 (SHT31) and the BME680 showed unspecific changes in the measured value due to the flushing of the sensor chamber but not because of  $H_2$ . The experiments show that MOx sensors have a higher sensitivity to  $H_2$  and a quicker sensor response than the electrochemical sensor as seen in **Figure 41**.

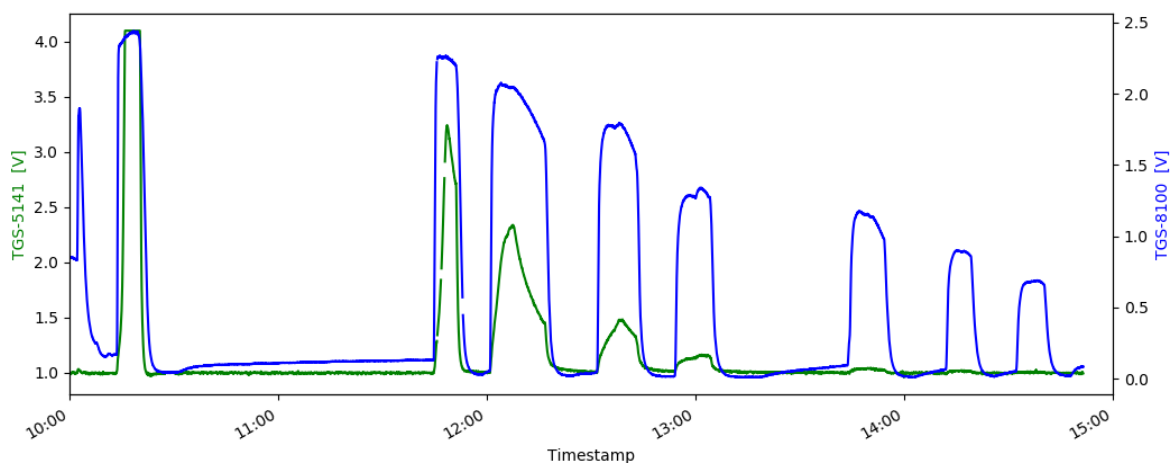


**Figure 41: Comparison of an electrochemical TGS-5141 (green) and a MOx TGS-8100 (blue) gas sensor in  $H_2$  measurements with decreasing concentration of  $H_2$ . The comparison shows the higher sensitivity and quicker response of the MOx sensor for  $H_2$  gas.**

Consequently, a MOx sensor (SGP30) was tested in 30 electrolysis experiments. **Figure 42** shows the sensor response to the produced  $H_2$  during the electrolysis. At the beginning of the experiment no voltage was applied between the test electrodes and the sensor was switched on. The sensor raw signals (given in ticks) increased. After the pixel 2 got stable at  $\sim 280$  s voltage was applied to the electrodes, current flows, bubble formation was observed on the electrodes and the gas sensor reacted with decreasing sensor pixel 2 ( $H_2$  sensitive pixel) and pixel 1 (VOC pixel) raw value. There was no constant  $H_2$  measurement because of the produced  $H_2$  bubbles, which detached randomly from the electrode surface depending on their size. Wang et al. described this bubble effect during electrolysis [117].

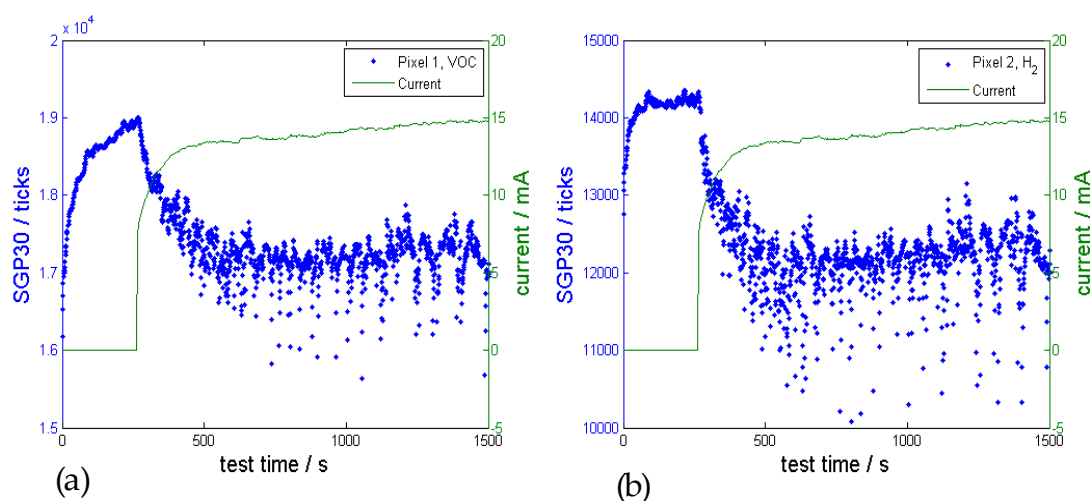


**Figure 42: One representative electrolysis experiment showing the reaction of the MOx gas sensor SGP30 (blue) during an electrolysis experiment (H<sub>2</sub> production) using tap water as electrolyte (4.15 V, 8 mm distance, 650 mm<sup>2</sup> surface area per electrode). The gas sensor resistance of (a) pixel 1 (VOC sensitive pixel) and (b) pixel 2 (H<sub>2</sub> sensitive pixel) changes exactly at the activation of the electrolysis.**

The sensor raw value, which is related to the logarithm of the measured resistance, decreases due to the reaction of produced H<sub>2</sub> with the absorbed oxygen on the sensor surface and consequential release of the chemisorbed e<sup>-</sup> into the conduction band of the semiconductor. Consequently, the measured resistance decreases. This observation of H<sub>2</sub> reacting with the MOx surface is as expected and published in literature [152,153].

### 5.3.2 Electrolyte vapor

For battery failure case b) electrolyte vapor, the chosen gas sensor response was investigated for different electrolyte mixtures (EC:DEC:DMC (12:12:1), EC:DMC (3:7)). The sensor platform was inside the sensor chamber and electrolyte vapor was added with a syringe through a septum inside the sample chamber. **Figure 43** shows the response of different sensors to battery electrolyte vapor (first injection of 0.02 ml, compressed air flow 7 L/min; second injection 0.02 mol, 2.2 L/min) in one representative experiment. A significant resistance drop of the MOx sensors inside the sensor chamber was observed immediately after the electrolyte was added to the sensor chamber: MiCS-6814 (pixel 1 (CO) and 3 (NH<sub>3</sub>)), SGP30 (all 2 pixels (VOC and H<sub>2</sub>)), SGP4x\_eng (all 4 pixels (VOC, NOx, VOC and S) and iAQ-core. TGS 8100 and MiCS-6814 pixel 2 (NH<sub>3</sub>) did not show a response to the electrolyte vapor in this experiment but did show a response in other electrolyte experiments. Although the reaction for MiCS-6814 pixel 2 was significantly lower than of pixel 1 and 3. Consequently, the MOx sensor TGS 8100 and the MiCS-6814 pixel 2 did not work properly and might be limited during the harsh conditions in previous experiments. IDT-SGAS H<sub>2</sub> did not show a reaction to electrolyte vapor.

The electrochemical reference sensor Alphasense NO<sub>2</sub> A43F showed a small change of the signal. Alphasense NO – A4 did not show a significant reaction, but the Alphasense-PID sensor did react to the electrolyte vapor. As expected, the SCD30 NDIR CO<sub>2</sub> sensor and the electrochemical sensor TGS 5141 did not react in these experiments as well as the humidity measurements with BME 280, BME 680, SCD30 and SHT31.

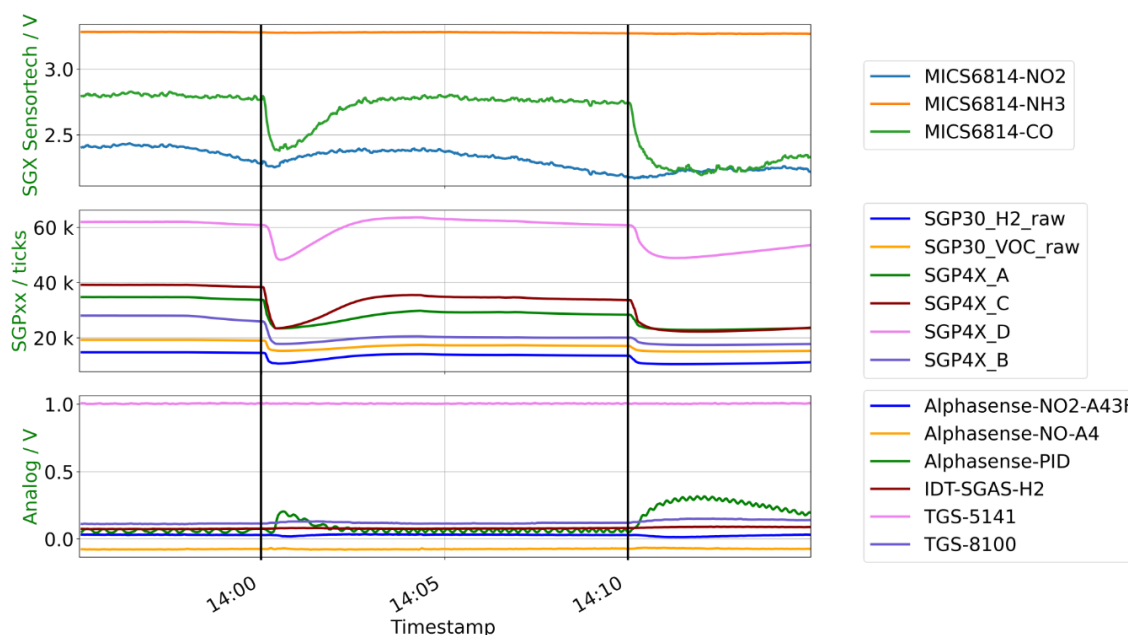


**Figure 43: Representative gas sensor response to battery failure case b) electrolyte vapor. The electrolyte vapor was added with a syringe at 14:00 and at 14:10 into the sample chamber. The temperature of the hot plate inside the sample chamber was kept constant at 25°C during this experiment.**

Due to sensor aging, connectivity issues and continuous updates of the sensor platform, all 16 sensors were never tested at once in the experiments with electrolyte vapor. MICS-5524, CCS811, TGS 2620 and Winsen MOx sensors (MQ-2, MQ-8) were not tested in this representative experiment in **Figure 43** but they did show a response to electrolyte vapor in former experiments. Although the Winsen sensors reacted to electrolyte vapor, they showed less response repeatability compared to MOx sensors from other manufacturers.

Since MOx sensors react to electrolyte vapor, this sensor technology is very promising for early battery failure detection. The result of the MOx sensors reacting to electrolyte vapor and used battery solvent is consistent with the observations in literature [104,108,110].

### 5.3.3 First venting and thermal runaway

Battery failure cases c) the first venting and d) the TR were analysed in a special constructed TR test bed described in chapter 3.2 and therefore these two failure cases are combined in one section.

The TR test bed is gas tight, filled with inert gas N<sub>2</sub> and has special feedthroughs for sensor measurements: for thermocouples, for voltage and current sensors. Due to the limited number of feedthroughs and the high costs and efforts put into the setup of the sensor platform, not the whole sensor platform was added into this TR reactor. Based on the known response of MOx sensors to electrolyte vapor and the huge amount of electrolyte vapor evolving at the first venting event, one selected MOx sensor was placed inside the reactor. Due to the easy handling of the Sensirion sensor bridge combined with flexPCB (flexible PCB) sensors and their multi-pixel feature, Sensirion sensors (mainly SGP30, but also SGP4x\_eng) were chosen. Experiments using three different TR triggers were conducted: overtemperature, overcharge and nail-penetration. In total more than 30 TR experiments were conducted using a gas sensor inside the TR test bed.

### 5.3.3.1 Overtemperature TR test

17 tests were conducted using the SGP30 sensor in overtemperature TR experiments of different large automotive LIBs. **Figure 44** shows the sensor response (blue) of SGP30 (a) pixel 1 and (b) pixel 2 compared to the temperature of a thermocouple mounted on the pouch cell cathode tab of one representative experiment. At  $\sim 3000$  s the cell case opened due to the gas generation inside the cell and the first venting was observed as a small increase/fluctuation of the temperature measurement on the cell tab ( $\Delta T = 4^\circ\text{C}$ ). The temperature sensors mounted on the cell surface did not show a peak at the first venting, here the thermocouple mounted on the cathode cell tab was the only temperature sensor detecting the first venting. In other experiments the only thermocouple detecting the first venting was positioned close to the weakest point of the cell housing. For hard case cells this would be the burst plate. In this representative experiment the pressure inside the reactor slightly increased at the first venting of this pouch cell ( $\Delta p = 0.01$  bar). This pressure increase can hardly be detected because the pressure inside the reactor also increased due to the rising ambient reactor temperature. The gas sensor pixel 1 and 2 clearly reacted with a significant signal drop within 10 s to the gases evolving from the cell at the first venting event. At  $\sim 5400$  s the exothermic reaction of the cell led to a significant increase of the temperature measured at the cell tab and again to a significant resistance drop of the sensor pixel 1 in the same second as the temperature on the cell tab started to rise. The ambient conditions during and after the TR (temperature peak up to  $150^\circ\text{C}$ , pressure increase up to 3.2 bar, complex gas mixture in high concentration) were far outside the recommended operation specifications of the tested sensor. Consequently, the sensor was in an undefined state after the TR although a signal was provided.

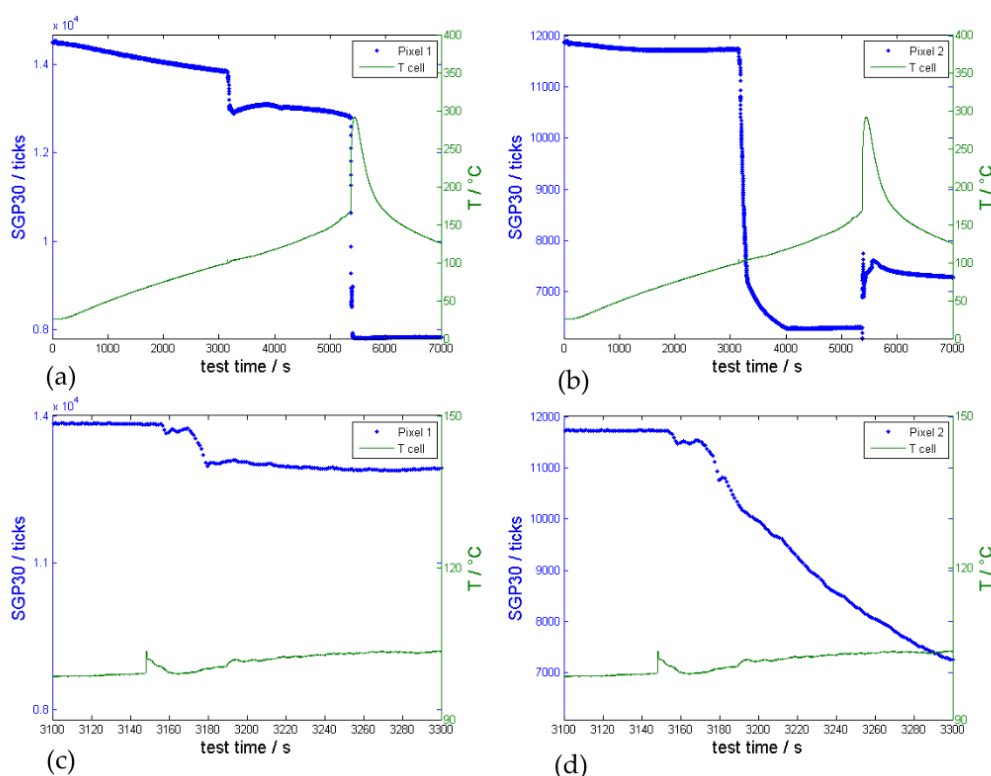


**Figure 44: Representative gas sensor SGP30 measurement (blue signal) during overtemperature triggered TR experiment of an automotive pouch cell (cell type #4) compared with measured temperature on the cell tab of the cathode (green). (a) shows the signal of sensor pixel 1 and (b) the signal of sensor pixel 2. The first venting happened at  $\sim 3000$  s and the TR at  $\sim 5400$  s. (c) shows the reaction of pixel 1 and (d) the reaction of pixel 2 compared to the temperature sensor on the cell tab during the first venting.**

The time between the first venting and the TR decreases with increasing heating rate and depends on the venting design of the cells. **Figure 44** shows the benefit of a multi-pixel evaluation: Pixel 1 showed two steps of resistance drops while pixel 2 showed only one resistance drop during the first venting event but an increasing resistance change during the TR. This can be explained by the different heating plate temperatures and different MOx-materials of the pixels on the SGP30, which allows to distinguish between different target gases and consequently to distinguish different failure cases.

The sensor signal in **Figure 44** before the first venting event was constantly decreasing because of an increasing ambient temperature. Wenger et al. also presented a decreasing MOx resistance with increasing ambient temperature in [104]. Inside the reactor, the ambient temperature increased due to the heater elements on the sample holder (see [5] and [11]). The heater elements on the sample holder and the sample holder plate itself heats up over 200°C during overtemperature experiments. Consequently, the decreasing sensor signal might indicate degassing material that has deposited onto the sample holder and could not be removed even by thorough cleaning.

### 5.3.3.2 Overcharge TR test

As shown in [11], the venting behavior strongly depends on the used TR trigger and failure case as well as on the cell type and design of the cell opening (when the cell housing opens due to increasing pressure inside the cell). In overtemperature and overcharge experiments of state-of-the-art automotive LIBs with liquid electrolyte, two degassing stages with a first venting and a TR event afterwards were observed [11]. The first venting in overcharge experiments with 1 C of large automotive cells with state-of-the-art chemistry happened 0:45 - 5:00 minutes before the TR [11]. A representative overcharge experiment is presented in **Figure 45**. The gas sensor reacted with a resistance drop in pixel 1 and 2 immediately after the first venting event which was identified with a thermocouple positioned in front of the cell burst plate.

During this experiment, the first venting could not be detected with the pressure sensor inside the TR reactor. In this experiment the extreme ambient conditions starting at the TR (T, p) damaged the gas sensor irreversibly and the last measured signal dropped to 0.

In general, the time between first venting and the TR reduces with increasing overcharge current. Wenger et al. also showed a dependency of the time between first venting and TR on the overcharge current [104]. In addition to that, they conducted an overcharge experiment on a 5 Ah cell and found that a manual shutdown of the overcharge current after detecting the first venting event could prevent the TR reaction [104]. However, this might not be the case for all state-of-the-art battery cells, needs further investigation, but is not content of this study.

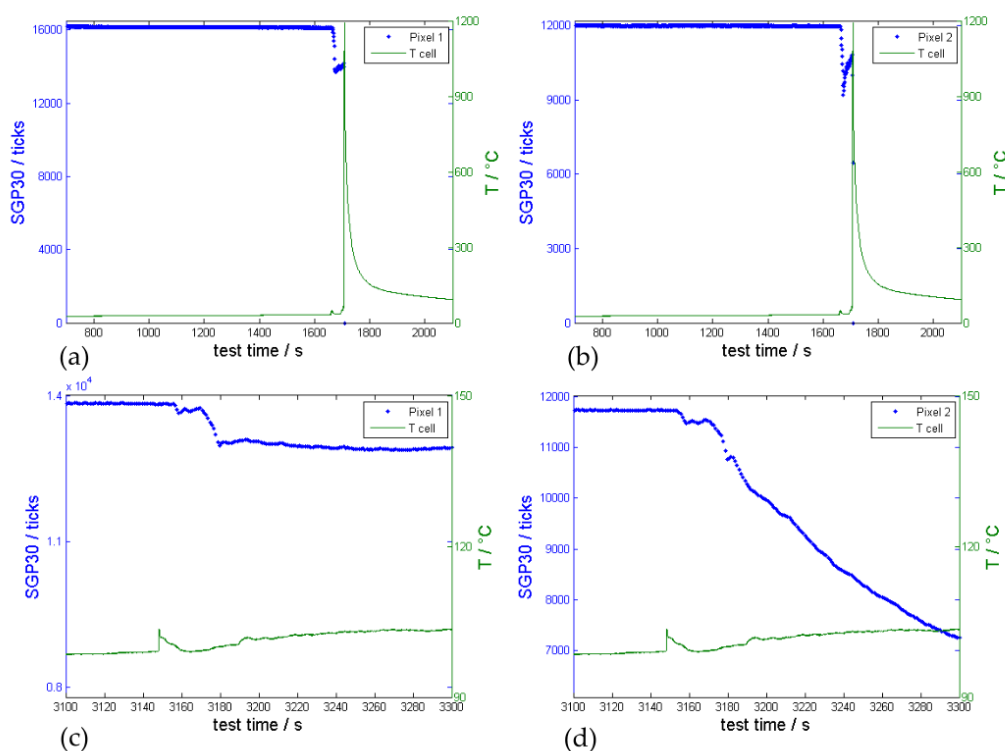


**Figure 45: Representative gas sensor SGP30 measurement (blue signal) during 1C overcharge triggered TR experiment of an automotive hard case cell (cell type #2) compared with measured vent gas temperature (green). The temperature sensor was mounted in front of the cell burst plate. (a) shows the resistance of sensor pixel 1 and (b) the resistance of sensor pixel 2. The first venting took place only 45 s before the TR. The TR destroyed the sensor functionality. (c) and (d) are detail plots to analyze the first venting event.**

### 5.3.3.3 Nail-penetration TR test

For nail-penetration trigger, the TR was overserved immediately after the nail had penetrated the cell [11]. **Figure 46** shows a nail-penetration experiment inside the TR reactor using the Sensirion SGP4x\_eng sensor with four MOx sensor pixels and the Sensirion SHT sensor for temperature and relative humidity measurements next to the MOx sensor.

In the nail-penetration experiments, the first venting and the TR took place at the same time. Here, the battery failure cannot be detected with gas sensors before the TR. But still, the benefit of using a gas sensor with 4 pixels can be also seen in **Figure 46** (a)-(d). The four pixels showed different responses because of slightly different selectivities to the produced TR gases. The gas sensor reacted with a significant signal drop for pixel 1, 3 and 4 in the same second as the temperature of the cell surface started to increase. Pixel 1 and 3 are optimized for VOCs, Pixel 2 is optimized for NO<sub>2</sub> and pixel 4 has an additional different selectivity to reducing gases as compared to the other pixels. Pixel 2 showed a short signal drop followed by an increasing resistance and a continuous drop afterwards. The humidity sensor also showed a response during the TR event (**Figure 46** (f)), while no response was observed during the first venting in overtemperature or overcharge tests.

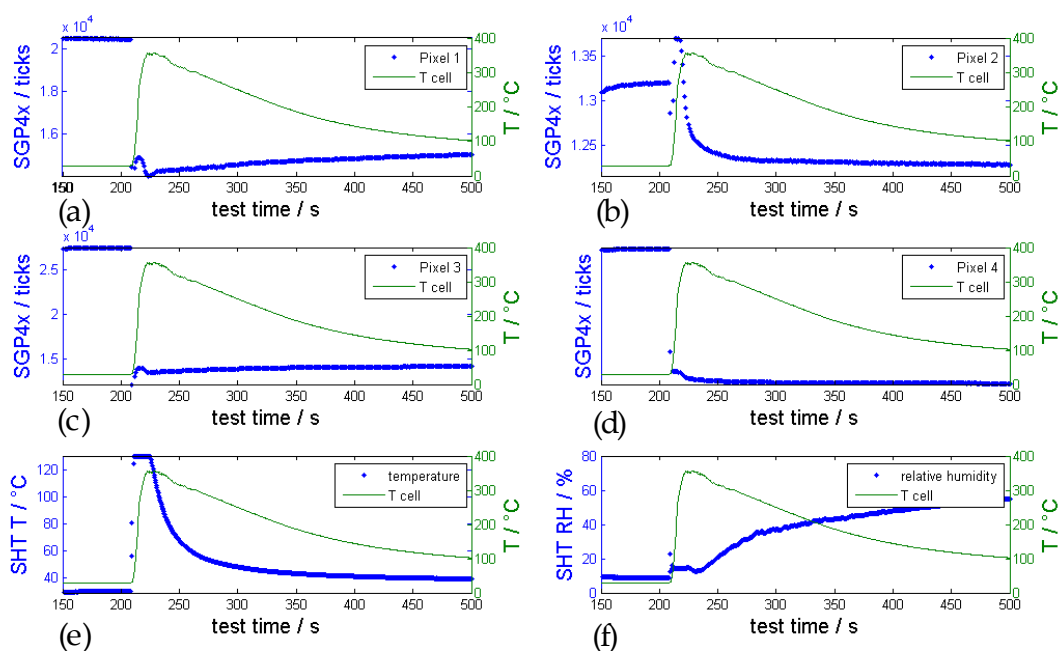


**Figure 46: Representative SGP4x eng gas sensor measurements (blue signals) during a nail-penetration triggered TR experiment using a type #4 cell compared with the measured temperature on the cell surface (green); (a) – (d) show the reaction of pixel 1 – 4 of the SGP4x eng MOx sensor to the evolved gases. (e) shows the temperature measured next to the sensor and (f) the relative humidity compared to the start of the experiment.**

In contrast to this results, in the nail-penetration setup of Koch et al. a first degassing of the cell before the TR could be measured [96]. Although using the same trigger method, the failing behavior is influenced by the investigated cells and the trigger parameter such as the properties of the nail. The presented nail trigger experiment in **Figure 46** fulfills the GB 38031-2020 description. The previous overtemperature and overcharge experiments show the ability of the gas sensors for detecting the first venting and the TR, but also suggests, that there is no guarantee of identifying vent gases several minutes before the TR. The reactivity of the gas sensor strongly depends on the appearance of the first venting, and this first venting highly depends on the used electrolyte components, the TR trigger, the cell type, and the design of the cell opening. This is in contrast to the publications of Liao et al. detecting the signal 7-8 minutes before the TR [18] or Hill et al. with 10 minutes before the TR [109]. What they observed in their experiments was the first venting and case opening of the cell several minutes before the TR, which generated a signal at the gas sensor.

Consequently, an early warning signal before TR using gas sensors can be expected at battery failures producing gases due to evaporation of electrolyte or decomposition of battery components resulting in a first venting and opening of the cell housing. But if the battery failures, such as intrusion of an object, lead to an abrupt short circuit resulting in an immediate TR, only gases from the TR itself can be measured. However, also detecting the TR at an early stage allows to initiate counteractions early. The observed MOx gas sensor signal drop, is the important parameter which can be used for further event detection. Furthermore, linear combinations of the response of the different sensor pixels enable to distinguish between different failure cases and might prevent false positives.

### 5.3.4 Additional failure cases

Additional to the mentioned battery failure cases, the gas sensors were also tested during the incomplete combustion of cable isolation materials (like polyvinyl carbonate, polyethylene and polyurethane). **Figure 47** shows the response of MiCS-6814 pixel for CO (pixel 1) and NO<sub>2</sub> (pixel 3) to one overheated cable starting at 200°C. At this temperature, no color change of the sample could be observed. The exact decomposition temperature of the cable isolation material and the associated outgassing amount depends strongly on the tested material. In the presented experiment in **Figure 47** a more temperature resistant cable was tested, others showed degassing reactions before 150°C. The response to the overheated insulation material is consistent with the publication of Seifert et al. [154]. They showed the response of MOx sensors to overheated PVC-based isolation materials.

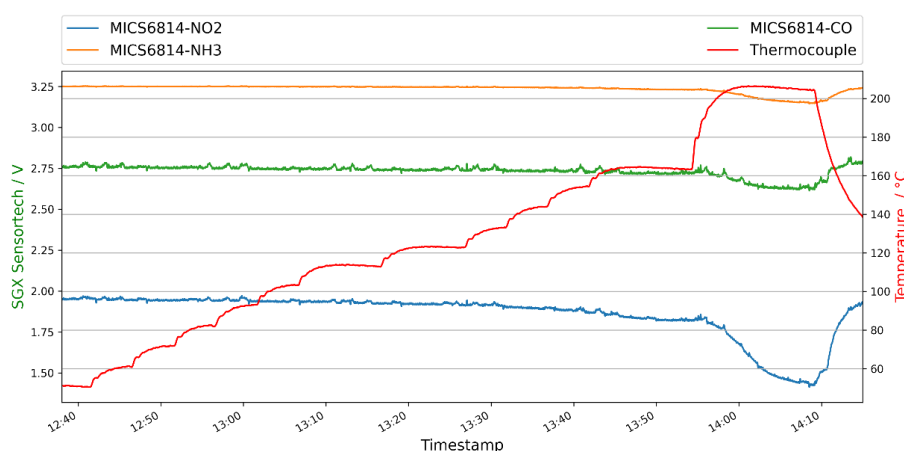


**Figure 47: MiCS-6814 MOx sensor response to one overheated cable isolation. The red curve (right y-axis) represents the temperature of the heating plate inside the sample chamber, on which the sample was positioned. The green (CO, pixel 1), orange (NH<sub>3</sub>, pixel 2) and blue (NO<sub>2</sub>, pixel 3) curve shows the behavior of the gas sensor pixels. In this experiment the heating was activated, and the temperature was stepwise increased in order to force degassing reaction of the sample.**

Furthermore, overtemperature of electric components was tested with the result that MOx sensors do also react to overheated electronic components. **Figure 48** shows the summary of detectable battery failure cases before TR with the usage of gas sensors. The four battery failure cases are summarized to two main target gases: H<sub>2</sub> and electrolyte vapor / VOCs. The detection of defective current conductors and overheated electronic components is added to the mentioned four battery failure cases, which can be reduced by concentrating on H<sub>2</sub> and electrolyte / VOC measurement.

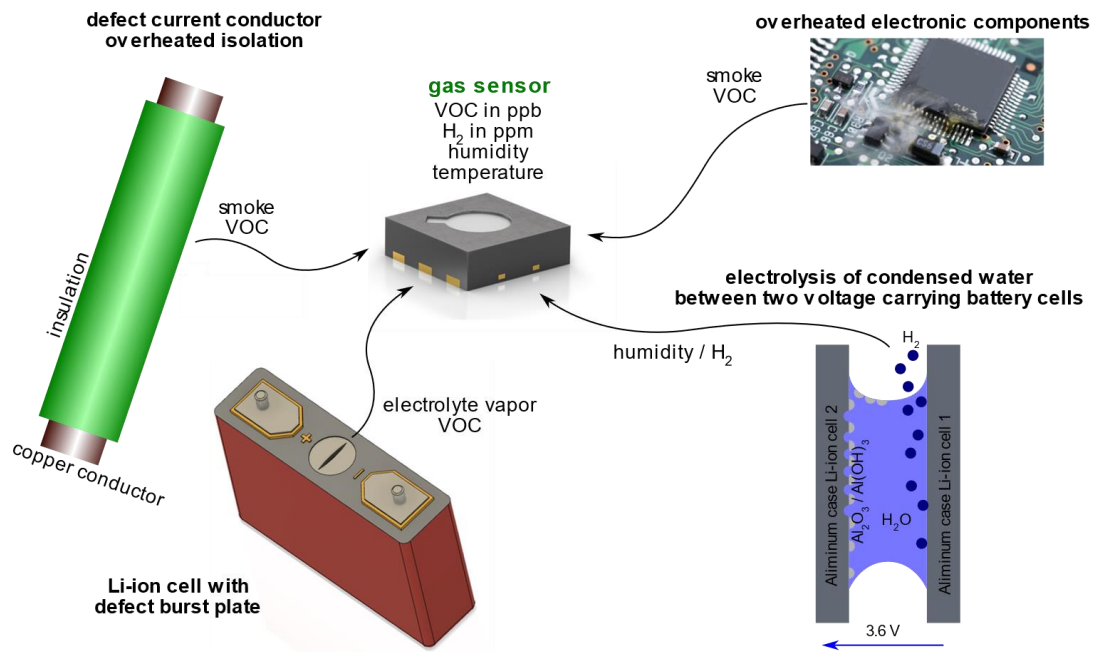


**Figure 48: Possible failure cases inside a battery pack, which can be detected by using (MOx) gas sensors.**

### 5.3.5 Event detector

**Figure 49** presents the low pass filtered SGP30 pixel 1 and pixel 2 sensor signal compared with the calculated BL according to equations (2) – (4) using values for MNG of -5 and MPG of +5. By varying these gradients, the baseline can be tuned to follow the low pass filtered values faster or slower. In order to detect a failure event fast, the derivative of the low pass filtered gas sensor signal can be used (ED1, see **Figure 49** second row). The difference of two neighboring low pass filtered values is significant for pixel 1 at the first venting (SNR = 105) and at the TR event (SNR = 551) in the presented representative overtemperature experiment. **Figure 49**, third row, presents the difference between the low pass filtered values and the calculated BL according to equation (4), which can be used as second event detector (ED2). By using ED2 even higher SNR values were reached in this experiment for pixel 1: for the first venting SNR = 1023 and for the TR event SNR = 9081.

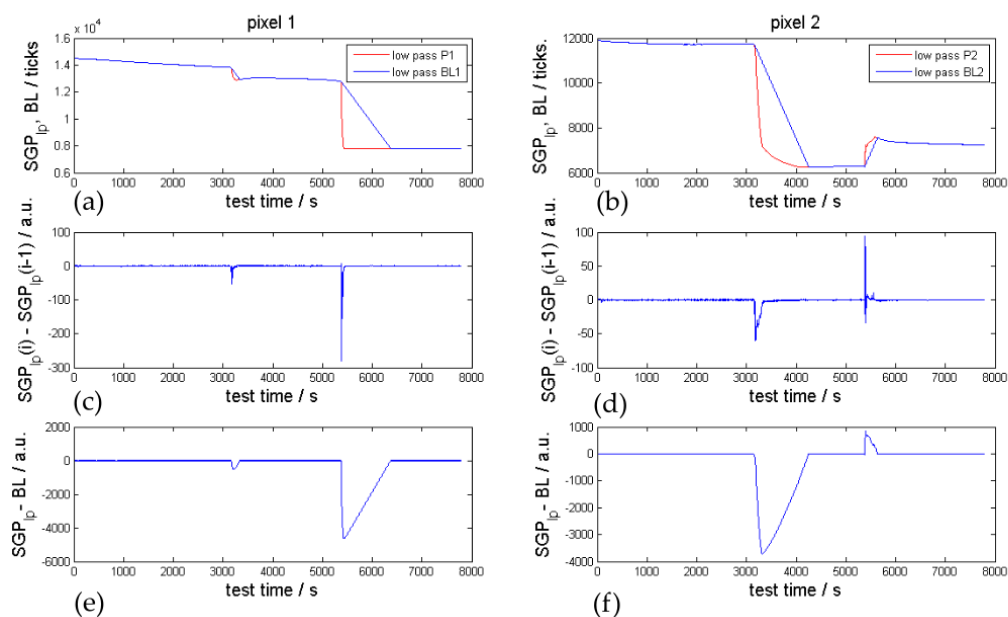


**Figure 49: SGP30 sensor signal analysis of the representative overtemperature TR experiment presented in Figure 44. (a) and (b): low pass filtered sensor signal (red) versus the calculated baseline (blue). (c) and (d): event detector 1 (ED1) derivative of the low pass filtered sensor signal for pixel 1 on the left and pixel 2 on the right-hand side. (e) and (f): event detector 2 (ED2) difference between low pass filtered sensor signal and the baseline.**

The first venting is detected by focusing on ED1 and ED2 with a SNR of  $> 5$  in all 21 overtemperature and overcharge TR experiments using the SGP30 inside the TR test bed. Measured SNR values for the first venting are presented in **Table 13**. The event detection with  $\text{SNR} > 5$  is valid for both readable Sensirion SGP30 pixels 1 and 2. In the most TR experiments the SNR value was even above 100. The ED2 can be tuned according to the failure cases and is proven to result in higher SNR for the first venting event, as can be seen in **Table 13**. Consequently, a possible alarm threshold for the Sensirion SGP30 or SGP4x\_eng sensors is at least a SNR of 5 for the presented event detectors.

**Table 13: Overview of the SGP30 signal-to-noise ratios (SNR) measured for the first venting event with event detector ED1 and ED2 in 21 different overtemperature and overcharge TR experiments on large automotive LIBs for pixels 1 and 2.**

Experiment NR.		1	2	3	4	5	6	7	8	9	10	11	12	13	14	15	16	17	18	19	20	21
ED1	Pixel 1	■	■	■	■	■	■	■	■	■	■	■	■	■	■	■	■	■	■	■	■	■
	Pixel 2	■	■	■	■	■	■	■	■	■	■	■	■	■	■	■	■	■	■	■	■	■
ED2	Pixel 1	■	■	■	■	■	■	■	■	■	■	■	■	■	■	■	■	■	■	■	■	■
	Pixel 2	■	■	■	■	■	■	■	■	■	■	■	■	■	■	■	■	■	■	■	■	■

SNR > 100 > 20 > 10 > 5

This simple event detection algorithm also works for the detection of  $\text{H}_2$  produced in electrolysis, and electrolyte leakage. If the harsh TR reaction takes place close to the sensor, the gas sensor might be damaged or enter an undefined state. The electrolysis fault is not a danger immediately after its occurrence but after certain time. The event detector algorithm works for the beginning of the electrolysis process but is not suitable thereafter due to the irregular  $\text{H}_2$  bubble formation and the resulting scattered signal. Nevertheless, this uncorrelated  $\text{H}_2$  signal can be used as identificatory for the electrolysis failure case. During the irregular and uncorrelated  $\text{H}_2$  production the standard

deviation of the low pass filtered gas sensor values increases clearly, which could be used as failure indicator.

In future work the difference between the raw values measured with the different sensor pixels need to be analysed and algorithms need to be developed to distinguish between the failure cases and prevent false positives.

## 5.4 Comparison of different sensor types

Important parameters for choosing the best suitable sensor for the detection of battery failure cases are detectability of the tracer gases, the sensor lifetime, and the cross sensitivity to interfering gases. The criteria of maximal allowed sensor size turned out to be not critical since all sensors were smaller than 35x23x7 mm<sup>3</sup> (dimensions of the largest sensor SCD30; although, the Figaro sensor including the module is 42x30x9.6 mm<sup>3</sup> in size). The tested MOx sensors are the most advanced in terms of miniaturization.

### 5.4.1 Detectability of tracer gases

The experiments show that classical monitoring systems inside the battery pack are capable of detecting a TR, because the voltage drops or the temperature sensor is close to the vent gas stream (as shown in **Figure 44**, **Figure 45**, and **Figure 46**). The detection of the first venting is possible, but very unlikely. The detectability of battery failure cases using the chosen and tested sensor principles is presented in **Table 14**.

**Table 14: Detectability of listed battery failure cases with different tested sensors and sensor principles.**

principle	example	electrolysis	electrolyte	1 <sup>st</sup> venting	TR	
MOx	SGP30	detectable	detectable	detectable	detectable	
electrochemical	TGS 5141	detectable	not detectable	not detectable	detectable	
NDIR (CO <sub>2</sub> )	MH-Z16	not detectable	not detectable	detectable	detectable	
hygrometer	SHT31	not detectable	not detectable	not detectable	detectable	detectable
FTIR	Bruker	not detectable	detectable	detectable	detectable	unlikely detectable
GC	Agilent	detectable	detectable	detectable	detectable	not detectable
voltage		not detectable	not detectable	not detectable	detectable	
current		not detectable	not detectable	not detectable	detectable	
temperature		not detectable	not detectable	unlikely detectable	detectable	

Voltage measurements will not show an immediate drop during the electrolysis failure case or a leakage of the cell housing. These failures can only be detected due to degradation of the cell performance. The current measurement cannot detect the opening of the cell housing or the electrolysis. Assuming that the temperature measurements inside the battery pack are ideally chosen and adjusted very close to the error source, then the first venting might be detected. Additionally, our experiments have shown that an ambient pressure sensor inside the TR reactor (120 l free volume)

can measure the pressure increase during the TR event itself but might have difficulties detecting battery failures before the TR, such as the decent first venting of a failing cell. We have shown in [11] that the amount of gas evolving at the first degassing and opening of the cell highly depends on the used cell type and the venting design of this cell. Consequently, using an ambient pressure sensor inside the battery pack does guarantee to measure the TR event, but not battery failure stages before. Adding gas sensors to the existing monitoring can significantly contribute to failure detection at an early stage. This study proves that a multi sensor reactive detection method consisting of temperature sensors combined with pressure sensors, voltage sensors and gas sensors can detect all failure cases a)–d) plus additional failure cases such as overheated cables or electronic components.

Concluding, the investigated battery failure cases can be detected with the following measurement systems:

How can we detect electrolysis inside the battery pack?

- Gas measurement – Focus on H<sub>2</sub>.

How can we detect electrolyte vaporization?

- Vent gas measurement – Focus on VOCs, such as the vaporizing electrolyte.

How can we detect the first venting event?

- Temperature measurement close to the burst opening.
- Vent gas measurement – Focus on VOCs, such as the vaporizing electrolyte; CO<sub>2</sub> is also possible but might fail in certain cases.
- Expansion of the cell before the first venting, and reduced force after the first venting.
- Measurement of the pressure inside the module (gas pressure) works for specific cell types.

How can we detect the second venting event, the TR?

- Temperature measurement; cell surface, near the cell vent, inside the module.
- Measurement of cell voltage.
- Measurement of the pressure inside the module (gas pressure).
- Vent gas measurement – Focus on CO<sub>2</sub>, CO, H<sub>2</sub>, VOCs.

### 5.4.2 Lifetime of the sensors

NDIR sensors have the longest lifetime of the tested sensors (Sensirion SCD30 15 years [155]). Typical lifetimes for electrochemical sensors are ranging below three years. In datasheets of MOx sensors the lifetime is usually not specified. For the new sensor product SGP40 (MOx), a lifetime of more than 10 years is stated [151]. Of course, the lifetimes of electrochemical sensors and MOx sensors highly depend on the ambient conditions of the sensors, such as temperature, humidity and pressure. No conclusions can be drawn from our experiments about long-term drift behavior and product lifetime.

### 5.4.3 Cross sensitivity

The cross sensitivity to interfering gases depends on the sensor principle. Electrochemical sensors show the highest selectivity to target gases and they have less cross-sensitivities. Infrared sensors can also be very selective, but sensitivity highly depends on the target gas and the chosen wavelength of the sensor. For instance, electrolyte components (EC, DEC, DMC, EMC) absorb light at similar

wavelengths. By choosing specific wavelength regions it is possible to distinguish between the single components. The sensitive MO<sub>x</sub> layer detects a broad range of VOCs [104] and consequently shows cross sensitivities to interfering gases. In the experiments the MO<sub>x</sub> sensor reacted to gasoline, ethanol, isopropanol and acetone, CO, H<sub>2</sub> and CH<sub>4</sub>. Chemical modifications (material doping), variation in hot plate temperature and multi-pixel evaluation allows to improve the selectivity. Moreover, Gröbel et al. reported on using neural networks for improving selectivity [156]. Illyaskutty et al. promote the use of a multi sensor array with different layers of tin oxide/additive combinations in order to identify specific gases [157].

#### 5.4.4 Most promising sensors for battery failure applications

As Koch et al. [96] and Liao et al. [18] stated in their publications, a sensor combination consisting of voltage, current, temperature and gas sensors leads to an improvement of battery safety. Concerning the gas sensors, the experiments show that out of the currently available and tested sensors, MO<sub>x</sub> sensors are the most promising sensor types for the detection of battery failures before the TR. This conclusion is based on the requirements listed in section 2.1.3 and applies in comparison to the tested electrochemical, NDIR sensors and hygrometer, as MO<sub>x</sub> sensors react to all investigated battery failure cases, have the highest sensitivity and a quicker sensor response as compared to electrochemical and IR sensors (Figure 41). The tested electrochemical and infrared sensors are more selective to target gases such as CO, CO<sub>2</sub> and H<sub>2</sub> (i.e., have less cross-sensitivities) but they could not cover all tested battery failures and are currently more expensive than MO<sub>x</sub> sensors.

In order to distinguish between real battery failures and false positives and to improve selectivity, multi-pixel MO<sub>x</sub> sensors are preferred. One drawback of the MO<sub>x</sub> sensor technology is its susceptibility to siloxane poisoning of the sensing material, which leads to a loss of sensitivity and response time [152]. Schultealbert et al. found that siloxanes change the sensor behavior differently for different gases. They showed a reduced sensitivity for acetone and carbon monoxide, while the sensitivity for hydrogen was only slightly reduced.

Based on the results of the sensors tested in here, the following suggestions for cost-efficient gas sensors used in addition to voltage, current, and temperature sensors for early detection of battery failures are MO<sub>x</sub> sensors with several readable pixels in order to distinguish between failure cases as for instance Sensirion SGP30 (2 pixels readable), SGX Sensortech MiCS-6814 (3 pixel readable) and Sensirion SGP4x\_eng (4 pixels readable). All three suggested sensors are miniaturized metal-oxide semiconductor sensors. The Sensirion SGP30, SGP4x\_eng and the SGX Sensortech MiCS-6814 proved to be very stable and highly sensitive to the target gases. Figaro TGS 8100 would also be an option but has only one readable pixel. The Sensirion SGP30 and SGP4x\_eng sensor are - among the tested sensors - the only digital sensors, which translates to smaller packaging, since the analog to digital conversion is done on the chip. There is also a further feature of the SGP30 and SGP4x\_eng such as siloxane resistance [158] (that increases the stability and lifetime of the sensor).

This conclusion is true for currently available and tested sensors but it should not rule out any future measurement technology that meets the requirements listed in section 2.1.3 and may be even more selective for battery vent gases.

## 6 Summary and conclusion

Serious failing incidents of batteries are known to be hazardous and lead to safety concerns. Open literature on early stages of LIB failure cases, TR influencing factors and early battery failure detection is rare. Consequently, a detailed investigation of the failing behavior of modern high capacity and high energy density LIBs, studying different failing influence factors as well as examining concepts for early failure detection was necessary. This chapter is structured according to the research topics.

### a. Comprehensive hazard analysis and influence of SOC

A comprehensive hazard analysis of modern automotive high capacity NMC/LMO—graphite pouch cells was performed at three overtemperature TR experiments. Safety relevant hazards are electrolyte vaporization, heat generation, gas emission including gas rate, gas composition including electrolyte and particle emission including size and content of the particles. The results confirm the influence of the SOC on the failing behavior of the LIB. The fully charged cell was triggered into TR, but the cells with  $\text{SOC} \leq 30\%$  could not be triggered into TR.

Main findings of the investigated automotive cells are:

- The first venting happened at 120–130°C cell surface temperature independent of the SOC.

For the 30% and 0% SOC cell:

- The main gas components after the first venting and constant gas production until the heating was stopped in descending order were  $\text{CO}_2$ , DEC,  $\text{H}_2\text{O}$ , CO,  $\text{H}_2$ ,  $\text{C}_2\text{H}_4$ ,  $\text{CH}_4$ ,  $\text{C}_3\text{H}_8$ .
- One presented hazard was electrolyte vaporization. Commonly used electrolyte components, such as EC, DEC, DMC, EMC in an unsealed cell, are critical due to the consequential irritant, toxic, cancerogenic and flammable atmosphere. In this cell type EC (irritant, PAC-1: 30  $\text{mg}/\text{m}^3$ ) and DEC (flammable, PAC-1: 2  $\text{mg}/\text{m}^3$ ) were the main electrolyte components. It is important to address this hazard especially in large traction battery EV applications, where significant amounts of electrolyte may vaporize inside a closed system (pack, garage, tunnel).

For the fully charged (100% SOC) pouch cell two venting stages were observed: A first venting and a second venting (TR). The second venting started above an average cell temperature of 212°C. The TR had the following hazards and consequences, which ended up as safety and health risks:

- Enormous heat was generated by the cell; the cell surface temperatures increased above 700°C. The main exothermic reaction developed to a rapid TR when the hottest measured part of the cell reached 231°C. Within 4.28 s the TR propagated through the cell. This high surface temperature can lead to TR propagation to neighboring cells and irreversible damage of the battery pack.
- Overall, 2.31 mol (57 L, 1.3 L/Ah, 0.06 mol/Ah) of gas was produced. The cell released 0.14 mol before the TR and additional 2.17 mol during the TR with a characteristic rate of 0.8 mol/s (18.7 L/s). 50% of the gas was produced in 1.4 s. The abrupt pressure increase at the TR is a serious risk inside a closed compartment.
- The cell mass reduced by 43% of the initial mass. This mass reduction can be explained as the sum of released gas and ejected particles at TR.
- The main gas components were: 38%  $\text{CO}_2$ , 23%  $\text{H}_2$ , 17% CO, 8%  $\text{H}_2\text{O}$ , 6%  $\text{C}_2\text{H}_4$ , 4%  $\text{CH}_4$  and 3% electrolyte vapor (DEC). The measured gas components were about 20% of the lost cell mass

during TR and 9% of the initial cell mass. Toxic (CO) and flammable (H<sub>2</sub>, CH<sub>4</sub>, DEC, etc.) gas components are dangerous when entering the passenger compartment.

- A large number of ejected particles were smaller than 10 μm<sup>2</sup>. Novel nondestructive sampling and analysis methods were used to evaluate the particle parameters: The smallest analyzed particles had an area of 0.1 μm<sup>2</sup>, thus a circle equivalent diameter of roughly 6 nm. A total of twelve elements were detected in the particles, including elements like Al, Ni or F. These ejected hot particles (~35% of the initial cell mass) may ignite the vent gas, are carcinogenic and respirable for humans.
- Although the new high-end FTIR spectrometer is suitable for HF measurement (>4 ppm), no HF could be detected for all investigated cell types. HF is expected to be released by the cell in small amounts but the highly reactive HF reacted with materials inside the test reactor, the analysis pipes and the ejected particles. Additionally, it is assumed that modern mass produced EV cells produce less HF than older cells.

To reach an acceptable level of safety in EVs a comprehensive analysis of hazards is very important. In order to define testing standards, the battery hazard influencing factors (such as energy content of the cell, chemistry, the failure case/trigger, cell design, SOC and SOH) must be characterized. The five presented hazards addressed in this study should also be considered for different cell types. We recommend including in the quantification of safety relevant parameters such as the maximum reached cell surface temperature, the amount of produced vent gas, the venting rate, the composition of the produced gases at the first venting and the TR including electrolyte vapor to cover the most significant hazards from battery failures. To improve safety at LIB applications it is important to be aware of potential safety and health risks originated from failing cells.

## b. Influence of thermal runaway trigger and cell type

The results show the influence of three different TR trigger (overtemperature, overcharge and nail-penetration) and two different cell design (pouch and prismatic hard case) on the failing behavior and safety relevant parameters. The TR results were compared in three main categories: thermal behavior, vent gas production and vent gas composition. The high impact of overcharge experiments on the amount of produced vent gas and the increased toxicity of the gas components was presented.

Comparison of the chosen trigger:

- The overcharge triggered TR was more intense than overtemperature and nail-penetration on both cell types and resulted in a higher amount of vent gas, a higher cell mass loss and the gas components shifted towards higher volume percent of flammable, explosive and toxic gas compounds such as H<sub>2</sub> and CO.
- In all three TR triggers for both cell geometries  $T_{cell}^{max}$  and  $T_{vent}^{max}$  were above 718°C and reached similar values. The lowest  $T_{cell}^{max}$  values were measured for the overcharged hard case cells, where the jelly roll was found outside the hard case after the experiments.
- The vent gas emission in general depends on the used trigger. Both cell types produced up to 2.8 L/Ah vent gas using the overcharge trigger, up to 1.6 L/Ah using the overtemperature trigger, and up to 1.7 L/Ah using nail-penetration. The venting rates  $\dot{n}_{ch}$  were for overtemperature TR lower than for overcharge or nail-penetration trigger. For cell type #1, the duration of the venting during TR was the shortest in nail-penetration and the longest in overcharge. For the hard case cell (#2), in contrast to the pouch cell, the duration of the venting

during TR was the fastest in overcharge and the longest in nail-penetration of all twelve experiments. Therefore, the venting rates depend on the TR trigger and on the cell type.

- The vent gas composition is also influenced by the trigger used. Variations were observed especially for CO, CO<sub>2</sub>, H<sub>2</sub>, C<sub>2</sub>H<sub>4</sub>, CH<sub>4</sub>, and electrolyte concentrations. For each cell type, the highest H<sub>2</sub> and CO values were measured in the overcharge failure case and the least H<sub>2</sub> values in the overtemperature trigger. Nail-penetration trigger forced both cell types to produce higher C<sub>2</sub>H<sub>4</sub> and CO<sub>2</sub> vol.% values and lower CH<sub>4</sub> vol.% values than for the other two triggers.

The two tested EV cell types showed differences in:

- Thermal behavior: The pouch cell bag opened in overtemperature trigger earlier at a lower surface temperature than the hard case cell. The second venting of cell type #1 happened at a higher average temperature than for cell type #2 in overtemperature trigger.  $T_{vent}^{max}$  for cell type #2, the hard case cell, reached at all three trigger types higher maximum values than the pouch cell.
- Vent gas emission: The different housing and cell design resulted in different total duration of the pressure increase during the TR in overtemperature and overcharged TR. The duration of the TR of cell type #1 was longer than for cell type #2, except for the nail-penetration test. For cell type #2 the venting time for 50% of the vent gas was lower than for cell type #1, what results in higher characteristic venting rates and possibly higher pressure peaks during the TR itself.
- Vent gas composition: The main gas compounds produced during the TR were the same and also in similar magnitude, but the exact gas composition varied with different electrolyte composition. Major variations in gas concentration from both cell types were observed in C<sub>2</sub>H<sub>4</sub>, CO, CO<sub>2</sub> and DMC values. Only minor changes were measured in H<sub>2</sub> and CH<sub>4</sub> values. Cell type #1 produced significant higher C<sub>2</sub>H<sub>4</sub> concentrations at all three triggers, which can be explained by the higher amount of EC used in cell type #1 and also CO<sub>2</sub> values were higher than for cell type #2.

The packaging of active material layers seems to influence the reaction time of the TR, and consequently safety relevant parameters such as the characteristic venting rate and maximum pressures reached inside a sealed volume. The reproducibility of the experiments was shown and confirmed with low standard deviations of the quantification of safety relevant parameters.

### **c. Influence of aging**

Automotive large LIBs were tested in overtemperature triggered TR experiments after three different aging paths (cyclic aging at -10°C (cy-10) and at 45°C (cy+45) and calendric aging at 60°C (ca60)) and compared with the results of fresh cells in three main categories: thermal behavior, the vent gas emission and vent gas composition.

The cyclic aged cells at 45°C showed the highest capacity fade and the calendric aged cells at 60°C exhibited the lowest capacity fade. All tested aged cells showed a reduced failing reaction compared to fresh cells. The expectation of a stronger reaction of the failing aged (cy-10°C) cell due to Li plating has not been confirmed. Because of the rest time after the Li plating, the plated Li might have intercalated or chemically reacted which had positive effects on the safety behavior of the cell during TR. In this study, using aged cells in overtemperature TR experiments ended up in reduced maximum

temperatures, lower amount of produced gas, significantly lower amount of CO in the vent gas and lower mass loss than in the same experiments using fresh cells.

For each cell a first venting before the TR was observed. The results showed that there were no significant changes for the first venting temperature,  $\bar{T}_{cell}^{v1}$ , between fresh cells to aged cells but a significant higher average temperature for the second venting,  $\bar{T}_{cell}^{v2}$ , for cyclic aged cells at 45°C, which means an increase in thermal stability. A decrease of thermal stability was observed for cells cycled at -10°C, because the second venting  $\bar{T}_{cell}^{v2}$  started at a lower temperature ( $\Delta T = -14^\circ\text{C}$ ). A clear reduction of the maximum measured temperature on the cell surface  $T_{cell}^{max}$  was observed for all aged cells.

The aged cells produced significant lower total amounts of gas than the fresh cells. Only a small amount of gas was produced after the first venting and the main amount of gas was produced during the TR reaction. A linear correlation between the total amount of produced vent gas and the current capacity of each cell before the TR experiment was observed and reported as a new finding. 0.06 mol/Ah vent gas in overtemperature TR triggered cells could be a possible relation in general for NMC (622)-graphite chemistry cells with liquid electrolyte mixture (EC, EMC, DMC, DEC).

After the first venting, the main vent gas components were independent of the different aging paths (electrolyte vapor (EMC), CO<sub>2</sub>, H<sub>2</sub>O), but the exact vent gas composition differs between the different aging paths. Different decomposition reactions of the used cell material were observed, such as the trans-esterification reaction of EMC into DEC and DMC during cyclic aging at -10°C. The main gas compounds produced during the TR (CO<sub>2</sub>, CO, H<sub>2</sub>) and higher hydrocarbons were independent of the aging path, but correlations to the aging were visible. The total amount of CO in the vent gas decreases with decreasing capacity. Also, the amount of CO<sub>2</sub>, H<sub>2</sub>, C<sub>2</sub>H<sub>4</sub> and CH<sub>4</sub> were reduced for failing aged cells compared to fresh cells.

Aging of LIBs and the aging paths have a significant effect on the failing behavior of LIBs during TR, and consequently on the safety relevant parameters such as gas emission, maximum reached cell surface temperatures and vent gas composition. A general rule might be that a less violent TR behavior is observed for aged cells with power and capacity fade in comparison to fresh cells, if no fresh metallic Li plating is produced. If fresh metallic Li plating is produced inside the cell, a stronger TR reaction is expected. If we exclude the case of Li plating, the experiments with fresh cells represent the worst case of TR reaction. Consequently, we recommend the use of fresh cells for the determination of safety-relevant parameters for the design of battery applications.

#### **d. Early failure detection of battery failures using gas sensors**

The produced gases in the four investigated failure cases (unwanted electrolysis of voltage carrying parts, electrolyte vapor, first venting of the cell and the TR) were studied in detail and it was discovered that H<sub>2</sub> and especially VOC gases (electrolyte vapor) are produced at battery failures before the TR. In electrolysis experiments up to 0.013 mol H<sub>2</sub> per hour were measured using water as electrolyte, metallic hard case can electrodes and 48 V. In the failure case of damaged cell housings and the first venting of failing cells especially electrolyte components (theoretically up to 1.4 mol for a 60 Ah cell) were measured. The main gas components of failing fully charged cells are, in descending order, after the first venting electrolyte vapor, H<sub>2</sub>O, CO<sub>2</sub>, CO, H<sub>2</sub> and depending on the used electrolyte decomposition products such as C<sub>2</sub>H<sub>6</sub>, C<sub>2</sub>H<sub>4</sub>, C<sub>4</sub>H<sub>10</sub> and C<sub>3</sub>H<sub>6</sub>. In a few gas composition measurements after the first venting no CO or CO<sub>2</sub> gas was identified, consequently a CO<sub>2</sub> or CO gas sensor could not detect all first ventings. Since the electrolyte of currently used LIBs consists of a varying mixture of

DMC, DEC, EMC and EC or PC, which are released after the opening of the cell housing, the electrolyte vapor is an attractive tracer gas for failure detection before the TR. During the TR the main amount of vent gas is produced consisting mainly of CO, CO<sub>2</sub>, H<sub>2</sub> and higher hydrocarbons.

This contribution shows that it is possible to detect battery failures involving gas emissions at an early stage fast and cost efficiently with gas sensors. In total 16 sensors for the potential application as battery failure detectors in series products were chosen, implemented on a sensor platform, and benchmarked. Different sensor principles (MOx, NDIR, electrochemical sensors, thermometer and hygrometer) and sensors from different manufacturers were compared. Currently MOx sensors turned out to be the most promising technology for early battery failure detection, as they show a significant reaction to all the mentioned battery failures within seconds, have a high sensitivity, are cheap and some can be easily connected with I<sup>2</sup>C to the BMS. Although the electrochemical and the NDIR (CO<sub>2</sub>) sensors are more selective than the MOx sensors, currently they are not recommended, because they are not able to detect all the introduced battery failures. Especially the MOx sensors Sensirion SGP30, the newer version of it the SGP4x\_eng and the MiCS-6814 fulfil defined requirements because of the high sensitivity to H<sub>2</sub> and electrolyte vapor and they use a multi-pixel sensor array for improving selectivity and enable the prevention of false positives. Under the assumption that the price range of MOx sensors at volumes reaching a few million pieces per year will be between 1 and 2 euros one can estimate an additional cost of less than 10-20 € for placing up to 10 sensors inside one battery pack. Among the investigated sensors in this study the MOx-technology is the most cost efficient one.

MOx gas sensors were tested inside a TR test bed using more than 30 state-of-the-art automotive LIBs in three different TR trigger. The results illustrate that the detection of the first venting event before the TR is possible with gas sensors in overtemperature and overcharge experiments. In nail-penetration experiments, the first venting took place at the same time as the TR. Consequently, in the nail-penetration failure case, only the TR can be detected. Two event detectors were suggested, which could detect each first venting event in 21 overtemperature and overcharge experiments, electrolysis and evolving electrolyte vapor of different state-of-the-art automotive LIBs with a SNR >>5.

To fulfil the new regulations GB 38031-2020 and EVS-GTR and warn the passengers at least five minutes before serious incidents, gas sensors may significantly contribute to failure detection and improvement of battery safety. The sensor combination allows for error allocation and potentially prevents false positives. With this combination of gas sensors, battery failures are detectable earlier than using only the current state-of-the-art monitoring systems. The high sensitivity of the proposed gas sensor enables to warn at certain gas concentrations inside the battery pack, before exposure, flammability or explosion limits are reached. The use of gas sensors for the detection of gases produced at battery failures is recommended for battery pack applications, but also for battery storage and transport.

## 7 Outlook

The current trend in automotive industry is to increase the range of the EVs and consequently to further increase energy (capacity and energy density) of the single cells. The most attractive cell chemistry is still NMC, but also NCA and LFP chemistries are gaining importance.

For NMC chemistries, increasing the Ni content (NMC 811 instead of NMC 622 or NMC 111) leads to a higher energy density. But increasing the content of Ni in the cathode material also requires structural changes and affects the release of oxygen during overtemperature [159] and consequently influences the failing behavior. With increasing energy density higher maximum cell surface temperatures, higher amount of produced non-condensed gas and a shift of gas composition towards higher amount of toxic CO [160] are expected.

Based on the results and the quantified hazards, further increasing the energy per cell (capacity and energy density) will lead to an increasing demand in safety measures, TR prevention and TR propagation prevention techniques. A future perspective for the use of NMC cells in EV battery packs might be the use of LIBs with a manageable capacity per cell and improve prevention of TR propagation. Methods for controlling the mitigation of TR of neighboring cells should be focused in future research like materials stopping abrasive gas and particle flow and thermal propagation.

After analyzing the criteria for a gas sensor, low-cost, compact, multi-pixel gas sensors need to be specifically developed and integrated into the battery applications. For current MO<sub>x</sub> gas sensors an automotive certification and secure algorithms against false positives are aspired.

Additionally, fast charging of the battery has also become an issue, which challenges the thermal management for the cells. Intelligent cooling and conditioning strategies are necessary and will become even more important in order to prevent Li plating and reduce aging effects. These trends need to be considered for the development and integration of early detection systems for series EVs.

Since the cell chemistry influences the failing behavior, for different future cell chemistries (advanced LIBs up to 5 V, all-solid-state LIBs, Li-sulfur and Li-air cells) a detailed analysis of the failing behavior and the effect of influencing factors is needed. In future investigations, cells with fresh metallic Li should be investigated immediately after the aging experiment inside the TR test rig in order to quantify the influence of fresh Li plating on the failing behavior. Furthermore, it will be interesting to identify the influence of the heat ramp in overtemperature trigger and further distinguish between the higher hydrocarbons in the vent gas. A detailed analysis of the vent gas producing reactions would be relevant to further improve the understanding of the different failing behaviors and influencing factors. In our upcoming work we aim to develop functional polymers, which release tracer gases before the first venting of the cell. These tracer gases can be measured with the presented gas sensors to further improve battery safety.

## 8 Publications

### 8.1 Journal publications

- Essl C, Golubkov AW, Fuchs A. Influence of aging on the failing behavior of automotive lithium-ion batteries. *Batteries* 2021 (accepted March 2021).
- Essl C, Seifert L, Rabe M, Fuchs A. Early detection of failing automotive batteries using gas sensors. *Batteries* 2021 (accepted March 2021).
- Essl C, Golubkov AW, Fuchs A. Comparing Different Thermal Runaway Triggers for Two Automotive Lithium-Ion Battery Cell Types. *Journal of The Electrochemical Society* 2020; 167: 130542. DOI: 10.1149/1945-7111/abbe5a.
- Essl C, Golubkov AW, Thaler A, Fuchs A. Comparing Different Thermal Runaway Triggers for Automotive Lithium-Ion Batteries. *ECS Transaction* 2020; 237th ECS Meeting: A02-0436.
- Essl C, Golubkov AW, Gasser E, Nachtnebel M, Zankel A, Ewert E, Fuchs A. Comprehensive hazard analysis of failing automotive Lithium-ion batteries in overtemperature experiments. *Batteries* 2020; 6(30): 1–28. DOI: 10.3390/batteries6020030.
- Essl C, Golubkov AW, Planteu R, Rasch B, Thaler A, Fuchs A. Transport of Li-Ion Batteries: Early Failure Detection by Gas Composition Measurements. *7th Transport Research Arena, Vienna, Austria*: 2018. DOI: 10.5281/zenodo.1491360.
- Golubkov AW, Planteu R, Rasch B, Essl C, Thaler A, Hacker V. Thermal runaway and battery fire: comparison of Li-ion, Ni-MH and sealed lead-acid batteries. *7th Transport Research Arena, Vienna, Austria*: 2018. DOI: 10.5281/zenodo.1491317.

### 8.2 Scientific presentations

- Essl C (04,2021), Advanced Battery Power 2021, online: “First and second degassing of automotive lithium-ion batteries at overtemperature experiments”, talk planned as of February 2021.
- Essl C (03,2021), International Battery Seminar and Exhibit 2021, online: “Influence of Different Thermal Runaway Trigger on the Failing Behavior of Automotive Lithium-Ion Batteries”, invited talk.
- Essl C (03,2019), International Battery Seminar and Exhibit 2019, Fort Lauderdale, Florida: “Risk estimation of failing automotive Li-ion batteries”, poster and talk.

- Essl C (09,2018), Graz Battery Days 2018, Graz, Austria: “Influence of Cost Reduction and Increasing Energy Density on Thermal Runaway Gas Emission of Li-Ion Batteries”, poster.
- Essl C (04,2018), Advanced Battery Power 2018, Münster, Germany: “Li-Ion Battery Failures: HF Concentration Measurement”, talk.
- Essl C (04,2018), Transport Research Arena 2018, Vienna, Austria: “Transport of Li-Ion Batteries: Early Failure Detection by Gas Composition Measurements”, poster and paper.
- Essl C (04,2017), Advanced Battery Power 2017, Aachen, Germany: “Experiments to measure the gas ejection rate of large Li-ion batteries during thermal-runaway”, talk.

## 9 Appendix

### 9.1 Supplementary material vent gas analysis

#### 9.1.1 FTIR spectrometer settings

The concentration of the gas components has an effect on the spectrum and absorbance peak height in FTIR spectrometer measurements. Therefore, the chosen analysis wavenumber-range for quantification has a huge impact on the calculated concentration. In order to evaluate different concentrations ranges, different wavenumber-ranges can be chosen for each gas component.

In this supplementary material the best wavenumber region for battery vent gas analysis for each gas component is documented in **Table S1**. In the chosen wavenumber-range the measurement is compared with a reference spectrum with a specific algorithm provided by Bruker GmbH in the software OPUS GA. No test gas is necessary for the quantification of each measured gas component  $C_m$ .

**Table S1: FTIR setting for the quantification of battery vent gases: wavenumber-range for quantification of gas components, possible interference with other gases in the chosen wavenumber-range and the detection limit.**

gas	start $\nu$ / $\text{cm}^{-1}$	end $\nu$ / $\text{cm}^{-1}$	interference	limit
$\text{C}_2\text{H}_2$	3304.9	3337.1	$\text{H}_2\text{O}$	0.8
$\text{C}_2\text{H}_2_{\text{update}}$	770	820	$\text{H}_2\text{O}$	0.8
$\text{C}_2\text{H}_4$	876.1	917.0	DMC, $\text{C}_4\text{H}_{10}$ , $\text{C}_6\text{H}_{14}$	0.7
$\text{C}_2\text{H}_6$	2982.0	3003.1	$\text{CH}_4$ , $\text{C}_2\text{H}_2$ , $\text{C}_4\text{H}_{10}$ , DMC, $\text{C}_6\text{H}_{14}$	0.5
$\text{CH}_4$	3139	3200.2	$\text{C}_2\text{H}_4$ , $\text{C}_2\text{H}_2$	0.8
$\text{CH}_4_{\text{update}}$	1190.0	1270.0	$\text{C}_2\text{H}_4$ , $\text{C}_2\text{H}_2$	0.8
$\text{CO}$	2021.0	2072.1	$\text{H}_2\text{O}$ , $\text{CO}_2$	0.6
$\text{CO}_2$	2242.7	2280.1	$\text{CO}$ , $\text{H}_2\text{O}$	0.8
$\text{CO}_2_{\text{high}}$	2242.0	2280.1	$\text{CO}$ , $\text{H}_2\text{O}$	0.8
$\text{CO}_{\text{high}}$	2020.0	2071.1	$\text{H}_2\text{O}$ , $\text{CO}_2$	0.8
DEC	1005.0	1065.0	EMC, DMC, $\text{C}_6\text{H}_{14}$ , $\text{C}_2\text{H}_4$ , EC, $\text{C}_4\text{H}_{10}$	0.8
DMC	955.0	1020.1	$\text{C}_2\text{H}_4$ , $\text{C}_4\text{H}_{10}$	0.8
EC	1825.0	1900.0	EMC, DMC, $\text{H}_2\text{O}$	0.8
EMC	1002.0	1065.0	DEC, DMC, $\text{C}_6\text{H}_{14}$ , $\text{C}_2\text{H}_4$ , EC, $\text{C}_4\text{H}_{10}$	0.71
$\text{H}_2\text{O}$	1518.1	1556.0	$\text{CH}_4$ , $\text{C}_2\text{H}_6$	0.8
$\text{C}_6\text{H}_{14}$	2826.0	2900.0	$\text{CH}_4$ , $\text{C}_4\text{H}_{10}$ , DMC, $\text{C}_2\text{H}_6$	0.7
HF	4034.9	4114.9	$\text{H}_2\text{O}$	0.5
$\text{C}_4\text{H}_{10}$	2900.0	3004.9	$\text{CH}_4$ , $\text{C}_6\text{H}_{14}$ , $\text{C}_2\text{H}_6$ , $\text{C}_2\text{H}_4$	0.7
$\text{C}_3\text{H}_6$	2820.0	3200.0	$\text{CH}_4$ , EMC, $\text{C}_2\text{H}_6$ , $\text{C}_2\text{H}_4$ , $\text{C}_6\text{H}_{14}$ , DEC, DMC, $\text{C}_4\text{H}_{10}$	0.8

General influences on gas quantification results with FTIR:

- Temperature inside the gas cell
- Pressure inside the gas cell
- Quality of used reference spectra for the quantification

- Interaction of molecules at high concentrations (CO and CO<sub>2</sub> in huge amounts → absorbance peak broadening)
- Interference with absorbance of other components on the same wavenumber range
- Chosen analysis wavenumber-range for quantification for each gas component

The accuracy of the FTIR concentration calculation depends on:

- Empirical standard deviation (**s**) spectrum to spectrum →  $s = <0.2\%$  of measured value

$$s = \sqrt{\frac{\sum_{i=1}^N (x_i - \bar{x})^2}{N - 1}}$$

- Accuracy in the comparison to test gas ( $\Delta\text{conc}$ ; systematic error)

The error propagation to calculate maximal error potential of the FTIR quantified gas components is:

$$\Delta FTIRconc = \Delta\text{conc} + s$$

### 9.1.2 Gas chromatography accuracy

The accuracy of the GC concentration calculation depends on:

- Accuracy of test gas used for calibration (rel.  $\Delta\text{test gas}$ ; see test gas specifications in chapter 9.1.3)
- Linearity of calibration for each gas component (gas component dependent response factor  $RF \pm \Delta RF$ )
- Empirical standard deviation (**s**) measurement to measurement →  $\sim 1\%$  of measured value

$$RF = \frac{\%Amount}{Area}$$

$$\%Amount = RF * Area$$

$$\Delta \%Amount = \Delta RF * Area + RF * \Delta Area$$

The empirical standard deviation of GC measurements already contains the variance of the measured area and therefore the term with  $\Delta Area$  is not included in  $\Delta GCconc$ .

Error propagation to calculate maximal error potential:

$$\Delta GCconc = \Delta\text{test gas} + \Delta RF + s$$

### 9.1.3 Specification of used test gases

Test gases from Linde Gas GmbH with test class 1 certificates according to DIN EN ISO 6141 were used (see Table S2).

**Table S2: Specification of used test gases in % (volume fraction = molar fraction) for the accuracy analysis of FTIR spectrometer and GC measurements**

PG_001	species	target value / %	actual value / %	rel. uncertainty / %
	H <sub>2</sub>	20.90	21.10	1
	C <sub>2</sub> H <sub>2</sub>	5.00	4.84	2
	C <sub>2</sub> H <sub>4</sub>	5.00	5.00	2
	C <sub>2</sub> H <sub>6</sub>	2.00	2.01	2
	CH <sub>4</sub>	10.00	10.00	1
	CO	0.10	0.10	2
	CO <sub>2</sub>	57.00	57.00	rest
<b>PG_002</b>	H <sub>2</sub>	35.00	35.10	1
	C <sub>2</sub> H <sub>2</sub>	2.50	2.43	2
	C <sub>2</sub> H <sub>4</sub>	2.50	2.50	2
	C <sub>2</sub> H <sub>6</sub>	1.00	0.99	2
	CH <sub>4</sub>	5.00	4.96	1
	CO	26.00	26.00	2
	CO <sub>2</sub>	28.00	28.02	rest
<b>PG_003</b>	H <sub>2</sub>	0.100	0.098	2
	N <sub>2</sub>	44.40	44.401	rest
	C <sub>2</sub> H <sub>2</sub>	0.100	0.100	2
	C <sub>2</sub> H <sub>4</sub>	0.100	0.101	2
	C <sub>2</sub> H <sub>6</sub>	0.100	0.100	2
	CH <sub>4</sub>	0.10	0.100	2
	CO	55.0	55.0	1
	CO <sub>2</sub>	0.100	0.100	2
<b>PG_004</b>	N <sub>2</sub>	≥ 99.999		
	O <sub>2</sub>	≤ 3 ppm		
	H <sub>2</sub> O	≤ 5 ppm		
	KW	≤ 0.2		
<b>PG_005</b>	O <sub>2</sub>	20		
	N <sub>2</sub>	rest		
	KW	≤ 0.1		
	NO <sub>x</sub>	≤ 0.1		

## 9.2 Supplementary material particle analysis

*This chapter is already published as supplementary material in:*

Essl C, Golubkov AW, Gasser E, Nachtnebel M, Zankel A, Ewert E, Fuchs A. Comprehensive hazard analysis of failing automotive Lithium-ion batteries in overtemperature experiments. *Batteries* 2020; **6**(30): 1–28. DOI: 10.3390/batteries6020030.

**Figure S1** shows (a) the SE image, (b) BSE image and (c) the EDX spectrum of a particle of class 2. The relevant elements of particles of class 2 were nickel, manganese, cobalt and oxygen. By comparing the weight fraction of all particles of this class, it can be assumed that the chemical formula for these particles is approximately  $(\text{Ni}_{0.45}\text{Mn}_{0.35}\text{Co}_{0.2})_3\text{O}_4$ .

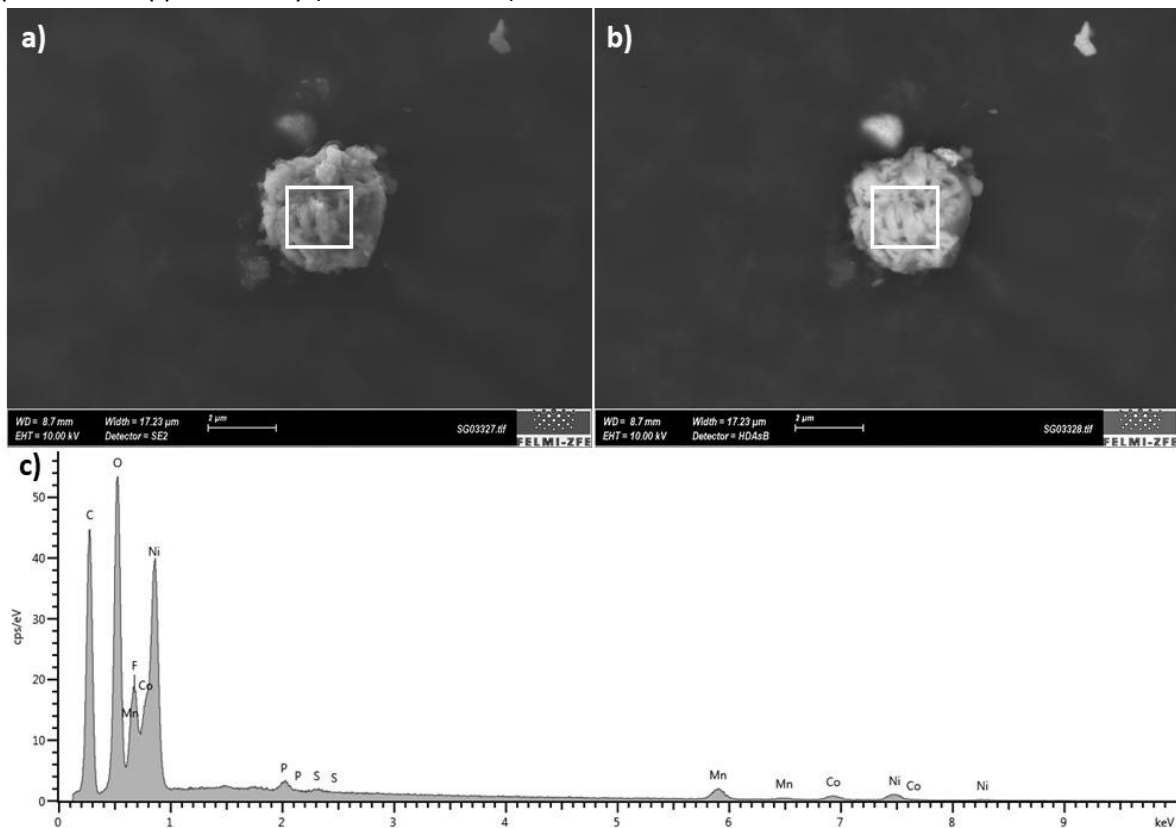


**Figure S1. Analysis of a particle of class 2: a) SE image, b) BSE image, c) EDX spectrum [5].**

**Figure S2** shows (a) the SE image, (b) BSE image and (c) the EDX spectrum of a particle of class 3. As can be seen in the EDX spectrum, the particle mainly consists of manganese and oxygen. For the particle of this class the chemical formula  $\text{Mn}_2\text{O}_3$  (weight fraction of 69.6 wt% Mn and 30.4 wt% O) can be estimated.

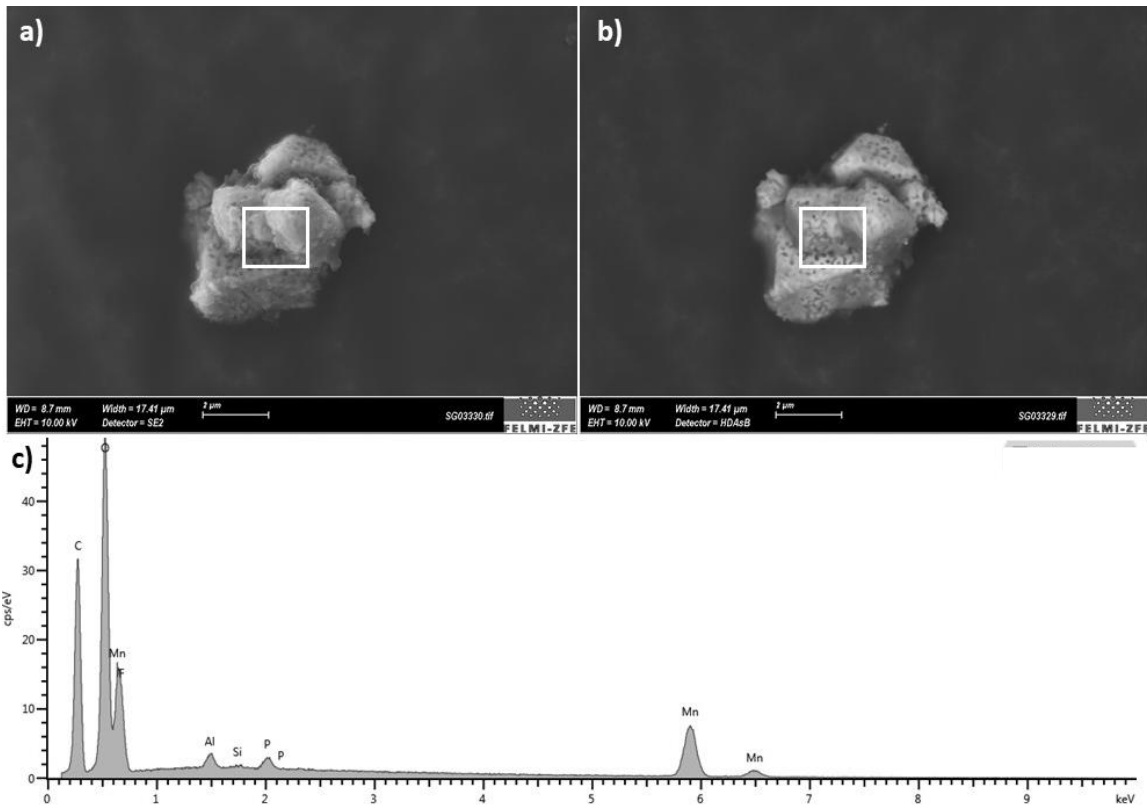


**Figure S2. Analysis of a particle of class 3: a) SE image, b) BSE image, c) EDX spectrum [5].**

In **Figure S3** (a) the SE image, (b) BSE image and (c) EDX Spectrum of a particle of class 4 is shown. Particles of this class consist mainly of carbon.

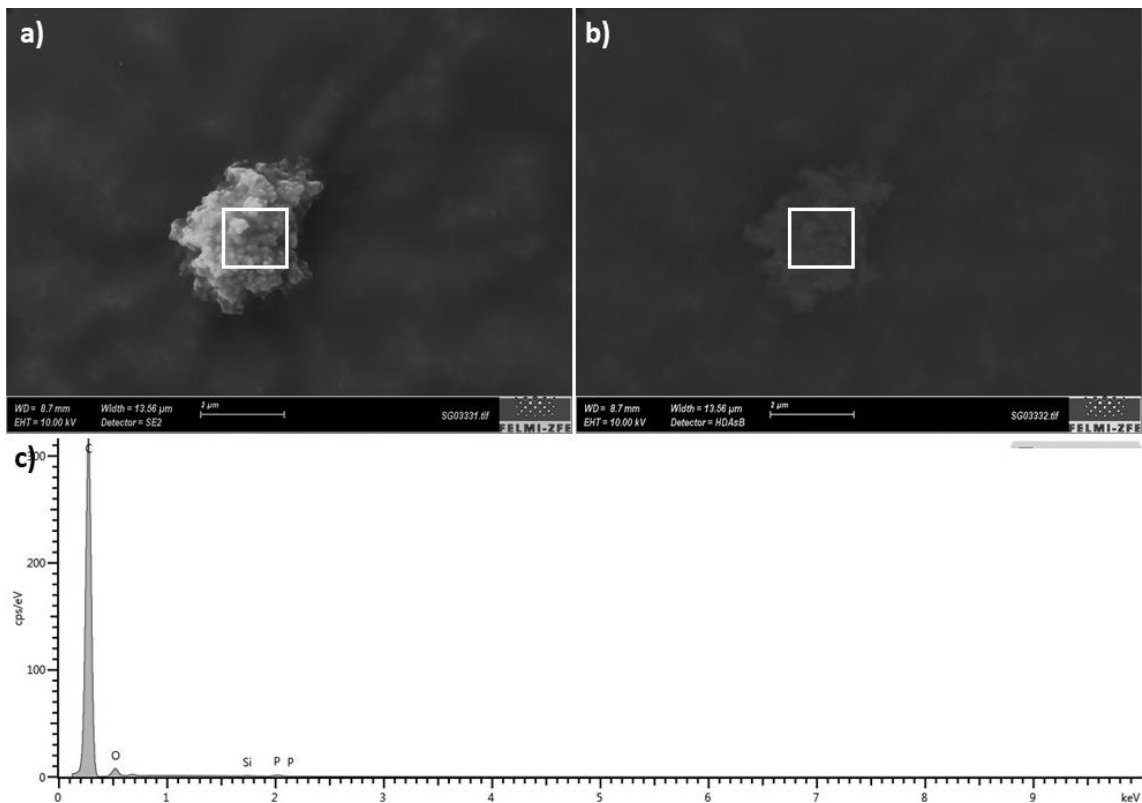


**Figure S3. Analysis of a particle of class 4: a) SE image, b) BSE image, c) EDX spectrum [5].**

**Figure S4** shows (a) the SE image and (b) BSE image of an agglomerate of different classes. This kind of particle is classified to class 5. In the BSE image it can be seen, that different kinds of particles stick on a main particle. The main particle belongs to class 1 (see **Figure S4(c)**), whereas the particles on the main particle belong to class 2 (see **Figure S4(d)**).

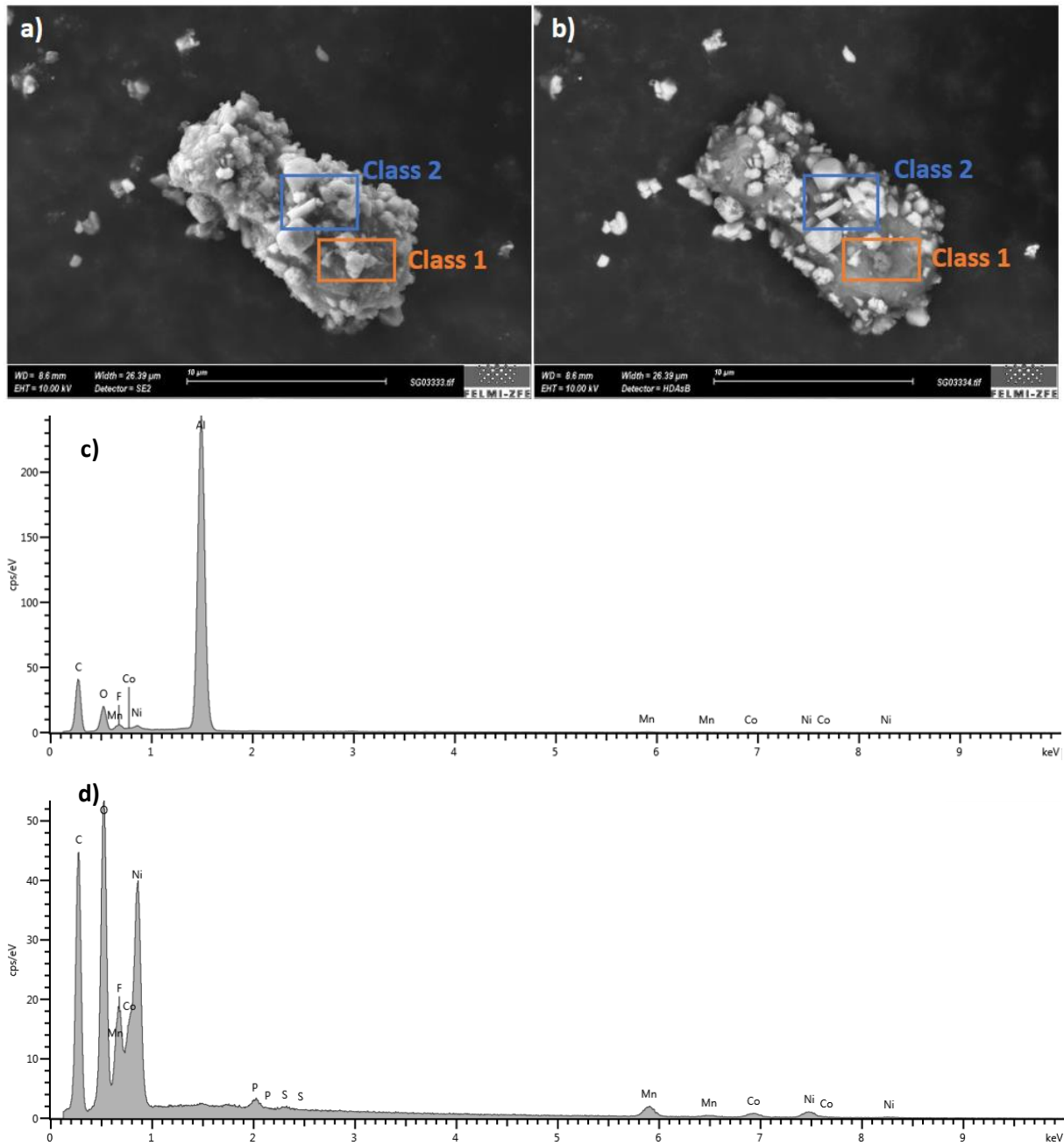


**Figure S4.** Analysis of a particle of class 5: a) SE image, b) BSE image, c) EDX spectrum of area marked Class 1, d) EDX spectrum of area mark Class 2 [5].

## 10 References

1. Winter M, Barnett B, Xu K. Before Li Ion Batteries. *Chemical Reviews* 2018; **118**(23): 11433–11456. DOI: 10.1021/acs.chemrev.8b00422.
2. Nowak S, Winter M. Elemental analysis of lithium ion batteries. *Journal of Analytical Atomic Spectrometry* 2017; **32**(10): 1833–1847. DOI: 10.1039/c7ja00073a.
3. Wagner I. 2017 - Statista -statistic\_id264754\_worldwide-vehicle-sales-by-propulsion-technology-2017-2030 (1).pdf. Statista 2017. <https://www.statista.com/statistics/264754/worldwide-vehicle-sales-by-propulsion-technology-2025/> [accessed March 2, 2020].
4. Ahlswede A. 2020 - Statista - statistic\_id681259\_absatz-von-elektroautos-in-ausgewaehlten-maerkten-weltweit-bis-2019.pdf. Statista 2020. <https://de.statista.com/statistik/daten/studie/681259/umfrage/absatz-von-elektroautos-in-ausgewaehlten-maerkten-weltweit/> [accessed March 2, 2020].
5. Essl C, Golubkov AW, Gasser E, Nachtnebel M, Zankel A, Ewert E, Fuchs A. Comprehensive hazard analysis of failing automotive Lithium-ion batteries in overtemperature experiments. *Batteries* 2020; **6**(30): 1–28. DOI: 10.3390/batteries6020030.
6. Sun P, Bisschop R, Niu H, Huang X. *A Review of Battery Fires in Electric Vehicles*. New York, NY, USA: Springer US; 2020. DOI: 10.1007/s10694-019-00944-3.
7. Pfrang A, Kriston A, Ruiz V, Lebedeva N, di Persio F. *Chapter Eight - Safety of Rechargeable Energy Storage Systems with a focus on Li-ion Technology*. vol. 1. Amsterdam, The Netherlands: Elsevier Inc.; 2017. DOI: 10.1016/B978-0-323-42977-1.00008-X.
8. Spotnitz R, Franklin J. Abuse behavior of high-power, lithium-ion cells. *Journal of Power Sources* 2003; **113**: 81–100. DOI: 10.1016/S0378-7753(02)00488-3.
9. Bandhauer TM, Garimella S, Fuller TF. A Critical Review of Thermal Issues in Lithium-Ion Batteries. *Journal of The Electrochemical Society* 2011; **158**(3): R1–R25. DOI: 10.1149/1.3515880.
10. Wang Q, Sun J, Yao X, Chen C. Thermal Behavior of Lithiated Graphite with Electrolyte in Lithium-Ion Batteries. *Journal of The Electrochemical Society* 2006; **153**(2): A329–A333. DOI: 10.1149/1.2139955.
11. Essl C, Golubkov AW, Fuchs A. Comparing Different Thermal Runaway Triggers for Two Automotive Lithium-Ion Battery Cell Types. *Journal of The Electrochemical Society* 2020; **167**(130542): 1–13. DOI: 10.1149/1945-7111/abbe5a.
12. Bisschop R, Willstrand O, Amon F, Rosengren M. *Fire safety of lithium-ion batteries in road vehicles*. Borås, Sweden: 2019.
13. Isidore C. Are electric cars more likely to catch fire? *CNNMoney (New York)* 2018. <https://money.cnn.com/2018/05/17/news/companies/electric-car-fire-risk/index.html> [accessed December 16, 2020].
14. Skarics R. Wie oft brennen Elektroautos im Vergleich zu Fahrzeugen mit Verbrennungsmotor. *Autorevue* 2017. <https://autorevue.at/ratgeber/statistik-brennen-elektroautos> [accessed December 16, 2020].
15. Larsson F, Anderson P, Mellander BE. Are Electric Vehicles Safer Than Combustion Engine Vehicles. *Systems Perspectives on Electromobility*, 2013.
16. National Standard of the People’s Republic China (GB). GB 38031-2020 Electric vehicles traction battery safety requirements. *43080* 2020: 1–42.
17. Kenichiroh K. Journey to a New Regulatory Option. *OICA Submission to IWG for GTR 20, Phase 2*, Berlin, Germany: 2019.
18. Liao Z, Zhang S, Li K, Zhang G, Habetler TG. A survey of methods for monitoring and detecting thermal runaway of lithium-ion batteries. *Journal of Power Sources* 2019; **436**(226879): 1–19. DOI: 10.1016/j.jpowsour.2019.226879.
19. Besenhard JO, Winter M. Insertion reactions in advanced electrochemical energy storage. *Pure and Applied Chemistry* 1998; **70**(3): 603–608. DOI: 10.1351/pac199870030603.

20. Winter M, Brodd RJ. What are batteries, fuel cells, and supercapacitors? *Chemical Reviews* 2004; **104**(10): 4245–4269. DOI: 10.1021/cr020730k.
21. Oeamtc.at. E-Autos in Österreich 2021. [www.oeamtc.at/thema/elektromobilitaet/alles-ueber-elektroautos-35420295](http://www.oeamtc.at/thema/elektromobilitaet/alles-ueber-elektroautos-35420295) [accessed January 26, 2021].
22. GoingElectric. Plug-in-Hybride: Übersicht und technische Daten. [www.goingelectric.de/wiki/Plug-in-Hybride-Uebersicht-und-technische-Daten](http://www.goingelectric.de/wiki/Plug-in-Hybride-Uebersicht-und-technische-Daten) [accessed January 26, 2021].
23. Hyundai. 2019 Nexo Specifications 2019. [www.hyundainews.com/en-us/models/hyundai-nexo-2019-nexo/specifications](http://www.hyundainews.com/en-us/models/hyundai-nexo-2019-nexo/specifications) [accessed January 26, 2021].
24. Liu K, Li K, Peng Q, Zhang C. A brief review on key technologies in the battery management system of electric vehicles. *Frontiers of Mechanical Engineering* 2019; **14**(1): 47–64. DOI: 10.1007/s11465-018-0516-8.
25. Rahimi-Eichi H, Ojha U, Baronti F, Chow MY. Battery management system: An overview of its application in the smart grid and electric vehicles. *IEEE Industrial Electronics Magazine* 2013; **7**(2): 4–16. DOI: 10.1109/MIE.2013.2250351.
26. Liu QQ, Xiong DJ, Petibon R, Du CY, Dahn JR. Gas Evolution during Unwanted Lithium Plating in Li-Ion Cells with EC-Based or EC-Free Electrolytes. *Journal of The Electrochemical Society* 2016; **163**(14): A3010–A3015. DOI: 10.1149/2.0711614jes.
27. Liu T, Tao C, Wang X. Cooling control effect of water mist on thermal runaway propagation in lithium ion battery modules. *Applied Energy* 2020; **267**(115087): 1–14. DOI: 10.1016/j.apenergy.2020.115087.
28. Coman PT, Darcy EC, Veje CT, White RE. Numerical analysis of heat propagation in a battery pack using a novel technology for triggering thermal runaway. *Applied Energy* 2017; **203**: 189–200. DOI: 10.1016/j.apenergy.2017.06.033.
29. Winter M, Besenhard JO, Spahr ME, Novak P. Insertion Electrode Materials for Rechargeable Lithium Batteries. *Advanced Materials* 1998; **10**(10): 725–763.
30. Aurbach D, Zaban A, Ein-Eli Y, Weissman I, Chusid O, Markovsky B, Levi M, Levi E, Schechter A, Granot E. Recent studies on the correlation between surface chemistry, morphology, three-dimensional structures and performance of Li and Li-C intercalation anodes in several important electrolyte systems. *Journal of Power Sources* 1997; **68**: 91–98. DOI: 10.1016/S0378-7753(97)02575-5.
31. Nowak S, Winter M. Review—Chemical Analysis for a Better Understanding of Aging and Degradation Mechanisms of Non-Aqueous Electrolytes for Lithium Ion Batteries: Method Development, Application and Lessons Learned. *Journal of The Electrochemical Society* 2015; **162**(14): A2500–A2508. DOI: 10.1149/2.0121514jes.
32. Blomgren GE. The development and future of lithium ion batteries. *Journal of the Electrochemical Society* 2017; **164**(1): A5019–A5025. DOI: 10.1149/2.0251701jes.
33. Zhang SS. A review on the separators of liquid electrolyte Li-ion batteries. *Journal of Power Sources* 2007. DOI: 10.1016/j.jpowsour.2006.10.065.
34. Birkl CR, Roberts MR, McTurk E, Bruce PG, Howey DA. Degradation diagnostics for lithium ion cells. *Journal of Power Sources* 2017; **341**: 373–386. DOI: 10.1016/j.jpowsour.2016.12.011.
35. Vortmann-Westhoven B, Winter M, Nowak S. Where is the lithium? Quantitative determination of the lithium distribution in lithium ion battery cells: Investigations on the influence of the temperature, the C-rate and the cell type. *Journal of Power Sources* 2017; **346**: 63–70. DOI: 10.1016/j.jpowsour.2017.02.028.
36. Ren D, Hsu H, Li R, Feng X, Guo D, Han X, Lu L, He X, Gao S, Hou J, Li Y, Wang Y, Ouyang M. A comparative investigation of aging effects on thermal runaway behavior of lithium-ion batteries. *ETransportation* 2019; **2**(100034): 1–13. DOI: 10.1016/j.etrans.2019.100034.
37. Ramadass P, Haran B, White R, Popov BN. Capacity fade of Sony 18650 cells cycled at elevated temperatures: Part I. Cycling performance. *Journal of Power Sources* 2002; **112**(2): 606–613. DOI: 10.1016/S0378-7753(02)00474-3.
38. Barai A, Tangirala R, Uddin K, Chevalier J, Guo Y, McGordon A, Jennings P. The effect of external

- compressive loads on the cycle lifetime of lithium-ion pouch cells. *Journal of Energy Storage* 2017; **13**: 211–219. DOI: 10.1016/j.est.2017.07.021.
39. Evertz M, Kasnatscheew J, Winter M, Nowak S. Investigation of various layered lithium ion battery cathode materials by plasma- and X-ray-based element analytical techniques. *Analytical and Bioanalytical Chemistry* 2019; **411**(1): 277–285. DOI: 10.1007/s00216-018-1441-8.
  40. Broussely M, Biensan P, Bonhomme F, Blanchard P, Herreyre S, Nechev K, Staniewicz RJ. Main aging mechanisms in Li ion batteries. *Journal of Power Sources* 2005; **146**: 90–96. DOI: 10.1016/j.jpowsour.2005.03.172.
  41. Müller V, Scurtu RG, Memm M, Danzer MA, Wohlfahrt-Mehrens M. Study of the influence of mechanical pressure on the performance and aging of Lithium-ion battery cells. *Journal of Power Sources* 2019; **440**(227148): 1–11. DOI: 10.1016/j.jpowsour.2019.227148.
  42. Peabody C, Arnold CB. The role of mechanically induced separator creep in lithium-ion battery capacity fade. *Journal of Power Sources* 2011; **196**(19): 8147–8153. DOI: 10.1016/j.jpowsour.2011.05.023.
  43. Dubarry M, Truchot C, Liaw BY. Synthesize battery degradation modes via a diagnostic and prognostic model. *Journal of Power Sources* 2012; **219**: 204–216. DOI: 10.1016/j.jpowsour.2012.07.016.
  44. Feng X, Ren D, Zhang S, He X, Wang L, Ouyang M. Influence of aging paths on the thermal runaway features of lithium-ion batteries in accelerating rate calorimetry tests. *International Journal of Electrochemical Science* 2019; **14**: 44–58. DOI: 10.20964/2019.01.14.
  45. Feng X, Zheng S, He X, Wang L, Wang Y, Ren D, Ouyang M. Time Sequence Map for Interpreting the Thermal Runaway Mechanism of Lithium-Ion Batteries With LiNi<sub>x</sub>Co<sub>y</sub>Mn<sub>z</sub>O<sub>2</sub> Cathode. *Frontiers in Energy Research* 2018; **6**(126): 1–16. DOI: 10.3389/fenrg.2018.00126.
  46. Feng X, Zheng S, Ren D, He X, Wang L, Cui H, Liu X, Jin C, Zhang F, Xu C, Hsu H, Gao S, Chen T, Li Y, Wang T, Wang H, Li M, Ouyang M. Investigating the thermal runaway mechanisms of lithium-ion batteries based on thermal analysis database. *Applied Energy* 2019; **246**: 53–64. DOI: 10.1016/j.apenergy.2019.04.009.
  47. Guo R, Lu L, Ouyang M, Feng X. Mechanism of the entire overdischarge process and overdischarge-induced internal short circuit in lithium-ion batteries. *Scientific Reports* 2016; **6**(30248): 1–9. DOI: 10.1038/srep30248.
  48. Yang H, Zhuang G V., Ross PN. Thermal stability of LiPF<sub>6</sub> salt and Li-ion battery electrolytes containing LiPF<sub>6</sub>. *Journal of Power Sources* 2006; **161**: 573–579. DOI: 10.1109/CISP.2008.381.
  49. Jhu CY, Wang YW, Wen CY, Shu CM. Thermal runaway potential of LiCoO<sub>2</sub> and Li(Ni<sub>1/3</sub>Co<sub>1/3</sub>Mn<sub>1/3</sub>)O<sub>2</sub> batteries determined with adiabatic calorimetry methodology. *Applied Energy* 2012; **100**: 127–131. DOI: 10.1016/j.apenergy.2012.05.064.
  50. Orendorff CJ, Lamb J, Steele LAM, Spangler SW, Langendorf J. *Quantification of Lithium-ion Cell Thermal Runaway Energetics*. vol. 0486. Albuquerque, NM, USA: 2016.
  51. Huang P, Wang Q, Li K, Ping P, Sun J. The combustion behavior of large scale lithium titanate battery. *Scientific Reports* 2015; **5**(7788): 1–12. DOI: 10.1038/srep07788.
  52. Feng X, Fang M, He X, Ouyang M, Lu L, Wang H, Zhang M. Thermal runaway features of large format prismatic lithium ion battery using extended volume accelerating rate calorimetry. *Journal of Power Sources* 2014; **255**: 294–301. DOI: 10.1016/j.jpowsour.2014.01.005.
  53. Finegan DP, Scheel M, Robinson JB, Tjaden B, Hunt I, Mason TJ, Millichamp J, Di Michiel M, Offer GJ, Hinds G, Brett DJL, Shearing PR. In-operando high-speed tomography of lithium-ion batteries during thermal runaway. *Nature Communications* 2015; **6**(6924): 1–10. DOI: 10.1038/ncomms7924.
  54. Harris SJ, Timmons A, Pitz WJ. A combustion chemistry analysis of carbonate solvents used in Li-ion batteries. *Journal of Power Sources* 2009; **193**: 855–858. DOI: 10.1016/j.jpowsour.2009.04.030.
  55. Mikolajczak C, Michael Kahn P, White K, Thomas Long R. *Lithium-Ion Batteries Hazard and Use Assessment Final Report*. Quincy, MA, USA: 2011.
  56. Roth EP, Doughty DH, Franklin J. DSC investigation of exothermic reactions occurring at

- elevated temperatures in lithium-ion anodes containing PVDF-based binders. *Journal of Power Sources* 2004; **134**: 222–234. DOI: 10.1016/j.jpowsour.2004.03.074.
57. Golubkov AW, Planteu R, Krohn P, Rasch B, Brunnsteiner B, Thaler A, Hacker V. Thermal runaway of large automotive Li-ion batteries. *RSC Advances* 2018; **8**: 40172–40186. DOI: 10.1039/C8RA06458J.
  58. Wang Q, Ping P, Zhao X, Chu G, Sun J, Chen C. Thermal runaway caused fire and explosion of lithium ion battery. *Journal of Power Sources* 2012; **208**: 210–224. DOI: 10.1016/j.jpowsour.2012.02.038.
  59. Gachot G, Ribière P, Mathiron D, Grugeon S, Armand M, Leriche JB, Pilard S, Laruelle S. Gas chromatography/mass spectrometry as a suitable tool for the li-ion battery electrolyte degradation mechanisms study. *Analytical Chemistry* 2011; **83**: 478–485. DOI: 10.1021/ac101948u.
  60. Dahn JR, Fuller EW, Obrovac M, von Sacken U. Thermal stability of  $\text{Li}_x\text{CoO}_2$ ,  $\text{Li}_x\text{NiO}_2$  and  $\lambda\text{-MnO}_2$  and consequences for the safety of Li-ion cells. *Solid State Ionics* 1994; **69**: 265–270. DOI: 10.1016/0167-2738(94)90415-4.
  61. Kumai K, Miyashiro H, Kobayashi Y, Takei K, Ishikawa R. Gas generation mechanism due to electrolyte decomposition in commercial lithium-ion cell. *Journal of Power Sources* 1999; **81–82**: 715–719. DOI: 10.1016/S0378-7753(98)00234-1.
  62. Lyness C, Fleischhammer M, Abert M, Barnett B, McCoy CH, Ofer D, Sriramulu S, Gilljam M, Weydahl H, Forseth S, Vie PJS, Lian T. Lithium-secondary cell: Sources of risks and their effects. *Electrochemical Power Sources: Fundamentals, Systems, and Applications Li-Battery Safety*, Elsevier B.V; 2018. DOI: 10.1016/B978-0-444-63777-2.00007-4.
  63. Turner JA, Kalnaus S, Wang H, Simunovic S, Kumar A, Gorti S, Allu S. *Crashworthiness Models For Automotive Batteries (Report No. DOT HS 812 736)*. Washington, DC: 2019.
  64. Nedjalkov A, Meyer J, Köhring M, Doering A, Angelmahr M, Dahle S, Sander A, Fischer A, Schade W. Toxic Gas Emissions from Damaged Lithium Ion Batteries — Analysis and Safety Enhancement Solution. *Batteries* 2016; **5**(2): 1–10. DOI: 10.3390/batteries2010005.
  65. Lebedeva NP, Boon-Brett L. Considerations on the Chemical Toxicity of Contemporary Li-Ion Battery Electrolytes and Their Components. *Journal of The Electrochemical Society* 2016; **163**(6): A821–A830. DOI: 10.1149/2.0171606jes.
  66. Roth EP, Orendorff CJ. How electrolytes influence battery safety. *The Electrochemical Society Interface* 2012; **21**: 45–49. DOI: 10.1149/2.F04122if.
  67. Larsson F. Thesis for the degree of Licentiate of Engineering: Assessment of safety characteristics for Li-ion battery cells by abuse testing. Chalmers University of Technology, 2014.
  68. Hollmotz L, Hackmann M. LITHIUM ION BATTERIES FOR HYBRID AND ELECTRIC VEHICLES – RISKS, REQUIREMENTS AND SOLUTIONS OUT OF THE CRASH SAFETY POINT OF VIEW. *International Technical Conference on the Enhanced Safety of Vehicles (ESV)*, Washington, DC, USA: 2011.
  69. Feng X, Ouyang M, Liu X, Lu L, Xia Y, He X. Thermal runaway mechanism of lithium ion battery for electric vehicles: A review. *Energy Storage Materials* 2018; **10**: 246–267. DOI: 10.1016/j.ensm.2017.05.013.
  70. Larsson F, Andersson P, Mellander BE. Lithium-Ion Battery Aspects on Fires in Electrified Vehicles on the Basis of Experimental Abuse Tests. *Batteries* 2016; **2**(9): 1–13. DOI: 10.3390/batteries2020009.
  71. Fernandes Y, Bry A, de Persis S. Identification and quantification of gases emitted during abuse tests by overcharge of a commercial Li-ion battery. *Journal of Power Sources* 2018; **389**: 106–119. DOI: 10.1016/j.jpowsour.2018.03.034.
  72. Somandepalli V, Marr K, Horn Q. Quantification of Combustion Hazards of Thermal Runaway Failures in Lithium-Ion Batteries. *SAE International Journal of Alternative Powertrains* 2014; **3**(1): 98–104. DOI: 10.4271/2014-01-1857.
  73. Koch S, Fill A, Birke KP. Comprehensive gas analysis on large scale automotive lithium-ion cells

- in thermal runaway. *Journal of Power Sources* 2018; **398**: 106–112. DOI: 10.1016/j.jpowsour.2018.07.051.
74. Zhao C, Sun J, Wang Q. Thermal runaway hazards investigation on 18650 lithium-ion battery using extended volume accelerating rate calorimeter. *Journal of Energy Storage* 2020; **28**(101232): 1–9. DOI: 10.1016/j.est.2020.101232.
75. Larsson F, Andersson P, Blomqvist P, Mellander BE. Toxic fluoride gas emissions from lithium-ion battery fires. *Scientific Reports* 2017; **7**(10018): 1–13. DOI: 10.1038/s41598-017-09784-z.
76. Essl C, Golubkov AW, Planteu R, Rasch B, Fuchs A. Transport of Li-Ion Batteries: Early Failure Detection by Gas Composition Measurements. *7th Transport Research Arena*, Vienna, Austria: 2018. DOI: 10.5281/zenodo.1491360.
77. Zhang Y, Wang H, Li W, Li C, Ouyang M. Size distribution and elemental composition of vent particles from abused prismatic Ni-rich automotive lithium-ion batteries. *Journal of Energy Storage* 2019; **26**(100991): 1–7. DOI: 10.1016/j.est.2019.100991.
78. Deng J, Bae C, Marcicki J, Masias A, Miller T. Safety modelling and testing of lithium-ion batteries in electrified vehicles. *Nature Energy* 2018; **3**: 261–266. DOI: 10.1038/s41560-018-0122-3.
79. Andersson P, Anderson J, Larsson F, Mellander BE. Modelling of thermal events in Lithium-ion batteries. *2nd IAFSS European Symposium of Fire Safety Science*, Nicosia, Cyprus: 2015.
80. Ruiz V, Pfrang A, Kriston A, Omar N, Van den Bossche P, Boon-Brett L. A review of international abuse testing standards and regulations for lithium ion batteries in electric and hybrid electric vehicles. *Renewable and Sustainable Energy Reviews* 2018; **81**: 1427–1452. DOI: 10.1016/j.rser.2017.05.195.
81. Coman PT, Rayman S, White RE. A lumped model of venting during thermal runaway in a cylindrical Lithium Cobalt Oxide lithium-ion cell. *Journal of Power Sources* 2016; **307**: 56–62. DOI: 10.1016/j.jpowsour.2015.12.088.
82. Feng X, Zheng S, Ren D, He X, Wang L, Liu X, Li M, Ouyang M. Key characteristics for thermal runaway of Li-ion batteries. *Energy Procedia*, vol. 158, Hong Kong, China: 2019. DOI: 10.1016/j.egypro.2019.01.736.
83. Gao S, Feng X, Lu L, Ouyang M, Kamyab N, White RE, Coman P. Thermal Runaway Propagation Assessment of Different Battery Pack Designs Using the TF5 Draft as Framework. *Journal of The Electrochemical Society* 2019; **166**(8): A1653–A1659. DOI: 10.1149/2.1081908jes.
84. Diaz F, Wang Y, Weyhe R, Friedrich B. Gas generation measurement and evaluation during mechanical processing and thermal treatment of spent Li-ion batteries. *Waste Management* 2019; **84**: 102–111. DOI: 10.1016/j.wasman.2018.11.029.
85. Golubkov AW, Scheikl S, Planteu R, Voitic G, Wiltsche H, Stangl C, Fauler G, Thaler A, Hacker V. Thermal runaway of commercial 18650 Li-ion batteries with LFP and NCA cathodes - Impact of state of charge and overcharge. *RSC Advances* 2015; **5**: 57171–57186. DOI: 10.1039/c5ra05897j.
86. Zhang Y, Wang H, Li W, Li C. Quantitative identification of emissions from abused prismatic Ni-rich lithium-ion batteries. *ETransportation* 2019; **2**(100031): 1–10. DOI: 10.1016/j.etrans.2019.100031.
87. Golubkov AW, Fuchs D, Wagner J, Wiltsche H, Stangl C, Fauler G, Voitic G, Thaler A, Hacker V. Thermal-runaway experiments on consumer Li-ion batteries with metal-oxide and olivin-type cathodes. *RSC Advances* 2014; **4**: 3633–3642. DOI: 10.1039/c3ra45748f.
88. Nagasubramanian G, Fenton K. Reducing Li-ion safety hazards through use of non-flammable solvents and recent work at Sandia National Laboratories. *Electrochimica Acta* 2013; **101**: 3–10. DOI: 10.1016/j.electacta.2012.09.065.
89. Perea A, Paoletta A, Dubé J, Champagne D, Mauger A, Zaghbi K. State of charge influence on thermal reactions and abuse tests in commercial lithium-ion cells. *Journal of Power Sources* 2018; **399**: 392–397. DOI: 10.1016/j.jpowsour.2018.07.112.
90. Waldmann T, Wohlfahrt-Mehrens M. Effects of rest time after Li plating on safety behavior—ARC tests with commercial high-energy 18650 Li-ion cells. *Electrochimica Acta* 2017. DOI: 10.1016/j.electacta.2017.02.036.

91. Garche J, Brandt K. *Electrochemical Power Sources: Fundamentals, Systems, and Applications: Li-Battery Safety*. Elsevier B.V; 2018.
92. Wang Q, Jiang L, Yu Y, Sun J. Progress of enhancing the safety of lithium ion battery from the electrolyte aspect. *Nano Energy* 2019; **55**: 93–114. DOI: 10.1016/j.nanoen.2018.10.035.
93. Haregewoin AM, Wotango AS, Hwang BJ. Electrolyte additives for lithium ion battery electrodes: Progress and perspectives. *Energy and Environmental Science* 2016; **9**(6): 1955–1988. DOI: 10.1039/c6ee00123h.
94. Wang H, Du Z, Rui X, Wang S, Jin C, He L, Zhang F, Wang Q, Feng X. A comparative analysis on thermal runaway behavior of Li (NixCoyMnz) O2 battery with different nickel contents at cell and module level. *Journal of Hazardous Materials* 2020; **393**: 1–19. DOI: 10.1016/j.jhazmat.2020.122361.
95. Liu Y, Sun P, Lin S, Niu H, Huang X. Self-heating ignition of open-circuit cylindrical Li-ion battery pile: Towards fire-safe storage and transport. *Journal of Energy Storage* 2020; **32**(101842): 1–12. DOI: 10.1016/j.est.2020.101842.
96. Koch S, Birke KP, Kuhn R. Fast thermal runaway detection for lithium-ion cells in large scale traction batteries. *Batteries* 2018; **4**(2): 1–11. DOI: 10.3390/batteries4020016.
97. Larsson F, Mellander BE. Abuse by External Heating, Overcharge and Short Circuiting of Commercial Lithium-Ion Battery Cells. *Journal of the Electrochemical Society* 2014; **161**(10): A1611–A1617. DOI: 10.1149/2.0311410jes.
98. Huang L, Zhang Z, Wang Z, Zhang L, Zhu X, Dorrell DD. Thermal runaway behavior during overcharge for large-format Lithium-ion batteries with different packaging patterns. *Journal of Energy Storage* 2019; **25**: 1–7. DOI: 10.1016/j.est.2019.100811.
99. Li Y, Feng X, Ren D, Ouyang M, Lu L, Han X. Thermal Runaway Triggered by Plated Lithium on the Anode after Fast Charging. *ACS Applied Materials and Interfaces* 2019; **11**(50): 46839–46850. DOI: 10.1021/acsami.9b16589.
100. Zhang J, Su L, Li Z, Sun Y, Wu N. The evolution of lithium-ion cell thermal safety with aging examined in a battery testing calorimeter. *Batteries* 2016; **2**(2): 1–9. DOI: 10.3390/batteries2020012.
101. Röder P, Stiaszny B, Ziegler JC, Baba N, Lagaly P, Wiemhöfer HD. The impact of calendar aging on the thermal stability of a LiMn 2O4-Li(Ni1/3Mn1/3Co 1/3)O2/graphite lithium-ion cell. *Journal of Power Sources* 2014; **268**: 315–325. DOI: 10.1016/j.jpowsour.2014.06.040.
102. Fleischhammer M, Waldmann T, Bisle G, Hogg BI, Wohlfahrt-Mehrens M. Interaction of cyclic ageing at high-rate and low temperatures and safety in lithium-ion batteries. *Journal of Power Sources* 2015; **274**: 432–439. DOI: 10.1016/j.jpowsour.2014.08.135.
103. Golubkov AW, Planteu R, Rasch B, Essl C, Thaler A, Hacker V. Thermal runaway and battery fire: comparison of Li-ion, Ni-MH and sealed lead-acid batteries. *7th Transport Research Arena, Vienna, Austria*: 2018. DOI: 10.5281/zenodo.1491317.
104. Wenger M, Waller R, Lorentz VRH, März M, Herold M. Investigation of gas sensing in large lithium - ion battery systems for early fault detection and safety improvement, 2014. DOI: 10.1109/IECON.2014.7049366.
105. Cai T, Stefanopoulou AG, Siegel JB. Early Detection for Li-ion Batteries Thermal Runaway Based on Gas Sensing Ting. *ECS Transactions* 2019; **89**(1): 85–97. DOI: 10.1149/08901.0085ecst.
106. Mateev V, Marinova I, Kartunov Z. Automatic system for li-ion battery packs gas leakage detection. *Proceedings of the International Conference on Sensing Technology, ICST, IEEE*; 2019. DOI: 10.1109/ICSensT.2018.8603567.
107. Swartz SL. Lithium Ion Battery Off-Gas Sensor for Battery Health and Safety Monitoring Joint Service Power Expo. *Joint Service Power Expo, Cincinnati, OH*: 2015.
108. Herold M. Detection of failure modes and protection solutions for Li-Ion energy packs by means of gas sensors. *Battery Power Conference*, 2015.
109. Hill D, Gully B, Agarwal A, Nourai A, Thrun L, Swartz S, Koslowske M, Cummings S, Butkowski J, Moore B. Detection of off gassing from Li-ion batteries. *2013 IEEE Energytech, Energytech 2013* 2013. DOI: 10.1109/EnergyTech.2013.6645307.

110. Cummings SR, Swartz SL, Frank NB, Dawson WJ, Hill DM, Gully BH. SYSTEMS AND METHODS FOR MONITORING FOR A GAS ANALYTE. US Patent Application US 201715637381 A1, 2017.
111. Swartz SL, Cummings SR, Frank NB, Dawson WJ. *LITHIUM ION BATTERY OFF-GAS MONITORING FOR BATTERY HEALTH AND SAFETY*.
112. Kovachev G, Schröttner H, Gstrein G, Aiello L, Hanzu I. Analytical Dissection of an Automotive Li-Ion Pouch Cell. *Batteries* 2019; 1–19. DOI: 10.3390/batteries5040067.
113. Gasser E. Characterization of Gas and Particle Released During Thermal Runaway of Li-Ion Batteries. Graz University of Technology, 2019.
114. Goldstein JI, Newbury DE, Michael JR, Ritchie NWM, Scott JHJ, Joy DC. *Scanning Electron Microscopy and X-Ray Microanalysis*. Fourth Ed. Springer, New York, NY; 2017. DOI: <https://doi.org/10.1007/978-1-4939-6676-9>.
115. Atkins PW, Jones L. *Chemie - einfach alles*. 2.Auflage. Weinheim: Wiley-VCH; 2006.
116. Schröder V. *Explosionsgrenzen von Wasserstoff und Wasserstoff/Methan-Gemischen*. Berlin, Germany: 2002.
117. Wang M, Wang Z, Gong X, Guo Z. The intensification technologies to water electrolysis for hydrogen production - A review. *Renewable and Sustainable Energy Reviews* 2014; **29**: 573–588. DOI: 10.1016/j.rser.2013.08.090.
118. Zhou T, Francois B. Modeling and control design of hydrogen production process for an active hydrogen/wind hybrid power system. *International Journal of Hydrogen Energy* 2009; **34**(1): 21–30. DOI: 10.1016/j.ijhydene.2008.10.030.
119. National Institute of Standards and Technology. Signal to noise ratio 2017. <https://www.itl.nist.gov/div898/software/dataplot/refman2/auxillar/snr.htm#:~:text=Description%3A+The+sample+signal+to,+s%7D%7B%5Cbar%7Bx%7D%7D> [accessed December 12, 2020].
120. Schröder DJ. *Astronomical optics*. 2nd ed. San Diego, CA: Academic Press; 2000. DOI: 10.1016/B978-0-12-629810-9.50018-9.
121. Self J, Aiken CP, Petibon R, Dahn JR. Survey of Gas Expansion in Li-Ion NMC Pouch Cells. *Journal of The Electrochemical Society* 2015; **162**(6): 796–802. DOI: 10.1149/2.0081506jes.
122. Onuki M, Kinoshita S, Sakata Y, Yanagidate M, Otake Y, Ue M, Deguchi M. Identification of the Source of Evolved Gas in Li-Ion Batteries Using <sup>13</sup>C-labeled Solvents. *Journal of The Electrochemical Society* 2008; **155**(11): A794–A797. DOI: 10.1149/1.2969947.
123. Wu K, Yang J, Liu Y, Zhang Y, Wang C, Xu J, Ning F, Wang D. Investigation on gas generation of Li<sub>4</sub>Ti<sub>5</sub>O<sub>12</sub>/LiNi<sub>1/3</sub>Co<sub>1/3</sub>Mn<sub>1/3</sub>O<sub>2</sub> cells at elevated temperature. *Journal of Power Sources* 2013; **237**: 285–290. DOI: 10.1016/j.jpowsour.2013.03.057.
124. Aurbach D, Weissman I, Zaban A, Dan P. On the role of water contamination in rechargeable Li batteries. *Electrochimica Acta* 1999; **45**(7): 1135–1140. DOI: 10.1016/S0013-4686(99)00312-6.
125. Du Pasquier A, Disma F, Bowmer T, Gozdz AS, Amatucci G, Tarascon J -M. Differential Scanning Calorimetry Study of the Reactivity of Carbon Anodes in Plastic Li-Ion Batteries. *Journal of The Electrochemical Society* 1998; **145**: 472–477. DOI: 10.1149/1.1838474.
126. Gachot G, Grugeon S, Jimenez-Gordon I, Eshetu GG, Boyanov S, Lecocq A, Marlair G, Pilard S, Laruelle S. Gas chromatography/Fourier transform infrared/mass spectrometry coupling: A tool for Li-ion battery safety field investigation. *Analytical Methods* 2014; **15**: 6120–6124. DOI: 10.1039/c4ay00054d.
127. Sun W, Yang B, Hansen N, Westbrook CK, Zhang F, Wang G, Moshhammer K, Law CK. An experimental and kinetic modeling study on dimethyl carbonate (DMC) pyrolysis and combustion. *Combustion and Flame* 2016; **164**: 224–238. DOI: 10.1016/j.combustflame.2015.11.019.
128. Spangl W, Kaiser A, Schneider J. *Herkunftsanalyse der PM10-Belastung in Österreich - Ferntransport und regionale Beiträge*. Vienna, Austria: 2006.
129. Schmidt R, Fitzek H, Nachtnebel M, Mayrhofer C, Schroettner H, Zankel A. The Combination of Electron Microscopy , Raman Microscopy and Energy Dispersive X-Ray Spectroscopy for the Investigation of Polymeric Materials. *Macromolecular Symposia* 2019; **384**: 1–10. DOI: 10.1002/masy.201800237.

130. Ren D, Feng X, Lu L, He X, Ouyang M. Overcharge behaviors and failure mechanism of lithium-ion batteries under different test conditions. *Applied Energy* 2019; **250**: 323–332. DOI: 10.1016/j.apenergy.2019.05.015.
131. Doh CH, Kim DH, Kim HS, Shin HM, Jeong YD, Moon SI, Jin BS, Eom SW, Kim HS, Kim KW, Oh DH, Veluchamy A. Thermal and electrochemical behaviour of C/LixCoO<sub>2</sub> cell during safety test. *Journal of Power Sources* 2008; **175**: 881–885. DOI: 10.1016/j.jpowsour.2007.09.102.
132. Ohsaki T, Kishi T, Kuboki T, Takami N, Shimura N, Sato Y, Sekino M, Satoh A. Overcharge reaction of lithium-ion batteries. *Journal of Power Sources* 2005; **146**: 97–100. DOI: 10.1016/j.jpowsour.2005.03.105.
133. Redondo-Iglesias E, Venet P, Pelissier S. Eyring acceleration model for predicting calendar ageing of lithium-ion batteries. *Journal of Energy Storage* 2017; **13**: 176–183. DOI: 10.1016/j.est.2017.06.009.
134. Bloom I, Cole BW, Sohn JJ, Jones SA, Polzin EG, Battaglia VS, Henriksen GL, Motloch C, Richardson R, Unkelhaeuser T, Ingersoll D, Case HL. An accelerated calendar and cycle life study of Li-ion cells. *Journal of Power Sources* 2001; **101**: 238–247. DOI: 10.1016/S0378-7753(01)00783-2.
135. Broussely M, Herreyre S, Biensan P, Kaszlejna P, Nechev K, Staniewicz RJ. Aging mechanism in Li ion cells and calendar life predictions. *Journal of Power Sources* 2001; **97–98**: 13–21. DOI: 10.1016/S0378-7753(01)00722-4.
136. Waldmann T, Wilka M, Kasper M, Fleischhammer M, Wohlfahrt-Mehrens M. Temperature dependent ageing mechanisms in Lithium-ion batteries - A Post-Mortem study. *Journal of Power Sources* 2014; **262**: 129–135. DOI: 10.1016/j.jpowsour.2014.03.112.
137. Vetter J, Novák P, Wagner MR, Veit C, Möller KC, Besenhard JO, Winter M, Wohlfahrt-Mehrens M, Vogler C, Hammouche A. Ageing mechanisms in lithium-ion batteries. *Journal of Power Sources* 2005; **147**(1–2): 269–281. DOI: 10.1016/j.jpowsour.2005.01.006.
138. Wohlfahrt-Mehrens M, Vogler C, Garche J. Aging mechanisms of lithium cathode materials. *Journal of Power Sources* 2004; **127**(1–2): 58–64. DOI: 10.1016/j.jpowsour.2003.09.034.
139. Waldmann T, Hogg BI, Kasper M, Grolleau S, Couceiro CG, Trad K, Matadi BP, Wohlfahrt-Mehrens M. Interplay of Operational Parameters on Lithium Deposition in Lithium-Ion Cells: Systematic Measurements with Reconstructed 3-Electrode Pouch Full Cells. *Journal of The Electrochemical Society* 2016; **163**(7): A1232–A1238. DOI: 10.1149/2.0591607jes.
140. Börner M, Friesen A, Grützke M, Stenzel YP, Brunklaus G, Haetge J, Nowak S, Schappacher FM, Winter M. Correlation of aging and thermal stability of commercial 18650-type lithium ion batteries. *Journal of Power Sources* 2017; **342**: 382–392. DOI: 10.1016/j.jpowsour.2016.12.041.
141. Xie S, Ren L, Yang X, Wang H, Sun Q, Chen X, He Y. Influence of cycling aging and ambient pressure on the thermal safety features of lithium-ion battery. *Journal of Power Sources* 2020; **448**(227425): 1–8. DOI: 10.1016/j.jpowsour.2019.227425.
142. Blomgren GE. Electrolytes for advanced batteries. *Journal of Power Sources* 1999; **81–82**: 112–118. DOI: 10.1016/S0378-7753(99)00188-3.
143. Chen S, Wang Z, Yan W. Identification and characteristic analysis of powder ejected from a lithium ion battery during thermal runaway at elevated temperatures. *Journal of Hazardous Materials* 2020; **400**(123169): 1–12. DOI: 10.1016/j.jhazmat.2020.123169.
144. Doughty DH, Roth EP, Crafts CC, Nagasubramanian G, Henriksen G, Amine K. Effects of additives on thermal stability of Li ion cells. *Journal of Power Sources* 2005; **146**(1–2): 116–120. DOI: 10.1016/j.jpowsour.2005.03.170.
145. Todeschini F, Onori S, Rizzoni G. An experimentally validated capacity degradation model for Li-ion batteries in PHEVs applications. *IFAC Proceedings Volumes (IFAC-PapersOnline)*, vol. 8, IFAC; 2012. DOI: 10.3182/20120829-3-MX-2028.00173.
146. Barré A, Deguilhem B, Grolleau S, Gérard M, Suard F, Riu D. A review on lithium-ion battery ageing mechanisms and estimations for automotive applications. *Journal of Power Sources* 2013; **241**: 680–689. DOI: 10.1016/j.jpowsour.2013.05.040.
147. Baghdadi I, Briat O, Delétage JY, Gyan P, Vinassa JM. Lithium battery aging model based on

- Dakin's degradation approach. *Journal of Power Sources* 2016; **325**: 273–285. DOI: 10.1016/j.jpowsour.2016.06.036.
148. Petit M, Prada E, Sauvart-Moynot V. Development of an empirical aging model for Li-ion batteries and application to assess the impact of Vehicle-to-Grid strategies on battery lifetime. *Applied Energy* 2016; **172**: 398–407. DOI: 10.1016/j.apenergy.2016.03.119.
149. Cannarella J, Arnold CB. Stress evolution and capacity fade in constrained lithium-ion pouch cells. *Journal of Power Sources* 2014; **245**: 745–751. DOI: 10.1016/j.jpowsour.2013.06.165.
150. Chen X, Chen G, Yue PL. Investigation on the electrolysis voltage of electrocoagulation Xueming 2007; **57**: 63–236. DOI: 10.1039/9781847557209-00063.
151. Sensirion AG. *Preliminary Datasheet SGP40 Indoor Air Quality Sensor for VOC Measurements*. Stäfa, Switzerland: 2020.
152. Schultealbert C, Uzun I, Baur T, Sauerwald T, Schütze A. Siloxane treatment of metal oxide semiconductor gas sensors in temperature-cycled operation - Sensitivity and selectivity. *Journal of Sensors and Sensor Systems* 2020; **9**: 283–292. DOI: 10.5194/jsss-9-283-2020.
153. Das S, Jayaraman V. SnO<sub>2</sub>: A comprehensive review on structures and gas sensors. *Progress in Materials Science* 2014; **66**: 112–255. DOI: 10.1016/j.pmatsci.2014.06.003.
154. Seifert R, Keller HB, Illyaskutty N, Knoblauch J, Kohler H. Numerical Signal Analysis of Thermo-Cyclically Operated MOG Gas Sensor Arrays for Early Identification of Emissions from Overloaded Electric Cables. *Sensors & Transducers* 2015; **193**(10): 74–79.
155. Sensirion AG. *Datasheet Sensirion SCD30 Sensor Module*. 2018.
156. Göpel W, Schierbaum KD. SnO<sub>2</sub> sensors: current status and future prospects. *Sensors and Actuators B Chemical* 1995; **26–27**: 1–12. DOI: 10.1016/0925-4005(94)01546-T.
157. Illyaskutty N, Knoblauch J, Schwotzer M, Kohler H. Thermally modulated multi sensor arrays of SnO<sub>2</sub>/additive/electrode combinations for enhanced gas identification. *Sensors and Actuators, B: Chemical* 2015; **217**: 2–12. DOI: 10.1016/j.snb.2015.03.018.
158. Andersson P, Rotzetter A. Resistive metal oxide gas sensor coated with a fluoropolymer filter. WO 2018/053655 A1, 2018.
159. Bak SM, Hu E, Zhou Y, Yu X, Senanayake SD, Cho SJ, Kim KB, Chung KY, Yang XQ, Nam KW. Structural changes and thermal stability of charged LiNi<sub>x</sub>Mn<sub>y</sub>Co<sub>z</sub>O<sub>2</sub> cathode materials studied by combined in situ time-resolved XRD and mass spectroscopy. *ACS Applied Materials and Interfaces* 2014; **6**(24): 22594–22601. DOI: 10.1021/am506712c.
160. Essl C, Golubkov AW, Thaler A, Fuchs A. Influence of Cost Reduction and Increasing Energy Density on Thermal Runaway Gas Emission of Li-Ion Batteries. *3RD GRAZ BATTERY DAYS*, vol. 3, 2018.